A New Apparatus for Quantum Simulation with Degenerate Mixtures of Erbium and Lithium

Dissertation
der Mathematisch-Naturwissenschaftlichen Fakultät
der Eberhard Karls Universität Tübingen
zur Erlangung des Grades eines
Doktors der Naturwissenschaften
(Dr. rer. nat.)

vorgelegt von
Alexandre De Martino
aus Paris/Frankreich

Tübingen
2026

Gedruckt mit Genehmigung der Mathematisch-Naturwissenschaftlichen Fakultät der Eberhard Karls Universität Tübingen.

Tag der mündlichen Qualifikation:	26.03.2026
Dekan:	Prof. Dr. Thilo Stehle
1.Berichterstatter:	Prof. Dr. Christian Groß
2.Berichterstatter:	Apl. Prof. Dr. Sebastian Slama

Zusammenfassung

Die Quantensimulation ist ein leistungsstarkes Werkzeug zur Untersuchung hoch korrelierter Systeme. Sie spielt eine entscheidende Rolle bei der Bereitstellung experimenteller Daten in Szenarien, in denen numerische Methoden die Komplexität von Vielteilchenproblemen nicht zuverlässig bewältigen können. In den letzten zehn Jahren haben Plattformen mit ultrakalten atomaren Gasen ihre Vielseitigkeit und Eignung als Quantensimulatoren unter Beweis gestellt.

Heute liegt ein zentraler Schwerpunkt auf dem Verständnis der Hochtemperatur-Supraleitung auf mikroskopischer Ebene, wo die Fermi-Flüssigkeitstheorie und die Beschreibung der Supraleitung durch Cooper-Paare versagen. Ironischerweise sind ultrakalte Atomplattformen trotz ihrer niedrigen absoluten Temperaturen immer noch zu heiß, um das gesamte Fermi-Hubbard-Phasendiagramm zu untersuchen. Es werden weiterhin neue Wege zur Senkung der Temperaturen erforscht, um bisher unzugängliche Bereiche zu erkunden.

In dieser Arbeit wird ein neues Quantengas-Experiment mit ^{166}Er-^{6}Li vorgestellt und die ersten experimentellen Ergebnisse präsentiert. Die Apparatur wird detailliert beschrieben, wobei der Schwerpunkt auf den Er-Subsystemen liegt. Die verschiedenen Kühlstufen werden charakterisiert: Die Zeeman-Kühlung- und die “Angled slowing”, die in Kombination mit einer schmalbandigen magneto-optischen Falle verwendet werden, bilden den Ausgangspunkt. Der anschließende Transfer in eine optische Dipolfalle und der Transport über große Entfernungen mit einem optischen Gitter werden ebenfalls detailliert beschrieben, wobei der Schwerpunkt auf dem Design und der Charakterisierung der Transportvorrichtung liegt.

Die transportierten Atome werden in eine zweite optische Dipolfalle übertragen, die in einer Glaszelle localiziert ist, dort wird anschließend die exakte Vermessung einter tune-out Wellelänge von Er vorgenommen. Die Anisotropie der Ausstimmung wurde verwendet, um den Tensorwert der Polarisierbarkeit von Er zu bestimmen. Der dissipationsfreie Charakter der Falle wurde durch Lebensdauermessungen beider Spezies in ihren jeweiligen Fallen bestätigt.

Schließlich wird über die erste Herstellung einer quantenentarteten Mischung aus ^{166}Er und ^{6}Li berichtet, die die Effizienz der sympathischen Kühlung von Li durch Er demonstriert. Dieses Ergebnis markiert den ersten Meilenstein für dieses Experiment, das darauf abzielt, mit einem Fermi-Gas ein bisher unerreichtes Maß an Entartung zu erreichen.

Abstract

Quantum simulation is a powerful tool for the investigation of strongly correlated systems. Its role is critical to provide experimental data in scenarios where numerical methods cannot reliably handle the complexity of the many-body problems. Over the past decade, ultracold atomic gases platforms have demonstrated their versatility and suitability as quantum simulators.

Today, a central point of interest is the understanding of high-temperature superconductivity on the microscopic scale, where the Fermi liquid theory and description of superconductivity by Cooper pairs break down. The governing Fermi-Hubbard model, which describes the behaviour of fermions in a lattice such as the electrons in a solid, is now implemented in quantum simulators built with cold atoms. Ironically, despite their low absolute temperatures, ultracold atoms platforms are sill too hot to probe the entire Fermi-Hubbard phase diagram. New routes to lower temperatures are still being explored, striving to reach previously inaccessible regimes.

In this thesis, a new quantum-gas experiment of ^{166}Er-^{6}Li is presented along with the first experimental results. The apparatus is described in detail with a focus on the Er subsystems. The different cooling stages are characterized: the Zeeman slower and Angled Slowing stages, used in combination with a narrow-line magneto-optical trap form the starting point. The subsequent loading in an optical dipole trap and long-range transport with an optical lattice are also detailed, with an emphasis on the design and performance of the transport setup.

The transported atoms are transferred in a second optical dipole trap built in a glass cell, where the measurement of Erbium's tune-out wavelength was performed. The anisotropy of the tune-out was used to extract the tensor value of Er's polarizability. The dissipationless character of the trap was confirmed by lifetime measurements of both species in their respective traps.

Finally, the first production of a quantum-degenerate mixture of ^{166}Er and ^{6}Li is reported, demonstrating the efficiency of the sympathetic cooling of Li by Er. This results marks the first milestone for this experiment, in its pursuit of reaching unprecedented levels of degeneracy with a Fermi gas.

Contents

List of Figures

List of Tables

Chapter 1

Introduction

The earliest stages of ultracold-atoms physics can be traced back to the 1970s and 1980s, with pioneering work on the effects of radiation pressure on atomic beams [1–3]. During this period, it became clear that laser light is not merely a probe, but a powerful tool for the control of atoms. This insight led to the realization of the first magneto-optical trap, demonstrated with ^{23}Na [4], in which the lowest attainable temperature was, in principle, set by the Doppler limit. By the late 1980s, this apparent bound was surpassed with the demonstration of sub-Doppler cooling in optical molasses, enabled by the Sisyphus effect, a polarization-gradient cooling mechanism [5, 6]. This milestone was the first in a series of advances that progressively extended the accessible temperature range and cooling mechanisms. Shortly thereafter, the recoil temperature limit was also surpassed, with a gas of ^{4}He cooled by velocity-selective coherent population trapping [7]. Finally, the 1990s marked the emergence of experimental ultracold-atoms physics as we know it, with the first realizations of Bose-Einstein condensates [8–10] and degenerate Fermi gases [11] by evaporative cooling [12].

From then on, the field expanded rapidly in both scale and scope, as the growing number of research groups working with ultracold atoms led to a broad diversification of research directions. Over the past two decades, a wide range of landmark results were achieved in bulk quantum-degenerate gases, including (but not limited to) the observation of matter-wave interference [13], the manifestation of Fermi pressure [14], or the detection of quantized vortices in connection with superfluidity and the BEC-BCS crossover [15–17]. In parallel, ultracold molecules emerged as a natural extension of these efforts, with the realization of molecular Bose-Einstein condensation [18–20], opening the way toward ultracold chemistry [21]. At the same time, loading atoms into optical lattices enabled the exploration of lattice-confined many-body systems, leading to the observation of bosonic and fermionic Mott insulators [22–24].

Arguably, the most powerful aspect of ultracold atoms in optical lattices is the exquisite level of control they provide to experimentalists. In essence, they constitute a clean platform to study the behaviour of atoms in periodic potentials, in which all relevant parameters can be tuned with unprecedented range and precision. For example, the characteristic length scale is set by the lattice spacing, determined by the laser wavelength and beam geometry, while the lattice geometry itself can be engineered through controlled interference of the lattice beams [25]. The relevant energy scales are given by the tunnelling t and the on-site interactions U, both readily adjusted *via* the lattice depth and by means of Feshbach resonances [26]. Finally, the natural time scales of the system are given by the corresponding tunnelling or interaction times. At that point, the connection with solid-state physics became

clear: ultracold atoms could serve as a platform for simulating condensed-matter systems through the direct implementation of analogous Hamiltonians.

This approach, where one system is used to emulate another, is known today as the field of *quantum simulation*. Although the experimental realization of quantum simulators is very recent, the idea has been around for several decades, following its proposal by Feynman [27]. His suggestion was to avoid the increasing computational complexity of quantum many-body problems with classical computers, and to "let nature do the work" instead. In this approach, the quantum simulator is engineered to realize a specific, simple but well-controlled Hamiltonian in a "bottom-up" fashion. The idea is to identify and understand the main contributions that can capture the physical phenomenon of interest, rather than figuring out the exact Hamiltonian which governs the real system; usually a prohibitively difficult task. This bottom-up philosophy is particularly well suited to the study of strongly correlated condensed-matter systems, where even minimal lattice models can give rise to rich, yet not fully understood physics. A prominent example is that of the Hubbard model [28], originally introduced to describe correlated electrons in solids and widely regarded as a minimal framework for high-temperature superconductivity [29].

Discovered in cuprate materials in 1986 [30], high-temperature superconductivity sparked intense experimental and theoretical efforts aimed at identifying its microscopic origin [31]. Despite these efforts, a complete microscopic understanding remains elusive. In solid-state systems, experimental probes are often limited to global observables, making it difficult to directly access local correlations and microscopic degrees of freedom. In contrast, the advent of quantum gas microscopes in the 2010s [32] has enabled site- and spin-resolved imaging of ultracold atoms in optical lattices, providing direct access to microscopic observables. This paradigmatic change in experimental accessibility further strengthened the connection between both fieds, and established cold atoms as a complementary platform for the investigation of Hubbard models.

From a theoretical standpoint, the need for complementary approaches is particularly acute for fermionic lattice systems described by the Fermi-Hubbard model. In the doped regime, the structure of the phase diagram remains the subject of ongoing debate, as numerical methods face severe challenges arising from the exponential growth of the Hilbert space and the fermionic sign problem [33, 34]. These limitations hinder reliable access to the low-temperature regime and have so far prevented a consensus on the nature of the ground state [35, 36]. From an experimental perspective, steady progress has been made towards lower temperatures over the past years. In bulk gases, an early experiment with a mixture of ^{23}Na-^{6}Li was capable of cooling a Fermi gas down to $T/T_F = 0.05$, at $93\,\mathrm{nK}$ [37]. Only ten years later was this record broken, with a ^{7}Li-^{6}Li mixture reaching $T/T_F = 0.03$ [38]. Until recently, typically accessible temperatures in lattice experiments were on the order of $T/t \simeq 0.25$, well above the regimes of interest associated with the pseudogap, strange metal, d-wave superconducting, or stripe phases; all unexplored phases with quantum simulators so far. However, ongoing advances in cooling and trap engineering, in particular the use of entropy redistribution and reservoir-based schemes [39, 40], resulted in a strong leap forward. Two groups, in Harvard and Munich, were able to lower the accessed temperatures down to $T/t = 0.15$ [41, 42] and $T/t = 0.05$ [43], stepping on the door of the pseudogap phase.

Importantly, the limitations encountered so far are technical in nature rather than fundamental. This motivates the investigation of alternative routes toward lower temperatures, including sympathetic cooling, which we pursue here using a Bose-Fermi mixture of ^{166}Er and ^{6}Li. The use of a heteronuclear mixture offers several advantages for this cooling strategy, which can be grouped into three main aspects. First, it enables a separation of roles, whereby one species carries the many-body physics of interest while the second acts as an entropy reservoir. Second, the mismatch in heat capacities between the two species can be exploited to enhance entropy removal from the target system [44] *via* the ratio T_C/T_F of the critical and Fermi temperatures. Third, atomic mixtures provide increased technical flexibility. Most notably, they enable species-selective trapping [45], which in turn can be used for selective evaporation. More broadly, heteronuclear mixtures can also offer access to different quantum statistics when suitable isotopes are available, and to a wide range of physical phenomena [46], including polarons and impurity physics, Efimov states, or exotic superfluidity. Although this approach does not rely on the complex implementation of trap-engineering techniques, it is not exempt from its own technical challenges. In particular, cooling efficiency is limited by the different scaling of bosonic and fermionic heat capacities $C_{B,F}$ in the quantum-degenerate regime [47], which can result in a reduced cooling power of the bosonic bath when $C_B < C_F$. In addition, a mass imbalance between the two species can lead to differential gravitational sag, potentially causing spatial separation of the trapped clouds. Finally, mean-field interactions may hinder cross-species thermalization if the mixture enters an immiscible regime, resulting in phase separation.

In light of these considerations, the ^{166}Er-^{6}Li mixture naturally appears as a promising candidate for efficient sympathetic cooling towards high quantum degeneracy. In this scheme, Erbium primarily serves as a coolant and entropy reservoir, while Lithium realizes the fermionic system of interest. Erbium has a very rich optical spectrum [48], with transitions ranging from broad to ultranarrow, whereas Li has essentially one strong optical transition at $671\,\mathrm{nm}$ [49]. A crucial ingredient is the existence of a tune-out wavelength for Er near its narrow transition at $841\,\mathrm{nm}$ [50], which allows the species-selective trapping of Li while remaining far-detuned from all optical transitions of both elements. In addition, the large mass imbalance is also favorable for efficient sympathetic cooling, notably through its influence on the ratio T_C/T_F. Finally, both species have stable bosonic and fermionic isotopes, thus providing flexibility for future experiments with different quantum statistics.

The remainder of this thesis is devoted to the design and characterization of our experimental apparatus, followed by the implementation of our species-selective trap, and conludes with the first realization of a quantum-degenerate mixture of ^{166}Er and ^{6}Li.

Outline

The thesis is structured as follows:

In Chapter 2, we introduce the Fermi-Hubbard model, and discuss how ultracold atom experiments have emerged as a particularly well-suited platform for its study. We then address the central role of low temperatures in this context, and briefly review the current limitations to access colder regimes. Finally, we motivate the choice of the ErLi mixture, showing how its properties make it favorable in both cases.

In Chapter 3, we describe the experimental apparatus, focusing on its three main subsystems: the vacuum system, the laser setups, and the magnetic coils.

In Chapter 4, we first detail and characterize the initial cooling stages of Erbium, consisting of the Zeeman Slower, Magneto-Optical Trap, and Optical Dipole Trap. We then present the design and performance of our long-range optical transport to the glass cell.

In Chapter 5, we present the measurements of Erbium's tune-out wavelength near its $841\,\mathrm{nm}$-transition, including its anisotropy. We also demonstrate the dissipationless character of the trap with lifetime measurements of Er and Li.

In Chapter 6, we report the first successful realization of a quantum-degenerate mixture of ^{166}Er-^{6}Li, and document the associated preliminary observations.

Publications

The following articles have been published in the context of this thesis:

> ***Dissipationless tune-out trapping for a lanthanide-alkali-metal quantum gas mixture***
> Alexandre De Martino*, Florian Kiesel*, Jonas Auch, Kirill Karpov, and Christian Groß
> Phys. Rev. A 112, L051304 (2025)

> ***Long-term stable laser injection locking for quasi-CW applications***
> Florian Kiesel*, Kirill Karpov*, Alexandre De Martino, Jonas Auch, and Christian Groß
> EPJ tech. instrum. 12.1, (2025)
> Patent application number EP24209446.4, 29 October 2024.

*Equal contributors

Chapter 2

The quest for ever lower temperatures

2.1 The 2D Fermi-Hubbard model

2.1.1 Quantum simulation of cuprates with cold atoms

The implementation of the Hubbard model can probably be considered one of the strongest achievements of cold atom platforms. This model, coming from the field of solid-state physics, was introduced in 1963 to explain the electron dynamics and magnetic properties of strongly correlated materials [28, 51, 52]. But the general interest for this model really caught on after the discovery of high-temperature superconducting cuprates in 1986 [30], and after Anderson proposed it as a minimal model that could capture the physics at hand [53]. Today, it is still regarded as the paradigmatic model to describe correlated systems of fermions on a lattice. In general, the Hubbard Hamiltonian relies on three assumptions: the system is in the lowest Bloch band, with only nearest-neighbor tunnelling and on-site interactions. It can be declined in two versions, the Bose-Hubbard and the Fermi-Hubbard Hamiltonians, depending on the particles under study. For bosons, the Bose-Hubbard Hamiltonian is:

$$H_{\mathrm{BH}} = -t \sum_{\langle i,j \rangle} \left(b_i^\dagger b_j + b_j^\dagger b_i \right) + \frac{U}{2} \sum_i n_i (n_i - 1) \tag{2.1}$$

where t is the tunnelling energy, U is the interaction energy between particles on the same site, $b_i^\dagger, b_i$ are the creation and annihilation operators for bosons on the lattice site i and $n_i = b_i^\dagger b_i$ is the particle number operator. For fermions, the Pauli exclusion principle restricts the amount of particles per site to one per spin state, and the Fermi-Hubbard model is given by:

$$H_{\mathrm{FH}} = -t \sum_{\langle i,j \rangle, \sigma} \left(c_{i,\sigma}^\dagger c_{j,\sigma} + c_{j,\sigma}^\dagger c_{i,\sigma} \right) + U \sum_i n_{i\uparrow} n_{i\downarrow} \tag{2.2}$$

where $(c_i^\dagger, c_i)$ are the creation and annihilation operators for fermions on the lattice site i with a spin $\sigma \in \{\uparrow, \downarrow\}$.

Despite the heavy theoretical work undertaken in past decades, the model still remains unsolvable, except for its 1D version [35, 54]. Additionally, numerical methods still struggle to compute the phase diagram for higher dimensions, including that of the 2D case, particularly relevant for cuprates. For the Fermi-Hubbard model (FHM), the infamous sign problem confronts the numerical simulations to an exponential barrier when the calculations are

made for low-temperature systems [34, 55]. Experimentally, solid-state experiments work with platforms where the typical length, time and energy scales are difficult to probe. For electrons in a solid, the lattice constant is on the order of $1\,\text{Å}$, tunnelling happens at the femtosecond scale, and the particle interaction is about $5\,\text{eV}$. Moreover, the experiments are limited to global observables, and can only probe the systems with bulk techniques such as X-ray and neutron scattering, or with two-points correlation measurements in momentum space *via* spectroscopic techniques such as ARPES (angle-resolved photoemission spectroscopy) or STS (scanning tunnelling spectroscopy) [29].

In contrast, cold atoms provide a complementary, yet promising approach to explore the Fermi-Hubbard phase diagram. The three assumptions used to derive the FHM are fulfilled with a vast majority of experiments and the control of the Hubbard parameters is unprecedented, leading to an almost perfect FHM implementation. In a real solid, the lattice is always distorted by impurities and phonons, and cannot be easily tuned for experiments. In cold atoms, because the lattice is made with lasers, the structure is defect-free, independent of the charge carriers and all the parameters can be tuned independently. For instance, the lattice depth provides control on the tunnelling t and interaction U, to control the parameter U/t. The interaction can also be tuned alone by exploiting Feshbach resonances [26]. A key parameter, doping, can also be tuned with the evaporation stage or with a state-preparation stage when the atoms are loaded on the lattice. Compared to the solid-state platforms, the diluteness of quantum gases changes the system scales to more convenient values. The typical lattice constant is $500\,\text{nm}$, the tunnelling is on the millisecond scale, and the Hubbard interaction is close to $U/h \approx 1\,\text{kHz} = 10^{-12}\,\text{eV}$. It means that the interaction dynamics are much slower than the ultrafast electron correlations, and resolvable in many-body systems. However, the dimensionless quantities which govern the system's behaviour, usually U/t and T/t can be tuned to match that of cuprates by careful choice of the lattice beams and magnetic fields parameters. With this level of control, cold atoms in a 2D lattice quickly became a major platform for simulating the more complicated copper oxides materials, whose high-temperature superconductivity is still not understood [29].

2.1.2 The 2D Fermi-Hubbard phase diagram

At half-filling

In the FHM introduced above, a rich phase diagram emerges from the competition between the kinetic energy (gain *via* delocalization over the lattice sites) and the on-site interaction. Here, a brief description is given as an overview, but a detailed discussion can be found in [35]. To understand its structure, it is instructive to begin with the simple case of a half-filled lattice in three dimensions, where each lattice site has on average one fermion and the spin populations are balanced. This special case is well understood theoretically, and a simplified representation of the temperature-interaction phase diagram is given in Fig. 2.1.

To describe it, it is convenient to separate the charge and spin sectors. They simply correspond to the motional and spin degrees of freedom respectively.[1] In the *charge sector*, three

[1]The terminology "charge" comes from condensed matter, where the carriers are only electrons. In cold atoms, the carriers are neutral but the wording stayed, and can be understood as "density".

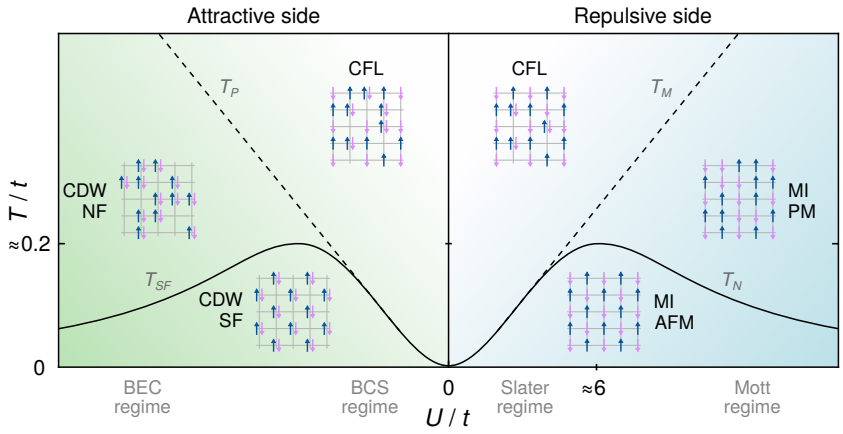

Figure 2.1 | Phase diagram of the FHM at half filling. In the charge sector, the system undergoes two crossovers (dashed lines), from CDW, to CFL, to MI. In the spin sector, it has two second-order phase transitions (solid lines), from CFL to either SF (attractive side) or AFM (repulsive side). The five distinct regimes are schematically represented for an ensemble of spin up (blue) and down (pink) particles on a lattice. Figure adapted from [35].

distinct regimes are found, separated by smooth crossovers. For strong repulsive interactions ($U \gg t$) and low temperatures, the system is in a Mott insulator (MI) phase, characterized by the pinning of the particles to their lattice sites and a vanishing compressibility. For strong attractive interactions and low temperature, the system is governed by stable pairs of fermions of opposite spins, also called charge-density waves (CDW). In both cases, the regimes are connected by a smooth crossover and happens at the Mott temperature T_M and critical "pairing" temperature T_P respectively. At intermediate interactions, the system is a correlated Fermi liquid (CFL), which is metallic and displays density fluctuations. In the *spin sector*, the system undergoes second-order phase transitions, where the ordering of the spins changes qualitatively. The phase transitions are driven by a competition between tunnelling, interactions and Pauli blocking. On the repulsive side, the transition separates the disordered paramagnetic (PM) and ordered anti-ferromagnetic (AFM) orders, situated above and below the Néel temperature $T_N = 4t^2/k_\mathrm{B}U$ respectively. On the attractive side, the transition distinguishes the Normal Fluid (NF) from the Superfluid (SF) states, characterized by the famous BEC-BCS crossover.

Two additional comments can be made. First, in the weakly interacting regime (Slater regime), the situation is more intricate than for a simple Mott insulator or superfluid phases. The charge and spin sectors cannot be separated any longer, and the freezing of charges and the anti-ferromagnetic orders take place simultaneously. Second, the symmetry of the phase diagram is not a coincidence, and finds its origin in the particle-hole symmetry inherent to bipartite lattices.[2] The paramagnetic Mott insulator is transformed into a disordered charge-density wave (the NF phase), and the anti-ferromagnetic MI is transformed into an ordered CDW (the SF phase) [56].

[2] A lattice is bipartite if its sites can be divided into two sublattices where sites in one sublattice only interacts with sites in the other sublattice. Common examples are square, cubic or honeycomb lattices.

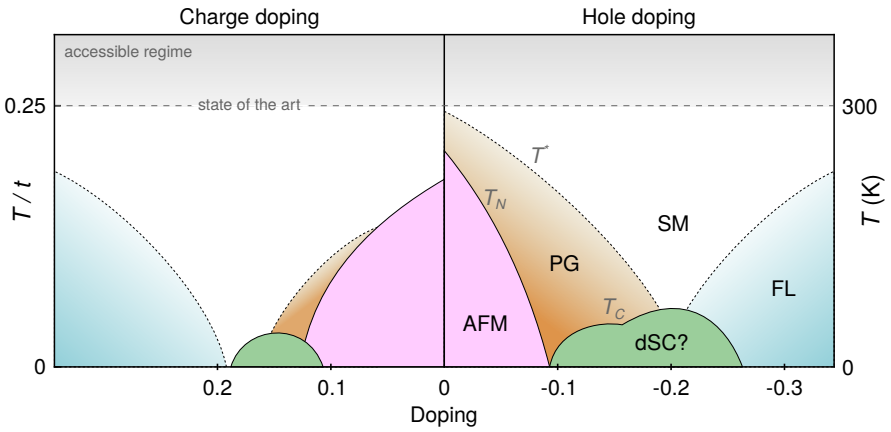

Figure 2.2 | Phase diagram of the doped FHM at generic interactions. The presence (absence) of additional charges from the half-filled case results in a richer phase diagram, with the appearance of the pseudo-gap (PG), d-wave superconductivity (dSC) and strange metal (SM). The Fermi Liquid (FL) corresponds to the Normal Metal (NM) in the language of solid-state physics. The numerical values are only here to give orders of magnitude and cannot be taken as exact. The temperature scale on the right is the equivalent temperature of the solid-state superconductors, where typically $U/t \approx 7$. The shadowed area shows the accessible regime for cold atoms experiments, with the exception of [41, 43], who reached $T/t = 0.2$ and $T/t = 0.05$ respectively. Figure adapted from [29, 35, 36, 57].

Away from half-filling: with doping

Although the half-filled system is already instructive and served as a benchmark for ultracold atoms experiments, the real interest for the FHM lies in the doped regime. For such a system, the proposed phase diagram presented in Fig. 2.2 could only be obtained after extensive experimental efforts with cuprates, in an attempt to understand the observed superconductivity in a regime where it was not expected. So far, the diagram itself is commonly admitted as being a qualitative representation, wherein the nature of the ground state depending on the parameters is still heavily debated.

The first striking feature of this phase diagram is the breaking of the particle-hole symmetry, explained by a difference in chemical potential depending on the nature of the doping. Intuitively, it can be understood as the difference between a hole or a doublon moving in the lattice: while the doublon is subject to the lattice occupancy, the hole can move around without an interaction energy cost. In both cases, the AFM order is preserved for small dopings, but it expands much farther in the particle-doping than in the hole-doping directions. Beyond a certain doping value, the insulator transitions into an unconventional superconductor whose phase (or pairing gap) exhibits a d-wave symmetry (dSC). Close to these phases, an interesting regime has been found: the pseudo-gap (PG). In this regime, the electronic excitations are selectively suppressed depending on their momentum, leading to the so-called "Fermi arcs", remnants of a Fermi surface which is breaking apart [58]. Although the underlying mechanism for the pseudogap has no consensus, most theories share a common feature: the short-range spin correlations inherited from the Mott insulator phase [58]. It is also presented as a precursor to the superfluid regime, where pairs start to

form but cannot condense because of thermal fluctuations. At further doping, the strange metal phase appears. It is characterized by a resistivity which is linear in temperature over a wide range, in contrast to the saturated resistivity of normal metals. In a normal metal, the saturation is usually explained by the comparison of the electron mean free path with their thermal (de Broglie) wavelength. When the temperature rises, the mean free path in the solid decreases, and the increased rate of collisions results in a higher resistivity. At high temperatures, unless the metal melts first, these characteristic lengths become similar, and the resistivity cannot increase further. In a copper oxide strange metal, the resistivity is linear for temperatures as high as they could be measured, even when the inferred mean free path is smaller than the thermal wavelength [29]. Finally, for an overdoped system, it seems that a normal Fermi liquid is recovered.

It is important to keep in mind that to this day, many questions remain open [35, 36]. Is the 2D Fermi-Hubbard model good enough to capture the high-temperature superconductivity of the cuprates [59]? Does it need additional terms, such as a diagonal hopping term or more complex geometries, as can be found in bilayer or mixed-dimensional systems? What is the origin of the pseudogap, and what is the nature of the strange metal [58, 60, 61]? What is the ground state of the doped model, when several orders compete against each other [62–66]? Are current numerical methods adequate to compute accurate results [33, 34]? It is now the ambition of cold atoms machines to shed a new light on these issues by exploring the phase diagram of doped systems, and tremendous progress has been realized in the past few years.

2.1.3 Fermi-Hubbard with cold atoms: where do we stand?

The contribution of the ultracold atoms community to the questions cited above is still very new, yet already abundant. Two recent reviews [35, 36] cover the topic in great details, and the interested reader will find ample information therein. However, it is interesting to have a brief historical perspective to understand how cold atoms platforms made their way into the Hubbard physics. The very first investigations started in the early 2000's, rather quickly after the first degenerate gases were produced. In these pioneering experiments, the Bose-Hubbard model was the first to be realized, where the superfluid to Mott insulator transition was observed in a gas of $^{87}\mathrm{Rb}$ [22] in 2002. The fermions followed the same path only a few years later, with the observation of the Fermi surface [67] in 2005 and of the anti-bunching effect [68] in $^{40}\mathrm{K}$ Fermi gases in 2006. At the same time, the first signature of long-range phase coherence [69] was reported in a strongly interacting Fermi gas of $^{6}\mathrm{Li}$. Then, in 2008 came the first fermionic Mott insulators [23, 24], observed with repulsively interacting Fermi gases of $^{40}\mathrm{K}$ in a 3D lattice. Finally, the first detection of short-range spin correlations was achieved in 2013 with $^{40}\mathrm{K}$ [70] and in 2015 with $^{6}\mathrm{Li}$ [71] experiments. All of these results were obtained with global, bulk quantities, derived from observations of the system in its entirety.

A real paradigm shift happened with the advent of quantum gas microscopes [32, 57]. Once again, bosons were the first to witness it in 2009, with single-site resolution imaging of $^{87}\mathrm{Rb}$ on a 2D lattice [72, 73], showing the famous wedding cake structure of the Mott insulator at the same time. Fermionic microscopes took longer to be realized, but 2015 marked the change with the imaging of $^{6}\mathrm{Li}$ [74, 75] and $^{40}\mathrm{K}$ [76–78]. This technical

prowess opened an entire realm of newly accessible measurements, where a real-space study of the system can be done at the microscopic scale. This new generation of experiments was able to establish several important milestones in the study of the 2D Fermi-Hubbard model. Among them are the observation of the Mott insulator [79, 80], spin correlations [81], spin and charge correlations in a doped system [82], long-range AFM order [40], or the equation of state of the 2D FHM [83].

Since then, several groups (Harvard [40, 81, 84, 85], Munich [86, 87], MIT [82, 88, 89], Princeton [90, 91] and Bonn [92]) have been pushing towards lower temperatures for fermions in a 2D lattice to try and observe the low-temperature phases (see Fig. 2.2). Between 2016 and 2025, the temperature in the lattice was always between $T/t \sim 1$ and $T/t = 0.3$, with the exception of [40], where $T/t = 0.25$ could be achieved by removing entropy from the system *via* very precise engineering of the lattice potential [39]. Very recently, this technique was brought a step further in both Harvard [42, 43] and Munich [41], where the record temperatures of $T/t = 0.05$ [43] and $T/t = 0.15$ [41, 42] were low enough to observe the pseudogap. With this milestone, cold atoms have entered a new era, effectively demonstrating that they are now on the doorstep of the "discovery regime" of quantum simulators [57].

For the sake of completeness, a few words can also be said about the new directions that cold atoms have taken. First, the detection methods are being enriched with new techniques. The quantum gas microscopes were improved with the addition of spin-resolved imaging [93–97], circumventing the parity-projection problem [32], and solid-state techniques are being imported in cold atoms with the first ARPES measurement [98]. Second, the FHM is also being probed outside the pure 2D case [25]. For example, recent experiments have realized different geometries [99–101], programmable lattices [96, 102, 103], bilayer systems [92, 104], or SU(N) anti-ferromagnets [105–108], to name a few.

2.2 Limits to achievable temperature

It is now clear that cold atoms need to reach even lower temperatures than the current state of the art, but the task is especially difficult with fermions. In this endeavor, two paths open to us: the atoms can be cooled further in the lattice directly (as demonstrated by the Harvard and Munich experiments), or they can be loaded in the lattice with a lower initial temperature *via* better prior cooling. Both routes have their own difficulties, and require challenging experimental techniques. Either way, the final temperature of a cloud is dictated by a balance between cooling and heating rates. Here we make a brief description of the problems at hand, but a thorough discussion can be found in the companion thesis [109].

2.2.1 Cooling limits

So far, evaporative cooling [12] has been the only technique which could be used to reach deep quantum degeneracy. Two exceptions stand out, with the Bose-Einstein condensation of $^{84}\mathrm{Sr}$ [110] and $^{87}\mathrm{Rb}$ [111] in two experiments where only optical techniques were

used. However, fermionic clouds are intrinsically difficult to cool down, and, for a single-component Fermi gas, evaporative cooling simply "does not work" [54]. The issue with forced evaporation is the following. After trapping atoms in an Optical Dipole Trap (ODT), the trap depth is continuously lowered to let the hottest atoms escape. The remaining atoms re-thermalize by (ideally) fast elastic collisions, and the cloud gets colder. When the temperature gets low enough (on the order of the millikelvin), the partial-wave collisions are suppressed for all but s-wave scattering. However, because of the Pauli exclusion principle, identical fermions cannot undergo s-wave collisions and the thermalization process halts. These issues prevent fermions from reaching degeneracy in a single-component Fermi gas dominated by contact interactions. A notable example that could reach degeneracy in a single-component gas is atoms that have a long-range interaction. This is found in magnetic atoms, such as Er and Dy, where the long-range Dipole-Dipole Interaction (DDI) is not suppressed, and prevents the elastic cross-section between identical fermions from vanishing. Using the DDI, it was possible to bring both species to degeneracy ($T/T_F = 0.2$) by direct evaporative cooling [112, 113]. For all other fermionic atoms, the solution to maintain a continuous thermalization is to bring another component in the trap, that the fermions can interact with. It can be either identical atoms with a different spin state, a different isotope, or a different atom altogether. Both types of mixtures have existed from the early ages of cold atoms, including in the first observations of a Degenerate Fermi Gas (DFG) [11, 14, 114]. However, they both have intrinsic issue with cooling.

Fermi-Fermi mixtures A Fermi-Fermi (FF) mixture will be limited by a vanishing collisional rate the same way that a single-component Fermi gas would, albeit at a typical temperature of $T/T_F \approx 0.15$. The reason is, again, Pauli blocking. Collisions can be seen as a re-arrangement of the particles among the energy levels of the system, and can occur only when both exit channels are free. For the cloud to cool down, the collisions need to distribute the particles so that they fill the lowest energy states, in particular the states below the Fermi energy. At high degeneracy, or low T/T_F, the probability for such a collision to happen is strongly suppressed, since most final states are already occupied. Therefore, the collision rate is reduced, and tends to zero as $(T/T_F)^2$ [115]. Equivalently, the thermalization time increases quadratically, and is effectively divergent for all purposes in the laboratory below $T/T_F \approx 0.1$ [116]. In the literature, many examples of such Fermi-Fermi mixtures can be found, where degeneracy was achieved. Among them, a few were able to reach the threshold of $T/T_F \lesssim 0.1$; in spin-mixtures of ^{6}Li [117–119], ^{40}K [18] and ^{87}Sr [120], and in heteronuclear mixtures of ^{6}Li-^{173}Yb [121] and ^{40}K-^{161}Dy [122]. As of today, the measured $T/T_F = 0.04$ from [18] still is one of the coldest DFG produced, despite being one of the first as well.

Bose-Fermi mixtures In contrast, a Bose-Fermi (BF) mixture is less affected by the Pauli blocking issue (although not fully exempt from it), but still has its own shortcomings. First, the bunching tendency of bosons can lead to a dramatically different size than a Fermi gas. In an identical trap, the DFG's size will be limited to the Fermi radius by the Fermi pressure; however bosons will condense into a Bose-Einstein condensate (BEC), for which the radius is that of the ground-state harmonic oscillator, enlarged by the particles' interaction. They

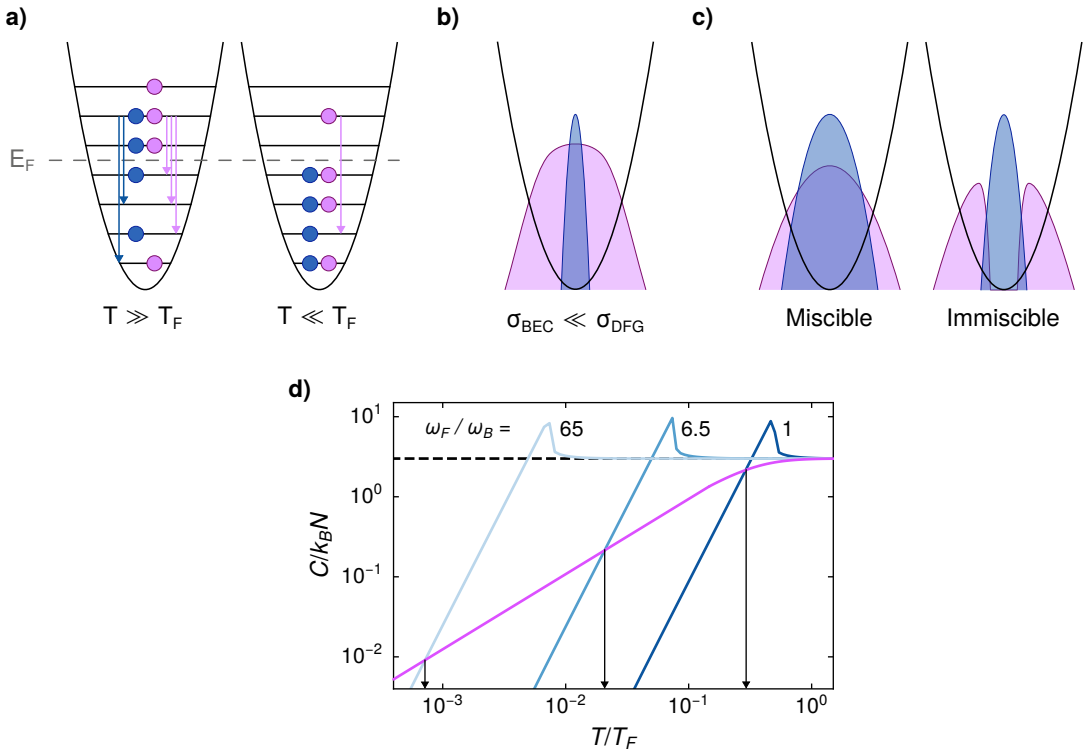

Figure 2.3 | Schematic representation of cooling-limiting processes. a) Pauli blocking of collisions. Above the Fermi temperature (left), many channels are available for fermions to scatter in a state below the Fermi energy. Below the Fermi temperature (right), the channels are suppressed and the collision rate decreases. Colors represent fermions with different spins. **b)** Typical size difference between a BEC (blue) and a DFG (pink) in the same trap, leading to a small overlap. **c)** Loss of overlap between two species when the interspecies scattering length lead to demixing. This process in particular can occur for any particles' statistics (bosons or fermions), but is easiest to observe with BB mixtures, since the presence of fermions adds a high energy cost to any density increase because of the Fermi pressure. The density distributions of **b** and **c** are only qualitative. **d)** Heat capacity of bosons (blue) and fermions (pink) in the degenerate regime. In first approximation, the cooling of fermions by bosons is efficient when $C_B > C_F$; at the crossing point, the bosons cannot remove the heat from the fermions and the cooling stops. Adapted from [109].

are given by, respectively:

$$R_F = 2E_F/m\omega^2 \quad \text{and} \quad R_B = \sqrt{2\mu/m\omega^2} \tag{2.3}$$

where $\mu = \left(\frac{15\hbar^2 m^{1/2}}{2^{5/2}} N\bar{\omega}^3 a\right)^{2/5}$ is the chemical potential of a Bose gas in a trap, and a the scattering length. The different behaviors, dictated by the quantum statistics of the particles, typically lead to the situation where the BEC is much smaller than the DFG. This effect can be exploited to use the BEC as a precise thermometer for the DFG to overcome the difficulty of direct temperature measurement with Fermi gases [123], but hinders the desired sympathetic cooling provided by a large reservoir. The second issue is the important mismatch between the two gases' heat capacity in the degenerate regime. Below their respective critical temperatures T_F and T_C, the Fermi and Bose gases' heat capacity decrease

as [44, 47]:

$$C_F \approx \pi^2 k_B N_F \left(\frac{T}{T_F}\right) \quad \text{and} \quad C_B \approx 10.8 k_B N_B \left(\frac{T}{T_C}\right)^3 \tag{2.4}$$

with

$$T_F \approx 1.82 \frac{\hbar\bar{\omega}_F}{k_B} N_F^{1/3} \quad \text{and} \quad T_C \approx 0.94 \frac{\hbar\bar{\omega}_B}{k_B} N_B^{1/3} \tag{2.5}$$

where $\omega_{B,F}$ is the trapping frequency and $N_{B,F}$ the atom number. Here, a conservative assumption can be made regarding the cooling power of the trapped mixture. As long as the bosons have a larger specific heat capacity than the fermions ($C_B > C_F$), they can reduce the fermions' temperature during the evaporation. As soon as the situation is reversed and $C_B < C_F$, their cooling power can be considered too low to be effective and the fermions' temperature settles at $T = T_{\text{eq}}/T_F$, determined by $C_F(T_{\text{eq}}) = C_B(T_{\text{eq}})$. In the simple case of similar fermions and bosons held together in a monochromatic trap with $\omega_F/\omega_B \approx 1$, their critical temperatures are already in a favorable position with $T_C/T_F \approx 0.5$, and the crossing happens at $T_{\text{eq}}/T_F \approx 0.3$. But this (conservative) limit can be pushed further, by acting directly on the ratio T_C/T_F. For example, lowering the trap frequency's ratio to $\omega_B/\omega_F \approx 6.5$, which corresponds to the ratio of Er and Li in a $1064\,\text{nm}$ ODT, already brings the crossing point to $T_{\text{eq}}/T_F \approx 0.02$. The ratio can be increased by adding a tightly confining beam for Li atoms only, at the tune-out wavelength of Er (see Section 2.3.1). In that case, a factor 10 can realistically be gained on the frequency ratio, leading to $\omega_B/\omega_F \approx 65$ and thus $T_{\text{eq}}/T_F < 0.02$.

Both issues can be experimentally addressed with a careful trap design, by acting on the trapping beams' size and wavelength, using bi-chromatic trapping, or a combination of it. These limits did not deter the experimentalists from making BF mixtures, with various isotopes of a single species, or with different species. In particular, mixtures of ^{6}Li-^{23}Na [37], ^{6}Li-^{41}K [124] and ^{6}Li-^{174}Yb [121] reported temperatures below $T/T_F \lesssim 0.1$. Once again, the very low $T/T_F = 0.05$ from [37] is still holding its position as one of the record temperatures for fermions today, after more than 20 years of tremendous experimental progress.

All mixtures Finally, all mixtures are subject to two additional technical issues, independently of the particles' nature, which come from a reduced overlap between the two clouds again. First is the mixture's mean-field effects. For strong enough interspecies interactions, a phase separation can be observed, where the two species can be made fully immiscible [46]. This effect is not specific to the particles' statistic, and has already been studied in BF [125] and (extensively) in BB [126] mixtures. Under the proper conditions, this mean-field effect can be used to, for example, trap a species by the other [127], or lead to a collapse of the gas [128]. The phase separation is harder to observe in FF mixtures, as strong interactions (on the scale of the Fermi energy) are required [129]. So far, only spin-imbalanced FF mixtures were able to detect a phase separation, and only between the paired and unpaired (*i.e.* superfluid and normal) components [117, 130]. Second is the differential gravitational sag in mass-imbalanced mixtures trapped in a single ODT. Because of their different mass, the gravitational potential has a different strength relative to the trap depth for the different species, and results in a spatial shift of the trap's minimum. In particular towards the end of an evaporation, when the trap is shallow, the mass difference

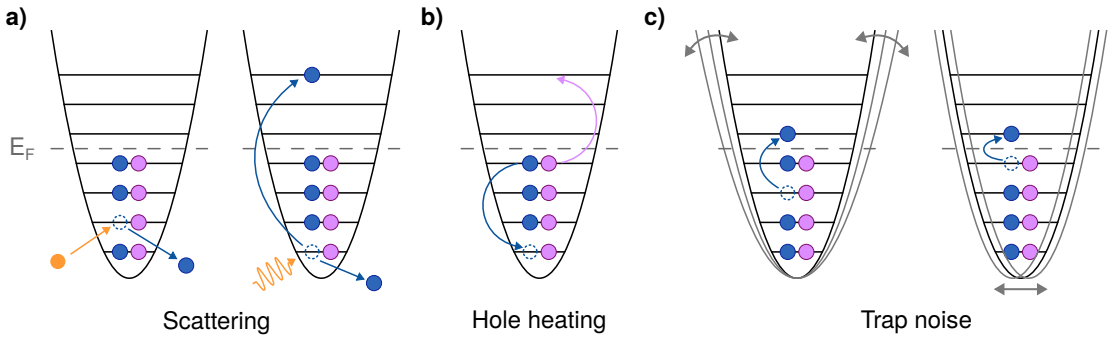

Figure 2.4 | Schematic representation of heating processes. a) Scattering processes: background atoms (left) and trap photons (right) can heat an atom to a bound state higher than E_F, or out of the trap if the energy is high enough. **b)** Fermi hole heating: After the loss of an atom, the rethermalization of the gas leads to a higher absolute temperature (see text). **c)** The intensity (left) and position (right) noises from the laser also lead to spurious parametric heating and promotes atoms to energies higher than E_F.

can result in a shift large enough to completely separate the clouds and prevent any form of interspecies thermalization.

2.2.2 Heating sources

Several processes can lead to heating of the gas and eventually particle loss. They have different physicals origins, but here we focus on two types: scattering processes (with either atoms or photons), and noise-induced heating. The first case usually leads to Fermi hole heating, while the second case usually leads to parametric heating.

Scattering processes We begin here with the collisional events. Collisions can come from the residual gas in the vacuum system, or from density-dependent mechanisms (*e.g.* dipolar relaxation, spin exchange, three-body recombination [131, 132]). Typically, the vacuum collisions occur between a particle from the cold gas and a residual particle at room temperature. The subsequent energy transfer is usually larger than $100\,\mathrm{mK}$, way above the trap depth, and results in a lost particle for every collision event. However, the collision rate is rather low, on the order of $1\,\mathrm{mHz}$ when the pressure is $10^{-11}\,\mathrm{mbar}$ [109, 133], and the induced heating is found to be negligible. Dipolar relaxation is an inelastic collisional process which involves atoms not in their absolute ground state, and transfers energy from the internal to external degrees of freedom; the electron spin state of one or both atoms change, and is transferred to the relative motion of the atoms as kinetic energy. Because it is driven by the magnetic dipole-dipole interaction, magnetic atoms such as Er or Dy are particularly sensitive to it, and non-spin polarized gases suffer from significant heating. On the other hand, non-magnetic atoms (such as Yb, Sr, or alkali in general) are well protected from it due to the weak dipolar interaction coupling.

We now move on to the photon scattering processes. The scattering of light by cold atoms is also a source of heating, where the energy input comes from the trapping light itself. A direct heating simply comes from the recoil energy $E_r = \hbar^2 k^2/2m$ for each

absorption and emission of a photon of wavelength $\lambda = 2\pi/k$, yielding a temperature increase of $T_r = 2E_r/k_B$ [134]. The scattering rate depends on the atom itself *via* its complex polarizability at the laser's wavelength, and on the light intensity (see Section 5.1). Again, two cases can be distinguished. Either the energy transfer is enough to expel the atom from the trap and the Fermi gas undergoes Fermi hole heating, or the atom stays in the trap and the deposited energy is entirely redistributed among the ensemble by normal thermalization.

A subtle, yet important issue when an atom is removed from a trapped DFG is the secondary heating process known as Fermi hole heating [135]. This form of heating arises from the loss of particles *inside* the Fermi sea. After the atom is lost, the Fermi gas rethermalizes through collisions: as one atom is sent inside the perforated Fermi sea to take the hole's place, another is promoted to a higher level in the trap, effectively heating the atomic ensemble, with an energy excess of $\frac{2}{5}E_F$ [136]. It is important to point out that this effect gains in severity for increasing degeneracy, where the temperature doubling time can become very small. For example, assuming only vacuum collisions with a background pressure of $10^{-11}\,\mathrm{mbar}$, the temperature doubling time is on the order of $200\,\mathrm{ms}$ at $T/T_F = 0.01$, but down to $1\,\mathrm{ms}$ in the optimistic case of $T/T_F = 0.001$ [133, 135]. Naturally, Bose gases are not affected by this process, since the Pauli blocking does not apply to them.

Trap noise When the light is used to form a trap, the laser noise also adds to the heating. It comes in two flavors: as Relative Intensity Nosie (RIN), and as beam pointing noise. For atoms kept in a off-resonant trap, they respectively translate into a fluctuation of the spring constant and of the trap center position (see Fig. 2.4c), ultimately leading to exponential and linear heating [137, 138].

A few remarks can be made on the situation of exponential heating due to intensity noise. In that case, the heating depends on the spectrum of the RIN: whenever a spectral component matches with twice the trap frequency (2ω), a parametric heating process promotes the atoms to higher levels in the trap, ultimately leading to strong atom losses. Especially in optical lattices, where the trap frequency is typically close to $100\,\mathrm{kHz}$, the noise cannot be regulated by our standard intensity PI-controllers [139], and the RIN can become the largest source of heating [140]. In principle, the theoretical description of situation relies on symmetry argument to demonstrate that parametric heating excites atom from the vibrational level $|n\rangle$ to $|n+2\rangle$. In practice, the required symmetries are most often broken one way or another. For example, gravity alone is responsible for tilting the trap potential unless actively compensated, thus breaking the symmetry in the vertical direction. As such, the $|n\rangle \to |n+1\rangle$ resonance and its first harmonics are visible when performing the measurement [141]. However, this heating process affects mostly the atoms close to the Fermi surface, since atoms at the bottom of the trap would require a very high harmonic to be excited. It also suggests that Fermi gases with higher degeneracy could be less affected by the trap noise, since the number of available channels for these processes decreases with the cloud's relative temperature.

2.3 The case of an Er-Li mixture

The conclusion that can be drawn from the previous section is, in a nutshell: most of the issues mentioned above are not physically fundamental, but of technical nature. The main ambition of our experiment is to address these issues from the beginning with a trapping configuration that circumvents them by design. The following considerations can be connected to one quantity: the ratio of the critical temperatures from Eq. (2.5). In its complete form, it can be written as:

$$\frac{T_C}{T_F} \approx \frac{1}{2}\frac{\omega_B}{\omega_F}\left(\frac{N_B}{N_F}\right)^{\frac{1}{3}} = \frac{1}{2}\sqrt{\frac{U_B}{U_F}\cdot\frac{m_F}{m_B}}\frac{w_0^F}{w_0^B}\left(\frac{N_B}{N_F}\right)^{\frac{1}{3}} \tag{2.6}$$

where $U_{B,F}$ and $w_0^{B,F}$ are the trap depths and waists for each atom; the trap frequency and beam waist are linked by $\omega = \sqrt{4U/mw_0^2}$. This form explicitly shows the parameters that are accessible to the experimentalist, namely: the atoms' mass, trap depths, trapping beam's waists, and atom number. For the following considerations, we can immediately drop the trap depth and atom numbers. As the evaporation takes place, both parameters are decreased (at least for the bosons), and ultimately all bosons have to be evaporated to reach the lowest temperature for the sympathetically cooled fermions. Instead, we focus on the qualitative aspect of this equation, through its two constant parameters: the atomic masses and trap sizes.

Since the goal is to bring fermions to the highest degeneracy, the point where the bosons condense into a BEC (and hence stop cooling the fermions) need to be as low as possible. In this simple picture, the final temperature of the fermions is directly given by T_C/T_F. It means that the ratios m_B/m_F and w_0^F/w_0^B have to be made as small as possible. This calls for two immediate conclusions: we need a strongly mass-imbalanced mixture with a light fermion and a heavy boson, and we need a differential trapping control for the two species, in the form of a species-selective trap.

2.3.1 Species-selective trapping

We focus first on the necessity for a Species-Selective Trap (SST). In order to minimize the ratio w_0^F/w_0^B, w_0^F can be made small by placing the fermions in a tight Dimple Trap (DT), while w_0^B can be made large by holding the bosons in a large Reservoir Trap (RT). When both traps are superimposed, it is crucial that the bosons are insensitive to the dimple in its center, otherwise they can also scatter from the large RT into the tightly confining DT and condense into a very small BEC [110]. On the other hand, if the dimple trap is deep enough for the fermions, the influence of the large reservoir's potential on the atoms becomes negligible in comparison. The most convenient way to implement such trapping configuration is by building a DT that operates on a *tune-out wavelength* of the bosons.

A tune-out wavelength is defined as a wavelength for which an atom (in a given internal state) is insensitive to the AC Stark shift (or light shift) induced by a laser beam. A complete derivation of this effect is given in Section 5.1, but it can be understood on the basis of a

single equation:

$$U_{\mathrm{dip}}^{(\mathrm{tot})}(\lambda) = \sum_i U_{\mathrm{dip}}^{(i)}(\lambda) = \sum_i \frac{\hbar\Omega_i^2}{4\Delta_{\mathrm{i}}(\lambda)} \tag{2.7}$$

This equation gives the trapping potential $U_{\mathrm{dip}}^{(\mathrm{tot})}$ felt by an atom placed in a light field of wavelength λ. The total trapping potential is calculated as the sum of all light shifts $U_{\mathrm{dip}}^{(i)}$ induced by the coupling between the laser light and the individual atomic transitions (denoted by the subscript i), for which Ω_i and Δ_i are the Rabi frequency and detuning respectively. On resonances, the trapping potential diverges as $1/\Delta_i$, whereas on tune-out wavelengths, the total contributions amounts to 0, *i.e.* the light shifts mutually cancel out and the trapping potential vanishes. It implies that for any atom with at least two transitions, there exists an associated tune-out wavelength located in between. For example, all alkali atoms have a tune-out located between their D_1 and D_2 lines [142], which are the only two strong optical transitions from their ground state. The same reasoning can be maintained for atoms with a more complex structure, whose spectrum can be much denser. As such, heavier atoms can offer numerous possibilities for SST, especially for those with narrow laser-cooling transitions. These are all the more interesting since the associated tune-outs are potentially situated close enough to the transitions that both can be addressed with the same laser system. Er and Dy are good illustrations of such atoms, since their narrow cooling transitions at $841\,\mathrm{nm}$ and $741\,\mathrm{nm}$ are approximately $10\,\mathrm{kHz}$ wide, and the nearby anisotropic tune-outs are found in the detuning ranges $78 - 245\,\mathrm{GHz}$ [50] and $8 - 30\,\mathrm{GHz}$ [143] on the blue side, depending on the angle between the laser polarization and the quantization axis (see also Chapter 5).

The idea of exploiting such tune-out wavelength for an SST was proposed in 2007 [45] and implemented in a ^{41}K-^{87}Rb mixture experiment [144] two years later. Since then, tune-out wavelengths of many different atoms have been measured and used in increasingly complex experiments, from alkali [145–154], to alkaline-earth metals [155], to lanthanides [50, 141, 143, 156]. Three mixture experiments also implemented SST, with ^{87}Rb-^{41}K [144, 157], ^{87}Rb-^{171}Yb [158], and ^{6}Li-^{133}Cs [159].

2.3.2 Light fermions

We now turn to the second ratio m_B/m_F. For the light fermion, only two species have been cooled down so far: ^{3}He and ^{6}Li. Here, the choice for ^{6}Li is quickly made. Although He is lighter, it bears several major flaws for our application. The fermionic isotope ^{3}He has a natural abundance of 0.0002%, and enriched samples are extremely expensive. The cooling scheme, just like ^{4}He, requires a metastable state as effective ground state, else one needs lasers in the far UV, which are famously inconvenient or simply non-existing. Once in its metastable state, the main cooling transition lies at $1083\,\mathrm{nm}$, close to the convenient $1064\,\mathrm{nm}$ commonly used for ODTs. Yet, this species was brought to the DFG state very recently with a sympathetic cooling scheme involving metastable ^{4}He*, down to a degeneracy of $T/T_F = 0.14$.

Going through the list of atoms that have been laser-cooled, the next candidate would be Na, but it only has one usable bosonic isotope. The next laser-cooled fermion would then be ^{40}K, but the much larger mass makes it less desirable.

2.3.3 Heavy bosons

For the heavy boson, several options are to be considered. The potential candidates would be, in decreasing mass order: Yb, Er, Dy, and Cs. Since the choice for the fermion is now fixed to ^{6}Li (and its laser-cooling transitions at $671\,\mathrm{nm}$), it is crucial to find a boson that matches the additional requirements, which we develop here.

First is Yb. The only, but major issue with this atom, is the position of its tune-out wavelength at $553\,\mathrm{nm}$ [141]. In that shape, the trap would need to be blue-detuned and the beams require more complicated shapes, however the scattering rate would be rather low, at $\gamma_{\mathrm{sc}}^{\mathrm{Li}}(553\,\mathrm{nm}) = 8.1\,\mathrm{mHz}/\mu\mathrm{K}$ (normalized to the trap depth of Li). Then, Er and Dy are both strong candidates due to their similar structure, with Er being slightly advantageous. Indeed, the mass ratio of $m_{\mathrm{Er}}/m_{\mathrm{Li}} \approx 28$ is the highest that can be found in quantum mixture experiments, and both have tune-out wavelengths in the near infrared. However, the tune-out of Dy at $741\,\mathrm{nm}$ is rather close to the Li transition and results in a much higher scattering rate, at $\gamma_{\mathrm{sc}}^{\mathrm{Li}}(741\,\mathrm{nm}) = 18\,\mathrm{mHz}/\mu\mathrm{K}$. In comparison, the tune-out of Er at $841\,\mathrm{nm}$ leads to $\gamma_{\mathrm{sc}}^{\mathrm{Li}}(841\,\mathrm{nm}) = 7.6\,\mathrm{mHz}/\mu\mathrm{K}$. Finally, the last heavy boson would be ^{133}Cs, with its tune-out wavelength at $880\,\mathrm{nm}$. Although it is the atom with the farthest tune-out wavelength, it is also notably lighter and the mass ratio would be $m_{\mathrm{Cs}}/m_{\mathrm{Li}} \approx 22$. Moreover, the scattering rate of Cs at its own tune-out is very high, because of the proximity of its D_1 and D_2 lines, resulting in $\gamma_{\mathrm{sc}}^{\mathrm{Cs}}(880\,\mathrm{nm}) = 1750\,\mathrm{mHz}/\mu\mathrm{K}$ (normalized to the trap depth of Li).

It is important to note that using a heavy boson as a reservoir for sympathetic cooling has an impact on the thermalization time with the light fermions. Because of the large mass ratio, a mixture of Er and Li has a penalty factor in the energy transfer which takes place during interspecies collisions [160]. In this case, the required number of collisions for cross-thermalization is increased by a factor 7, which translates into a penalty factor of 2.7 for the thermalization time [109].

2.3.4 Comparison with other SST mixtures

So far, three other mixtures have already exploited the existence of tune-out wavelengths to build a species-selective trap. First was a ^{87}Rb-^{41}K mixture [144, 157], where the tune-out wavelength of Rb at $790\,\mathrm{nm}$ was used to trap K. The second mixture was ^{87}Rb-^{174}Yb [158], where a different tune-out of Rb was used, at $423\,\mathrm{nm}$, to trap Yb. Finally, the third mixture is ^{133}Cs-^{6}Li [159], for which the $880\,\mathrm{nm}$-tuneout of Cs was used to trap Li. Here, a comparison can be done with our ^{166}Er-^{6}Li mixture by evaluating two quantities: the atoms' polarizability, and their photon scattering rate. The numerical simulations are reported in Fig. 2.5, and were done in the following way. The polarizability of alkali (Li, K, Rb, Cs) was obtained directly from [161]; that of Er was taken from the dataset of [162], and that of Yb was calculated by accounting for the contribution of the neighbouring transition at $399\,\mathrm{nm}$ only[3]. The scattering rates were calculated according to:

$$\gamma_{\mathrm{sc}}^{(\mathrm{tot})} = \sum_i \gamma_{\mathrm{sc}}^{(i)} = \sum_i \frac{3\pi c^2}{2\hbar\omega_{0,i}^3} \frac{\Gamma_i^2}{\Delta_i^2} I \tag{2.8}$$

[3] Although Yb has more transitions, the situation is very similar to Er where the polarizability is dominated by the contributions of the transitions in the near-UV, close to $400\,\mathrm{nm}$ (see also Section 5.1 and [50]).

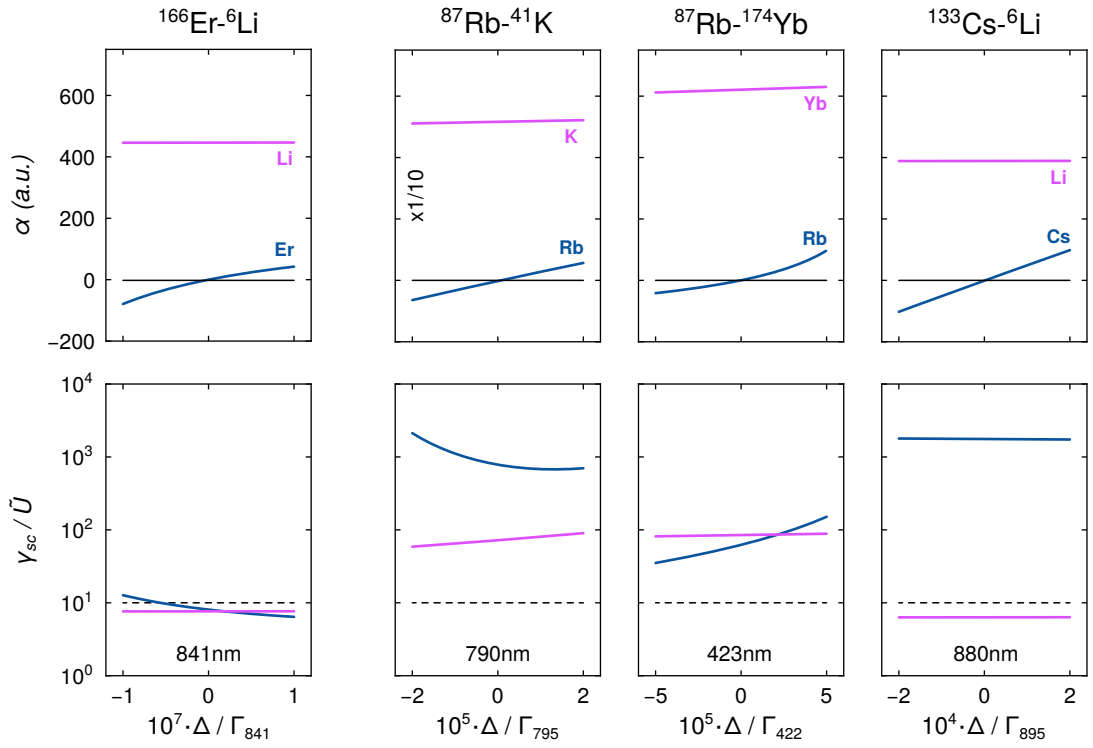

Figure 2.5 | Comparison of the existing species-selective traps. The polarizability (top row) in atomic units and scattering rates (bottom row) in $\mathrm{mHz}/\mu\mathrm{K}$ of the atoms involved in SST mixtures. The tuned-out species (Er, Rb, Cs) are drawn in blue, the trapped species in pink. For each mixture (columns), the horizontal axis is the detuning Δ from the tune-out wavelength, scaled to the nearest transition's linewidth Γ of the tuned-out species. The scattering rate γ_{sc} is rescaled to the potential $\tilde{U}$ felt by the trapped species. The solid black line (top row) is drawn along $\alpha = 0$, and the dashed black line (bottom row) indicates the scattering rate of the common situation of Rb atoms in a $1064\,\mathrm{nm}$ ODT.

Li	K	Rb	Cs	Er	Yb
671/671	770/767	795/780	895/852	all	556
	404/405	422/420			399
		359/359			

Table 2.1 | Accounted transitions for the calculations of scattering rates. The pairs correspond to the D_1/D_2 transitions for alkali. The Er lines were taken from the spectroscopic data of [162]. The values are the different transitions' wavelength in nm.

where $\omega_{0,i}$ is the frequency of the transition i, Γ_i the inverse lifetime of the excited state, Δ_i the detunig from the transition i and I the laser intensity required for a $1\,\mu$K-deep trap (see also Eq. (5.21) from Section 5.1). There, the scattering rate was calculated by accounting for the relevant or dominant lines for each atom, a list of which can be found in Table 2.1. For the tuned-out species (Er, Rb, Cs), the scattering rate is normalized to the trap depth of the other atom.

From the calculations of Fig. 2.5, the Rb-K mixture stands out from the rest with the very large polarizability of K at $790\,\mathrm{nm}$ (note the factor 1/10 in the vertical axis of the upper row for this mixture). The reason is the proximity of the K transitions at $770/767\,\mathrm{nm}$ from the SST wavelength at $790\,\mathrm{nm}$. However, the advantage of this near-resonant trap (an optical tweezer in their experiment) is the low power requirement to confine atoms. This results in a reasonable scattering rates for K with $\gamma_{\mathrm{sc}}^{\mathrm{K}}(790\,\mathrm{nm}) = 74\,\mathrm{mHz}/\mu\mathrm{K}$, but a comparatively very large rate for Rb at $\gamma_{\mathrm{sc}}^{\mathrm{Rb}}(790\,\mathrm{nm}) = 800\,\mathrm{mHz}/\mu\mathrm{K}$. The Cs-Li mixture also has an interesting behaviour: the polarizability of Li is rather low at $880\,\mathrm{nm}$, and the scattering rate is the lowest of all calculations here with $\gamma_{\mathrm{sc}}^{\mathrm{Li}}(880\,\mathrm{nm}) = 6.35\,\mathrm{mHz}/\mu\mathrm{K}$. However, the tune-out wavelength of Cs lies between its D_1 and D_2 lines, which means a small relative detuning and thus leads to the largest calculated scattering rate of $\gamma_{\mathrm{sc}}^{\mathrm{Cs}}(880\,\mathrm{nm}) = 1750\,\mathrm{mHz}/\mu\mathrm{K}$. The last mixture of Rb-Yb is an interesting combination, for which the tune-out wavelength of Rb at $423\,\mathrm{nm}$ is very close to the $420/422\,\mathrm{nm}$ transitions, yet the photon scattering rate is reasonable, at $\gamma_{\mathrm{sc}}^{\mathrm{Rb}}(423\,\mathrm{nm}) = 65.6\,\mathrm{mHz}/\mu\mathrm{K}$. Similarly, Yb has a strong transition at $399\,\mathrm{nm}$, yet the corresponding scattering rate is $\gamma_{\mathrm{sc}}^{\mathrm{Cs}}(423\,\mathrm{nm}) = 107\,\mathrm{mHz}/\mu\mathrm{K}$.

Finally, the advantageous configuration of Er-Li becomes apparent in two (related) ways. First, the scattering rate of *both* species is low, at $\gamma_{\mathrm{sc}}^{\mathrm{Er}}(841\,\mathrm{nm}) = 8.1\,\mathrm{mHz}/\mu\mathrm{K}$ and $\gamma_{\mathrm{sc}}^{\mathrm{Li}}(841\,\mathrm{nm}) = 7.6\,\mathrm{mHz}/\mu\mathrm{K}$. Second, the range of the natural, or relative detuning is the largest, reaching a value of $\Gamma/\Delta \propto 10^7$ for both Er and Li, compared to maximum 10^5 in the other cases (see Fig. 2.5).

2.4 Properties of Er and Li

Now that we explained the choice of Er and Li for our quantum mixture, their respective properties are described in the following section. Here we put an emphasis on the properties of Erbium, while a detailed presentation of Lithium is given in the complementary thesis [109]. Otherwise, a thorough description of each atomic species can be found in [163] and [49] for Er and Li respectively.

2.4.1 Basic properties

Erbium is a rare-earth element, of the lanthanide series, with the atomic number Z=68 and a mass of $167.27\,\mathrm{amu}$[4]. It is found in compound minerals, along with several other rare-earth elements, and it requires a complex separation process to obtain a sample with high purity. In its pure form, at standard conditions of pressure and temperature, Erbium is a soft, silvery metal which can react with water. It has high melting and boiling points,

[4] $1\,\mathrm{amu} = 1.66 \cdot 10^{-27}\,\mathrm{kg}$

at $1529\,^{\circ}\mathrm{C}$ and $2900\,^{\circ}\mathrm{C}$. Erbium has six isotopes, of which five are bosonic ($^{162}\mathrm{Er}$, $^{164}\mathrm{Er}$, $^{166}\mathrm{Er}$, $^{168}\mathrm{Er}$, $^{170}\mathrm{Er}$), and one is fermionic ($^{167}\mathrm{Er}$). Except for $^{162}\mathrm{Er}$ and $^{164}\mathrm{Er}$, the natural abundances are all above $15\,\%$, which means that a sample of Erbium can be used for most desired isotopes. Combined with the small isotope shift of the laser-cooling transition (approx. $1\,\mathrm{GHz}$), selecting the cooled isotope is rather straightforward, and it makes Erbium a very versatile choice for experimentalists (see Section 2.4.4 and [163, 164]).

As of today, Erbium mining happens almost exclusively in southern China, along with the other rare-earth elements used in industry. Arguably, the most successful use-case of Erbium has been in telecom technologies, where it is used in its ionic form (Er^{3+}) as a light amplifier. Thanks to their optical transition at $1550\,\mathrm{nm}$, Erbium-doped fiber amplifiers (EDFA) are widely used in submarine cables, leading to the fast internet we know today.

On the other hand, Lithium is an alkali metal with the atomic number Z=3 and mass $6.94\,\mathrm{amu}$. It is also a silvery-white soft metal, with the lowest density and a high reactivity, including fast oxidization when put in air and explosive reactions when put in contact with water. It has much lower phase transition points, at $180\,^{\circ}\mathrm{C}$ and $1344\,^{\circ}\mathrm{C}$ for melting and boiling respectively. Lithium has two isotopes, fermionic ($^{6}\mathrm{Li}$) and bosonic ($^{7}\mathrm{Li}$). Contrarily to Erbium, changing the laser-cooled isotope is non-trivial, since the large isotope shift (approx. $10\,\mathrm{GHz}$) and different hyperfine splitting would require a different laser system. However, it is still interesting to note that an Er-Li mixture can offer all flavours of quantum statistics.

The heaviest contribution of Lithium to global industry is not in telecom, but rather in batteries. Today, more than three-quarters of the extracted Lithium goes to the Lithium-ion batteries, used in any and all type of devices, including smartphones, laptops, or cars. The impact of these batteries on technology in general is immense, and was awarded by a Nobel Prize in Chemistry in 2019. The extraction however, is also complex and has its own environmental implications, which go beyond the scope of the thesis. It is done mostly in South America from continental brine, or in Australia and China from hard-rock mining.

In the following sections, we focus on the properties of one isotope per species, namely $^{166}\mathrm{Er}$ and $^{6}\mathrm{Li}$, which are the only isotope currently addressed in our apparatus.

2.4.2 Electronic configuration

Erbium atoms host 68 electrons in total, that fill the atomic orbitals following the Madelung rule. Consequently, the $6s$ shell is filled before the $4f$, resulting in the so-called *submerged-shell* configuration. Written explicitly, the electronic configuration of Er is:

$$1s^2 2s^2 2p^6 3s^2 3p^6 3d^{10} 4s^2 4p^6 4d^{10} 5s^2 5p^6 4f^{12} 6s^2$$

also shortened to:

$$[\mathrm{Xe}] 4f^{12} 6s^2$$

where [Xe] is the full electronic configuration of Xenon. Having two missing electrons on such a high shell ($4f$), Erbium has an unusually large angular momentum, calculated in

the standard LS-coupling scheme to be:

$$^3\mathrm{H}_6$$

with L=5 and S=1, written in the standard $^{2S+1}L_J$ notation. Additionally, the strong anisotropy of the electronic wavefunction in the $4f$ shell leads to highly anisotropic potentials and interactions, as explained in Sections 2.4.4 and 5.1. For excited states, the spin-orbit coupling is not adequate to describe the angular coupling, and one needs to use the jj-coupling instead. In that case, the angular momentum l and spin s of each inner electron[5] couple independently *via* spin-orbit coupling to form an angular momentum J_1, which is then coupled to the angular momentum J_2 of the excited electron. The two angular momenta are then summed up to the total angular momentum $\mathbf{J} = \mathbf{J_1} + \mathbf{J_2}$, noted $(J_1, J_2)_J$. For example, the $401\,\mathrm{nm}$-excited state has an electron promoted from the $6s$ to $6p$ orbital, and the intermediate LS-coupling terms are $^3\mathrm{H}_6$ and $^1\mathrm{P}_1$ for the inner and excited electrons respectively. Then, these momenta are jj-coupled and the excited state is written as:

$$[\mathrm{Xe}]4f^{12}(^3H_6)6s6p(^1P_1)(6,1)_7$$

with $J_1 = 6, J_2 = 1, J = 7$. Finally, all bosonic isotopes of Erbium have a vanishing nuclear spin ($I = 0$), preventing the emergence of a hyperfine structure. The fermionic isotope $^{167}\mathrm{Er}$ however, has a large nuclear momentum $I = 7/2$, leading to a total angular momentum $F = 19/2$ [165].

Lithium atoms have a much simpler electronic configuration, well described by a single valence electron. The full shell occupation is simply:

$$1s^2 2s^1$$

with $L = 0$, $S = 1/2$, $J = 1/2$, $I = 1$, $F = \{1/2,\ 3/2\}$, leading to a ground state:

$$^2S_{1/2}$$

Just like all other alkali, the valence electron in the s-shell leads to $L = 0$ and $S = 1/2$. The particularity of Li is its small hyperfine splitting of $228\,h \cdot \mathrm{MHz}$ (the smallest of all alkali), originating from the small yet non-vanishing nuclear spin.

2.4.3 Magnetic properties

Magnetic moment

The magnetic moment of an atom characterizes the magnetic field produced by the atom itself, arising primarily from the spin and angular momentum of its electrons. In general, it is defined by:

$$\mu = m_i g_i \mu_B \tag{2.9}$$

where $\mu_B = e\hbar/2m_e \approx 1.4\,h \cdot \mathrm{MHz/G}$ is the Bohr magneton, and the subscript i denotes the relevant angular quantum number, either J or F depending on the ground state at

[5] Here, *inner electrons* are the ones occupying the [Xe], $4f$ and $6s$ shells

hand. Erbium, like several other lanthanides, has one of the largest magnetic moment from the periodic table. These high values are an immediate consequence of their electronic configuration and associated large angular quantum numbers. In particular, the high value of J implies a potentially high value for its projection on the quantization axis m_J, resulting in a high magnetic moment. In contrast, Lithium (like all other alkalis) has a small magnetic moment, again due to its valence electron occupying a spherical s-shell.

The numerical values can be determined *via* a good knowledge of the Landé g-factor and coupling scheme. For example, in the perfect LS-coupling scheme, this factor is given by:

$$g_J = 1 + (g_S + 1)\frac{J(J+1) - L(L+1) + S(S+1)}{2J(J+1)} \tag{2.10}$$

with $g_S \approx 2.00232$ [166]. Again, the case of Erbium is not perfectly described with a pure LS-coupling scheme, and small corrections (on the order of $0.3\,\%$) need to be included [167]. These corrections result in a theoretical value of $g_J^{\text{th}} = 1.1637985$, compared to an experimental value of $g_J^{\text{exp}} = 1.163801(1)$ [168]. However, the description works well for Lithium, and its own g-factor can be calculated with:

$$g_F = g_J\frac{F(F+1) - I(I+1) + J(J+1)}{2F(F+1)} + g_I\frac{F(F+1) + I(I+1) - J(J+1)}{2F(F+1)} \tag{2.11}$$

where $g_I \approx -0.0004476540$ [166]. This leads to two different values depending on F: $g_{F=1/2} = -2/3$, while $g_{F=3/2} = +2/3$.

The magnetic moments of both atoms can now be calculated, for the specific states that are relevant to our experiments. For Erbium, we only look at the $m_J = -6$ Zeeman substate, because the Erbium ensemble is spin-polarized in this state during the MOT phase (see Section 4.1.2). For Lithium, we look at the three lowest hyperfine states, usually noted $|1\rangle$, $|2\rangle$, $|3\rangle$, corresponding to $|F, m_F\rangle = |1/2,\ 1/2\rangle$, $|1/2,\ -1/2\rangle$ and $|3/2,\ -3/2\rangle$ respectively. These hyperfine states are the only ones that are routinely manipulated in our experiment as well, because these spin-mixtures are stable against dipolar losses [109]. In the end, their magnetic moments are:

$$\begin{aligned}
\text{Er} &: \mu = +6.98\mu_B \\
\text{Li}|1\rangle &: \mu = -1/3\mu_B \\
\text{Li}|2\rangle &: \mu = +1/3\mu_B \\
\text{Li}|3\rangle &: \mu = +1\mu_B
\end{aligned}$$

The large magnetic moment of Er, surpassed only by Tb and Dy with $\mu = 10\mu_B$ and Ho with $\mu = 8\mu_B$, can be used to magnetically levitate the atoms with a very moderate gradient. To compensate gravity, a gradient of $\nabla B = mg/\mu = 4.2\,\text{G/cm}$ is enough to lift the large mass of Er atoms. In comparison, the small magnetic moment of Li implies that a gradient of $3.2\,\text{G/cm}$ ($1.1\,\text{G/cm}$) is needed to levitate Li$|1\rangle$ (Li$|3\rangle$), despite the considerable mass difference.

Zeeman shift

When an external magnetic field B is applied, the Zeeman manifold of an atom splits into $2J+1$ (or $2F+1$) Zeeman substates. At low fields, the induced energy shifts ΔE depend on the magnetic moment of each level according to:

$$\Delta E = \mu B = m_i g_i \mu_B B \tag{2.12}$$

At high fields, a decoupling between I and J can be observed, corresponding to the well-known Paschen-Back regime.

In the case of Erbium, the Paschen-Back regime is never reached within the typical fields used in the laboratory. Because the energy associated with the fine structure of Er is high (on the order of $\Delta E_{\mathrm{FS}} \approx 200\,h \cdot \mathrm{THz} \equiv 1500\,\mathrm{nm}$), the decoupling cannot happen, and the Zeeman shift remains linear up to several hundreds of Gauss [167]. In particular, for the $m_F = \pm 6$ substates, the Zeeman shift is $\pm 9.77\,\mathrm{h} \cdot \mathrm{MHz/G}$. Otherwise, the splitting between two neighbouring Zeeman substates of the ground state manifold grows linearly with a slope of $1.63\,\mathrm{MHz/G}$. For the fermionic isotope, the non-vanishing nuclear spin also induces a quadratic shift [163].

The situation is, once again, reversed for Li. In the Zeeman regime, the substates are well defined by the quantum number F, and are grouped according to $F = 1/2$ or $F = 3/2$. In the Paschen-Back regime, the states' properties are governed by the electron spin, and its orientation indicate the low- or high-field seeking behaviour of the atoms. Because the ground state's hyperfine splitting of Li is small compared to other alkali ($\Delta E_{HFS} \approx 228\,h \cdot \mathrm{MHz}$), the crossover from one regime to the next happens at $B \approx 20\,\mathrm{G}$ only.

Feshbach resonances

Er has an extremely rich Feshbach spectrum, where every single isotope has a different set of resonances. While Li has one resonance close to $830\,\mathrm{G}$, whose exact position depends on the spin mixture, ^{166}Er has no less than 190 Feshbach resonances below $70\,\mathrm{G}$ [169]. A recent investigation of the three-body losses in BECs of ^{166}Er at low field also revealed six additional loss features below $3\,\mathrm{G}$ [170], attributed there to trimer (three-body bound state) resonances. Furthermore, two magnetic fields were identified for efficient evaporation and production of a large ^{166}Er BEC where the three-body loss coefficient is very low, at $1.4\,\mathrm{G}$ (where $a_s = 73\,\mathrm{a_0}$) and at $2\,\mathrm{G}$ (where $a_s = 80\,\mathrm{a_0}$). In both cases, the loss coefficient was calculated to be $L_3 = 10^{-12}\,\mu\mathrm{m}^6/\mathrm{s}$.

The inter-species Feshbach spectrum was also measured recently in the Kyoto group, with mixtures of ^{166}Er, ^{168}Er, Li$|1\rangle$ and Li$|2\rangle$, although with atomic ensembles still in the thermal regime, at a few microkelvins [171]. The same group pushed the study a step further with the measurement of Feshbach resonances in a ^{167}Er-^{6}Li mixture [172]. Two mixtures are of particular interest to us: ^{166}Er-^{6}Li$|1\rangle$ and ^{166}Er-^{6}Li$|2\rangle$. In the first case, the first Feshbach resonance was observed at $18.9\,\mathrm{G}$, and 32 more resonances were found for fields up to $680\,\mathrm{G}$. All resonances here were measured to be narrower than $100\,\mathrm{mG}$, except for two resonances with $\Delta B \approx 200\,\mathrm{mG}$ at $316.7\,\mathrm{G}$ and $579.6\,\mathrm{G}$. In the second case, the lowest resonance was observed at $13.3\,\mathrm{G}$, with 20 additional resonances for $B \leq 680\,\mathrm{G}$. Three resonances are

much broader than the others: at $57\,\mathrm{G}$ with $\Delta B = 1.7\,\mathrm{G}$, at $247\,\mathrm{G}$ with $\Delta B = 4.2\,\mathrm{G}$ and at $259\,\mathrm{G}$ with $\Delta B = 1.3\,\mathrm{G}$. Interestingly, the predicted broad resonances in the ^{166}Er-^{6}Li$|1\rangle$ mixtures, expected at $\approx 20\,\mathrm{G}$ and $\approx 80\,\mathrm{G}$ [173] were not observed.

Dipole-Dipole Interaction

For magnetic atoms such as Er, the Dipole-Dipole Interaction (DDI) leads to a *universal dipolar scattering* in the ultracold regime [174]. This interaction, originating from the magnetic moments $\boldsymbol{\mu_1}$ and $\boldsymbol{\mu_2}$ of the atoms, is defined by:

$$U_{\mathrm{dd}}(\mathbf{r}) = \frac{\mu_0}{4\pi r^3}\left[(\boldsymbol{\mu_1}\boldsymbol{\mu_2}) - \frac{3}{r^2}(\boldsymbol{\mu_1}\boldsymbol{r})(\boldsymbol{\mu_2}\mathbf{r})\right] \tag{2.13}$$

where $\boldsymbol{r}$ is the interparticle distance and μ_0 is the magnetic constant. Although the strength of this interaction does not depend on an external magnetic field, it does depend on the relative orientation of the dipoles. Fortunately, magnetic atoms will align themselves to the magnetic field's direction, hence in usual experimental conditions the atomic ensemble becomes polarized along the quantizaton axis. As a result, the magnetic moments are all parallel and the DDI simplifies to:

$$U_{\mathrm{dd}} = \frac{\mu_0\mu_1\mu_2}{4\pi}\frac{1-3\cos\theta^2}{r^3} \tag{2.14}$$

where θ is the angle between the quantization axis and the interparticle axis. The two most striking features of the DDI become apparent in this formula. First, this interaction is long-range. While Van der Waals (contact) interaction decay with distance as r^{-6}, the DDI decays as r^{-3}. Second is the DDI's anisotropy. Emerging from the $1-3\cos\theta^2$ term, the DDI can change from repulsive in a *side-by-side* configuration when $\theta = \pi/2$, to attractive in *head-to-tails* configuration when $\theta = 0$. The sign change occurs at $\theta \approx 54.7\,^\circ$, where the whole expression vanishes.

Experimentally, observing the dipolar nature of some particles (such as Cr [175], Dy [176] or Er [177]) requires to "filter" out the contact interactions by turning off the s-wave scattering length a_s with a Feshbach resonance. Then, the only remaining interaction is the DDI, with its natural length scale, the so-called *dipolar length*:

$$a_{\mathrm{dd}} = \frac{m\mu_0\mu_1\mu_2}{4\pi\hbar^2} \tag{2.15}$$

In this dipolar regime, the universal behaviour appears in the expression of the elastic dipolar scattering cross-section:

$$\sigma = \frac{32\pi}{15}a_{\mathrm{dd}}^2 \tag{2.16}$$

where the only parameters are the particles' mass and dipole moment [174]. This finite cross-section leads to a very interesting phenomenon, where fermions can manage to thermalize, despite the usual Pauli-blocking problem which normally leads to $\sigma = 0$. As such, it is possible to reach the quantum regime and make degenerate Fermi gases without the addition of a second component. For example, in [112], the authors were able to reach a temperature of $T/T_F = 0.2$, with $N = 4\cdot 10^4$ atoms of ^{167}Er. Exploiting the DDI also led to new quantum

phases of matter, namely quantum droplets [178, 179] and supersolid [180–182], where the mean-field theory breaks down and additional correction terms (Lee-Huang-Yang) are required to describe the system.

2.4.4 Cooling transitions

Here we present the laser-cooling transitions of both atoms. These transitions are typically used as the first cooling steps, before trapping the atoms in an Optical Dipole Trap (ODT) and performing further cooling, generally *via* evaporation. Here, it is instructive to give the relevant physical quantities related to the cooling process. First, all transitions are characterized by their wavelength λ, linewidth Γ, and the excited state's lifetime τ. When these transitions are used to make a magneto-optical trap, a natural lower boundary limits the achievable temperature: the Doppler temperature $T_{\mathrm{D}} = \hbar\Gamma/2k_B$ (see also Section 4.1.2); the associated Doppler velocity is simply given by $v_{\mathrm{D}} = \sqrt{2k_B T_{\mathrm{D}}}$. In certain cases, it is possible to go below this limit [183], and hit a second boundary with the recoil temperature $T_r = \hbar^2 k^2/2mk_B$. This temperature corresponds to the energy transfer during a single absorption or emission event, which becomes relevant when the system becomes cold enough that the recoil energy is not negligible compared to the atom's kinetic energy anymore.

Erbium The sheer amount of energy levels for Erbium naturally results in a large amount of dipole-allowed transitions, with widely different characteristics, from very broad to ultra-narrow. Although a rich spectrum typically entails a higher complexity for laser cooling due to the large number of non-closed transitions and hence decay channels (a common issue with ultracold molecules [184]), it proved to be an advantage for Erbium. In terms of laser cooling, five have transitions been identified as potentially interesting by [48], at $401\,\mathrm{nm}$, $583\,\mathrm{nm}$, $631\,\mathrm{nm}$, $841\,\mathrm{nm}$ and $1299\,\mathrm{nm}$. Since then, all except for the $631\,\mathrm{nm}$ transition have been used in various experiments, although for different applications. In particular, the ultra-narrow $1299\,\mathrm{nm}$-transition, with a $1\,\mathrm{Hz}$-linewidth, has been observed and characterized in [185], where a coherent population control between the ground and excited state was also achieved.

First is the blue transition at $401\,\mathrm{nm}$. Its large linewidth of $29.7\,\mathrm{MHz}$ makes this transition suitable for any application which requires a high scattering rate. Additionally, being in the high-frequency part of the visible spectrum is interesting for a fast energy transfer, since a momentum kick from a blue photon conveys more energy than that of a (infra-)red photon. However, the Doppler temperature is high compared to all the other transitions, and the transition itself is not perfectly closed. As such, this transition is used in pre-cooling stage like Zeeman slowing and transversal cooling, but not for actual trapping.[6] It is also used for normal absorption imaging, and recently fast site-resolved imaging was demonstrated as well [187].

The yellow transition at $583\,\mathrm{nm}$ is now the standard wavelength for an Erbium MOT, after the demonstration of a direct loading from a Zeeman slower operating on the $401\,\mathrm{nm}$ transition [188]. This transition was found to be particularly well suited for this task, since

[6] It is not used for trapping in our apparatus, nor in other recent experiments, however trapping is possible and a blue MOT was the first implementation for an Erbium trap [186].

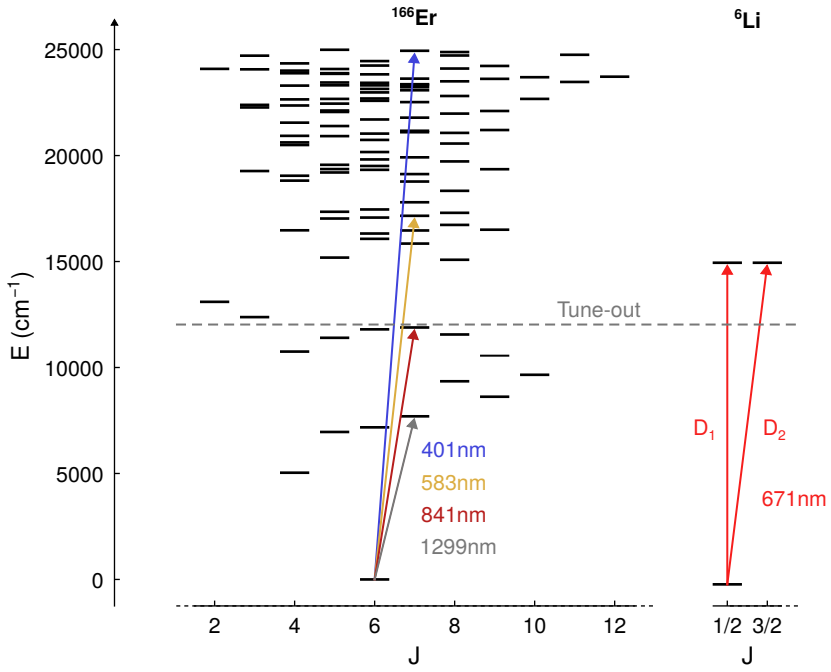

Figure 2.6 | Energy levels and laser-cooling transitions of Er and Li. The spectrum of Er (left) is much richer than that of Li (right), and results in numerous electronic transitions. The diagram shows levels up to $25000\,\mathrm{cm}^{-1}$ ($400\,\mathrm{nm}$), but Er has levels going up to $47000\,\mathrm{cm}^{-1}$ ($212\,\mathrm{nm}$), for a reported total of 671 levels known so far. The tune-out is $\sim 245\,\mathrm{GHz}$ blue-detuned from the $841\,\mathrm{nm}$ (not to scale here, see Chapter 5). The data was obtained from [191].

the $186\,\mathrm{kHz}$ linewidth comes with a low Doppler temperature of $4.6\,\mu\mathrm{K}$. Even though the capture velocity of such a yellow MOT is rather low (order of $5\,\mathrm{m/s}$, see also Section 4.1.2), it can be increased by spectral broadening and matched with the final exit velocity of the Zeeman slower.

Finally, the infrared transition at $841\,\mathrm{nm}$ can be used as a second MOT stage, following a transfer from a yellow MOT. With its narrow linewidth of $8\,\mathrm{kHz}$, the Doppler temperature sits just above the recoil temperature at $190\,\mathrm{nK}$ and $163\,\mathrm{nK}$ respectively. After the demonstration of a very efficient cooling strategy in [189] using this transition, an attempt was also done during the apparatus' construction. However, the limited gain in atom number and temperature that we could obtain after the optical transport in the glass cell (see Chapter 3 and Section 4.2.2) was considered not good enough to justify the additional complexity, and was removed afterwards [190].

Lithium In its ground state, ^{6}Li has two experimentally accessible transitions, at $323\,\mathrm{nm}$ and $671\,\mathrm{nm}$. By far the most frequently used transition is the $671\,\mathrm{nm}$ transition, or rather the D_1 and D_2 lines resulting from the fine-splitting of the excited state. These lines excite the valence electron to the $2^2\mathrm{P}_{1/2}$ and $2^2\mathrm{P}_{3/2}$ states respectively, separated by a $10\,\mathrm{GHz}$ energy gap. More precisely, the Li MOT operates on the transition between the $2^2\mathrm{S}_{1/2}$, $F = 3/2$ ground state, and the $2^2\mathrm{P}_{3/2}$ excited state in its $|F, m_F\rangle = |5/2,\ 5/2\rangle$ hyperfine

		^{166}Er			
Wavelength	λ	401 nm	583 nm	841 nm	1299 nm
Linewidth	$\Delta\nu$	29.7 MHz	189 kHz	8 kHz	0.9 Hz
Sat. intensity	I_S	60.3 mW/cm^2	0.13 mW/cm^2	1.75 μW/cm^2	50 pW/cm^2
Doppler temp.	T_D	713 μK	4.5 μK	192 nK	0.02 nK
Doppler velocity	v_D	189 mm/s	15 mm/s	3.1 mm/s	0.03 mm/s
Recoil temp.	T_r	359 nK	170 nK	82 nK	34 nK
Recoil velocity	v_r	4.2 mm/s	2.9 mm/s	2.0 mm/s	1.3 mm/s

		^{6}Li	
Wavelength	λ	323 nm	671 nm
Linewidth	$\Delta\nu$	159 kHz	5.87 MHz
Sat. intensity	I_S	0.62 mW/cm^2	2.54 mW/cm^2
Doppler temp.	T_D	18 μK	140 μK
Doppler velocity	v_D	158 mm/s	442 mm/s
Recoil temp.	T_r	15 μK	3.5 μK
Recoil velocity	v_r	146 mm/s	70 mm/s

Table 2.2 | Properties of the laser-cooling transitions of Er and Li. Data taken from [48, 163, 185] and [49, 192] for Er and Li respectively.

level. However, because the hyperfine manifold of the excited state is not resolvable by the D_2 transition[7], atoms excited to the $F = 5/2$ manifold can also populate the other $F = 3/2,\ 1/2$ manifolds, and later decay in the ground state $F = 1/2$ manifold, thus lost from the cooling cycle. An additional laser beam, detuned from the first beam by the ~ 228 MHz ground state hyperfine splitting, needs to be used to optically pump the atoms back in the process. These beams have been commonly called *cooler* and *repumper* beams, and are a shared feature of all alkali experiments. A specificity of Li, compared to the other alkali, is the unresolved D_2-excited state, which prevents it from undergoing Sisyphus cooling [6, 193]. This issue hinders the cooling efficiency of the MOT, and restricts the final temperature to typically $\sim 300\,\mu$K.

A second transition, in the UV-range at 323 nm, can also be used to implement a MOT. So far, it has been used as a second cooling stage after the 671 nm MOT [75, 192], to reach $\sim 50\,\mu$K. However, handling laser light at this wavelength is difficult, and the potentially small gain in Doppler temperature obtained from the smaller linewidth was not considered worth the attempt. Instead, one can implement Gray Molasses (GM) cooling [6, 183], which operates on the D_1 line. Although it comes with its technical challenges as well, it is rather straightforward to incorporate the D_1 path in a standard Li laser system, and the resulting temperature is usually in the $50\,\mu$K range as well. In our experiment, GM-cooling was demonstrated to be capable of reaching a final temperature of $13\,\mu$K [109].

[7] The hyperfine splitting of the excited state is approximately 4.4 MHz in total, compared to the 5.9 MHz-linewidth of the transition.

2.5 Summary

A mixture of Er and Li has many interesting properties for novel types of experiments. They display drastically different scales in all their characteristics, which can be used for a tailored trapping configuration. Their optical properties are particularly favorable for SST, where Li atoms can be trapped in a far red-detuned ODT operating on the tune-out wavelength of Erbium. Then, their large mass imbalance is beneficial for sympathetic cooling, further improved by the different quantum statistics of the selected isotopes. In particular, combining SST and the large specific heat capacity of Er in its classical state could prove instrumental in reaching unprecedented levels of degeneracy with a Fermi gas of Li. Finally, the ErLi mixture is very versatile regarding quantum statistics, since both atoms have fermionic and bosonic isotopes. Although changing from ^{6}Li to ^{7}Li entails an important modification to the laser system, Er can be selected rather easily thanks to its comparatively small isotope shifts.

However, describing Er as a double-edged sword would be accurate as well. Its large mass makes it difficult to keep in a shallow trap due to the strong gravitational tilt imposed on the trapping potential. Its large magnetic moment also makes it very sensitive to stray magnetic fields and gradients, making it prone to escape from shallow traps. Moreover, magnetic trapping is not possible since Er atoms are manipulated in their lowest Zeeman substate, which is a high-field seeker.

Chapter 3

Experimental apparatus

Over the course the PhD thesis, the most prominent part of the work was, undoubtedly, the design and construction of our new apparatus. Our approach was to rely on established techniques, which already proved successful in other experiments. The interested reader can find extensive discussions about aforementioned techniques in References [183, 194–196] for laser cooling and trapping, and in References [197, 198] for the vacuum.

At the start of the design phase, although Lithium was already a widespread element in the cold atoms community, Erbium had only been cooled to degeneracy in two research groups: Innsbruck [177], and Harvard [189]. It was also a component in only one mixture experiment: the Erbium-Dysprosium mixture [199], from Innsbruck as well. Finally, there were hints that Erbium and Lithium could be stable together because lanthanide-alkali mixtures had already been demonstrated [121, 200, 201]. However, the machine's architecture was chosen to be a "2-in-1" experiment, where the two species are handled separately in their own dedicated subsystems. Most of the arguments behind that decision were of technical nature. For example, the ovens alone would already be an issue because of their large difference in operating temperatures. The Zeeman Slowers (ZS) and Magneto-Optical Traps (MOTs) require very different parameters as well, mostly because of Erbium's sensitivity to magnetic fields. Although dual-species ZS have been demonstrated [202, 203], it would potentially require important compromises. The MOTs also require different magnetic gradients, typically much higher for Lithium than for Erbium. In particular, having the ZS and MOT fields combined as it is for our Lithium section [109] would not be possible for Erbium. There was also no guarantee that Erbium and Lithium could be loaded simultaneously in their MOT or in a common ODT. If not, one can go for a sequential loading of each species, but that also comes at the price of higher technical complexity [159].

An overview of the machine can be seen in Fig. 3.1. The direction we opted for was chosen to minimize the technical difficulties inherent to mixture experiments. By going along this "2-in-1" path, the goal was to build two single-species subsystems with already established techniques regarding laser cooling, while avoiding most cross-talk situations. This way, all the initial steps (such as ZS, MOT or ODT loading) can be optimized for each species independently. It resulted in having two separated ZS and MOT chambers, with a glass cell on the side for a future quantum gas microscope. The major downside to this approach is the long transport, over a distance of $50\,\mathrm{cm}$ for Erbium and $1\,\mathrm{m}$ for Lithium.

This chapter describes the three core systems of our apparatus, each in their separate part. We start with the description of our vacuum manifold and its main components in Section 3.1. Then, Section 3.2 depicts the different groups of magnetic coils built around

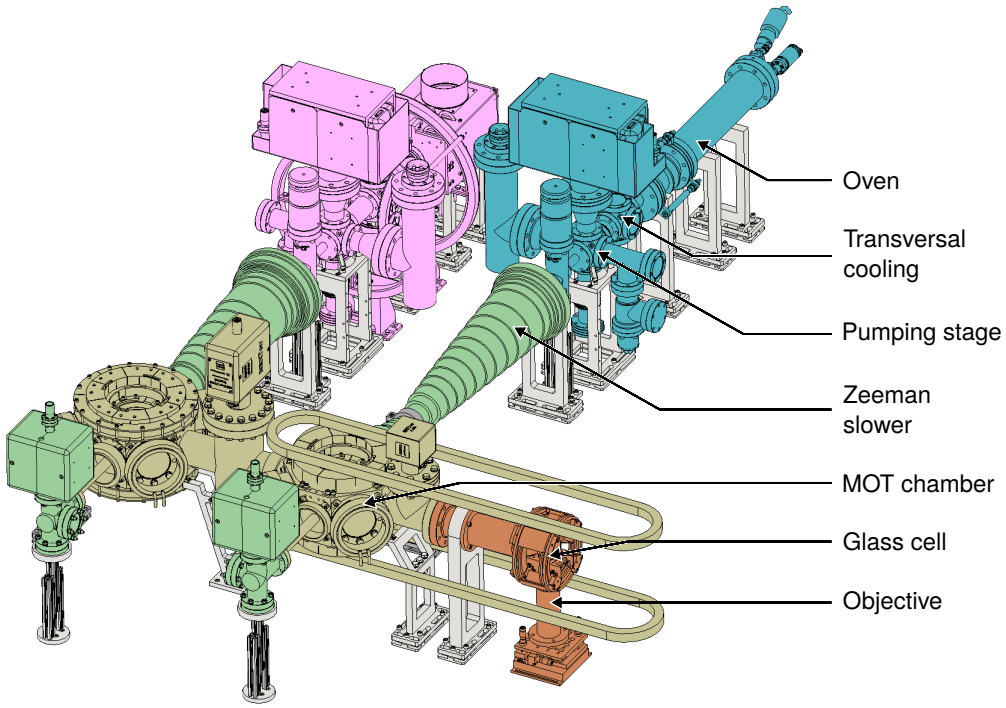

Figure 3.1 | Vacuum system overview. The HV sections of Erbium (blue) and Lithium (pink) are connected to UHV section via the Zeeman slowers (green), which act as a differential pumping tube. The UHV section hosts the MOT chambers (light brown) and the glass cell (dark brown). The Zeeman mirrors (green) are on the other side of the MOT chambers, also separated by a differential pumping tube. The legend is pointing to the Er side of the machine, but the Li side has the same components.

the Erbium side of the machine. Finally, the different laser setups implemented for the cooling and trapping of Erbium are presented in Section 3.3.

3.1 Vacuum system

3.1.1 Global overview

Design considerations Our vacuum system, shown in Fig. 3.1, was designed with (mostly) one requirement in mind: obtaining the highest possible vacuum, to prepare the cleanest environment in our science chamber. As explained in Section 2.2, the motivation to get such a good vacuum is to prevent the passive heating of our cold gas and extend its lifetime, by reducing the rate of collisions with particles still present in the chamber. This approach led to several general design choices.

The first choice was to make the vacuum manifold's topology as simple as possible. Since the vacuum is high enough for particles to be in the molecular flow regime (*i.e.*, they do not collide with each other but only with the walls), any kind of corner will effectively behave as a differential pumping tool. It means that, for example, placing an ion pump

behind a corner will reduce its performance, but also that it can be used as a way to isolate a low-pressure area. With that in mind, we applied the following reasoning: the pumps should be placed in a way to maximize their efficiency, and the low-pressure areas should be as well protected as possible from the rest of the experiment. In our case, it led to a very simple topology, which boils down to three straight lines: the Lithium line, the Erbium line, and the transport line. Along these lines, all the ion and getter pumps were placed as close as possible to the atoms' path and with the largest possible opening. On the contrary, the sharp angle between the Erbium or Lithium lines and the transport line protects the glass cell from the hot atomic gas coming from the ovens.

Then, the second choice was to trim any unnecessary component from the machine, starting with the pressure gauges. Because their sensitivity only goes down to about $10^{-11}\,\mathrm{mbar}$ and they can measure the pressure only locally, it was considered non-essential. To know the inside pressure, we directly read it from the ion pumps' current instead. That way, it is possible to have a precise idea of the vacuum quality down to $\sim 10^{-10}\,\mathrm{mbar}$, below which the pumps' sensitivity reaches its limit as well. We also chose to place only two gate valves in the whole machine: one in front of each oven, before the Zeeman slowers. The idea was that we would (hopefully) need them only when refilling an oven, and placing them here is enough to keep the vacuum intact.

Finally, it was also decided to avoid any active component inside the vacuum, especially magnetic coils. Although there are advantages to it (it allows the coils to be closer to the atoms and thus being smaller and ran at lower currents), it is also possible for them to degrade the vacuum quality. For example, reaching the Lithium Feshbach resonance at $830\,\mathrm{G}$ requires typical currents of more than $100\,\mathrm{A}$ through the coils. Of course, such a current will warm up the coils, which in turn will start emitting undesired particles from their surface and contaminate the environment.

On the logistic side, because of the Covid pandemic, we tried to mitigate the extended delivery times by using off-the-shelf components as much a possible. For that reason, most components except for the MOT chambers are standard vacuum components. They are all made of 316LN stainless steel, an alloy interesting for its mechanical, magnetic and thermal properties, widely used in vacuum systems.

Overview With that in mind, we can now take a look at our vacuum system. The different subparts are highlighted in the Fig. 3.1, and can be grouped in three main areas: the Erbium and Lithium High Vacuum (HV) sections, and the Ultra-High Vacuum (UHV) section. Each HV section includes a high-temperature effusion cell, a transversal cooling chamber, and a first pumping stage. The transversal cooling stage is also used as an optical pumping stage for Lithium, which proved to be a very efficient way to increase the atomic flux in the main chamber [109]. The UHV section includes the MOT chambers, the in-vacuum mirror chambers for the Zeeman slowers, and the science chamber. In between, these sections are connected by the gate valves[1] and the Zeeman slowers. Each of these three sections also has its own corner valve[2] to connect a turbomolecular pump. With this architecture, it was

[1] VAT GmbH, all-metal gate valve, Series 481, CF16
[2] VAT GmbH, "Easy-close" all-metal corner valve, Series 541, CF40

possible to reach $10^{-8}\,\mathrm{mbar}$ for the Lithium HV, $10^{-9}\,\mathrm{mbar}$ for the Erbium HV, and at least $10^{-11}\,\mathrm{mbar}$ in the UHV section.

3.1.2 Main components

Oven The Erbium oven is a commercial effusion cell from CreaTec[3], shown in Fig. 3.2. It is a dual-filament effusion cell, with a crucible and a hot lip that can be maintained at different temperatures by the two heating filaments. These parts are made of Tantalum, to withstand an operating temperature of up to $1400\,^{\circ}\mathrm{C}$. In the case of Erbium, its low vapor pressor requires the oven to typically run at $1100\,^{\circ}\mathrm{C}$ ($1200\,^{\circ}\mathrm{C}$) for the crucible (hot lip) (see Fig. 3.2).

This oven is a variant from the other Erbium machines [163, 164, 204], with a larger crucible volume. This one has a reservoir of $40\,\mathrm{cc}$ where we could place $100\,\mathrm{g}$ of Erbium (with natural isotopic abundance), in order to delay any refilling procedure as much as possible. The hot lip's apertures are also similar, with a diameter of $3.5\,\mathrm{mm}$ and a tube of $40\,\mathrm{mm}$ length. We placed an additional aperture further, behind the planned transversal cooling, to help with the atomic beam collimation and to be able to check the oven output.

It is possible to estimate the longitudinal velocity distribution of the atoms coming out of this specific geometry, by looking at a modified 1D-Boltzmann distribution [205–207]. The distribution is given by:

$$f(v,T) = \left(\frac{\pi D}{2}\right)^2 \cdot \frac{p_{\mathrm{vap}}(T)}{k_{\mathrm{B}}T} \cdot \left(\frac{m}{2\pi k_{\mathrm{B}}T}\right)^{3/2} \cdot v^3 e^{-\frac{mv^2}{2k_{\mathrm{B}}T}} \cdot \sin^2\theta \tag{3.1}$$

where D is the aperture diameter, θ the solid angle covered by the atomic beam exiting the oven and p_{vap} the Erbium vapor pressure. The calculated distribution is an important factor when planning the Zeeman slower's field to determine its capture velocity, as explained in Section 3.2.1. The vapor pressure of Erbium is calculated via the formula [163, 208]:

$$p_{\mathrm{vap}}(\mathrm{T}) = 10^{A-\frac{B}{C-T}},\ \text{with}\ A_{\mathrm{Er}} = 7.103, B_{\mathrm{Er}} = 12170, C_{\mathrm{Er}} = 100 \tag{3.2}$$

where A, B, C are empirical dimensionless values, and the temperature T is in Celsius.

Vacuum-wise, the oven is encased in a vacuum tube with a CF63 flange, and connected to the rest of the machine via a port aligner to help reduce the mechanical stress and eventually align the oven's output direction. However, this port aligner turned out to be more problematic than helpful. Due to the large output angle of the atomic beam, rotating the oven does not really impact the atomic flux in the MOT chamber. Moreover, the port aligner was responsible for some leaks at some point, because its aligning screws were too tight and it was making a small opening at the connection between the port aligner and the flange reducer. The leaks were closed by completely releasing the aligning screws, and the oven is now mechanically fixed by external mounts that block it on both sides, preventing any movement.

[3] CreaTec Fischer & Co. GmbH, model DFC-63-40-WK-2B

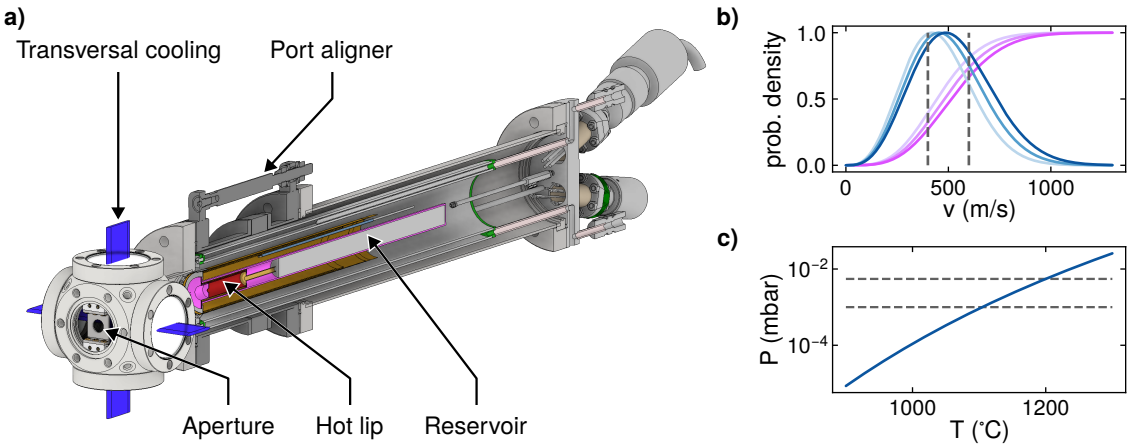

Figure 3.2 | Erbium oven overview. a) The oven has two sections: the reservoir ($1000\,^{\circ}\mathrm{C}$) and the hot lip ($1200\,^{\circ}\mathrm{C}$). The atomic beam is collimated by the hot lip's apertures and the planned transversal cooling. **b)** Distribution of longitudinal velocities (blue) and their cumulated counterpart (purple) for atoms exiting the oven from $900\,^{\circ}\mathrm{C}$ (light) to $1300\,^{\circ}\mathrm{C}$ (dark). The vertical dashed lines correspond to velocities of $400\,\mathrm{m/s}$ and $600\,\mathrm{m/s}$. All distributions were normalized for convenience. **c)** Vapor pressure of Erbium depending on the oven temperature. The horizontal dashed lines correspond to the oven temperatures in our experiment ($1100\,^{\circ}\mathrm{C}$ and $1200\,^{\circ}\mathrm{C}$).

Transversal cooling stage The Transversal Cooling (TC) stage, visible on Figs. 3.2 and 3.3, was planned to be as close as possible to the oven output, in a CF40 cubic chamber[4]. It is a 2-dimensional optical molasses which operates on the wide transition of Erbium at $401\,\mathrm{nm}$, whose purpose is to reduce the transversal velocity of the atoms exiting the oven, effectively collimating the atomic beam. Because the hot atoms exit the oven with a large fan angle [163, 207], we wanted to make the TC impactful by collimating the atomic beam at the earliest point, to maximize the amount of atoms going in the Zeeman slower. However, while this section was built and functional for a time, it had to be removed temporarily to divert the optical power towards the Angled Slowing setup (see Section 4.1.1). Once the Erbium MOT operational, its loading rate was high enough for Er not be a bottleneck in our experimental cycle, and the necessity of increasing the atomic flux in the chamber never arose. Since then, the TC setup has not been finalized, and could be a future improvement if a higher MOT loading rate is required.

Pumping stage The pumping stage of our HV section is placed right after the transversal cooling, in a CF40 cubic chamber[4] as well. It supports a $55\,\mathrm{L/s}$ ion pump[5] and a titanium sublimation pump[6]. Both of them are connected to the chamber with a custom conical CF40 to CF60 adapter, to increase their pumping performance. In steady-state operation, this section of the experiment has a stable pressure of $10^{-9}\,\mathrm{mbar}$. It hosts the Erbium HV section's corner valve as well, which is used to connect the turbomolecular pump. Finally, it has a bellow on the bottom, which was planned to hold a shutter for the atomic beam,

[4] Kimball MCF275-SphCube-C6
[5] Agilent Technologies, StarCell VacIon Plus 55
[6] Agilent Technologies, TSP Filament Cartridge CF40

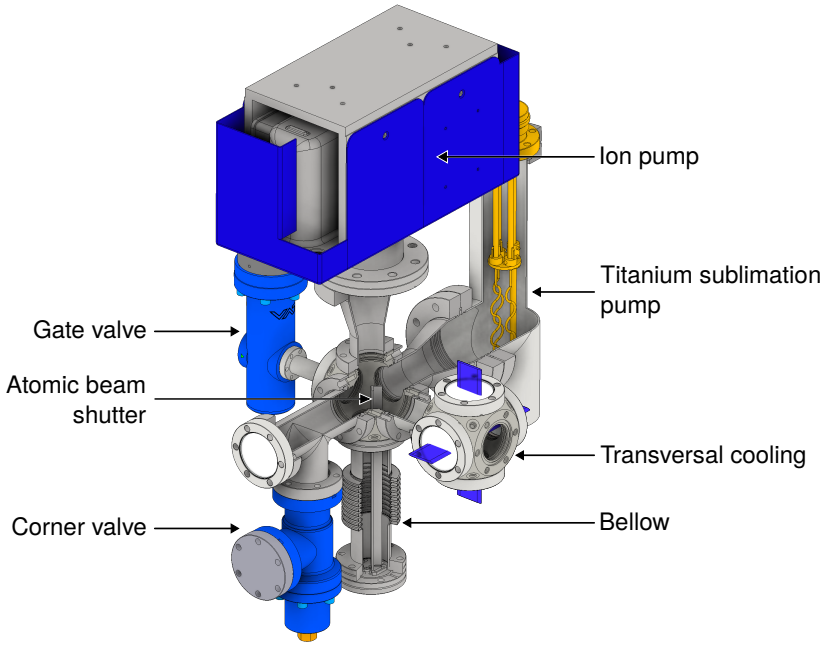

Figure 3.3 | Pumping stage of the Erbium HV section. The vacuum is maintained by a large ion pump and a titanium-sublimation pump, which needs to be reactivated periodically. The transversal cooling and shutter were designed and incorporated to the apparatus, but had to be removed during the building phase of the experiment (see text).

inspired from the Potassium lab's cold finger [209]. The shutter itself is simply a metallic stick, screwed on the bellow's bottom flange, which would block the atomic beam when the bellow is at rest. The idea was to push the bellow from the bottom to angle the shutter away from the path, thus allowing the atoms to go in the MOT chamber and load our Erbium collection trap. However, during the pumping process, both Lithium and Erbium bellows contracted more than we expected, and it was not possible to apply this idea anymore. Instead, the shutter is now fixed at an angled position to leave the path open, and should never be touched again.

Zeeman slower The Zeeman slower comes in two parts: the tube of the slower itself, and its in-vacuum mirror on the other side of the MOT chamber (see Fig. 3.4), used to send the slowing beam towards the oven output. Vacuum-wise, the Zeeman slower's tube acts as a differential pumping stage. It is $800\,\mathrm{mm}$ long, for an inner diameter of $10\,\mathrm{mm}$, with a CF16 flange on each side. With these dimensions, it maintains the UHV section at a pressure three orders of magnitude lower than the HV section due to its limited conductance (see for example [198]). As explained in Section 3.2.1, the coils were wound around a completely independent tube, in order to decouple the vacuum part from the rest. It prevents any kind of heating from the coils (which would increase outgassing), but also avoids any vibration or mechanical stress that could go on the small CF16 flanges.

On the other side of the machine, the in-vacuum mirror shown in Fig. 3.4 is a common trick used in cold atoms experiments. Without it, the viewport required to shine the Zeeman slower's beam would sit in direct line of sight from the oven, quickly covering it with an

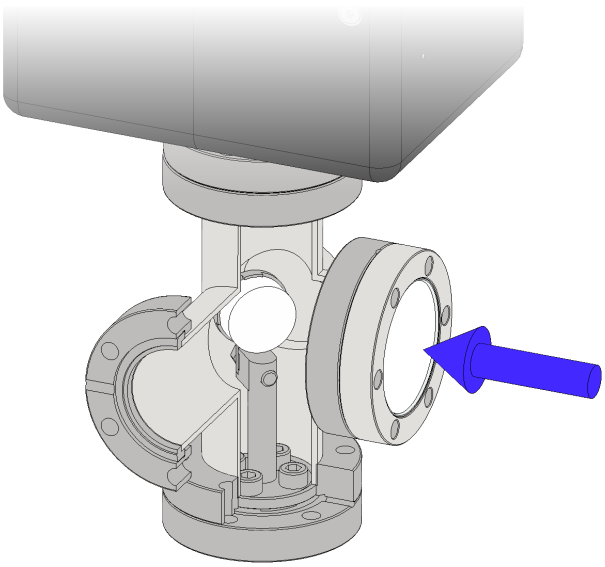

Figure 3.4 | In-vacuum Zeeman mirror. The in-vacuum mirror used to send the Zeeman slowing beam is made of and coated with aluminum. The light goes in through a CF40 viewport and is reflected by the mirror to be aligned with the atomic beam. The custom mount was designed to minimize the surface-to-surface contacts and the screws are vented, to allow the pumping without leaving high-pressure pockets. All parts were made of 316LN stainless steel for low magnetic permeability and mechanical stability.

Erbium coating. Based on the observations of other experiments [163, 210, 211], using an aluminum mirror is a good solution in that case, where the mirror's reflectivity does not decrease even where there is a layer of Erbium on it. In our case, the vacuum mirror is a $1''$ aluminum mirror[7], mounted on a post which is directly screwed on a blind flange below. This mirror was also put in a small separate chamber, connected to the MOT chamber by a small tube (visible in Fig. 3.1), and with a small ion pump[8] on top. The small tube also acts as a differential pumping element, with about one order of magnitude of pressure difference. This setup then collects and eventually pumps the hot particles coming from the oven, and prevents it from accumulating in the MOT chamber.

MOT chamber Our (double) MOT chamber is a large custom part[9] which incorporates both Erbium and Lithium chambers together. The chambers are connected via a large tube where we placed a NEG pump[10]. A second NEG pump[11] was also placed between the Erbium chamber and the glass cell. Both pumps were placed in a way such that their getter part stands exactly $10\,\mathrm{mm}$ above the transport axis, to maximize their performance while staying out of the way. One could also be concerned about the stray magnetic field from their strong permanent magnets when going that close. However, we were assured by the company that

[7] Edmund Optics, Aluminum substrate, protected Aluminum coating
[8] Agilent Technologies, StarCell VacIon Plus 20
[9] Manufactured by PINK GmbH Vakuumtechnik
[10] SAES NEXTorr D1000 StarCell
[11] SAES NEXTorr Z300

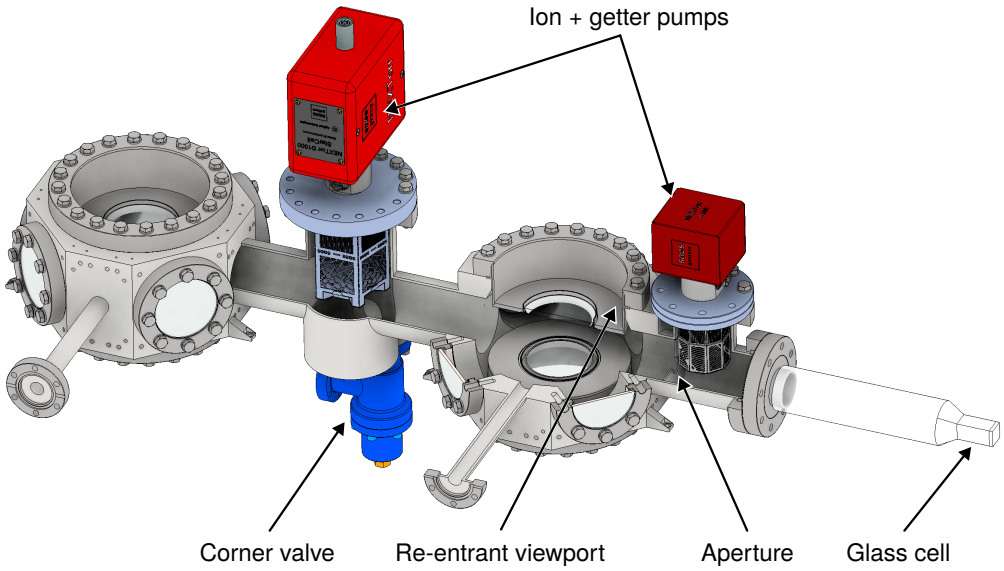

Figure 3.5 | Main vacuum chambers. The UHV section hosts the MOT chambers of Lithium (left) and Erbium (middle), and the glass cell (right). The view is partially cut to show the different features of our UHV section. The MOT chambers have CF160 re-entrant viewports on the vertical axis with 73mm clear aperture, and CF63 viewports on the sides. The glass cell is a rectangular, non-coated, fused silica cell. It is isolated from the MOT chambers by a 20mm aperture to limit the amount of particles reaching inside, and the pump is placed there to maximize its performance for the cell. The corner valve (blue, center) is used for the turbomolecular pump during the initial evacuation. The orientation of the figure is the same as Fig. 3.1.

their fields should be on the order of $100\,\mathrm{mG}$ at this point, and we never saw any problem that we could link to it.

Both chambers feature four CF63 viewports with anti-reflection (AR) coatings[12] for several wavelengths: $401\,\mathrm{nm}$, $583\,\mathrm{nm}$, $671\,\mathrm{nm}$, $841\,\mathrm{nm}$ and $1064\,\mathrm{nm}$. With all these wavelengths, the viewports are very versatile and it is possible to use all interesting wavelengths for both atoms everywhere. On the Lithium side, we also placed a CF40 viewport for the transport direction, with the same coatings. On the vertical axis, we opted for re-entrant CF160 viewports[13] with a clear aperture of $73\,\mathrm{mm}$ for both Erbium and Lithium. These special viewports confer several advantages: the volume of the vacuum is reduced (which helps with the pumping), the large windows provide a better optical access, and it becomes possible to put magnetic coils inside to get them much closer to the atoms (see Section 3.2 and Fig. 3.7). It would also be possible to build a high-resolution imaging system (see for example [211]), but we decided instead to exploit this design for a vertical dipole trap setup, as explained in Section 4.1.3.

These chambers are, compared to many other experiments, rather large. The distance between their respective center is exactly $50\,\mathrm{cm}$, which is also the distance between the Erbium chamber and the glass cell. It implies that the distance between the Zeeman slower's end and the MOT center is also large, at $20\,\mathrm{cm}$. There, despite the large MOT beams, it

[12] Viewports: Hositrad B.V. (fused silica), Coatings: Laseroptik GmbH
[13] Manufactured by UKAEA Special workshop

led to a weak loading rate and we had to circumvent the issue with an additional slowing region just before the MOT (see Section 4.1.1).

Science chamber Our science chamber is a custom rectangular glass cell made of quartz[14], with inner dimensions of $12 \times 12 \times 38\,\mathrm{mm}$ and $4\,\mathrm{mm}$ thick walls, connected to the Erbium MOT chamber by a CF63 flange. We decided to use fused silica to avoid the thermal lensing of the more common Borofloat when using high power lasers. However, it comes at the price of an uncoated cell: because of the necessary high temperature to bond the quartz plates, the coating can be damaged if it is done beforehand. For that reason, cells made of fused silica are usually coated on the exterior surfaces only. In our case, we chose to leave the glass uncoated to keep a uniform reflectivity of $4\,\%$ for all wavelengths. Using fused silica came with an additional price: the length of its metal-to-glass transition ("connection tube"). The minimum length that could be done between the CF63 flange and the fused silica part was $24\,\mathrm{cm}$ (for a total length of $28\,\mathrm{cm}$), which imposed to have a long transport distance in our experiment.

A specificity of our glass cell is the unusually large diameters of its flange and connection tube. Here, the idea was to maximize the getter pump's performance by keeping a large conductance between the cell and the pump. The conductance heavily depends on the tube's inner diameter, and we opted for the largest connection tube the manufacturer could do, with a $48\,\mathrm{mm}$ inner diameter tube, welded to the CF63 flange. Furthermore, the pump was dedicated to the glass cell by the addition of a separation between the cell and the other chambers. This was done by placing a disk in the vacuum, between the Erbium MOT chamber and the pump, with a small $\varnothing 20\,\mathrm{mm}$ circular aperture. Such an aperture is effectively a differential pumping element: it is used to limit the amount of stray particles random-walking in the glass cell, while the Erbium and Lithium atoms can still be transported through the aperture. With this configuration, according the ion pump there, the vacuum has reached the low $10^{-12}\,\mathrm{mbar}$ range[15].

3.2 Magnetic coils system

3.2.1 Zeeman slower coils

A Zeeman slower (ZS) is a tool commonly used in cold atoms experiments, to decelerate an atomic beam down to a velocity that can be captured by a Magneto-Optical Trap (MOT). Its principle is rather simple: it consists in shining a laser beam towards an atomic beam to slow it down, while maintaining the atom-light resonance by combining the Zeeman and Doppler effects with a varying magnetic field. The technique was developed in the 1980s [2, 3, 212], and quickly led to the first optical molasses [5, 193]. It has been described extensively in the literature [2, 195, 196] and will be described only shortly here.

[14] Cell: JapanCell Co. Ltd, Glass: Ohara Corp., SK-1300

[15] This value is below the reliable detection range of the pump and can only be taken as a broad indication of the vacuum quality.

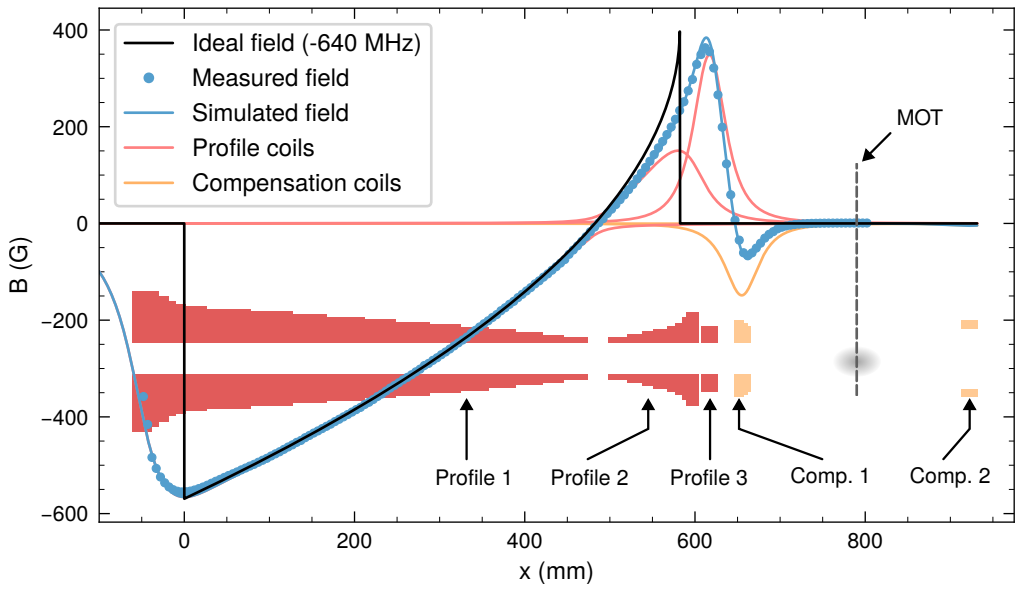

Figure 3.6 | Coils layout and field for the Erbium Zeeman slower. The increasing, spin-flip field's profile is shaped by three independent coils: Profile 1, 2 and 3 (light red). Profile 1 makes the negative $\mathrm{B_x}$ part, responsible for the slower's capture velocity. Profile 2 shapes the positive part, and Profile 3 shapes the end part of the field, responsible for the exit velocity. The two Compensation coils (light orange), are designed to bring the field to zero at the MOT position, indicated by the gray dashed line. The ideal field (black) for a detuning of $640\,\mathrm{MHz}$ is matched well by the simulated total field (blue) except for its end part, where the compensation coil shifts the maximum's position. The measured field is indicated by the blue dots.

When the slowing laser beam is resonant with the desired atomic transition, the atoms absorb photons from the laser beam, and re-emit them in random directions via spontaneous emission. The repeated momentum kicks from the laser beam, combined with the isotropic spontaneous emission, result in a reduction of the atoms' axial velocity component. The radial components however, is increased via the spontaneous emissions and secondary absorptions, resulting in radial (or transversal) heating of the atomic beam [213]. The laser beam sent towards the atoms has an effective detuning, emerging from three contributions:

$$\Delta = \Delta_L + \mathbf{k}\cdot\mathbf{v} + \mu B/\hbar \tag{3.3}$$

where Δ_L is the laser detuning from the bare atomic resonance, $\mathbf{k}\cdot\mathbf{v}$ is the Doppler effect and $\gamma B/\hbar$ is the Zeeman effect. The Doppler effect depends on external degrees of freedom only, with $\mathbf{k}$ the laser wavenumber and $\mathbf{v}$ the atomic velocity. In contrast, the Zeeman effect depends on the atomic transition, with $\mu = (g_{J'}m_{J'} - g_J m_J)\mu_B = -1.13719\mu_B$ the differential magnetic moment of the ground and $401\,\mathrm{nm}$-excited states (see Section 2.4 and [163]); B is the magnetic field and $\hbar$ is the reduced Planck constant. The atom-light resonance is maintained over the whole slowing distance by locally adapting the magnetic field to the atoms' velocity. The latter is calculated by assuming a constant deceleration a from an initial velocity v_0:

$$v(x) = \sqrt{v_0^2 - 2ax} \tag{3.4}$$

and finding the corresponding magnetic field is done simply by calculating the resonance condition $\Delta = 0$, to obtain:

$$B(x) = \frac{\mu}{\hbar}\left(\Delta_L + k\sqrt{v_0^2 - 2ax}\right) \tag{3.5}$$

The last relevant quantity for the design of a Zeeman slower is the deceleration. For a given atomic transition, its linewidth (and the resulting light scattering) puts a limit on the attainable deceleration, which can be written as:

$$a = \frac{F_{\text{scatt.}}}{m} = \underbrace{\frac{\hbar k\Gamma}{2m}}_{a_{\max}} \cdot \underbrace{\frac{s}{1+s}}_{\eta} \tag{3.6}$$

where Γ is the transition linewidth, m is the atom's mass and $s = I/I_{\text{sat}}$ is the saturation parameter. The term $\hbar k\Gamma/2m$ can be understood as the maximum deceleration for a given transition, weighted by the second term $s/(1+s)$ for a finite laser intensity.

As stated before, the high melting point of Erbium ($1523\,^\circ\text{C}$) requires the oven to function at high temperature ($1200\,^\circ\text{C}$) to reach sufficiently high vapor pressure and atomic flux. The corresponding distribution of longitudinal velocity of atoms exiting the oven through the hot lip is straightforward to calculate [205, 206] and peaks around $450\,\text{m/s}$ (see Fig. 3.2), depending on the exact temperature. Until now, other Erbium experiments have been using a Zeeman slower with a capture velocity of $400\,\text{m/s}$ [163, 164, 214], and $500\,\text{m/s}$ [204]. It is also interesting to note that an atomic beam source has been demonstrated with a 2D MOT instead of a ZS for Dysprosium [215], which could be adapted to Erbium easily.

In our case, the field of our spin-flip ZS (shown in Fig. 3.6) is made by the contribution of five separate coils in total. Three coils are shaping the slower's field profile, and two additional coils are here to compensate the magnetic field at the MOT position. It was initially designed with capture and exit velocities of $v_c = 600\,\text{m/s}$ and $v_e = 5\,\text{m/s}$ over a distance of $58\,\text{cm}$, at a laser detuning of $\Delta = -640\,\text{MHz}$ from the blue transition at $401\,\text{nm}$. The corresponding fields at the entrance and exit of the ZS are then $550\,\text{G}$ and $390\,\text{G}$ respectively. With these parameters, the so-called safety factor of our ZS is $\eta = 0.6$. The motivation for a higher capture velocity is that, when looking at the cumulated velocity distribution, the number of atoms addressed by the ZS can be doubled while remaining at reasonable magnetic fields. Higher velocities could also be achieved, although it would yield diminishing returns. However, we changed the exit velocity of our ZS at a later date to incorporate a slowing stage in front of the MOT beams (see Section 4.1.1). In short, we lowered the exit field to increase the output velocity and keep the atomic beam more collimated over the gap between the ZS exit and the MOT capture area.

The ZS coils were wound directly on a $40\,\text{mm}$ diameter aluminum tube, so that we could bring it around the CF16 flanges of the vacuum tube when building the experiment. It has the advantage of completely decoupling the coils from the vacuum parts themselves, thus avoiding any heating or vibrations from the slower. The copper wire has a large rectangular profile of $4 \times 3\,\text{mm}$ and is hollow, with a round opening of $\varnothing 2\,\text{mm}$ inside for water cooling. Although the layers of a coil share an electrical connection, it cannot be the same for the water. For example, our largest coil has a total wire length of $280\,\text{m}$, and the pressure drop

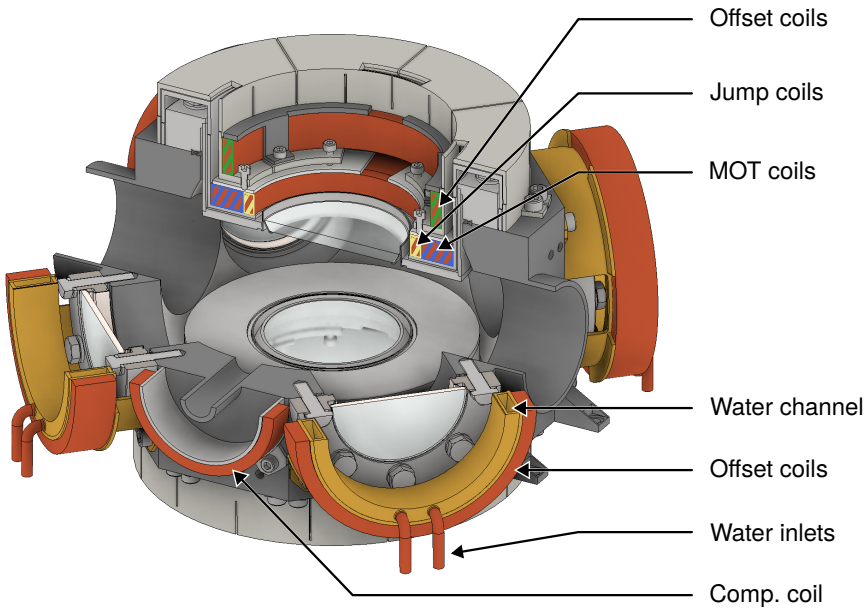

Figure 3.7 | Coils layout for the Erbium MOT chamber. The re-entrant viewports host three pairs of coils: the MOT (blue stripes), vertical offset (green stripes), and jump (yellow stripes) coils. The horizontal offset coils were mounted on water-cooled mounts made of brass, and placed around the side viewports. All the coils and their mounts were designed to be incorporated without blocking optical access.

over this distance would be too important to have an effective cooling. In general, the large coils were wound by pairs of layers, in series for the electrical current but in parallel for the water. Finally, all layers were individually glued and isolated with a Kapton layer. In their operational steady-state, the coils maintain a temperature between $22\,^{\circ}\mathrm{C}$ and $26\,^{\circ}\mathrm{C}$.

3.2.2 MOT chamber coils

The Erbium MOT chamber holds six pairs of coils, all controlled independently. The first pair of coils, named here MOT coils, is dedicated to the field's gradient, which can be used for the MOT or for magnetic levitation. Three more pairs, named offset coils, are mounted around the chamber to provide control of the field's magnitude and direction at the center of the chamber. One pair, the jump coils, was added along the vertical axis, to have a fast control of the magnetic field in this direction. These three pairs were designed to keep the optical access provided by the inverted viewport's clear aperture unobstructed. The last pair of coils is the ZS compensation coils (see Section 3.2.1), mounted on each side of the MOT chamber to cancel out the ZS field at the MOT position.

The global layout is shown on Fig. 3.7, where it is easy to see why the re-entrant viewports are convenient. Three pairs of coils were placed inside: the MOT coils, the vertical offset coils, and the jump coils. These coils were assembled in an independent set of mounts, so

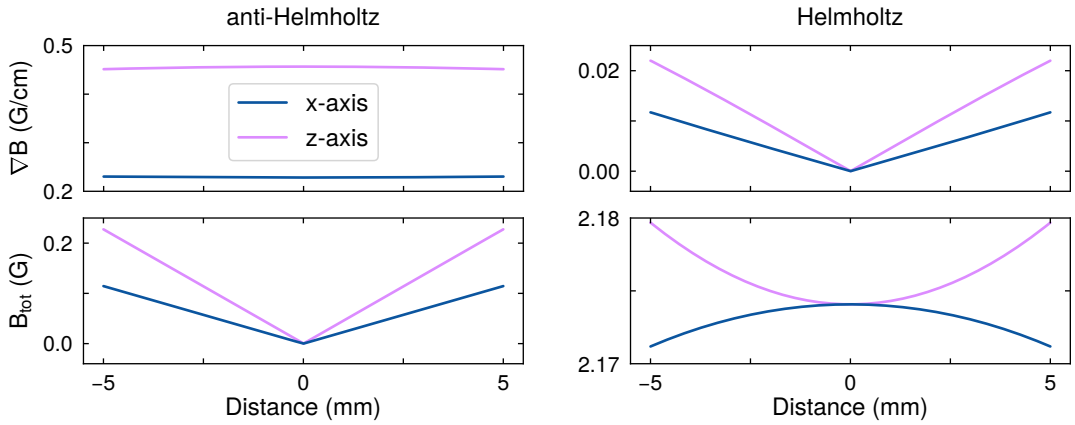

Figure 3.8 | MOT coils fields. All calculations are done for a current of $1\,\mathrm{A}$ per coil. They produce a gradient of $0.45\,\mathrm{G/cm/A}$ in anti-Helmoltz (upper left) or a field of $2.175\,\mathrm{G/A}$ in Helmholtz (lower right) configuration. They provide a field (gradient) homogeneity of $0.2\,\%$ ($1\,\%$) over the range of $\pm 5\,\mathrm{mm}$ in Helmholtz (anti-Helmholtz) configuration. The deviation from the ideal Helmholtz coils' dimensions for can be seen by the small stray field offset (lower left) and gradient (upper right). Here, x-axis is horizontal, z-axis is vertical, and the coils' axis is along z.

that we could easily bring them around the vacuum chamber after the bakeout was done. The mounts were also cut with a series of slit to remove the radial symmetry, thus mitigating the eddy currents.

MOT coils The Erbium MOT coils were designed to be usable for Lithium as well, for maximum versatility. At that point in the design phase, the transport to the glass cell was not fully planned yet, and it was important that we could perform evaporative cooling on a Lithium cloud in the Erbium chamber if necessary. They were designed with six layers of three windings, using the same hollow copper wire as the Zeeman slower for water cooling. They have an inner diameter of $108.4\,\mathrm{mm}$ and are separated by $66\,\mathrm{mm}$. At the center, it is capable of producing either a homogeneous field of $870\,\mathrm{G}$ at a current of $400\,\mathrm{A}$ when put in Helmholtz configuration, and a gradient of $183\,\mathrm{G/cm}$ in anti-Helmholtz configuration (see Fig. 3.8). With this current, the dissipated heat which needs to be carried out with water cooling amounts to almost $2.5\,\mathrm{kW}$. However, the reachable field is currently limited to $\sim 600\,\mathrm{G}$ due to the low water flow in the copper wire.

On the Lithium side, these coils are being used for an evaporation in the ODT before being transferred to the transport lattice. Although it is not possible to reach the main Feshbach resonance at around $830\,\mathrm{G}$ for the $|1\rangle$-$|2\rangle$ and $|2\rangle$-$|3\rangle$ mixtures, the evaporation is possible at a much lower field for a $|1\rangle$-$|3\rangle$ mixture. In that case, the scattering lengths between the two hyperfine states of Lithium is close to $-900\,a_0$ near $300\,\mathrm{G}$, and provides good parameters for a forced evaporation. Here, the states $|1\rangle$, $|2\rangle$ and $|3\rangle$ refer to the three lowest hyperfine states of Lithium; the procedure is described in the complementary thesis [109].

Offset coils The offset coils were all designed to be capable of generating a field of $10\,\mathrm{G}$ at a maximum current of $15\,\mathrm{A}$. They come in two different shapes, for the vertical and the

horizontal directions. Along the vertical axis, the offset coils were wound with the same hollow wire as the ZS and MOT coils, to provide water cooling. They have an inner diameter of $120.8\,\mathrm{mm}$, for two layers of five windings and a spacing of $107.8\,\mathrm{mm}$. Along the horizontal axes, the offset coils were wound with a non-hollow wire, with a smaller profile of $2 \times 1\,\mathrm{mm}$, due to the limited space available. They have an inner diameter of $118.5\,\mathrm{mm}$, for six layers of ten windings per coil and a spacing of $278.3\,\mathrm{mm}$. Their mounts were designed to go around the side CF63 viewports without blocking any optical access, while providing the water cooling. They are made of brass, and include a $50 \times 20\,\mathrm{mm}$ channel for the water. The four brass mounts were also connected in series for the water circuit, which turned out to be a very effective way to cool the coils with a minimal usage of space.

Jump coils The jump coils were designed for fast changes in the magnetic field along the vertical axis. It can be achieved by having coils with low inductance, and placing them close to the atoms. In this case, it was natural to place them inwards of the MOT coils, close to the re-entrant viewport's window (see Fig. 3.7). At that position, using the hollow copper wire, it was possible to design them to reach $11\,\mathrm{G}$ at $15\,\mathrm{A}$ with two layers of three windings. The calculated inductance is then $0.19\,\mu\mathrm{H}$, yielding rise times of $\approx 60\,\mu\mathrm{s}$. However, at the time of writing, these coils still have not been used (thus not characterised either) in the experiment cycle.

3.2.3 Transport coils

As it has been explained in Sections 2.4 and 4.2, the Erbium atoms require the help of magnetic levitation by a field gradient of $4.2\,\mathrm{G/cm}$ to be transported from the MOT chamber to the glass cell. In brief, this requirement appears because of a combination of factors: the large mass of Erbium, and the limited laser intensity that can be reached in our transport 1D-lattice setup. The oblate traps formed by the lattice are strongly confining in the axial direction, but weaker in the radial direction; too weak to hold the atoms against gravity. To prevent the atoms from falling through the traps, we built a pair of coils designed to counter the effect of gravity over the entire transport distance.

An important design choice was to make the transport's magnetic levitation static. Although several experiments have been using magnetic transport with many pairs of coils [216], our approach was to make the sequence as simple as possible. That was achieved by having a pair of elongated "racetrack" coils and a single round "launch" coil, which are turned on during transport to provide magnetic levitation, at a fixed current for the whole transport duration. This configuration gets rid of the need for a complex timing sequence with many different parts.

The coils are shown on Fig. 3.1, and typical fields are shown in Fig. 3.9. Due to the limited space available around the chamber, the racetrack coils could not be elongated arbitrarily, and some edge effects (side gradients, mostly) are to be expected at the Erbium MOT and glass cell locations. For this reason, the "launch" coil was added on the Erbium MOT chamber, to account for the side gradient imparted by the racetracks' edge effect. On the science chamber side, it was possible to extend the racetracks further and an additional coil was not required.

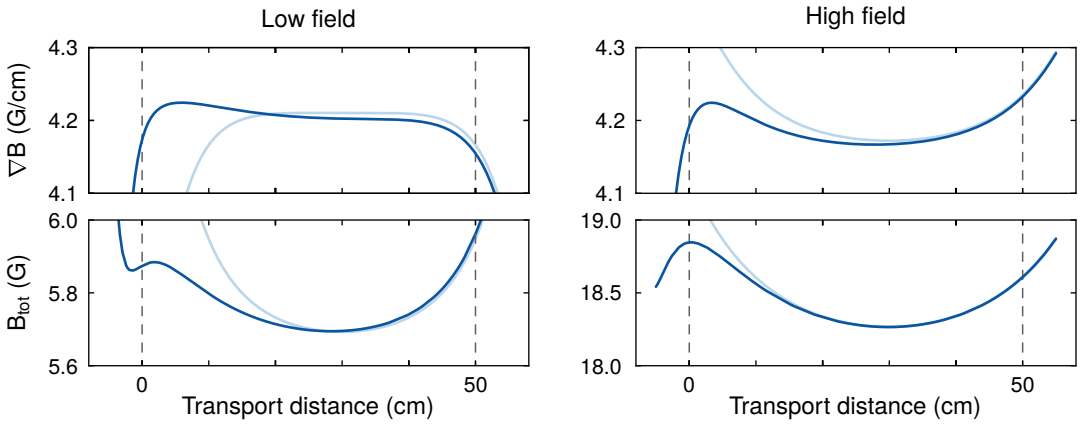

Figure 3.9 | Transport coils fields. Transporting Erbium atoms requires magnetic levitation at a non-zero magnetic field to keep the atoms polarized. The field is generated by the racetrack and launch coils (see text), and needs to be constant over the whole transport distance. The field gradient (top row) has to be at $4.2\,\mathrm{G/cm}$ for magnetic levitation. The absolute field (bottom row) has to be away from any Feshbach resonance to avoid atom loss. Two examples are given, at low field (left column) and high field (right column), where no Feshbach resonance are in the vicinity. The effect of the launch coil at the MOT position ($0\,\mathrm{cm}$) can be seen by comparing the field generated by all coils (dark blue) or by the racetracks alone (light blue).

The racetracks were wound on a custom aluminum L-shape profile, and are fixed to the middle and top layers breadboards with S-shaped aluminum plates. They were wound with the same hollow wires as most other coils to provide water cooling. Their shape can be described as a rectangle of $125 \times 775\,\mathrm{mm}$ with a semicircle of $125\,\mathrm{mm}$ diameter on each side for their inner dimensions. Then, both coils were wound with six layers of five windings, and mounted with a spacing of $210\,\mathrm{mm}$ between them. The launch coil was wound directly on the Erbium vacuum chamber with the non-hollow wire. It has an inner diameter of $72.8\,\mathrm{mm}$ for five layers of twelve windings and stands under the racetracks'end, $15\,\mathrm{cm}$ away from the atoms.

3.2.4 Science chamber coils

Our science chamber has its own layout for magnetic field control, shown in Fig. 3.10, which is using the same typical ingredients as the MOT chambers. In total, five pairs of coils were designed to go around the glass cell, all mounted wounded on a common aluminum mount, itself fixed to a large stainless steel foot. This design allowed us to fully prepare the coils on the mount, before sliding the whole setup around the glass cell and along its tube with minimal danger for the cell. The different coils from this setup were intended to provide three different functions, described below: Feshbach resonance, spin-separation, and field offset.

Feshbach coils These coils were designed to generate a magnetic field high enough to reach the Lithium Feshbach resonance at $830\,\mathrm{G}$, just like the MOT coils described above (see

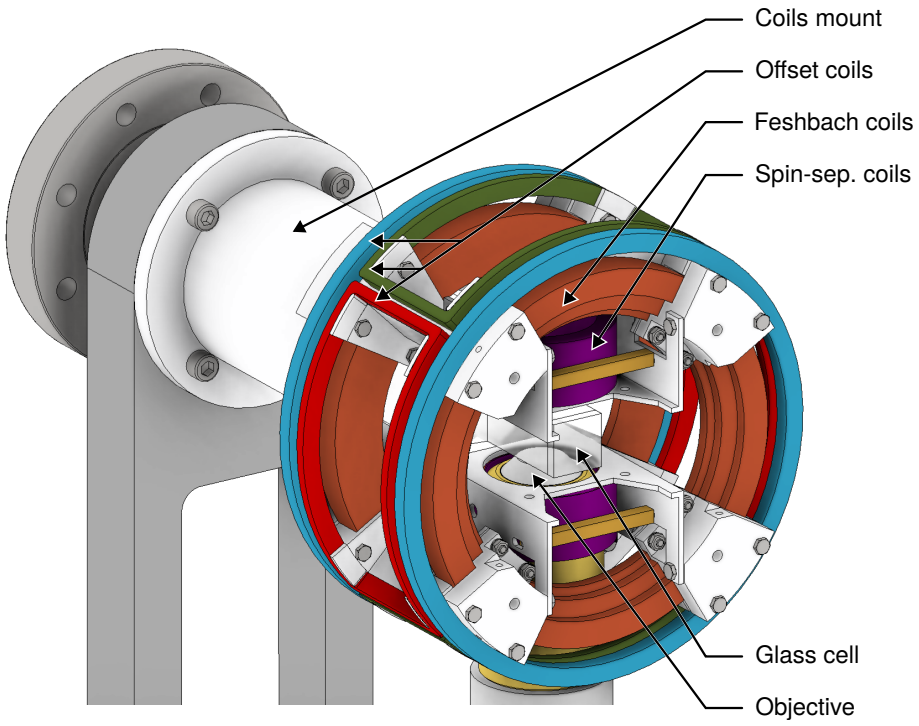

Figure 3.10 | Coils layout for the glass cell. The glass cell was equipped with five pairs of coils, similarly to the MOT chamber. Three pairs of offset coils (red, green, blue) provide fine control over the field's magnitude and direction; one pair (orange) was designed to be in Helmholtz configuration for the Lithium Feshbach resonance; the last pair (purple) was designed to provide a strong gradient in the vertical direction. The latter was designed to be able to spatially separate two spin states of Lithium atoms by applying a vertical magnetic gradient, for a future spin-resolved imaging system.

Section 3.2.2). The major difference with the MOT coils is their shape and positioning. By careful placement of the coils' windings, it is possible to stay very close to a perfect Helmholtz configuration, so that the generated magnetic field (or gradient) is highly homogeneous at the atom position in the glass cell, as depicted in Fig. 3.11. For that purpose, the coils have to maintain a "staircase" shape, so that each winding matches the Helmholtz condition individually, as can be seen on Fig. 3.10.

Here, we decided to orientate the coils along the transport direction, instead of putting their axis vertically. This configuration brings two big advantages. First, it gives the possibility of using a side gradient in the magnetic field, to be able to evaporate Lithium atoms from an oblate trap, or horizontal lattice plane. Second, it allows the coils to be on the small end for their intended purpose: because they go around the cell, they can be placed very close to each other, and the Helmholtz condition implies that their radius is small as well. Having small Feshbach coils means that the electric current running through it is lower than that of larger coils for the same magnetic field, and their inductance is lower as well. On a pragmatic note, the lower electric current implies weaker Joule heating (and thus heat removal), but also using a smaller power supply, which is a non-negligible argument for

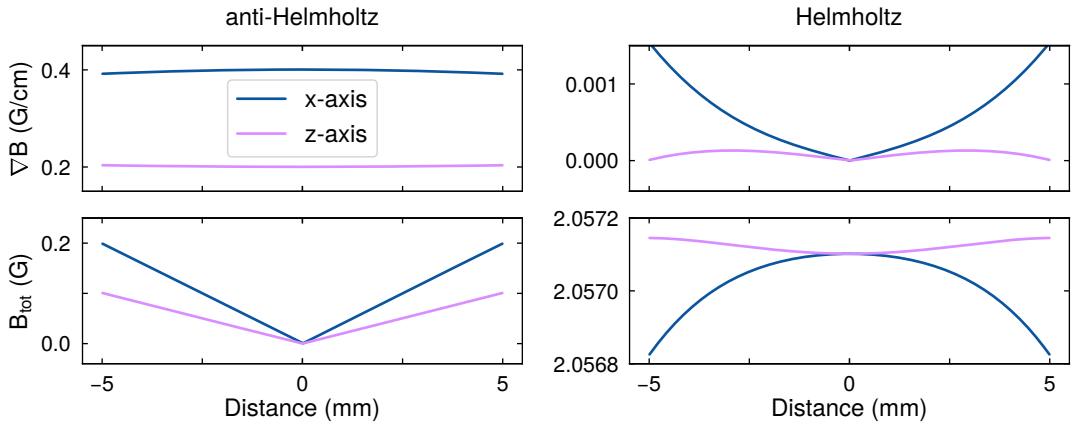

Figure 3.11 | Feshbach coils fields. All calculations are done for a current of $1\,\mathrm{A}$ per coil. They produce a gradient of $0.4\,\mathrm{G/cm/A}$ in anti-Helmoltz (upper left) or a field of $2.06\,\mathrm{G/A}$ in Helmholtz (lower right) configuration. They provide a field (gradient) homogeneity of $0.01\,\%$ ($2\,\%$) over the range of $\pm 5\,\mathrm{mm}$ in Helmholtz (anti-Helmholtz) configuration. The deviation from the ideal Helmholtz coils' dimensions for can be seen by the small stray field offset (lower left) and gradient (upper right). Here, x-axis is horizontal, z-axis is vertical, and the coils' axis is along x.

high power. Of course, because every choice is a compromise, it comes at the price of a slightly obstructed optical access around the glass cell. This issue was mitigated by having a tapered end on the glass tube (see Fig. 3.5), which opens the optical access on the side of the coils pair.

Just like most of our coils, the targeted high current requires strong cooling, so these coils have been wound with our hollow copper wire ($3 \times 4\,\mathrm{mm}$, with $2\,\mathrm{mm}$ hole). They have an inner diameter of $100.5\,\mathrm{mm}$, for a spacing of $50\,\mathrm{mm}$, and wound with six layers of 1, 2 or 3 windings depending on their distance to the center. This way, they can generate a homogeneous field of $820\,\mathrm{G}$ or a gradient of $160\,\mathrm{G/cm}$ at $400\,\mathrm{A}$. However, running the coils at this current still dissipates about $1.9\,\mathrm{kW}$ despite their small size.

Spin-separation coils These coils were designed to provide a strong magnetic field gradient in the vertical direction, in order to spatially separate two hyperfine states of Lithium at the end of an experiment. This is a very simple way to obtain a powerful tool: spin-resolved imaging [93]. Combined with site-resolved imaging, this is currently the state-of-the-art when it comes to quantum gas microscopy [32].

In our setup, these coils were a late addition to the whole layout, and had to be placed either above and below the Feshbach and offset coils, or placed inside for a much reduced size. We chose to place them inside, following the principle of smaller size for high-field coils, despite losing optical access on the vertical facets of the glass cell. Their inner diameter was fixed at $40\,\mathrm{mm}$ to accommodate the high-NA objective, with a spacing of $34\,\mathrm{mm}$ between the coils. They were wound with four layers of two windings using the hollow copper wire. With this shape, they can generate a gradient of $348\,\mathrm{G/cm}$ at $400\,\mathrm{A}$, or eventually an offset of $550\,\mathrm{G}$ at $400\,\mathrm{A}$ if a strong field is required in the vertical direction. In that case, their small size induces a Joule heating of $400\,\mathrm{W}$, much lower than their Feshbach counterpart.

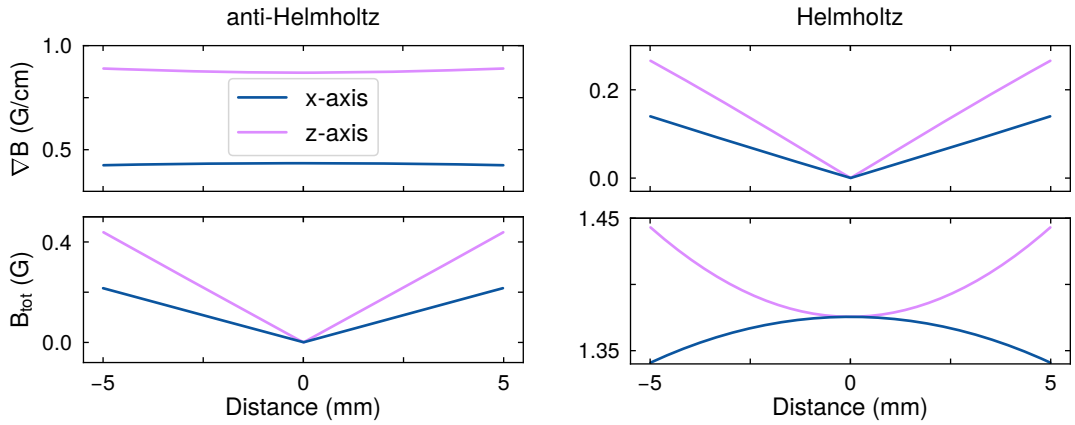

Figure 3.12 | Spin-separation coils fields. All calculations are done for a current of $1\,\mathrm{A}$ per coil. They produce a gradient of $0.87\,\mathrm{G/cm/A}$ in anti-Helmoltz (upper left) or a field of $1.38\,\mathrm{G/A}$ in Helmholtz (lower right) configuration. They provide a field (gradient) homogeneity of $5\,\%$ ($2.3\,\%$) over the range of $\pm 5\,\mathrm{mm}$ in Helmholtz (anti-Helmholtz) configuration. The deviation from the ideal Helmholtz coils' dimensions for can be seen by the small stray field offset (lower left) and gradient (upper right). Here, x-axis is horizontal, z-axis is vertical, and the coils' axis is along z.

Offset coils The offset coils were wound directly on the aluminum mount, with the goal of not blocking optical access any more than the Feshbach coils already do. For that reason, they were placed in the line of sight of the Feshbach coils, and in the dead angles of the glass cell. These angles are the four wall connections at $\pm 45\,^\circ$, $\pm 135\,^\circ$ around the transport axis. They can be considered dead angles simply because it is not possible to shine intense laser light at these angle, otherwise it can permanently damage the bonding between the glass cell walls and compromise the vacuum.

Following these considerations, the offset coils which are orthogonal to the transport axis were designed to be rectangular and bent along the circle provided by the aluminum mount (see Fig. 3.10). The offset coils which are coaxial with the transport are more traditional, being simply round and wound around the Feshbach coils. All of them had to be wound with the non-hollow wire due to the restricted space. The rectangular coils have inner dimensions of $100 \times 50\,\mathrm{mm}$ with a spacing of $120\,\mathrm{mm}$, were wound with three layers of three windings, and can generate an offset field of $6.3\,\mathrm{G}$ at $15\,\mathrm{A}$. The round coils have an inner diameter of $153\,\mathrm{mm}$ with a spacing of $68\,\mathrm{mm}$, were wound with three layers of three windings, and can generate an offset field of $16\,\mathrm{G}$ at $15\,\mathrm{A}$.

3.3 Laser system

This section is dedicated to the different laser systems used in our experiment, with a selection on the Erbium systems. The Lithium systems are not mentioned here, and the reader is referred to the complementary thesis [109] for this aspect of our machine. The laser cooling and trapping of Erbium requires widely different wavelengths, used for different applications. First, the wide transition at $401\,\mathrm{mm}$ is used for applications where a high

scattering rate is important, such as Zeeman Slowing (ZS), Transversal Cooling (TC) and imaging (IMG). Although commercial lasers at this wavelength are available, we derive this laser light from a $802\,\mathrm{mm}$ system, and frequency-double it. These systems are described in Sections 3.3.2 and 3.3.3 respectively. Second, the transition at $583\,\mathrm{mm}$ is used to magneto-optically trap the slowed Erbium atoms. Its narrow linewidth makes it a suitable tool for efficient laser cooling down to the microkelvin range, and the system generating this laser light is presented in Section 3.3.4. Third, a setup dedicated to the production of $841\,\mathrm{mm}$ is described in Section 3.3.5. This laser light is a versatile tool, used to either address the very narrow Erbium transition, or to optically trap Lithium atoms (see Section 2.4 and Chapter 5). The last laser systems presented here are the various $1064\,\mathrm{mm}$ setups, described in Section 3.3.6. This laser light is used exclusively as far off-resonant light, for optical dipole traps and evaporation cooling. Finally, most of these lasers are locked to our reference cavity which is shortly described first, in Section 3.3.1.

3.3.1 Reference cavity

Most of our laser systems, either Erbium or Lithium, are using a commercial Ultra Low Expansion (ULE) cavity[16] as a stable frequency reference. Its stability is inherent to the ULE glass it is made from, and to its fabrication process. The base part is a large cylinder ($\varnothing = 10\,\mathrm{cm}$) of ULE glass, wherein four bores are drilled to make the different reference cavities used to lock our lasers. Each bore has a pair of mirrors bound to it via optical contact; one is plane and the other is spherical, with a radius of curvature $R = 10\,\mathrm{cm}$. They are separated by $10\,\mathrm{cm}$; the corresponding Free spectral Range (FSR) is thus $1.5\,\mathrm{GHz}$ and their finesse is specified by the manufacturer to be between 5000 and 20000 depending on the wavelength.

The cavity is isolated from the environment by placing it in a vacuum chamber, as shown in Fig. 3.13. The isolation goes further with the help of two copper shields, a very efficient design inspired from references [209, 217]. There, the cavity is only lying on two rests made of Peek plastic, with Viton rubber for a soft contact and isolation from vibrations. Both materials were chosen for their reasonable mechanical and vacuum (outgassing) properties. The thermal contact between the copper shields is assured by a single copper rod, and the contact between the outer copper shield and the aluminum external housing is made by a single Peltier element. Without these contact points, the temperature would not be fully under control, and especially the inner copper shield would simply follow the average temperature there, potentially leading to fluctuations. Instead, the temperature is enforced[17] via the Peltier element, the outer copper shield thermalizes to the imposed temperature, and the inner shield follows via the contact point. In the end, the ULE glass is maintained at the desired temperature exclusively via radiation from the inner copper shield. This way, any undesired effects, such as temperature gradients or air movement leading to changes in refractive index, are strongly suppressed. The last isolation step was to place the whole vacuum chamber (and the surrounding optics) on a vibration isolation stage.

[16] Stable Laser Systems, SLS-6010-1-4bore
[17] Controller: Meerstetter TEC-1092

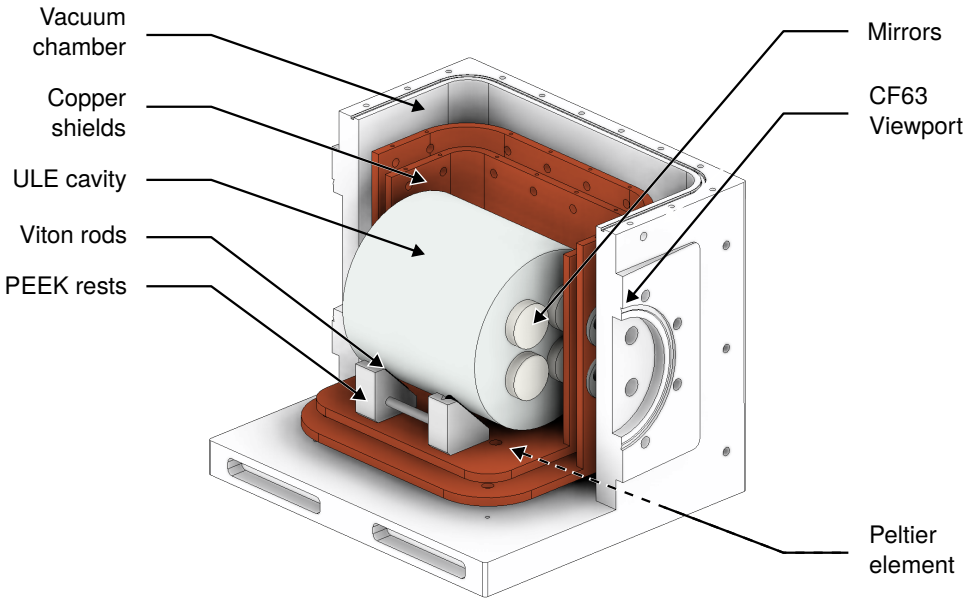

Figure 3.13 | ULE cavity design. The ULE cavity has four bores to lock multiple lasers at once. It is enclosed in a vacuum chamber, and further isolated with two copper shields. The temperature control is done with a Peltier element, which is the only contact point between the copper shield and the vacuum chamber. The whole vacuum chamber is resting on a vibration isolation stage.

Because the vacuum requirements are not very demanding, a pressure of $6 \cdot 10^{-8}\,\mathrm{mbar}$ was reached with a small ion pump[18]. The zero-expansion point, i.e. the temperature at which the thermal expansion of the ULE glass is minimal, was measured at $35.0\,^{\circ}\mathrm{C}$ [109]. The finesse was measured for different wavelengths, typically when locking the lasers in question to the cavity. The different measurements show a finesse $\mathcal{F}_{770} \approx 10000$ for $770\,\mathrm{nm}$ [218], $\mathcal{F}_{841} \approx 15000$ for $841\,\mathrm{nm}$ [190], and $\mathcal{F}_{1166} \approx 13000$ for $1166\,\mathrm{nm}$ [219].

3.3.2 802nm

The root of our red (and hence blue) setup is a single-mode laser diode used in a home-built external cavity diode laser (ECDL). The diode is locked to our ULE by a Pound-Drever-Hall (PDH) scheme [220, 221], and its emitted light is amplified by several tapered amplifiers (TA) before a frequency-doubling step. A summary of the frequency scheme for the $802\,\mathrm{nm}/401\,\mathrm{nm}$ setup is shown in Fig. 3.14, and a simplified schematic of the setup is shown in Fig. 3.15. Before going in the details, it is interesting to note that the following laser setup was designed to have most of the frequency shifts done on the laser light at $802\,\mathrm{nm}$ instead of $401\,\mathrm{nm}$, for two reasons. First, the optical elements are all performing better at this wavelength: both the coatings and the materials are easier to manufacture, and undesired effects are less visible. Second, all frequency shifts done on the red light are doubled when converting to blue light, effectively reducing the required number of

[18] Gamma Vacuum, Titan 3S

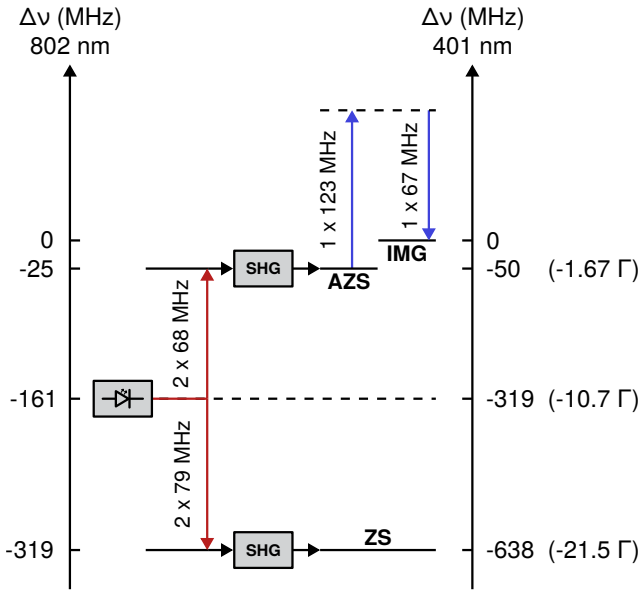

Figure 3.14 | Frequency scheme. The master laser is locked to the ULE at $-319\,\mathrm{MHz}$ from the atomic resonance after conversion to blue light. The $802\,\mathrm{nm}$ ($401\,\mathrm{nm}$) laser frequencies are shifted via double (single) pass AOMs to reach the targeted values. The ZS beam is shifted to larger detuning, while the AZS and IMG beams are shifted closer to resonance. The frequency at $-50\,\mathrm{MHz}$ was added over the course of the thesis to include the AZS, and was possible to add by modifying the laser's locking point and the AOMs' frequencies only.

frequency-shifting components. Finally, the four TAs in this setup were put in their own local interlock. Their temperature and seed power are continuously monitored; if one of them goes beyond a set threshold, it immediately turns off all the TAs, without triggering anything else.

The laser diode[19] is used at a current of $135\,\mathrm{mA}$ and temperature[20] of $18.4\,^{\circ}\mathrm{C}$ for an output of $36\,\mathrm{mW}$, and is protected from back-reflected light by an optical isolator[21]. The light goes through a first TA[22] (TA1) to generate enough power to seed the next amplifiers. It is used at a current of $1.2\,\mathrm{A}$ for an input/output of $28/375\,\mathrm{mW}$, and is also protected by an optical isolator[21]. The laser beam is then coupled to an optical fiber[23], used here mainly for maintenance purposes: it splits the setup in two compartments, making any part replacement and laser realignment easier. After the optical fiber, the path is split in two for the different frequencies used in the experiment. One path goes to the Zeeman slower (ZS) and needs to be further red-detuned, while the other path is used for angled Zeeman slowing (AZS) and imaging (IMG), thus closer to resonance.

[19] Eagleyard EYP-RWE-0810-03010-1300-SOT02-0000
[20] Meerstetter TEC-1091
[21] LD, TA2: Qioptiq Linos FI-810-5TVC, TA1, TA3: Thorlabs IO-3-780-HP, TA4: Thorlabs IOT-5-780-VLP
[22] TA1, TA2, TA4: Eagleyard EYP-TPA-0795-02000-4006-CMT04-0000, TA3: Coherent TA-795-3000
[23] OZ Optics, PMJ-3A3A-633-4/125

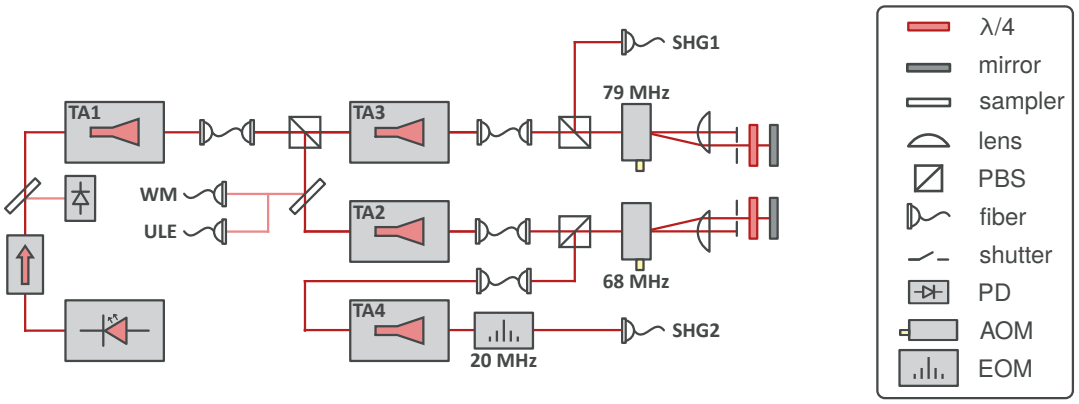

Figure 3.15 | 802nm setup. The laser source is a home-built ECDL, which is split along two paths. Several stages of amplification with TAs were necessary to reach high enough power and generate blue light with doubling cavities. The AOMs are used for frequency control of the generated blue light.

ZS path On this path, the light goes through a TA[22] (TA3) to be amplified from $45\,\mathrm{mW}$ to $1\,\mathrm{W}$ by running the chip at $1.8\,\mathrm{A}$. The amplified light is coupled to a high-power fiber[24], before going through an optical isolator[21] and a double-pass Acousto-Optic Modulator (DPAOM)[25]. The AOM imparts its frequency shift of $-79\,\mathrm{MHz}$ two times by going double-pass, for a total of $-158\,\mathrm{MHz}$, doubled to $-316\,\mathrm{MHz}$ when converted to blue light. With the additional red-detuning of the laser diode, locked away from the atomic resonance, the final blue beam reaches a total detuning of $-638\,\mathrm{MHz}$, as required for the ZS (see Sections 3.2.1 and 4.1.1). The laser beam then goes through a second high-power fiber, before reaching its frequency-doubling cavity (SHG1). There, the delivered power is $370\,\mathrm{mW}$ in front of the fiber, and $220\,\mathrm{mW}$ in front of the cavity.

AZS and IMG path On this path, the light follows the same first steps: it goes through a TA[22] (TA2) to be amplified from $45\,\mathrm{mW}$ to $400\,\mathrm{mW}$ by running the chip at $1.95\,\mathrm{A}$, goes through an isolator[21], is coupled to a high-power optical fiber, and goes through a DPAOM. The AOM is used in the other frequency shift direction at $+68\,\mathrm{MHz}$, for a total of $136\,\mathrm{MHz}$ doubled to $272\,\mathrm{MHz}$ when converted to blue light. Again, when accounting for the laser diode locking point, the resulting detuning of the converted blue beam is $-50\,\mathrm{MHz}$, as required for the AZS (see Section 4.1.1). However, due to higher power needs, one last TA[22] (TA4) was placed before the high-power fiber going to the second frequency-doubling cavity (SHG2). With this additional TA, the light is amplified from $45\,\mathrm{mW}$ to $1.9\,\mathrm{W}$ by running the chip at $2.6\,\mathrm{A}$. It yields a laser power of $1.2\,\mathrm{W}$ in front of the fiber, and $520\,\mathrm{mW}$ in front of the cavity.

[24] Schäfter & Kirchhoff, PMC-E-780-5.3-NA012
[25] Gooch & Housego, GH 3080-125, VCO controlled: ZOS-100+

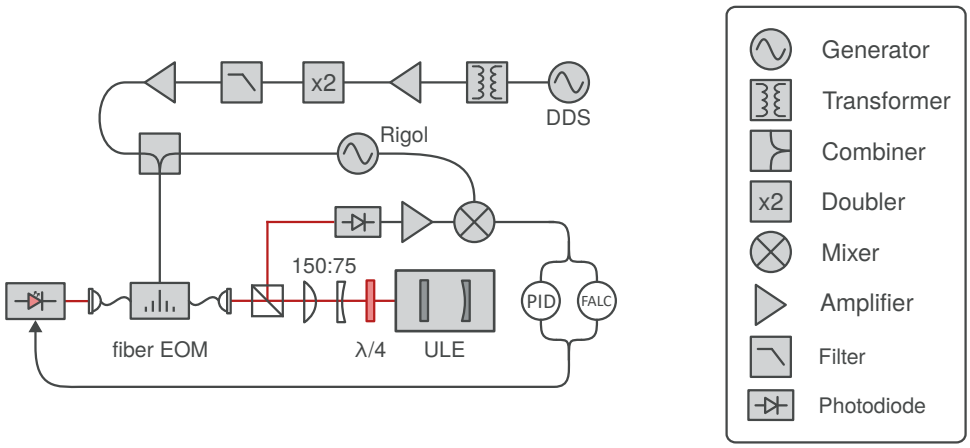

Figure 3.16 | 802nm lock. The laser light is modulated with a fiber EOM to impart two sets of sidebands. The DDS generates the tuning sidebands used to tune the laser, and the signal generator adds the locking sidebands used for the PDH lock (see text). The feedback is done via an in-house PID box and a fast analog regulator (FALC).

Laser lock The laser diode is locked to our ULE cavity with a PDH scheme, where the complete electronics setup[26] is shown on Fig. 3.16. The light is taken after the first fiber, before going through TA2. A sampler was placed to extract a small amount of light, which is sent to our wavemeter[27] and to our ULE cavity through a fiber EOM[28]. The fiber EOM is a phase modulator used to impart two series of sidebands on the laser light: the tuning sidebands from the DDS, and the locking sidebands from a signal generator. This way, it becomes possible to tune the laser by locking it to the ULE *not* on its carrier wave, but on one of the tuning sidebands. Then, the tuning sideband is maintained resonant with the cavity and keeps its fixed frequency, while changing the DDS modulation frequency will change the frequency of the carrier wave instead. The locking sidebands are the ones used for the PDH technique, to derive the error signal and be able to lock onto one of the tuning sideband. Finally, the feedback to the laser is divided in two loops: a slow and a fast loop. The slow loop uses our in-house PID lockbox and acts on the laser piezo. The fast loop uses a commercial regulator[29] and acts on the laser current.

In our setup, approximately $350\,\mu\mathrm{W}$ of $802\,\mathrm{nm}$ light reach the ULE cavity, and a coupling of $50\,\%$ to the cavity was achieved. The DDS signal can be tuned from 0 to $400\,\mathrm{MHz}$ and is frequency-doubled, thus producing tuning sidebands over a range of $1.6\,\mathrm{GHz}$, slightly more than the cavity's free spectral range (FSR) of $1.5\,\mathrm{GHz}$. The signal generator is used to produce the locking sidebands at $10\,\mathrm{MHz}$ for the PDH error signal.

[26] **DDS branch**: Trafo: FTB-1-1*-A15+, Amplifier: ZFL-500HLN, Doubler: MK-2, Filter: SLP-850+, Amplifier: ZFL-1000H+, Combiner: ZFSC-2-5-S+, Generator: Rigol DG1022SZ.
Photodiode branch: Amplifier: ZFL-500LN+, Mixer: ZFM-3-S+
[27] High Finesse, WS6-200
[28] Jenoptik, PM830
[29] Toptica FALC 110

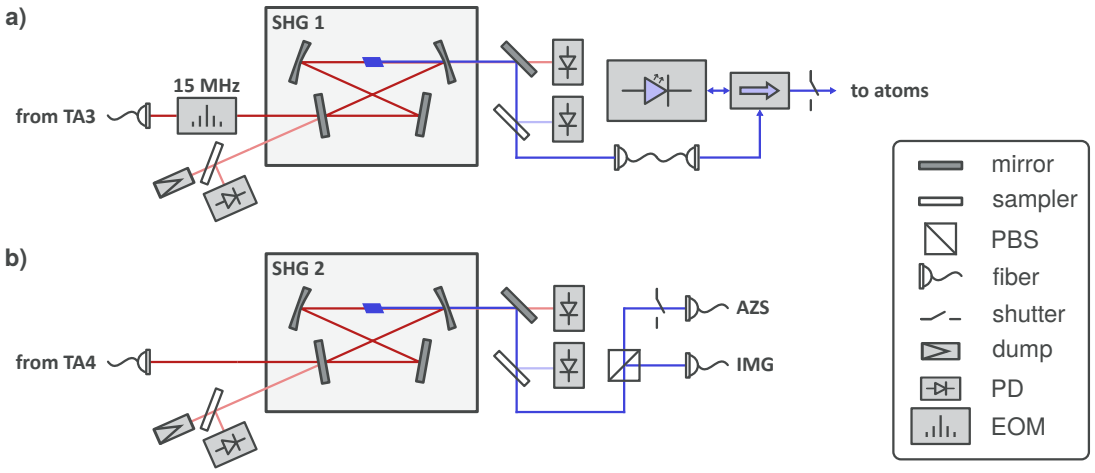

Figure 3.17 | 401nm setup. The blue light ($401\,\mathrm{nm}$) is generated by frequency-doubling of the red light ($802\,\mathrm{nm}$) in SHG cavities. The system has the two paths for different target frequencies: the ZS path (a) and the AZS/IMG path (b). The SHG1 (ZS path) generates $15\,\mathrm{mW}$ of blue light to seed a slave diode on the main table via injection lock. The slave diode amplifies the seed light to $150\,\mathrm{mW}$ for Zeeman slowing. The SHG2 (AZS/IMG path) generates $100\,\mathrm{mW}$ of blue light and is enough to be used directly for angled slowing and imaging.

3.3.3 401nm

The $401\,\mathrm{nm}$ light is derived from the $802\,\mathrm{nm}$ setup presented above, and addresses the Erbium wide transition between the ${}^3H_6$ ground state and the ${}^1P_1$ $401\,\mathrm{nm}$-excited state (see Section 2.4). It is used for three different applications where a high scattering rate is needed: Zeeman slowing (ZS), angled Zeeman slowing (AZS), and imaging (IMG). A simplified scheme of the system is shown in Fig. 3.17, and the important subsystems are described below.

Doubling cavities The $401\,\mathrm{nm}$ laser setup revolves around our two doubling cavities. They were built in-house, although their design was developed at the Max Planck Institute in Garching [222–224]. Many technical details from our setup can be found in previous theses from our group [190, 225], and only the main characteristics are presented here. In brief, the doubling cavities rely on second-harmonic generation (SHG) of light [226] by a non-linear Beta-Barium Borate (BBO) crystal[30]. Because non-linear optical processes generally require large intensities, the crystal has to be placed in an enhancement cavity.

The cavities' design is shown in Fig. 3.18, where one can see the different components. They are bow-tie cavities, placed in an outer chamber which can be evacuated through its vacuum port if a gain in stability is needed. The outer chamber also has four electrical feedthroughs, to be able to use electronic components even with vacuum inside. The different cavity's components are screwed to a $4\,\mathrm{cm}$ thick aluminum inner cavity board that lies on three magnetic seats[31], themselves fixed to the chamber. These magnetic seats are

[30] GWU Lasertechnik / Castech, BBO with Brewster cut
[31] Thorlabs KBS98

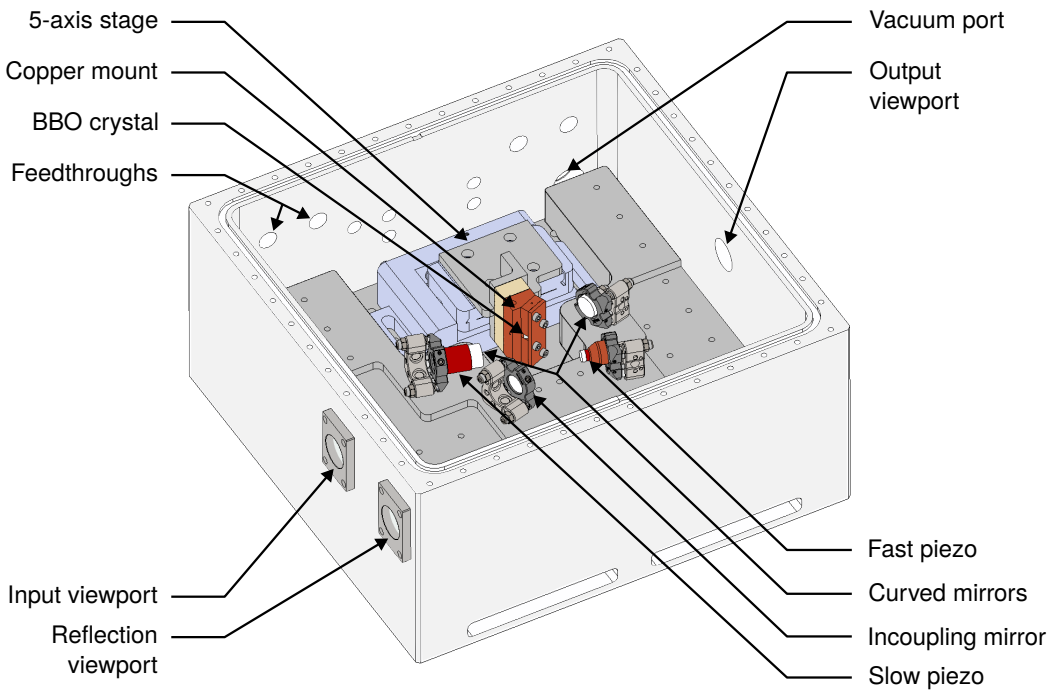

Figure 3.18 | Doubling cavity design. The SHG cavities generate blue light with a BBO crystal placed in a bow-tie enhancement cavity. The outer chamber (light grey) can be evacuated for better stability. The optics components are all screwed to a separate board (dark grey) which lies on magnetic seats. The crystal is placed in a copper mount (orange) and aligned with a 5-axis stage (light blue). The cavity length is adjusted with two piezos (red) and the light is focused through the crystal by two curved mirrors.

there to prevent mechanical stress and optical misalignment in case of an eventual cavity evacuation.

The crystal itself is mounted in a copper enclosure and encapsulated in indium foil, for better thermal contact and lower mechanical stress when put in the enclosure. It needs to be kept at high temperature (here maintained at $80\,^{\circ}\mathrm{C}$), especially if the cavity is not evacuated or flooded with a specific gas (usually inert gases such as Argon), to avoid a deterioration of its surfaces from the surrounding moisture. The temperature is stabilized by a combination of an electric heater, an NTC thermistor and a PID regulator[32]. The entire copper mount is isolated from its 5-axes stage[33] by a spacer made of Vespel, a plastic interesting for its thermal stability and low out-gassing properties. The 5-axes stage is necessary for the precise alignment of the crystal to the laser cavity, and offers three translation axes and two rotation axes, which are accessible from the outside of the chamber as long as it is not evacuated.

[32] Heater: Thorlabs HT15W, Thermistor: EPCOS B57861S, PID: in-house
[33] Newport 9081-M

The mirrors are placed in bow-tie configuration using stainless steel mounts[34], with the crystal sitting at the center of the cavity's long arm. Among the four mirrors, three are $12.7\,\mathrm{mm}$ in diameter and $6\,\mathrm{mm}$ thickness, and one is smaller at $6.35\,\mathrm{mm}$ in diameter. Two of them, on each side of the long arm, are curved to focus the laser beam through the crystal down to a waist of approximately $50\,\mu\mathrm{m}$, in order to increase the SHG conversion efficiency. The incoupling mirror is the larger flat mirror, coated for a nominal reflectivity of $98.8\,\%$ at $802\,\mathrm{nm}$. All other mirrors have a high-reflectivity coating, with a given reflectivity of at least $99.95\,\%$ at $802\,\mathrm{nm}$. Finally, the outcoupling mirror has an additional high-transmission coating of $99\,\%$ at $401\,\mathrm{nm}$ on both sides.

For the ZS path, the SHG1 cavity has an input of $220\,\mathrm{mW}$ of $802\,\mathrm{nm}$ light and generates up to $12\,\mathrm{mW}$ of $401\,\mathrm{nm}$ light. This was obtained for a cavity coupling of $50\,\%$, yielding a conversion efficiency of approximately $10\,\%$ [225]. On the AZS path, the SHG2 cavity has an input of $520\,\mathrm{mW}$ of $802\,\mathrm{nm}$ light and generates up to $100\,\mathrm{mW}$ of $401\,\mathrm{nm}$ light. There, the coupling to the cavity is much higher, at $80\,\%$, yielding a conversion efficiency of approximately $25\,\%$ [190]. Finally, the SHG2 cavity has been measured to have a finesse of 300. Combined with a calculated FSR of $928\,\mathrm{MHz}$, it yields a resonance linewidth of $3.1\,\mathrm{MHz}$; already narrower than the atomic transition's linewidth of $30\,\mathrm{MHz}$. As such, the exact linewidth of the laser itself was not measured.

Cavity lock A reliable SHG output can only be obtained if the cavity is locked to the incoming laser light, to maintain a resonance between them and thus reach high enough intensities. In this design, it is done by adjusting the cavity length with two piezoelectric actuators. A large piezo[35] is used for the slow feedback, to follow large drifts of several microns, usually over long time scales. A smaller piezo[35] is used for the fast feedback, providing quick adjustments to the cavity length. For this piezo, it is important to minimize its mechanical load to increase the feedback bandwidth. For that reason, both the piezo and the driven mirror are smaller than the others, with $6.35\,\mathrm{mm}$ in diameter and $2\,\mathrm{mm}$ thickness. The mirror is glued on the piezo, and the piezo is glued to a conical copper mount filled with lead to dampen its vibrational resonances [227].

The feedback itself is derived from a digital, FPGA-based device[36] (Red Pitaya) instead of the usual analog circuits. The Red Pitaya has two analog inputs and outputs, each used here in their respective feedback loops with the large and small piezos. This setup offers a few advantages compared to our standard PID lockboxes. First, it has the ability to automatically relock the cavity. The intra-cavity power can be monitored by measuring the output power of $802\,\mathrm{nm}$ light. When this power falls below a user-given threshold, the Red Pitaya disables the lock and starts scanning the piezos with increasing amplitude, from the parameters were the lock was lost. Whenever the emitted light's power goes above the threshold, the regulating loops starts again and the cavity is relocked. Another advantage is convenience. The Red Pitaya offers independent control on the two regulating loops, whether they work separately or together. The PID parameters are also easily modified, saved or reloaded to the user's convenience, and the target point can also be tuned to account for residual offsets

[34] Thorlabs Polaris-K05S2

[35] Large piezo: Thorlabs PK44M3B8P2, Small piezo: Thorlabs PA44RKW

[36] Red Pitaya STEMLab 125-14, firmware and interface from Fabian Schmid: https://github.com/schmidf/rp-lockbox

in the PDH signal. However, such a system is limited to a lower bandwidth than that of the analog regulators, and can only be used for this situation in our experiment.

Injection lock The ZS beam requires a large amount of power to ensure a high enough saturation parameter for the atoms to be slowed down. This is done by using a slave diode laser[37] on our main experiment table, which acts as an amplification stage before shining the light on the atoms. The principle of injection lock is that the slave diode laser will emit light on the same mode as the seed light, provided that the latter has enough power and coupling to the internal cavity of the slave laser to enforce stimulated emission on that mode [228]. The slave diode is protected from unwanted back-reflections by an optical isolator[38], which is also used to send the seed light towards the slave via its side port (see Fig. 3.17). The crucial point here was to exploit the small amount of slave light filtered out by the optical isolator. This weak beam is reflected out through the same side port that is used for the seed, and coupling this beam to the high power fiber ensures that the seed is coupled to the slave laser. By symmetry, the coupling efficiency of the weak slave beam to the high-power fiber is exactly the same as the coupling efficiency of the seed beam to the slave's internal cavity. However, having a reliable injection lock is not trivial and requires an Arduino to relock the laser before every experimental cycle. The universal technique developed for our injection locks, currently used in both Er and Li laser systems, is explained in details in the associated publication [229] and in the companion thesis [109] of this work.

In our setup, $4.5\,\mathrm{mW}$ of seed light reach the main table, and $2.2\,\mathrm{mW}$ reach the slave diode. The slave diode back-coupling to the fiber is approximately $20\,\%$, indicating that around $440\mu W\,\mathrm{mW}$ of seed light is coupled to the slave diode. This amount of seed power is enough to lock the slave on the desired mode and obtain $160\,\mathrm{mW}$ for the ZS beam at the vacuum viewport.

Imaging distribution Absorption imaging can be done in the Erbium chamber and in the glass cell. Both locations have two imaging directions, and the light is delivered by four different optical fibers[39]. The imaging beam comes from the SHG2 cavity (see Fig. 3.17), and is distributed into the four fibers in a separate optical setup (see Fig. 3.19). There, we use two AOMs[40] in single pass to bridge the remaining $-50\,\mathrm{MHz}$ of detuning from the $401\,\mathrm{nm}$ transition. Although their center frequencies are $110\,\mathrm{MHz}$ and $80\,\mathrm{MHz}$ respectively, they are used at $+123\,\mathrm{MHz}$ and $-67\,\mathrm{MHz}$. The $6\,\mathrm{MHz}$ difference (between the $-50\,\mathrm{MHz}$ gap and the $60\,\mathrm{MHz}$ AOM shift) can be explained by several reasons. First, the limited bandwidth of the AOMs did not allow for further detuning without significant power loss. Second, the absorption imaging is usually done at a non-zero magnetic field (usually $6\,\mathrm{G}$ in the chamber and $5\,\mathrm{G}$ in the cell), which shifts the resonance by approximately $1\,\mathrm{MHz/G}$. Finally, any frequency shift on the imaging beam has to be done with the double-pass AOM in the $802\,\mathrm{nm}$ setup, otherwise the single-pass AOMs in this distribution setup would misalign the beam from the optical fiber and no imaging would be possible. This AOM's frequency

[37] Nichia NDV4B16
[38] Thorlabs IO-3D-405-PBS
[39] OZ Optics, QPMJ-3A3A-400-3/125
[40] Gooch & Housego I-M110-3C10BB-3-GH27 and 3080-125

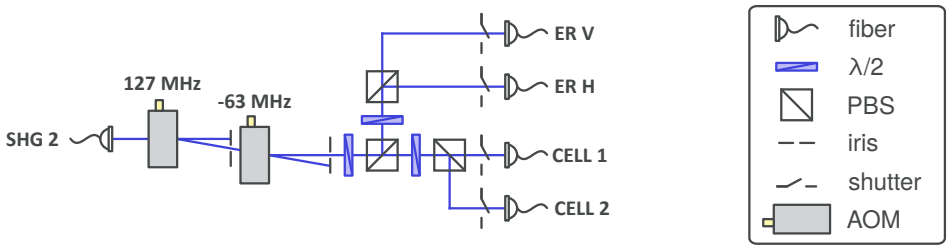

Figure 3.19 | Imaging distribution setup. The light from SHG2 cavity is distributed through four fibers, which deliver the light to the main experiment. The AOMs are used in single pass to bring the light in resonance with the $401\,\mathrm{nm}$ transition, and act as fast shutters. Every fiber has an additional mechanical shutter. The frequency can be tuned via the DPAOM in the $802\,\mathrm{nm}$ setup.

is ramped between its best loading value for AZS and its best imaging value during our experiment cycles.

On the main experiment table, we can use the imaging in four different configurations. In the Erbium chamber, the images can be taken in the horizontal direction through the CF63 viewports, or in the vertical direction through the re-entrant viewports. In both cases, a magnification of 0.5 was chosen for a large field of view and the possibility to image long time-of-flights. For the glass cell, the absorption imaging can either be done from the side of the cell, close to the tapered end of the glass tube, or orthogonally to its side walls, through a cut lens.

3.3.4 583nm

The $583\,\mathrm{nm}$ light, used to operate the MOT on the Erbium narrow transition between the ${}^3H_6$ ground state and the ${}^3P_1$ excited state (see Section 2.4), is generated by a commercial laser[41] based on VCSEL technology and SHG cavity to produce yellow light. The optical setup, shown in Fig. 3.20, is straightforward and does not need many components. The yellow beam is simply sent through a DPAOM[42], before being split in four different fibers[43]. Three of these fibers are used for the MOT, and the last one is used as a spare. This additional fiber proved very useful for temporary tasks, such as spectroscopy measurements or aligning the objective. A late addition to the setup, not shown on the figure, was to include intensity control on the vertical MOT beam, to reduce the jittering of the MOT due to power fluctuations when compressed. This control loop was implemented by measuring the laser power leaking through a mirror on the experiment table, and the feedback is done on the AOM.

[41] Vexlum Valo SHG SF
[42] Gooch & Housego 3100-125
[43] OZ Optics, QPMJ-3A3A-488-3.5/125

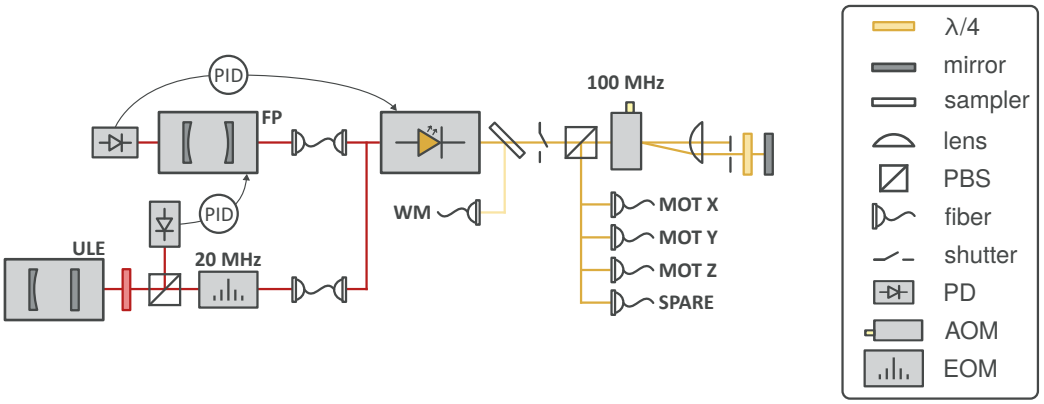

Figure 3.20 | 583nm setup. The yellow light source is a commercial VCSEL laser, pumped by a $1166\,\mathrm{nm}$ and frequency-doubled to $583\,\mathrm{nm}$ in its internal SHG cavity. The light in distributed in three fibers for the MOT beams, and is tuned via a DPAOM. This AOM is additionally modulated to broaden the beam's spectrum for the MOT loading phase. The lock is done via the $1166\,\mathrm{nm}$ fundamental light and requires a transfer cavity (see text).

Laser lock Although the optical setup is rather simple, locking the laser proved to be much more difficult, and is documented in detail in a previous thesis from our group [219]. The locking scheme is represented in detail in Fig. 3.21, and uses the $1166\,\mathrm{nm}$ fundamental light. Here, it was necessary to use a Fabry-Perot (FP) cavity in addition to our ULE cavity, to "pre-stabilize" the laser. Without this cavity, we could see acoustics- and vibrations-induced frequency jumps over a range of $1\,\mathrm{MHz}$ for measurement times of $500\,\mathrm{ms}$, which resulted in average locking times to the ULE of $250\,\mu\mathrm{s}$. These frequency jumps could not be compensated by feedback to the laser piezo, which was limited to $\sim 10\,\mathrm{kHz}$, and the laser was jumping out of the ULE locking range. The purpose of the FP cavity was to provide a much larger locking range thanks to a low finesse and a side-of-fringe (SOF) lock. Once the laser locked to this cavity, it becomes possible to use the ULE cavity as a stable frequency reference, and lock the FP cavity to it. This way, the feedback loop goes from the ULE cavity to the FP cavity, and then to the laser.

In our setup, the FP cavity is built with two curved mirrors of $10\,\mathrm{cm}$ radius, distanced by $10\,\mathrm{cm}$, to be in confocal configuration. One of the mirrors is mounted on a piezo[44] with a large stroke of $15\,\mu\mathrm{m}$ to adjust the cavity length. With these parameters, the cavity has an FSR of $1.5\,\mathrm{GHz}$, and its finesse was measured at 18. Since the laser is locked to this cavity by SOF technique, it is possible to use the transmission signal directly as an error signal simply by applying an offset to it. It means that the low finesse directly translates into the locking range, which is here on the order of $50\,\mathrm{MHz}$. Two more details are important for this lock. First, the laser power used for the SOF lock has to stay low, otherwise the FP cavity drifts beyond its piezo's regulating capabilities because of thermal effects due to intra-cavity optical power. For that reason, only $5\,\mu\mathrm{W}$ of $1166\,\mathrm{nm}$ light reach the FP cavity. Second, the FP cavity was installed in a wooden box with acoustic isolation, and suspended mid-air above the optical table with a spring. Doing so improved the lock stability further by protecting it from most acoustic or mechanical noise.

[44] Thorlabs, PK44M3B8P2

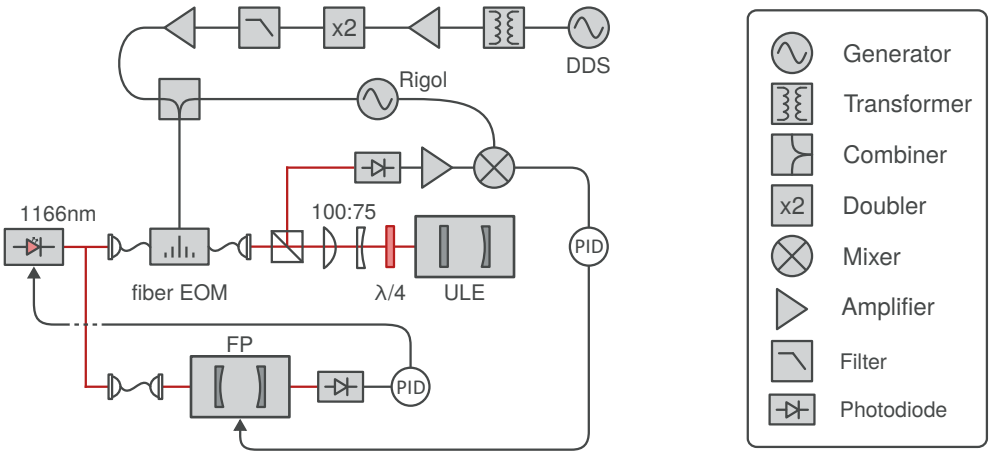

Figure 3.21 | 1166/583nm lock. The yellow laser is locked via its $1166\,\mathrm{nm}$ fundamental light. The feedback loop has an additional FP cavity to pre-stabilize the laser. The laser is locked to the FP cavity with SOF, and the FP cavity is locked to the ULE cavity with PDH.

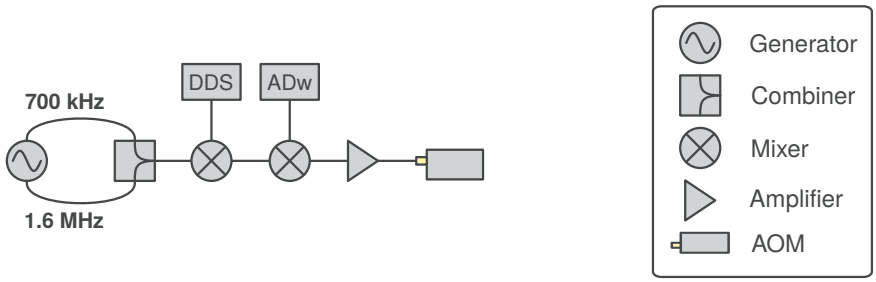

Figure 3.22 | 583nm broadening. The yellow light is broadened by modulating the DPAOM for the MOT loading phase, so that the additional sidebands increase the MOT capture velocity and make it closer to a wide-MOT behaviour. The DDS provides the carrier wave used for the AOM, and the signal generator is used for the sidebands. The broadening is turned off with the ADwin and the second mixer during the compression ramp for a smooth transition to single-frequency narrow-line MOT.

The ULE cavity setup is similar to the $802\,\mathrm{nm}$ one. The laser light is sent through a fiber EOM[45] and $100\,\mu\mathrm{W}$ reach the ULE cavity for PDH lock. A coupling of $18\,\%$ was achieved, and the cavity finesse was measured to be 13000. The difference here is that the PDH error signal is sent to the FP cavity and not the laser. This way, an error signal coming from the ULE is compensated for by the FP cavity piezo, and the laser follows.

Laser linewidth An important consideration for this laser is its linewidth. Because it is used for a narrow-line MOT, it is important that the laser linewidth is smaller than the atomic transition linewidth of $200\,\mathrm{kHz}$ to reach the Doppler temperature. This measurement can only be done with either a laser linewidth analyzer, or with a self-heterodyne measurement [230]. However, a pessimistic (upper-bound) estimate can be done via the ULE

[45] Jenoptik, PM1170

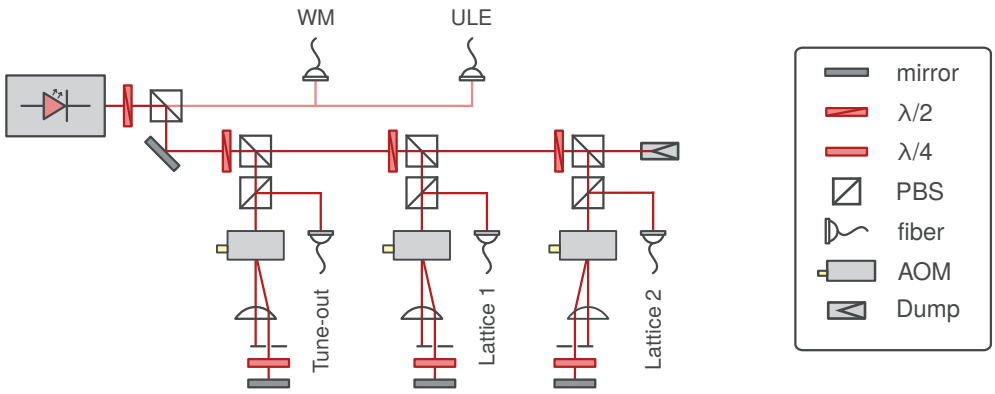

Figure 3.23 | 841nm setup. The light source is a commercial TiSa laser, locked to our ULE via PDH and distributed in three high-power fibers.

transmission signal [219]. The upper bound was determined to be a linewidth of $50\,\mathrm{kHz}$, which is already good enough for MOT operation, thus the exact measurement was not done.

Although the laser linewidth has to be smaller than $200\,\mathrm{kHz}$, loading the MOT this way would be very inefficient due to its narrow-line nature (see Section 4.1.2). Our approach for spectral broadening was to modulate the DPAOM with a signal generator[46] as shown on Fig. 3.22, which can be programmed via a Python interface. Here, one could expect to find an optimum for sidebands at multiples of the atomic transition linewidth, but our measurements indicated an optimized MOT loading for sidebands of $700\,\mathrm{kHz}$ and $1.6\,\mathrm{MHz}$. This was attributed to power broadening due the large saturation parameter in the MOT beams, as well as harmonics of the sidebands due to the signal's strength from the generator. During an experiment cycle, the MOT broadening is ramped down at the start of the MOT compression, so that a smooth transition to single-frequency narrow-line MOT can be achieved (see Section 4.1.2).

3.3.5 841nm

The $841\,\mathrm{nm}$ light can be used for two applications: for a narrow-line MOT of Erbium, or as a Lithium trap on the tune-out wavelength of Erbium (see Section 2.4 and Chapter 5). The narrow-line MOT can be done by addressing the $8\,\mathrm{kHz}$-wide Erbium transition, which has a very low Doppler temperature of $190\,\mathrm{nK}$. Such a MOT has been demonstrated recently [189], and shows very good properties for fast and efficient laser cooling. However, after attempting to use it in our experiment [190], its usefulness was not considered good enough and this red MOT was removed from the apparatus. On the other hand, the tune-out trapping is a central feature of our experiment, and this laser system is designed to provide the trapping beams used in the science chamber.

[46] Rigol DG1022SZ

The laser source is a commercial laser, with a Titanium:Sapphire (TiSa) crystal placed in a ring cavity and pumped by a $532\,\mathrm{nm}$ green laser[47]. This laser can output up to $7\,\mathrm{W}$ at the desired wavelength, which is enough for optical trapping of a cold Lithium cloud. The optical setup, presented in Fig. 3.23, is straightforward and simply consists in splitting the produced beam in two main paths, to go into five different fibers. The first path, at low power, is used for locking and monitoring. A small amount of light is picked out of the main line and is coupled to two optical fibers, to go to our wavemeter or to the ULE cavity. The second path, or main line, is where the high power beam is coupled to three high power fibers[48]. For each of the three directions, the laser beam is tuned and intensity-controlled by their respective DPAOM[49]. One direction is used for the tune-out trap, and the remaining two are prepared for a future lattice in the science chamber.

Laser lock Like most our laser systems, this laser is locked to our ULE cavity by PDH technique. However, the electronics used for the feedback are also commercial and were delivered with the laser. There, a low power of $200\,\mu\mathrm{W}$ combined with a coupling of $80\,\%$ to the ULE cavity showed very good locking behaviour. It was also interesting to use a linewidth analyzer[50] to reduce the laser linewidth for MOT operation. By adjusting the locking parameters, it was possible to bring it down to $10\,\mathrm{kHz}$.

3.3.6 1064nm

Seed laser

Several of our high power lasers, emitting light at $1064\,\mathrm{nm}$ for off-resonant traps, are amplifiers (called here "ALS lasers") and require a seed to function. The seed laser has to be stable, both in power and frequency, and fiber-coupled to each ALS laser. A reliable solution is to use a commercial laser[51] ("Mephisto"), known for its stability and capable of delivering $2\,\mathrm{W}$ of laser power. The distribution setup is shown in Fig. 3.24. The seed laser is used in four different applications: as a seed for three different lasers, and as a source for a future setup with a Digital Micromirror Device (DMD).

The setup presented here is straightforward: the seed laser is protected by an optical isolator[52] and fiber-coupled to all lasers for the next amplification stage (ALS1, ALS2, ALS3). A key point here is the presence of two double-pass AOMs, used in series, towards the laser ALS1. This laser is used in our transport setup (see Sections 3.3.6 and 4.2), where atoms are being moved from their MOT chamber to the glass cell by a running lattice. This lattice is created by the overlap of the ALS1 and ALS2 lasers, and translated by shifting the frequency of ALS1. The frequency shift is done by the two double-pass AOMs[53], designed specifically for low thermal drifts.

[47] TiSa: Sirah Matisse CR, Pump: Sirah Millennia eV
[48] Schäfter & Kirchhoff, PMC-780-3-18E-1000
[49] Tune-out: Gooch & Housego 3100-125, Lattice1: G&H 3080-125, Lattice2: G&H 3080-122
[50] High Finesse LWA-1k
[51] Coherent, Mephisto 2000
[52] IPOptica, HPKT 1064nm
[53] Gooch & Housego, 3110-197

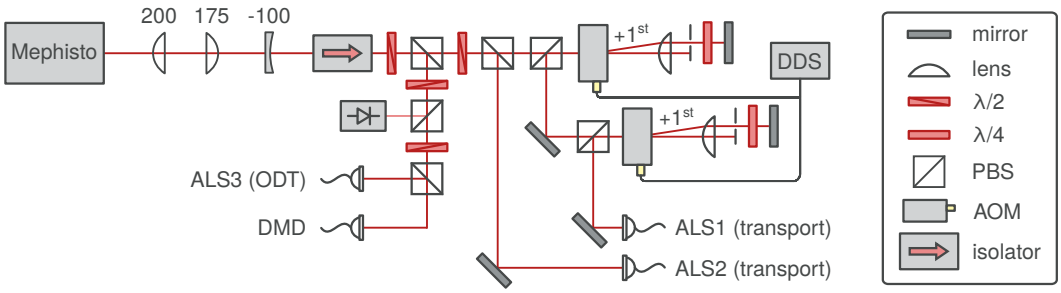

Figure 3.24 | 1064nm setup for the seed laser. The seed is distributed to the high-power lasers by optical fibers. The AOMs are used to shift a transport laser's frequency. The photodiode is used as a monitor for the laser output power.

It was critical for this setup to reduce the phase noise of the lattice as much as possible. Here, the problem was addressed in two places: the two lasers share the same seed to prevent relative frequency drifts, and the RF sources driving the AOMs need to have a linewidth narrow enough to prevent heating. The RF sources used for the AOMs went under several rounds of optimization, based on the lifetime on Li atoms trapped in the standing lattice. The source was changed from our in-house DDS with its $10\,\mathrm{MHz}$ internal clock, to the DDS with an external $1\,\mathrm{GHz}$ clock[54], to a VCO[55] phase-locked to the DDS, to finally a direct control from a commercial ("Wieserlabs") DDS[56]. In the final configuration, the RF signal was measured with a linewidth of $\sim 10\,\mathrm{kHz}$, and resulted in an increase of Li lifetime from $100\,\mathrm{ms}$ to $2\,\mathrm{s}$. More precisely, the AOMs are driven by a VCO[57] by default, and an RF-switch[58] is used to change to the Wieserlabs DDS for every experimental sequence. The goal is to protect the ALS lasers, by making sure that the frequency-control AOMs are always turned on, and that the seed is always fiber-coupled towards the lasers. For this specific reason, using our in-house DDS was never attempted because its output is momentarily turned off when it is being programmed. Here, the ALS lasers are all seeded by approximately $100\,\mathrm{mW}$, providing a comfortable overhead from the minimum $15\,\mathrm{mW}$ necessary for safe operation. This overhead also allows one to tune the AOMs without worrying about the reduction in seed power coming from the lower AOM diffraction efficiency.

Erbium and Cell dipole traps

The setup presented in Fig. 3.25 is an exception compared to the other setups shown in this chapter, because it does not correspond to the current setup in the experiment at the time of writing. Instead, this setup was used for the measurements of the tune-out wavelength of Erbium presented in Chapter 5, and was modified soon after. The current version of this laser system is detailed in the companion thesis [109] of this work.

[54] Crystek Microwave, CRBSC-01
[55] Minicircuits, ZOS-150+
[56] Wieserlabs, WL-FlexDDS-NG
[57] Minicircuits, ZOS-150+
[58] Minicircuits, ZASWA-2-50DRA+

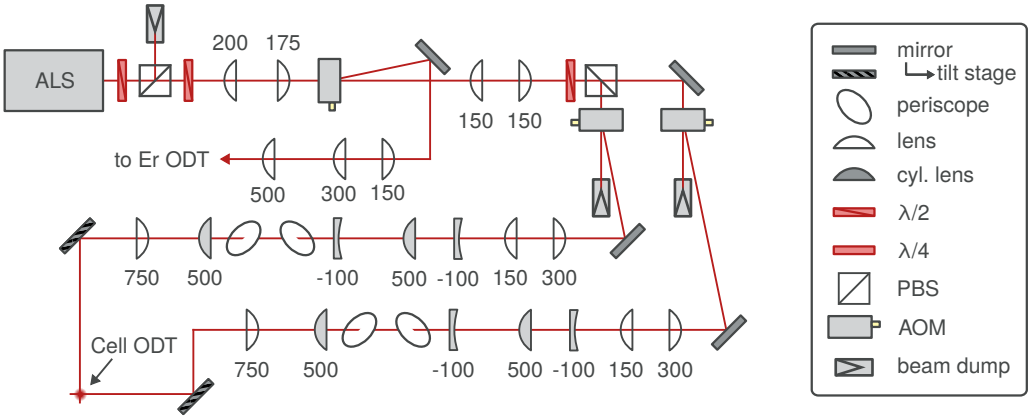

Figure 3.25 | 1064nm setup for the Erbium and cell ODTs. Both traps are derived from the same laser source and used at different times in the sequence. The Erbium ODT is made by round beams of waist $w = 85\,\mu\mathrm{m}$. The cell ODT is formed with two independent, elliptical beams of waist $w = 34 \times 588\,\mu\mathrm{m}$. The two beams are frequency-shifted in opposite directions by their respective AOM and use orthogonal polarizations.

Here, the laser source is a single-mode fiber laser[59] ("ALS laser") that amplifies the seeding light from the Mephisto. This laser was shared between two Optical Dipole Traps (ODTs), one in the Erbium chamber and the other in the glass cell. Because it was used for ODTs, the light is very far off-resonant from any transition for either Erbium or Lithium, and thus does not require frequency lock. However, the beam intensity needs precise control to prevent heating from intensity noise, and to be able to ramp down the power for evaporation. The intensity control was performed for each beam separately, via a shear-mode AOM[59] and a photodiode which is illuminated by the leakage of a mirror in the optical path to the atoms.

To distribute the light between different applications, it is possible to use several AOMs placed in series. In this approach, one can use the diffracted light from an AOM for one application, while the non-diffracted light goes on to the next AOMs. A limitation of this approach is the synchronicity: it is possible to use all the optical power only for one trap at a time. It is also possible to use the AOMs simultaneously, but in that case the total optical power has to be distributed among the different traps, and might result in an additional intensity noise due to the cross-talk between the intensity regulation loops.

In our setup, the Erbium ODT is derived from the first AOM, where the beam comes from the first diffraction order. There, the optical path is straightforward, as it only requires minor beam shaping to get a waist of $85\,\mu\mathrm{m}$. The setup for the Cell ODT is more complex, as it requires two beams with intensity control and a very elliptical shape (see Chapter 5). The two beams are derived from the first AOM's non-diffracted light, and go through identical optical setups, starting with an AOM and followed by three telescopes. The two AOMs were used in opposite diffraction orders ($\pm 1^{\mathrm{st}}$) and with orthogonal polarizations to prevent interferences in the trap. Then, a 1:2 spherical telescope contracts the beams and two 1:5 cylindrical telescopes enlarge the horizontal waists, to obtain two beams of waists $w = 34 \times 588\,\mu\mathrm{m}$.

[59] Seed: Coherent, Mephisto 2000, Amplifier: ALS-IR-1064-50-A-SF, AOM: Gooch & Housego, 3080-1990

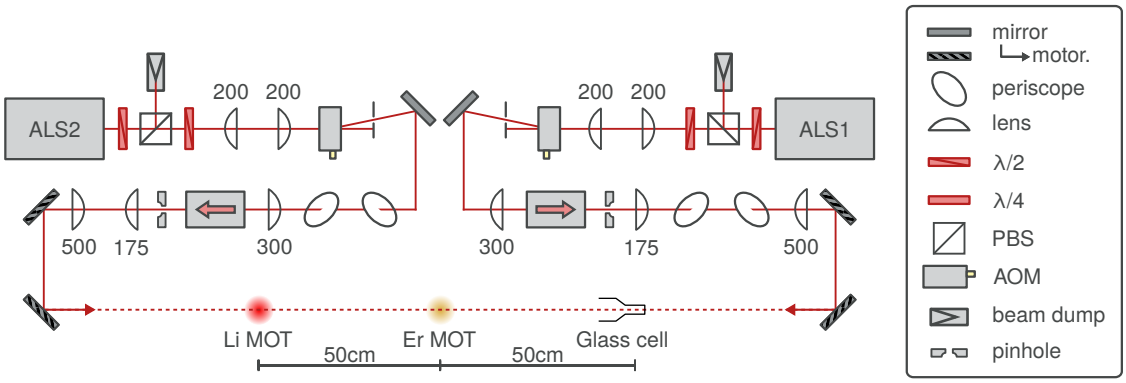

Figure 3.26 | 1064nm setup for transport. The two transport lasers'output beam are overlapped over the entire vacuum setup to make a 1D lattice. The lattice is moved by ramping the frequency of ALS1.

The alignment of the beams is done with the two high-precision motorized mirror mounts[60]. These mounts are controlled by piezo actuators in closed feedback loop for active stabilization and control, with an angular resolution of $20\,\mathrm{nrad}$. They were placed in the setup not only for convenience and precise alignment, but also to be able to move the trap during a sequence if needed. This movement opens several possibilities for our sequence, of which two are of particular interest. First, it can be used to prevent spatial separation of the Erbium and Lithium clouds when the gravitational sag becomes non-negligible. This can be achieved when the Lithium-specific trap, operating on the Erbium tune-out wavelength, is used in the experiment. Second, it can be used to lift the trap above the transport beams, if one needs to bring the atomic species in the glass cell sequentially. For example, the Lithium cloud can be transported to the glass cell, transferred in the trap, and moved upwards. Then, the Erbium cloud can be transported there as well, and the trap moved downwards to overlap the two species. Both situations have been tested and demonstrated to work during test measurements in our experiment.

Transport

The laser setup for the transport of atoms, visible in Fig. 3.26, was made by using two more ALS lasers[61]. Their output beams are overlapped across the vacuum system to form a 1D lattice. In the experiment, the atoms are loaded into the standing wave in their respective MOT chambers. Then, the frequency of one laser, here ALS1, is ramped to turn the lattice into a running wave, thus carrying the atoms to the desired position.

The laser ALS1, outputting up to $50\,\mathrm{W}$, is placed on the glass cell side. The laser ALS2, outputting up to $100\,\mathrm{W}$, is placed on the Lithium chamber side. Their optical path is identical, and boils down to beam shaping and intensity control. The AOMs used here[62] are the same as the other $1064\,\mathrm{nm}$ systems, designed for thermal stability, and used exclusively

[60] PI GmbH, S-330.2SH
[61] ALS1: ALS-IR-1064-50-A-CC-SF, ALS2: ALS-1064-130-E-CC-SF-ANRS
[62] Gooch & Housego, 3080-1990

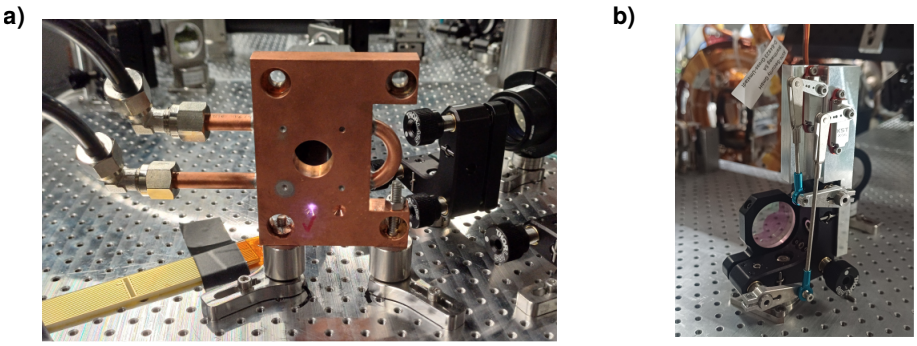

Figure 3.27 | High-power pinhole and motorized mirror. **a)** The pinholes are made of copper, watercooled and used as additional protection for the isolator and the lasers themselves. The red glow is the laser beam seen by the camera, hitting the copper part. The water is brought by the tubes visible on the left. **b)** The mirror mount in motorized by the two servomotors fixed to the aluminum block. The servomotors' rotation is transferred to the screws' axes by the rod and clamp. It is screwed to a standard Thorlabs mount and has a minimal footprint.

for intensity control. The frequency ramp of ALS1 cannot be done here without losing the beam alignment, and occurs in the seed laser setup instead (see Fig. 3.24). An important detail is the position of each focus. As explained in Section 4.2, the optimal way to transport the atoms with such a lattice was by displacing the foci: they are neither at the center of the transport area (i.e. the Erbium MOT), nor at the transport extremities (i.e. the Lithium MOT and glass cell). Instead, each beam is focused $15\,\mathrm{cm}$ away from their closest transport boundary, towards the transport center. That is, ALS1 is focused $15\,\mathrm{cm}$ away from the glass cell and ALS2 is focused $15\,\mathrm{cm}$ away from the Lithium MOT, both towards the Erbium chamber. Both are focused to a waist of $w = 300\,\mu\mathrm{m}$.

The sources of the AOMs used here for intensity control went under a few iterations as well, during our attempts at reducing the lattice (intensity and phase) noise. The changes were the same as the AOMs used for frequency control on the seed side (see Section 3.3.6), going progressively towards the final solution where the driver is a static $80\,\mathrm{MHz}$ source[63].

Finally, two components deserve special attention; they are shown in Fig. 3.27. The first component is the watercooled pinhole. Because the laser beams are very precisely overlapped, it was important to add a protection even in addition to the high-power isolators[64]. The pinhole is made out of copper, with a hole of $\varnothing 1\,\mathrm{mm}$, and is watercooled to prevent any local heating from misaligning optics or inducing air flow. A good side effect of having displaced foci is that it breaks the symmetry between the beams, and they do not have identical waists at any given point along the path. It made it possible to block most of the undesired light by placing such a pinhole on each side, at an advantageous position. For example, the pinhole close to ALS1 is placed at a position where the beam of ALS1 is small, while the beam of ALS2 is large. This way, it is possible to have full transmission of the ALS1 beam, while blocking 90% of the ALS2 beam power. They can also be used as an aligning tool if a laser needs to be replaced.

[63] QuanticWenzel Premium 80MHz Sprinter Crystal Oscillator
[64] EOT Eurys 1045-1080nm 5mm-CA

The second component is the home-built motorized mirror mount. The idea was simply to turn the mirror mounts' screws in a precise, controlled and reliable way. It was also designed to be integrable to an existing system easily by being added to a standard mirror mount (for example, a Thorlabs mirror mount here). Each mirror mount's screw is controlled by a servomotor[65], via a rod and a clamp to transmit the movement. The servomotors can then be interfaced with Python and easily controlled during an experimental sequence. A coarse alignment has to be done manually first, but a very precise overlap can be achieved with the servomotors as a second step. The low-profile integration is clearly visible on the picture: the mount holding the servomotors can be brought from the top, and simply screwed to the side of the mirror mount. All-in-all, this home-built motorized mirror proved to be a great low-cost solution for alignment issues, and was a key part to having a working long-distance transport.

[65] KST X06

Chapter 4

The path to degeneracy

This chapter is dedicated to the characterization of the machine at its different steps towards generating a quantum gas of Erbium. As per the rest of the thesis, it will be focused on the Erbium processes, while the Lithium side is developed in depth in the complementary thesis of Florian Kiesel [109]. We begin with the laser cooling steps in Section 4.1 which take place in the Erbium chamber. This section covers the Zeeman slowing (ZS) and Angled Zeeman Slowing (AZS) processes in Section 4.1.1, moves on to the description of the Magneto-Optical Trap (MOT) in Section 4.1.2, and finally describes the Optical Dipole Trap (ODT) in Section 4.1.3. The second part of this chapter presents the long-range transport in Section 4.2, where a running lattice is used to transport atoms (Erbium and Lithium) from their respective chambers to the glass cell.

In order to give quick overview, a simplified schematic of the optics setup built around the Erbium vacuum chamber is shown in Fig. 4.1. There, all the beams necessary for the steps described in this chapter are displayed, from the ZS beams up to the transport lattice beams. The ZS and AZS beams (blue) are brought to the experiment by fiber optics. There, the ZS beam is amplified locally by a slave diode via injection lock as explained in Section 3.3.3, and sent towards the atomic beam by an in-vacuum aluminum mirror. The MOT beams (yellow) are delivered with optical fibers as well, simply enlarged before going in the vacuum chamber, and retro-reflected to cover all directions. Their generation is detailed in Section 3.3.4. The off-resonant beams at $1064\,\mathrm{nm}$ (red) are generated by lasers placed directly on the experiment table due to their high-power requirements. These beams are used for the ODT, which was built in the vertical plane, and for the transport, which is built along a line-of-sight going from the Lithium MOT to the glass cell. More information on their setup can be found in Section 3.3.6.

Finally, the results presented in this chapter were obtained during the writing of this thesis, with only minor optimizations to the machine. The goal was to present the standard steps as they happen in day-to-day operation in the lab, at a good representative performance level.

4.1 Laser cooling

The laser cooling steps covered in this section are the first steps towards generating ultracold gases of Erbium in our glass cell. These steps all take place in the Erbium chamber, and are powerful enough to bring atoms from a high temperature oven at more than $1100\,^{\circ}\mathrm{C}$, down

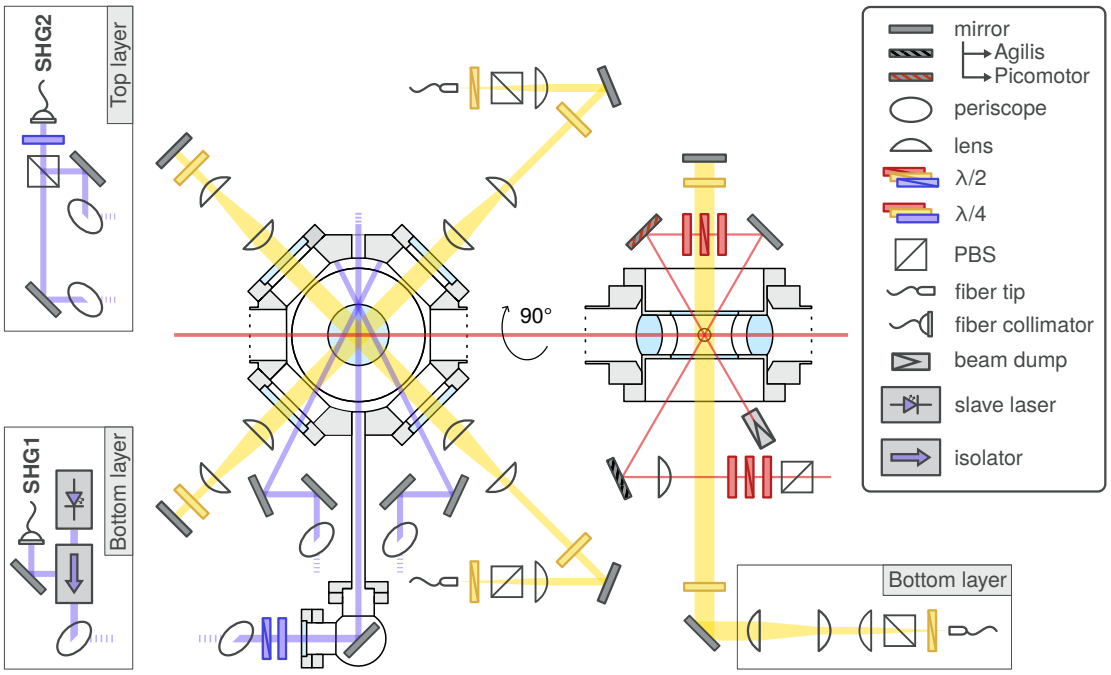

Figure 4.1 | MOT and ODT optics setup. Top view (left) and side view (right) of the Erbium chamber, showing a cut in the horizontal (vertical) plane with their respective laser beams. The ZS and AZS beam are drawn in blue, the MOT beams in yellow, and the off-resonant beams in red. The ODT was built in the vertical plane (right), and the transport lattice is the horizontal beam common to both views. Here, the Lithium chamber is towards the left, and the glass cell towards the right of the drawn Erbium chamber. For the sake of clarity, the imaging beams were not drawn here.

to the microkelvin range. Three stages are necessary to reach this level: Zeeman Slowing (ZS), Angled Zeeman Slowing (AZS), and Magneto-Optical Trapping (MOT).

4.1.1 Zeeman slowing

The first step towards quantum degeneracy is the Zeeman slowing process. Its purpose is to slow down atoms coming out of the oven at high velocity, down to the capture velocity of the MOT. It uses laser light resonant with the $30\,\mathrm{MHz}$-wide transition of Erbium at $401\,\mathrm{nm}$, which provides a rapid slowing of the atoms. The ZS magnetic field, introduced in Section 3.2.1, was designed to reach initial velocities up to $600\,\mathrm{m/s}$ with a laser beam detuned from the atomic resonance by $-640\,\mathrm{MHz}$, and reduce it down to $5\,\mathrm{m/s}$. In practice, the design of the ZS coils and vacuum chamber was such, that the distance between its end point (where the slowing stops) and the MOT was too large. There, because of the radial heating and the reduction of the longitudinal velocity, atoms exit the ZS with a large fan angle and only a small fraction of these atoms effectively reach the capture volume of the MOT, imposed by the size of its beams.

A solution for this issue was to split the slowing in two, by increasing the exit velocity of the ZS, and by adding a second slowing stage in front of the MOT. This technique, called

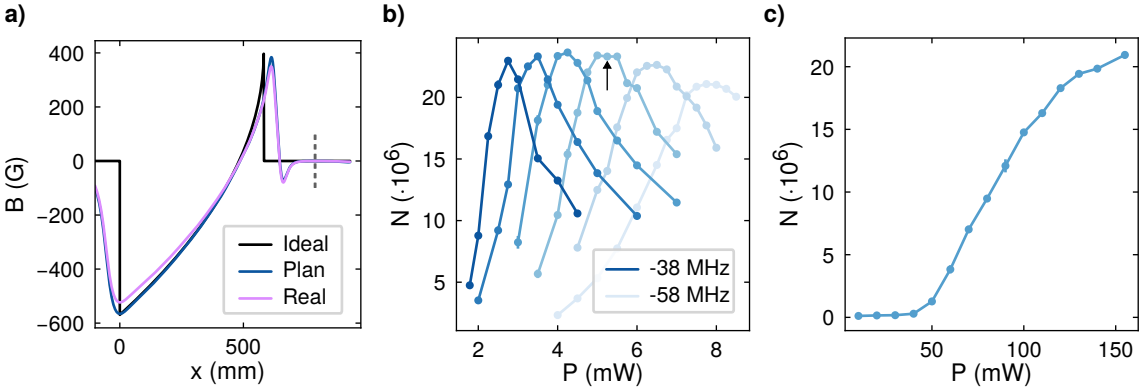

Figure 4.2 | Zeeman slower overview. a) Comparison between the calculated ideal (black), planned (blue) and real (purple) fields of the ZS. The real field is calculated with the actual currents sent though the ZS coils. The ZS entrance has a field of $-523\,\mathrm{G}$ instead of the planned $-565\,\mathrm{G}$, which corresponds to a ZS capture velocity of $590\,\mathrm{m/s}$ instead of $617\,\mathrm{m/s}$. The ZS exit has a field of $350\,\mathrm{G}$ instead of $384\,\mathrm{G}$, which corresponds to an exit velocity of $33\,\mathrm{m/s}$ instead of $11\,\mathrm{m/s}$. **b)** Measurement of the MOT loading rate for varying AZS power and frequency, from a detuning of $-38\,\mathrm{MHz}$ (dark blue) to $-58\,\mathrm{MHz}$ (light blue) with steps of $4\,\mathrm{MHz}$. The arrow indicates the chosen working point, at $5.3\,\mathrm{mW}$ per beam and detuning of $-50\,\mathrm{MHz}$. **c)** Measurement of the MOT loading rate for varying ZS power. The saturation effect comes from the limited MOT beams power and not from a saturation of the ZS beam itself. Both **b)** and **c)** figures were measured for a MOT loading of $1\,\mathrm{s}$ with 5 repetitions; the error bars corresponding to the standard deviation are smaller than the markers.

here Angled Zeeman Slowing (AZS), was demonstrated shortly before in Er [231], Dy [232] and Yb [233] systems. To increase the exit velocity of the ZS, one only needs to decrease the final value of the magnetic field. In our case, the magnetic field used in our experiment is shown in Fig. 4.2. The value at the exit point was changed from $384\,\mathrm{G}$ to $350\,\mathrm{G}$, for a longitudinal velocity increase from $11\,\mathrm{m/s}$ to $33\,\mathrm{m/s}$. The second slowing stage (the AZS part) comes in with two additional laser beams, aligned to intersect just in front of the MOT (see Fig. 4.1). Although they address the same atomic transition, their frequency has to be much closer to resonance because of the local magnetic field and atoms' velocity. Finally, the lower slowing rate over the remaining distance requires a lower power than that of the main ZS beam. These reasons make this technique advantageous over a blue MOT [186, 234], a core-shell MOT [235] or a two-stage MOT [176]: it is technically simpler to implement and has easier requirements.

The current setup is using a ZS beam of $\varnothing = 10\,\mathrm{mm}$ at $150\,\mathrm{mW}$ with a slight focussing towards the oven, and AZS beams of $\varnothing = 10\,\mathrm{mm}$ at an angle of approximately $30\,^\circ$ with the atomic beam. There, it appears that the AZS can work for a rather large range of detuning and power (see Fig. 4.2), but the best configuration was determined to be for a power of $5.3\,\mathrm{mW}$ per beam at a detuning of $-50\,\mathrm{MHz}$. This configuration yields the highest MOT loading rate, with the widest maximum power-wise, thus protecting it from small power fluctuations over time. Finally, the influence of the ZS beam power on the MOT loading rate was also measured. It appears that the loading rate saturates for high enough ZS power, although this effect comes from the yellow MOT beams. At the time of measurement, the yellow laser was slightly misaligned and the output power was only half of its usual value.

When the same measurement is done at high MOT beam power, no saturation can be seen on the ZS beam power influence.

4.1.2 Narrow-line Magneto-Optical Trap

Basic principles

Magneto-optical Traps (MOT) have been a ubiquitous tool for cold atoms experiments since their first realization a few decades ago [4]. They allow the trapping of atoms and their subsequent cooling down to the Doppler temperature, often in the microkelvin range. From a historical standpoint, narrow-line MOTs attracted a lot of attention in the ultracold atoms community after their first realizations in 1999 for Yb atoms [236] on the $556\,\mathrm{nm}$ line and for Sr atoms [237] on the $689\,\mathrm{nm}$ line. In both cases, the narrow-line MOT was loaded from a wide MOT, on the $461\,\mathrm{nm}$ and $398\,\mathrm{nm}$ lines respectively. Lanthanides were trapped a few years later, starting with Er [186, 188, 238] and Dy [234, 239]. In particular, the main point of interest of [188] was the demonstration of direct loading of the narrow MOT, avoiding a precooling stage and thus greatly reducing the experimental complexity.

Their working principle relies on a combination of radiation pressure and magnetic gradient to generate two types of forces on the atoms [195, 196]. In general, this is achieved by shining three pairs of counter-propagating laser beams, red-detuned from an atomic transition, and by adding a magnetic gradient imposed by a pair of coils. The laser beams form a so-called optical molasses which imparts a velocity-dependent force on the atoms: an atom moving in any direction will see an imbalance in the radiation pressure and absorb more from the beam closer to resonance due to the Doppler effect. An additional position-dependent force emerges thanks to the magnetic field gradient, which also brings an imbalance in the radiation pressure due to the Zeeman effect. The first contribution slows down the atoms and prevents diffusion, while the second contribution effectively creates a restoring force which brings the atoms back to the center of the trap.

A key point of this technique is its fundamental cooling limit: the Doppler temperature. It is determined only by the intrinsic parameters of the atomic transition, namely: $T_D = \frac{\hbar\Gamma}{2k_B}$, where Γ is the transition width. This is precisely where a narrow-line MOT is powerful: by using a narrow transition, the reachable temperature is much lower than that of a wide transition. For example, in our experiment the MOTs of Lithium and Erbium rely on $5.8\,\mathrm{MHz}$- and $190\,\mathrm{kHz}$-wide transitions, yielding Doppler temperatures of $138\,\mu\mathrm{K}$ and $4.6\,\mu\mathrm{K}$ respectively.

However, using a narrow-line MOT is a bit more technically involved than its wide counterpart. To understand it, one can look at the force exerted on atoms in the trap. A simple 1D model is qualitatively good enough and can be described by the MOT scattering force [183]: $F_{\mathrm{sc}} = F_+ + F_-$ where $F_\pm$ are the forces exerted by each counter-propagating beam and are given by:

$$F_\pm = \pm\frac{\hbar k\Gamma}{2} \cdot \frac{I/I_{\mathrm{sat}}}{1 + I/I_{\mathrm{sat}} + 4(\Delta - k\cdot v \mp \mu\nabla B x/\hbar)^2/\Gamma^2} \tag{4.1}$$

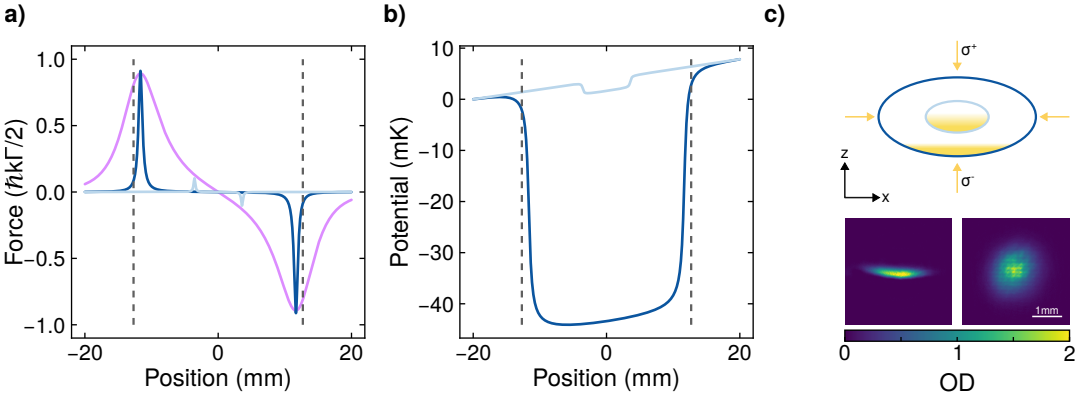

Figure 4.3 | MOT concept. a) Scattering force exerted on an atom at rest by a narrow-line MOT, in a 1D model with two counter-propagating beams, normalized to the maximum scattering force. The calculations in dark (light) blue were done with our experimental parameters during loading (compressed) phase. An example of scattering force exerted in a wide MOT (purple) is shown by multiplying the linewidth by a factor 10 for comparison. The gray dashed lines indicates the size of our smallest MOT beam and confirms that our optimal loading parameters match well with our MOT beams' size. **b)** Trapping potential exerted by the loading (dark blue) and compressed (light blue) MOT along the vertical axis. The narrow nature of the MOT is visible by the typical box-shape of the trapping potential, and by the visible influence of gravity with the potential tilt. **c)** Top: representation of the atomic cloud in the MOT during loading and compressed phases. The atoms are spatially displaced to the bottom (gravitational sag) and scatter more light from the upward σ^- beam. Bottom: In-situ imaging of the cMOT with horizontal (left) and vertical (right) imaging, after $1\,\mathrm{s}$ MOT loading.

Here, the Doppler effect appears as $k \cdot v$ where k is the laser wavevector and v the atom velocity; the Zeeman effect appears as $\mu \nabla B x/\hbar$ where μ is the differential magnetic moment between the two atomic states and I_{sat} is the saturation intensity of the transition. This shows that the force exerted by the MOT is non-negligible only in localized positions, namely $x = \mp|\Delta|/\mu\nabla B$, as can be seen in Fig. 4.3. Contrarily to a wide MOT, a narrow-line MOT effectively exerts pressure "walls" on the atoms, instead of a continuous force in the whole trapping volume. It also creates a box potential, with an additional tilt when gravity is taken into account.

This particular situation has one main downside: the capture velocity of such a MOT is rather low. For Erbium, the capture velocity (which depends on the exact trap configuration and size) is only on the order of $v_c \approx 5\,\mathrm{m/s}$. To overcome the problem, it is possible to enlarge the effective linewidth with power broadening and with frequency sidebands, imparted on the laser beams with (in our case) a modulation on the AOM (see Section 3.3.4).

Finally, a strong advantage of a narrow MOT is its ability to exploit the gravitational sag. Thanks to the rather weak radiation pressure exerted by the MOT beams, the atoms accumulate at the bottom of the trap. During the loading phase, it prevents undesired scattering from the blue light of the (A)ZS beams. The spatial displacement also increases the scattering rate from the σ^- MOT beam coming from the bottom compared to the one coming from the top. The scattering imbalance leads to a spontaneous spin polarization in the gas, where the atoms are optically pumped in the lowest $|J, m_J\rangle = |6, -6\rangle$ Zeeman

substate. This effect can also be used to create a MOT made only of five beams, where the downward beam is removed [240]. This technique can free optical access for other systems, such as high-NA imaging with an objective for a quantum gas microscope [241].

MOT loading

Our approach for the Erbium MOT was to follow the example of the already existing experiments at that time [188, 189], and to load the yellow MOT directly from the ZS. Initially, the MOT beams were planned to have a diameter of $25\,\mathrm{mm}$. However, it proved to be too small for an efficient capture, and compensating with a high magnetic gradient provided a limited improvement. We believe the reason was that the atoms did not have enough time to scatter light from the MOT beams before exiting the trapping volume, effectively leading to a very small capture velocity. This issue, along with the large distance between the ZS and the MOT, pointed to using larger MOT beams to reach proper loading rates.

Expanding our MOT beams' size led to a somewhat exotic geometry, where all three beams have a different size. One horizontal beam has a diameter of $\varnothing = 50\,\mathrm{mm}$. The second horizontal beam has an effective diameter of $\varnothing = 40\,\mathrm{mm}$, because it is clipped on the CF40 viewport there. Unfortunately, the planned CF63 viewport became leaky during the machine's bake-out, and had to be exchanged for the current CF40 one. The vertical beam has an effective diameter of $\varnothing = 25\,\mathrm{mm}$ because the optics and breadboard around the vacuum chamber were planned for a $1\,"$ beam, and it was not reasonable to change them for larger a beam size when we decided to increase the MOT volume. Nevertheless, it was important that all beams were shaped with the same optical components and path, so that their intensity is identical even if the beams are clipped at different sizes. The beam expansion was made by placing the fiber only in a fiber holder[1], using the fiber's high NA to let the beam expand and collimating it with a lens placed by hand a few centimeters away. This trick proved to be very space- and cost-efficient, avoiding purchasing any beam expander or using large telescopes around the vacuum chamber.

The main characteristics of our setup are given in Fig. 4.4. In short, our setup is able to trap up to $\sim 7 \cdot 10^8$ atoms at an initial loading rate of $50 \cdot 10^6$ atoms/s, and the $1/\mathrm{e}$-lifetime of the full trap was measured at $\sim 150\,\mathrm{s}$. These numbers are reached when the different laser setups are optimized and the laser beam power is maximized. With our current beam configuration, this is achieved when there is at least $45\,\mathrm{mW}$ per MOT beam, corresponding to a peak intensity of $35 I_{\mathrm{sat}}$. The results shown here were obtained with a yellow power of $20\,\mathrm{mW}$ per beam, meaning a peak intensity of $\sim 16 I_{\mathrm{sat}}$, and ultimately yielding about half the loading rate, at $24 \cdot 10^6$ atoms/s. The atom number was measured here with the vertical absorption imaging of the MOT chamber, after compressing the MOT to its standard parameters (see Chapter B).

During the loading phase, the magnetic field gradient is set at $\nabla B = 4.85\,\mathrm{G/cm}$, and the beams' frequency is detuned by $\Delta = -10.8\,\mathrm{MHz}$ ($\approx 57\Gamma$), spectrally broadened by $700\,\mathrm{kHz}$ and $1.6\,\mathrm{MHz}$ sidebands imparted on the AOM by a signal generator (see Section 3.3.4). Combined with power broadening, these sidebands are enough to cover a large range of

[1] Thorlabs, S120-APC or equivalent

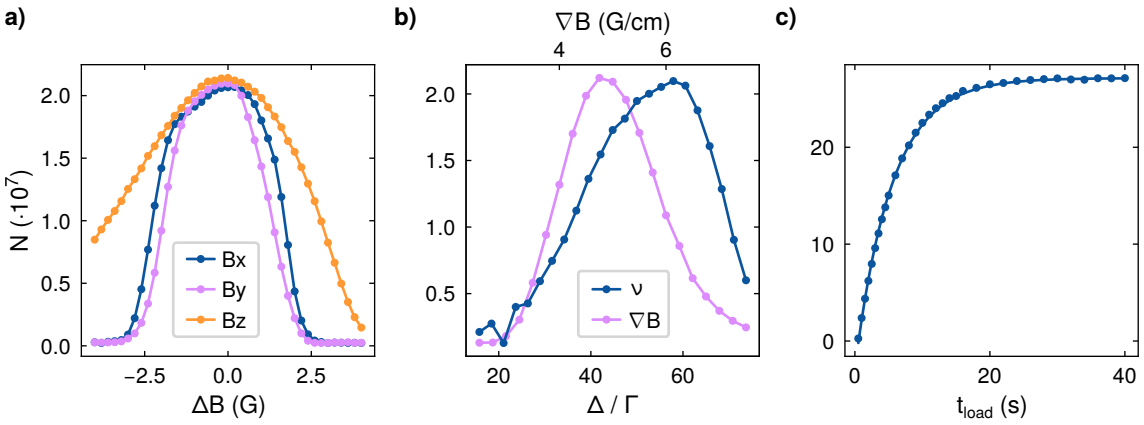

Figure 4.4 | MOT overview. a) Atom number in the MOT after $1\,\mathrm{s}$ loading, for magnetic offsets deviating from their optimal values $B_x = B_y = 0.7\,\mathrm{G}$ and $B_z = 1.25\,\mathrm{G}$. **b)** Atom number in the MOT after $1\,\mathrm{s}$ loading, for varying laser detuning (blue) and magnetic gradient (purple). Each curved was measured when the other was on its optimal value, at $\Delta = -57\,\Gamma$ and $\nabla B = 4.85\,{}^{\mathrm{G}}/_{\mathrm{cm}}$ respectively. **c)** Atom number in the MOT for varying loading time. The line is an exponential fit to the data points. All error bars were omitted for better readability.

velocity classes addressable by the MOT, thus increasing its capture velocity. The position of the MOT can be controlled by the magnetic field offsets, and has to be optimized for high loading rates. The magnetic gradient was also optimized with the detuning, by measuring 2D maps to look for a global maximum at different B_z values; the procedure is explained more thoroughly in Chapter A.

The first set of measurements presented in Fig. 4.4 shows the MOT loading rate when displaced from its optimal position via the magnetic offsets. Interestingly, the magnetic field offsets can be tweaked by rather large values, up to $\pm 2\,\mathrm{G}$ for the horizontal position (B_x and B_y), and even further for the vertical position (B_z). This robust loading proved to be important to survive the crosstalk with the Lithium chamber. In particular, when the Lithium atoms are being evaporated at high field ($320\,\mathrm{G}$) in their ODT [109], the impact on the Erbium chamber is on the order of $0.5\,\mathrm{G}$. With this large range, it is still possible to load the Erbium MOT without worrying about a compensation of the field change in the Lithium chamber.

The second set of measurements shows the MOT loading rate when the resonance condition is changed, with either the laser detuning or the magnetic gradient. These parameters effectively change the resonance conditions of the MOT, by changing the size of the "shell" where the atoms are being trapped. The best parameters correspond to the situation where the resonance conditions match with the beam size (see Fig. 4.3). The asymmetry in the curves can be explained by the MOT's bowl shape, where a large detuning or small gradient lead to a fast decrease of the loading rate.

The loading curve shown in Fig. 4.4 was obtained with these parameters, and fitted with the following exponential growth function: $N(t) = N_{\mathrm{sat}}(1 - e^{-t/\tau}) + c$. From that fit, we extract the loading rate of $24 \cdot 10^6$ atoms/s, the saturation value at $2.7 \cdot 10^8$ atoms and the half-loading time of $\tau_{1/2} = 3.8\,\mathrm{s}$.

MOT compression

After loading the MOT, the (A)ZS beams are shut off and the compression occurs. During the compression, all remaining parameters: the yellow power, broadening and detuning, the magnetic gradient, and the magnetic offsets are ramped simultaneously. The broadening is ramped down in $150\,\mathrm{ms}$, while the other parameters are ramped in $300\,\mathrm{ms}$. The yellow beams are brought closer to resonance, from $\Delta = -10.8\,\mathrm{MHz}$ ($\approx 57\Gamma$) to $\Delta = -2.4\,\mathrm{MHz}$ ($\approx 13\Gamma$), and their power is reduced from $20\,\mathrm{mW}$ ($16 I_{\mathrm{sat}}$) to $30\,\mu\mathrm{W}$ ($0.02 I_{\mathrm{sat}}$). The magnetic gradient is also reduced, from $\nabla B = 4.85\,\mathrm{G/cm}$ to $\nabla B = 3.5\,\mathrm{G/cm}$. With these parameters, the compressed MOT (cMOT) does not lose atoms, and yields a temperature of $T = 8.5\,\mu\mathrm{K}$, about twice the Doppler temperature. The observed cMOT atom number, cloud size and temperature give can be used to estimate the Phase Space Density (PSD), with an average value of $\sim 2 \cdot 10^{-6}$ and a peak value of $\sim 8 \cdot 10^{-6}$.

A more complete study of the compression itself is presented in Section A.2. The important message therein, is that the temperature is the cMOT is influenced a lot more strongly by the yellow intensity than by the frequency. The temperature is measured by time-of-flight thermometry, which is explained in Chapter B.

4.1.3 Optical Dipole Trap

Design considerations

The Erbium Optical Dipole Trap (ODT), used to collect the atoms after the cMOT stage, was implemented for two main reasons. First, it was important to have the possibility of cooling the atoms further via evaporation, in case the loading into the transport was not good enough with the cMOT temperature. Second, the main motivation was to ensure that the transported cloud would be dense and as small as possible, in order to transfer the transported cloud in the glass cell's trap with minimal heating. Otherwise, if the cloud size is comparable to the trap size, some heating can occur due to the atoms loaded from the traps' wings. For these atoms, the difference in potential energy from their position to the center of the trap will to be converted in kinetic energy, and the whole atomic ensemble will heat.

The current ODT setup is the result of a few iterations. For a long time, the laser light was derived from an ALS[2] laser. Currently, the ODT is derived from an IPG Yb fibre laser instead[3], which is used sequentially to trap Lithium and Erbium atoms after their respective MOT stages. The main advantage of using the IPG laser over the ALS laser is the amount of power it can provide to the trap: the IPG laser can output as much as $150\,\mathrm{W}$, compared to an effective $35\,\mathrm{W}$ with the ALS laser. However, its multimode emission proved to be problematic for Lithium atoms, where it was not possible to perform in-trap cooling with the Lithium gray molasses [109]. For the Erbium trap, the reason why we had to switch from ALS to IPG was a sequence issue. Because the ALS laser was used in both the Erbium chamber and the glass cell, the issue arose when we tried a combined sequence to overlap

[2] ALS-IR-1064-50-A-SF
[3] IPG YLR-200-LP-WC

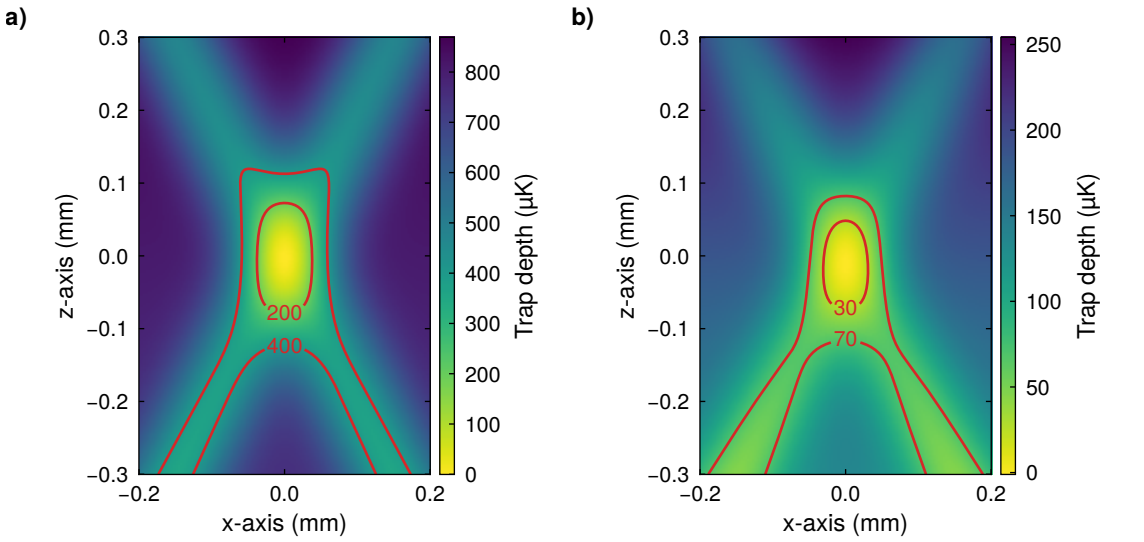

Figure 4.5 | ODT calculations. The trap depth is calculated for two different beam powers, at $130\,\mathrm{W}$ (**a**) and $30\,\mathrm{W}$ (**b**) per beam. The potential reference is taken at the deepest point of the trap, close to the center. The equipotential lines (red) show the opening of the trap in both cases, occurring at $400\,\mu\mathrm{K}$ and $70\,\mu\mathrm{K}$ respectively.

the two species in the glass cell. At that point, we were transporting Lithium atoms to the glass cell first and held it in a dipole trap. Meanwhile, Erbium atoms were still in the MOT stage, hence the timing conflict: loading the Erbium in their ODT was simply not possible because the laser was already in use to hold the Lithium atoms in the glass cell. The solution was to share the light from the IPG laser, which was used exclusively for the Lithium ODT until then. An Arduino-controlled waveplate was built, in order to send the laser light either to the Lithium chamber or to the Erbium chamber during the sequence. The details of that setup are given in the complementary thesis [109].

The Erbium trap was built in the vertical plane, as can be seen on Fig. 4.1. The motivation was to minimize the footprint taken by the setup on the optical access around the Erbium chamber. The trap is made by a single beam that we recycle, *i.e.* that we use to overlap with itself and close the trap. However, the orientation of the trap is problematic when it comes to the gravitational sag. The trap potential calculations shown on Fig. 4.5 demonstrate that the weak axis of the trap cannot properly hold the atoms against gravity on its own. The calculations were made for the real setup parameters, where the trap itself is formed by the two beams, focused to waists of $w = 90\,\mu\mathrm{m}$ and intersecting at an angle $\theta = 53\,^\circ$. The transport beams are also included in the calculations, although their impact is minor and can barely be seen on the plots. With this geometry, the trap can reach a depth of $850\,\mu\mathrm{K}$ when the beams are set at $130\,\mathrm{W}$ each. Naively, that number would look very good on the paper, but the issue is that the laser beams open the trap at a much lower depth. On Fig. 4.5, it is clearly visible when looking at the equipotential lines. Even at full power, the trap has an effective depth of $\sim 200\,\mu\mathrm{K}$ only, and goes down to a depth of $\sim 30\,\mu\mathrm{K}$ when the power is reduced to $\sim 30\,\mathrm{W}$ per beam. The issue is that the atoms fall through the trap via the arms, unless magnetic levitation is applied. It also means that the trap cannot be used for a full evaporation, because either the atoms are lost, or their temperature reaches a plateau imposed by the magnetic levitation [242].

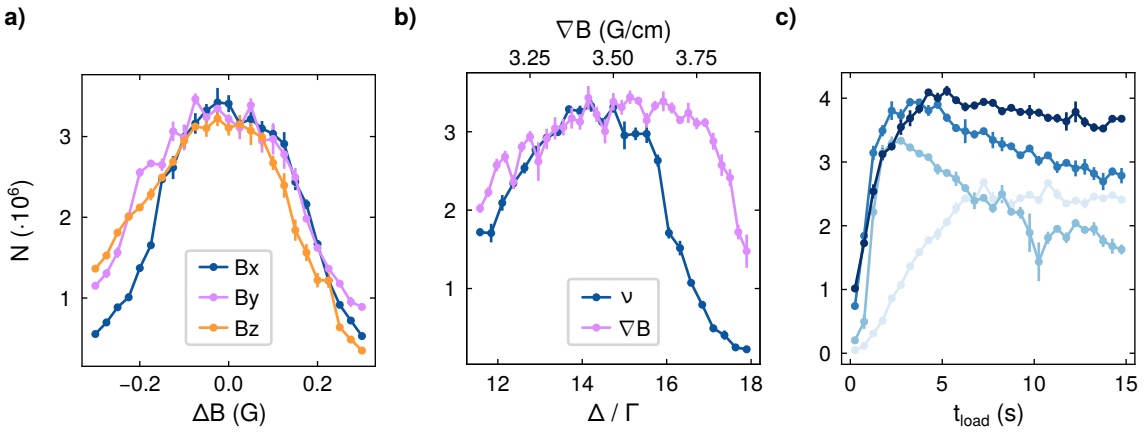

Figure 4.6 | ODT overview. a) Atom number in the ODT for magnetic offsets deviating from their optimal values $B_x = 0.27\,\mathrm{G}$, $B_y = 0.37\,\mathrm{G}$ and $B_z = -0.1\,\mathrm{G}$. **b)** Atom number in the ODT for varying laser detuning (blue) and magnetic gradient (purple). Each curved was measured when the other was on its optimal value, at $\Delta = -14.8\,\Gamma$ and $\nabla B = 3.5\,\mathrm{G/cm}$ respectively. **c)** Atom number in the ODT, for varying MOT loading time. The curves are obtained for cMOT thermalization times of $50\,\mathrm{ms}$ (light blue), $100\,\mathrm{ms}$, $200\,\mathrm{ms}$ and $300\,\mathrm{ms}$ (dark blue). All measurements were done after $500\,\mathrm{ms}$ holding in the trap and with levitating field.

The interferences are suppressed by using orthogonal polarizations in the two beams. To ensure a clean polarization, one can use an optical setup made of one Polarized Beam Splitter (PBS), followed by a $\lambda/4$-, a $\lambda/2$- and a $\lambda/4$-waveplate, in this order (see Fig. 4.1). With these components, one can make any arbitrary polarization on a laser beam, which is very convenient to compensate for imperfections coming from the other optical components on the path (mirrors, viewports, etc.). The "triple waveplates" technique is used for both beams, to maximize the polarization purity. In our setup, it was possible to measure the polarization purity with a PBS on the upper breadboard, where an extinction ratio of more than 10^4 was measured. The overlap is controlled by two motorized mirror mounts. Under the vacuum chamber, the first beam is coarsely aligned with a $1\,\mu\mathrm{rad}$-sensitive mount[4]. Above the vacuum chamber, the second beam is overlapped precisely with a $0.5\,\mu\mathrm{rad}$-sensitive mount[5].

ODT loading

An overview of the ODT loading is given in Fig. 4.6. The transfer from the cMOT to the ODT was optimized in a way similar to the MOT optimization, and the procedure is detailed in Section A.3. For these measurements, the MOT was loaded for $2\,\mathrm{s}$, compressed in $300\,\mathrm{ms}$ and held in the cMOT for $200\,\mathrm{ms}$ of thermalization time. The ODT beams are turned to full power before the compression starts, and the atoms kept in the trap for $500\,\mathrm{ms}$ after shutting off the MOT beams. During this holding time, the atoms are levitated with a magnetic gradient of $4.2\,\mathrm{G/cm}$; the long delay is to make sure that non-trapped atoms are not present on the absorption pictures. There, it appears that the cMOT position is quite

[4] Agilis AG-M100N
[5] New Focus, Picomotor 8821

critical, and deviations of $\pm 0.2\,\mathrm{G}$ are enough to move the cMOT away from the ODT. This order of magnitude is in the range of the Lithium coils' influence, and thus need to be taken into account. For example, depending on the experimental sequence, the Lithium coils can be on or off, leading to a displacement of the cMOT large enough to prevent loading in the ODT. The narrow range of acceptable parameters is also reflected on the final cMOT frequency and gradient. The detuning is constrained to a $\pm 2\Gamma$ range, and the gradient in a $\pm 0.3\,{}^{\mathrm{G}}/_{\mathrm{cm}}$ range. Finally, the ODT saturation was measured against the MOT loading time. The measurements shown on the right-most figure correspond to different thermalization times, which turned out to be more critical than we anticipated. There, it seems that the ODT can saturate at $4 \cdot 10^6$ atoms for thermalization times longer than $200\,\mathrm{ms}$, but the trap loading behaviour changes qualitatively at short times. This effect was attributed to slow dynamics during the compression and thermalization steps, because of to the narrow nature of the yellow transition.

4.2 Transport

4.2.1 Design considerations

Transporting trapped atoms is, on the paper, rather simple: one only needs to move the trap which holds the atoms. In practice, many technical details (such as the adiabaticity or the overall noise) have to be carefully taken into account to successfully transport an atomic cloud, which depend on the exact transport technique. Many different approaches have already been demonstrated, and they can be decomposed in three major groups: the moving trap can be purely magnetic, optical, or a combination of both. The first approach can be applied to magnetically trappable atoms, *i.e.* atoms in a low-field seeking state, and is realized with coils in anti-Helmholtz configuration. In that case, either a whole chain of coil pairs can be used sequentially [216, 243], or a single coil pair can be translated to move the quadrupole's field center [244, 245]. The second approach is more universal and can be executed in various ways, all relying on a movable ODT. It can be done by displacing the trap itself with a translation stage as well [246, 247], by moving the trapping beam's focus via a tunable lens [248–251], or by lattice transport [252–254]. The latter is done by superimposing two counter-propagating beams to create a standing wave (the 1D lattice), and the atoms are transported by detuning one of the lasers, thus creating a running lattice. Finally, the third approach uses a combination of magnetic and dipole trapping, usually using a single far-detuned beam in combination with a magnetic offset and gradient [255, 256]. The above introduction is by no means an exhaustive list, and more exotic techniques have been employed, such as guiding atoms through hollow-core fibers [257, 258] or blue-detuned hollow beams [259].

In our experiment, the transport setup had to be (coarsely) designed hand-in-hand with the vacuum system and its intrinsic mechanical constraints. Based on the overall shape of the apparatus and the size of the glass cell, it was clear that the transport could not be done with a movable focus. The long distance (up to $1\,\mathrm{m}$) as well as the small aperture of the glass cell's front face ($12 \times 12\,\mathrm{mm}$) simply do not provide enough space for a highly focused beam. Moreover, a magnetic-trap-based transport setup was not possible either, because Erbium atoms are spin-polarized in their lowest Zeeman state, which is a high-field seeking

state. For these reasons, the final setup, inspired from [253, 254], naturally converged towards a lattice-based solution.

A preliminary study was done on the lattice beam shape [260], to determine whether a Bessel beam [253, 261, 262] would be advantageous thanks to their non-diffracting properties. However, a high-quality Bessel beam requires a high-quality axicon lens, and is very sensitive to the alignment between the beam and the lens; any pointing drift would result in a degraded beam shape over time. Additionally, the amount of power in the central spot of the Bessel profile (the fraction of the beam effectively used for transport) is rather low, with about $10\,\%$ of the total power. Interestingly, the low power is balanced with the small size of the spot and results in a similar intensity than can be achieved with Gaussian beam, however at the cost of a much smaller trapping volume and fewer transported atoms. Following these considerations, the design was chosen to be a lattice transport made by two Gaussian beams, and the optimal parameters were determined numerically.

The calculations of the beams' waists and focus positions, and the resulting trapping potential are summarized in Fig. 4.7. The optimal parameters for the waist and focus were determined by looking at the beam intensity and interferences depth along the path. Using the well-known equations of a gaussian beam, the intensity can be calculated, for any position along the propagation axis x, as:

$$I(x,y,z) = I_0(x) e^{-\frac{2(y^2+z^2)}{w(x)^2}} \tag{4.2}$$

where $I_0(x)$ and $w(x)$ are the peak intensity and beam radius at the position x, given by

$$I_0(x) = \frac{2P}{\pi w(x)^2} \tag{4.3}$$

and

$$w(x) = w_0 \sqrt{1 + \left(\frac{x - x_f}{x_R}\right)^2} \tag{4.4}$$

where P is the beam power, w_o the beam waist and x_R the Rayleigh range. For counter-propagating beams, the lattice structure emerges from the interferences, yielding a varying intensity described by

$$I(x,y,z) = I_1 + I_2 + 2\sqrt{I_1 I_2}\cos(2kx) \tag{4.5}$$

where the subscripts 1 and 2 denote the two beams, and the coordinate dependence of I_1 and I_2 have been omitted for clarity. From these definitions, it is straightforward to determine the lattice's barrier height and total trap depth, along and perpendicular to the propagation axis respectively. The former is given by the amplitude of the interferences only (hence a lower value than the trap depth), and the latter by the overall intensity:

$$U_{\text{latt}} = 4\alpha\sqrt{I_1 I_2} \tag{4.6}$$

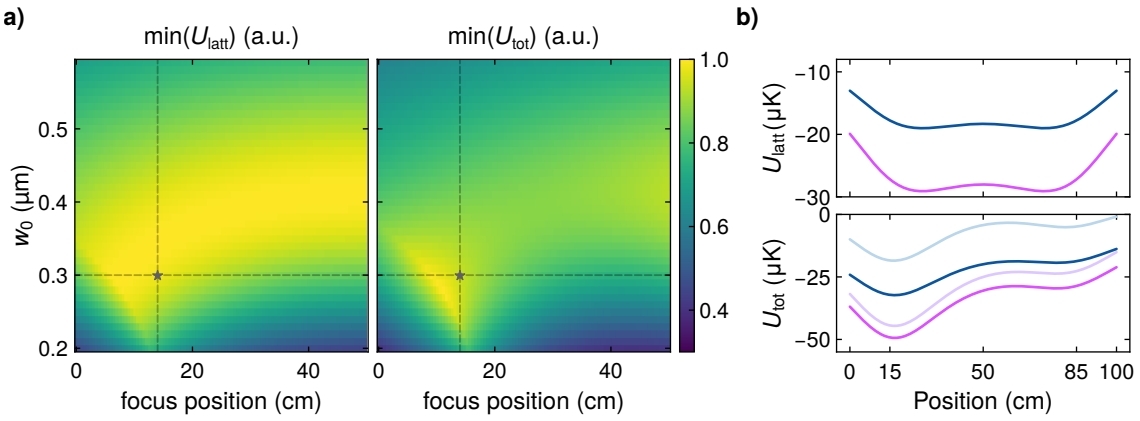

Figure 4.7 | Transport beams design calculations. a) Minimal value of the lattice height (left) and total depth (right) of the transport beams along the whole transport direction, for beam powers of $30\,\mathrm{W}$ and $80\,\mathrm{W}$. Both plots are normalized to their maximal value and the star denotes the current operating parameters. **b)** Lattice height (top) and trap depth (bottom) for Er (blue) and Li (pink) along the transport path, calculated with (light) and without (dark) gravity. For Er, the gravitation was scaled down to $15\,\%$.

and

$$U_{\mathrm{tot}} = \alpha \left(I_1 + I_2 + 2\sqrt{I_1 I_2} \right) \tag{4.7}$$

where α is the polarizability of the atom.

The best parameters for the transport beams were determined by calculating the minimal value of both quantities along the transport distance, for various pairs of focus positions x_f and beam waists w_0. The calculations were initially done for a symmetric scenario, where both transport beams had $80\,\mathrm{W}$ of power and therefore their foci were made equidistant from the center.[6] However, the laser on the glass cell side (ALS1) had to be replaced by another with half the output power (see Section 3.3.6), but the setup was not modified further. The plots shown on Fig. 4.7a were calculated for our current setup, where the beams have $80\,\mathrm{W}$ and $30\,\mathrm{W}$ respectively. The optimum pair of $(x_f, w_0) = (10\,\mathrm{cm}, 260\,\mu\mathrm{m})$ is slightly shifted from our current operating parameters of $(x_f, w_0) = (15\,\mathrm{cm}, 300\,\mu\mathrm{m})$, built when we had two identical lasers. The difference has no impact regarding the bottleneck of this setup: the total depth. With beams as large as $w_0 = 300\,\mu\mathrm{m}$, the intensity cannot be high enough to create deep traps for Er atoms and hold them against gravity.

The problem is clear when one looks at the lattice height and total depth along the transport distance, calculated for both Er and Li in Fig. 4.7b. While U_{latt} is not affected by gravity, U_{tot} needs to contain an additional $-mgz$ term in its definition (see Eq. (4.7)) to properly represent the situation. For Li, the light mass makes this new contribution small compared to the optical potential: adding the gravity term only lowers the trap depth by $\sim 10\,\%$. For Er, the tilted potential was calculated for a downscaled gravitational potential; with a downwards vertical force of $0.15 \cdot F_{\mathrm{grav}}$, the trap already opens over the entire Erbium

[6] The position x_f is defined as the distance from the transport's edge towards the center. At $x_f = 0\,\mathrm{cm}$ the beams are focused on the Li MOT and glass cell respectively, at $x_f = 50\,\mathrm{cm}$ they are both focused on the Er MOT.

transport distance. The problem was solved by levitating Er with a magnetic gradient to remove the tilt from the gravitational potential.

The magnetic levitation of Er is done by only a single, static pair of coils which spans over the whole transport, already introduced in Section 3.2.3. The main reason behind this choice was experimental simplicity. Among the transport setups mentioned earlier, the ones which include a magnetic system are invariably dynamical in nature: the coils are either translated or used sequentially, and both approaches have their own issues. A translation stage can be a significant source of mechanical noise, and needs to be both precise enough in position and velocity, over $1\,\mathrm{m}$. The footprint is also large, in an area where the real estate is expensive, and cannot be as fast as the lattice. Finally, time-varying fields also bring their own share of issues, from undesired induced currents, to slow time scales compared to the optical setup again. The transport setup built here only requires to be turned on when the Er transport step starts, and turned off when it is over. The main issue in our current design is the speed of the transport coils: because they are very large (about $80 \times 12\,\mathrm{cm}$), they have a large inductance and can be used in typical ramps of $\sim 200\,\mathrm{ms}$ minimum.

4.2.2 Transport characterization

Standard sequence After loading the ODT (see Section 4.1.3), the atoms are transferred to the transport lattice in three steps. First, to prevent the atoms from falling through the trap, the MOT and vertical offset coils are used to levitate the atoms. The gradient is ramped to $4.2\,\mathrm{G/cm}$ and the vertical offset to $6\,\mathrm{G}$, both in $10\,\mathrm{ms}$. The offset is necessary to push the magnetic field zero under the atoms, so that the magnetic gradient is vertical and not pulling the atoms to the side. Then, the MOT coils are replaced by the racetracks and launch coils, with simultaneous ramps of $200\,\mathrm{ms}$. In the final setup, top racetrack, bottom racetrack and launch coils are ramped to $20\,\mathrm{A}$, $48\,\mathrm{A}$, and $25\,\mathrm{A}$ respectively. The racetracks provide the gradient over the transport distance, and the launch coil helps with the starting point (see Section 3.2.3). Finally, the ODT is ramped down in $500\,\mathrm{ms}$ at a vertical offset of $2.7\,\mathrm{G}$, and the atoms are trapped in the transport lattice. The transport itself is made by ramping the detuning to $11.6\,\mathrm{MHz}$ in $20\,\mathrm{ms}$, corresponding to a maximum velocity of $v = \frac{\Delta\nu\cdot\lambda}{2} = 6.2\,\mathrm{m/s}$, for an acceleration of $a_{\mathrm{latt}} = 0.58\,\mathrm{MHz/ms} \equiv 308\,\mathrm{m/s^2}$. The atoms are transported at maximum velocity for $60\,\mathrm{ms}$ and, when reaching the glass cell, they are decelerated in the same way as the initial acceleration. No heating was detected during the transport: the cloud's temperature was measured at $4.5\,\mu\mathrm{K}$ and $3.2\,\mu\mathrm{K}$ before and after transport respectively. The small temperature difference comes from the loss of atoms, which can be understood as evaporative cooling.

Beyond these default values, the transport setup was characterized in three sets of measurements, reported in Fig. 4.8. First, we measure the number of atoms reaching the glass cell when the racetrack coils are set to different values (Fig. 4.8a). The second measurement was done for different accelerations and maximum velocities (Fig. 4.8b). The third measurement was done to properly estimate the transport efficiency (Fig. 4.8c), by transporting the atoms back into the MOT chamber. The last measurement was necessary because the imaging conditions in the glass cell were not optimal: the atoms are transported in the cell and imaged directly, with the magnetic fields still present. In this configuration, the atoms are aligned along the vertical axis, imposed by the field, and the absorption

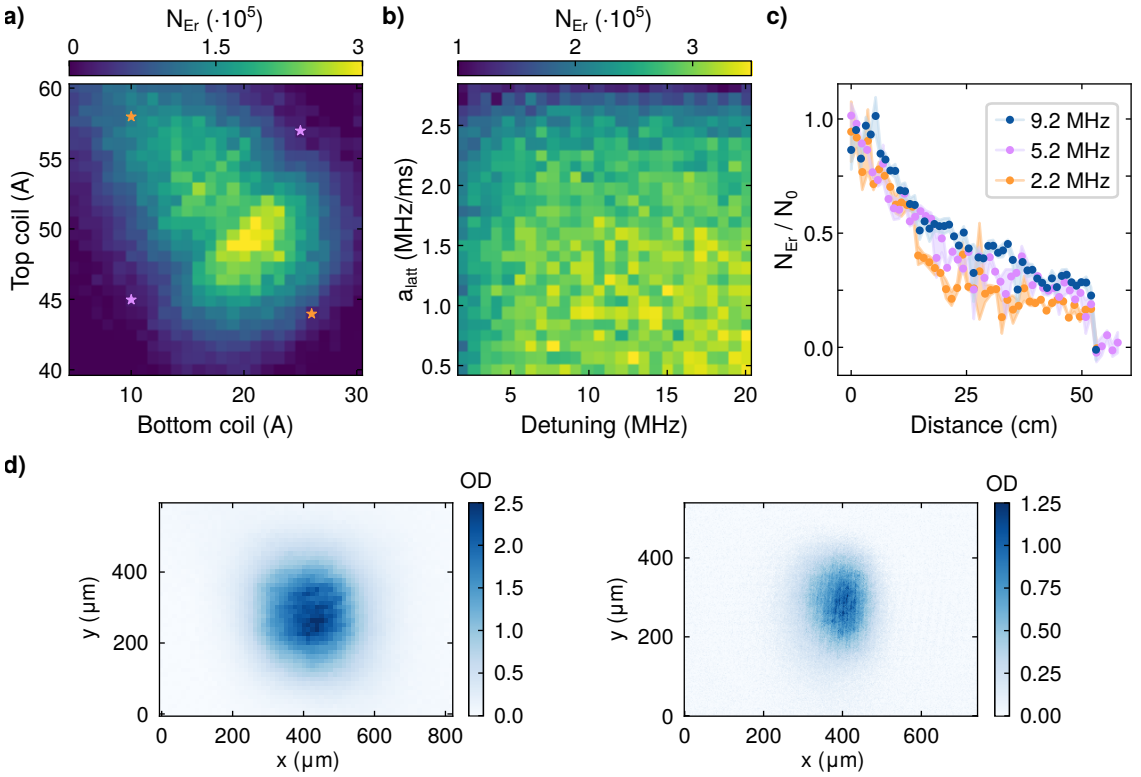

Figure 4.8 | Transport overview. a) Atom number in the glass cell after transport, for various currents in the racetrack coils and at a fixed offset of $B_z = 2.7\,\mathrm{G}$ during the ODT evaporation. The purple stars indicate the constant-offset diagonal of $20\,\mathrm{G}$, for gradients of $3.2\,\mathrm{G/cm}$ (lower left) and $4.8\,\mathrm{G/cm}$ (upper right). The orange stars indicate the constant-gradient diagonal of $4.0\,\mathrm{G/cm}$, at offsets of $25\,\mathrm{G}$ (upper left) and $12\,\mathrm{G}$ (lower right). **b)** Atom number in the glass cell after transport, for various accelerations and maximum velocities. Both quantities are given in the units of the lattice detuning, which are the relevant numbers for an experimentalist working in the laboratory. The atom number increases for higher maximum velocities and lower acceleration values, measured up to $20\,\mathrm{MHz}$ ($\equiv 10\,\mathrm{m/s}$) and $2.8\,\mathrm{MHz/ms}$ ($\equiv 1.5\,\mathrm{km/s^2}$). The range is chosen to be relevant for Li as well, but atom number could be increased for lower accelerations (see text). **c)** Roundtrip efficiency for various maximum velocities, at constant accelerations of $0.7\,\mathrm{MHz/ms}$ ($\equiv 370\,\mathrm{m/s^2}$). For the lowest velocity ($2.2\,\mathrm{MHz} \equiv 1.17\,\mathrm{m/s}$), the lower efficiency is due to the long holding time of more than $400\,\mathrm{ms}$ to complete the roundtrip. The sudden drop in atom number at $52\,\mathrm{cm}$ happens when the transport goes far enough for the atoms to be slammed against the glass cell's wall. **d)** Absorption pictures of the clouds before (left) and after (right) transport, taken at $5\,\mathrm{ms}$ and $0\,\mathrm{ms}$ TOF respectively. The change in optical density is due to atom loss during transport and non-optimal imaging in the glass cell.

imaging cannot be done with a closed transition because the imaging beam is horizontal. Although it was possible to image the cloud, the detected atom number only gives a low boundary on the real atom number. It was also not possible to remove the levitation, for two reasons. Either the atoms would fall out of the transport beams, or they would need to be transferred in a dipole trap, in which case the measured transport efficiency would be biased because the transfer is not lossless.

Transport fields To evaluate the impact of the transport fields, the racetracks were set at different pairs of currents $(I_b, I_t) = ([0, 30]A,\ [40, 60]A)$ during the sequence described above. The region where atoms are detected lies nicely along the decreasing diagonal (upper left to lower right), where the gradient is constant. The maximum atom number is found at[7] $(I_b, I_t) = (20, 40)$ A, where the gradient is $4.0\,\mathrm{G/cm}$, with atoms detected only for vertical gradients between $3.2\,\mathrm{G/cm}$ and $4.8\,\mathrm{G/cm}$. Regarding the offset, whose constant values lie along the second diagonal, an important loss feature is detected around $(I_b, I_t) = (18, 50)$ A. This atom loss is attributed to the presence of a Feshbach resonance during the transfer from the ODT to the lattice in the Er chamber, instead of the transport itself. During this transfer (described in the sequence above), the total magnetic field is given by the contributions of the racetracks coils, but also that of the MOT coils and the Earth field. When accounting for all contributions, the field's magnitude is close to $20\,\mathrm{G}$, in the vicinity of the Feshbach resonances of Erbium [169]. In particular, the strongest loss feature seen around the point at $(I_b, I_t) = (18, 50)$ A lies on the wide resonance at $20.5\,\mathrm{G}$.

At the default parameters, the offset from the racetracks varies from $15.5\,\mathrm{G}$ at the starting point, to $13.5\,\mathrm{G}$ at the end of transport. Again, when taking the field of Earth in consideration, the additional contribution brings the transport into a region densely populated by Feshbach resonances. However, our assumptions regarding the absence of detection of these resonances are twofold: the atoms are still rather hot, in the classical regime, and the resonances are suppressed by the lattice. The first aspect imposes a selection on the detectable resonances: at this temperature, long holding times are required to see an effect, and only the wider resonances can be observed [26]. The second aspect comes from the confinement of the atoms in the lattice sites. The lattice turns the cloud into a series of 2D classical gases, for which the scattering amplitude never diverges. In other terms, the lattice could suppress the collision channels to form Feshbach molecules, leading to a strong suppression of the atom losses for a classical gas [263, 264]. However, these assumptions would require a proper investigation for conclusive statements.

Transport dynamics The acceleration and maximum velocity were scanned together (Fig. 4.8b) to determine how fast the transport can be, without losing or heating the atoms. The results show that the number of transported atoms is rather unaffected for acceleration below $a_{\mathrm{latt,max}} = 1.5\,\mathrm{MHz/ms} \equiv 800\,\mathrm{m/s^2}$, and maximum velocities above $v_{\mathrm{min}} = 1.3\,\mathrm{m/s}$, reached at the detuning $\Delta\nu = 2.5\,\mathrm{MHz}$. Although some transport resonances were visible for certain transport velocities (see Section A.4), their impact was minor and the transported cloud's density was constant over this whole area. These resonances also displayed a strong dependence on the beams'alignment, and the pattern has been changing after each realignment procedure, even after the addition of servomotors to control the beams' position (see Section 3.3.6).

Interestingly, the cloud can be accelerated and transported faster than we anticipated. As a reference, we defined the "natural acceleration" as the quantity $a_{\mathrm{nat}} = a_{\mathrm{ho}}\nu_{\mathrm{ho}}^2$, derived from the harmonic oscillator length $a_{\mathrm{ho}} = \sqrt{\hbar/m\omega_{\mathrm{l}}}$ and frequency $\nu_{\mathrm{ho}} = w_{\mathrm{l}}/2\pi$. For atoms

[7] All values of magnetic field gradient and offset at given for the start position of the transport, where atoms are loaded in the lattice.

in a lattice, the trap frequency can be obtained from:

$$E_l = \hbar\omega_l = 2E_r\sqrt{\frac{V_0}{E_r}} \tag{4.8}$$

where $E_r = h^2/8md_l^2$ is the recoil energy and V_0 the trap depth. In our case, the lattice depth at the transport start is given by $U_{\mathrm{latt}}(0) = 12.5\,\mu\mathrm{K}$ for Erbium, yielding a trap frequency of $\omega_l = 2\pi \cdot 215\,\mathrm{kHz}$ and a natural acceleration $a_{\mathrm{nat}} \approx 47\,\mathrm{m/s^2}$, about 17 times lower than $a_{\mathrm{latt,max}}$. The same phenomenon was observed in a Cesium transport setup [265], where accelerations of $4\,\mathrm{km/s^2}$ were achieved, also on the order of $12a_{\mathrm{nat,Cs}}$. However, the transport is also limited in time: a slow transport runs into losses for times that become comparable to the lifetime of trapped clouds of Erbium, measured at $200\,\mathrm{ms}$ on the starting point. Moreover, Lithium tends to provide higher transport efficiencies for high accelerations, on the order of $1.4\,\mathrm{km/s^2}$ [109]. To transport both species together (see Chapter 6), a compromise has to be found to get enough atoms in the cell.

Transport efficiency The roundtrip measurements are the only tool at our disposal for the initial transport beams' alignment. They are done by transporting the atoms to increasing distances, and back to the starting point. By mapping the transport time to the atoms' position, it is possible to know when they are lost and hence when the beams lose overlap. These measurements also proved necessary to estimate the survival of Erbium in transport, because of the poor imaging conditions in the glass cell mentioned before.

The measurements shown in Fig. 4.8c were obtained for three velocities: $1.17\,\mathrm{m/s}$, $2.77\,\mathrm{m/s}$ and $4.90\,\mathrm{m/s}$ (detuning of $2.2\,\mathrm{MHz}$, $5.2\,\mathrm{MHz}$, $9.2\,\mathrm{MHz}$ resp.), with a common acceleration of $370\,\mathrm{m/s^2}$ ($0.7\,\mathrm{MHz/ms}$). For these measurements, the travel time for a full roundtrip took $95\,\mathrm{ms}$, $180\,\mathrm{ms}$ and $430\,\mathrm{ms}$ respectively. The plots were normalized to the travelled distance and atom number at the start, extracted from exponential fits to the different curves. The fact that they all collapse on the same curve illustrates well the fact that our losses are mostly position-dependent. Mostly, because slowest transport shows a noticeably lower efficiency, for which the additional losses are simply due to its long holding time of $400\,\mathrm{ms}$, comparable to the trap lifetime of $450\,\mathrm{ms}$ at the starting point. In terms of atom losses, the three fits to the curve give a decay of:

$$\gamma_{1/e}(t) = 15 \cdot 10^3\,/\mathrm{s},\ 13 \cdot 10^3\,/\mathrm{s},\ \text{and}\ 6.5 \cdot 10^3\,/\mathrm{s}$$

for the fastest to slowest transports. However, normalized to the distance, the decays are:

$$\gamma_{1/e}(d) = 23 \cdot 10^3\,/\mathrm{cm},\ 26 \cdot 10^3\,/\mathrm{cm},\ \text{and}\ 49 \cdot 10^3\,/\mathrm{cm}$$

in the same order, where it becomes clear that the slowest transport has additional losses because of the longer holding time. The roundtrip efficiency of $25\,\%$ gives a single-way efficiency of $50\,\%$, which can be considered a low boundary to our current setup. Since the measurement was taken, several improvements were done to the setup, and one can expect the efficiency to be higher now, but would need to be remeasured to know the exact number.

Chapter 5

Species-selective trapping of Er-Li

5.1 Theory of dynamical polarizability

The concept of polarizability is of crucial importance in the field of matter-light interactions, as it encapsulates the response of a system to an electric field. In ultracold atoms experiments, the system under study is typically an ensemble of atoms (from several millions in many-body systems, down to single atoms in few-body systems), and the electric field is typically that of a laser beam. For example, Optical Dipole Traps (ODTs) are still one of the most important tools at the disposal of experimentalists to study low-energy physics, and their working principle relies entirely on this concept. As we shall explain in this chapter, the precise knowledge of an atom's electronic structure and its levels is instrumental in determining its polarizability. In turn, a good understanding of an atom's polarizability is a precious guide for any experiment, especially when it comes to the choice of a laser's wavelength depending on to its intended purpose.

5.1.1 Classical picture

The following considerations on the polarizability can be found in several textbooks, and here we broadly follow the approach taken in References [134, 266, 267]. In general, for an electric field $\mathbf{E}$, the system's induced dipole moment $\mathbf{p}$ can be written as:

$$\mathbf{p} = \alpha \mathbf{E} \tag{5.1}$$

where the polarizability α can be decomposed in two parts: static and dynamic. The static polarizability is a scalar quantity which characterizes the response of a system to a constant electric field. The dynamic polarizability characterizes the system's response to an oscillating field, and cannot be reduced to a scalar; in general, this quantity is complex and frequency-dependent. Two important quantities can be derived in a classical framework. First, the interaction potential between the induced dipole and the oscillating field $\mathbf{E}(\mathbf{r}, t) = \hat{e}\mathbf{E}(\mathbf{r})e^{-i\omega t} + c.c.$ is given by:

$$U_{\text{dip}}(\mathbf{r}) = -\frac{1}{2}\langle \mathbf{p} \cdot \mathbf{E} \rangle = -\frac{1}{2\epsilon_0 c}\mathfrak{Re}(\alpha) I(\mathbf{r}) \tag{5.2}$$

Second, by considering the light as a stream of photons $\hbar\omega$, one can also derive the scattering rate:

$$\Gamma_{\text{sc}}(\mathbf{r}) = \frac{\langle \dot{\mathbf{p}} \cdot \mathbf{E} \rangle}{\hbar\omega} = \frac{1}{\hbar\epsilon_0 c}\mathfrak{Im}(\alpha) I(\mathbf{r}) \tag{5.3}$$

In both equations, the brackets are the time average of the oscillating terms and $I = 2\epsilon_0 c|E|^2$ is the field intensity. As explained later, these two quantities are the basis of dipole-trapping, and depend on the real and imaginary part of the polarizability respectively.

At this point, there is no additional knowledge of the polarizability itself. An intuitive picture is drawn by the Lorentz model. This model is a simplistic approach to the description of an atom placed in an oscillating electric field, where the electron (of mass m_e and charge e) is elastically bound to the nucleus. Here, under the long-wavelength and far-field approximations, the equation of motion $\ddot{x} + \Gamma_\omega \dot{x} + \omega_0^2 x = -eE(t)/m_e$ is that of a damped oscillator with eigenfrequency w_0 and damping rate Γ_ω given by:

$$\Gamma_\omega = \frac{e^2\omega^2}{6\pi\epsilon_0 m_e c^3} \tag{5.4}$$

This damping stems from the emitted radiation as described by the Larmor formula and depends on the frequency ω of the driving field. The polarizability can be extracted from the integration of the equation of motion, and put in the commonly written form:

$$\alpha = \frac{e^2}{m_e}\frac{1}{\omega_0^2 - \omega^2 - \mathrm{i}\omega\Gamma_\omega} = 6\pi\epsilon_0 m_e c^3 \frac{\Gamma/\omega_0^2}{\omega_0^2 - \omega^2 - \mathrm{i}(\omega^3/\omega_0^2)\Gamma} \tag{5.5}$$

where $\Gamma \equiv \Gamma_{\omega_0} = (\omega_0/\omega)^2\Gamma_\omega$ is the damping rate on resonance. This approach, although (almost) fully classical, already provides a good description of the atom-light interaction, and captures many phenomena, such as absorption and refraction, or the different (Rayleigh, Thomson, and resonant) scattering regimes. It is now possible to use this expression of the polarizability to write the dipole potential and the scattering rates as:

$$U_{\mathrm{dip}}(\mathbf{r}) = -\frac{3\pi c^2}{2\omega_0^3}\left(\frac{\Gamma}{\omega_0 - \omega} + \frac{\Gamma}{\omega_0 + \omega}\right) I(\mathbf{r}) \tag{5.6}$$

$$\gamma_{\mathrm{sc}}(\mathbf{r}) = \frac{3\pi c^2}{2\hbar\omega_0^3}\left(\frac{\omega}{\omega_0}\right)^3 \left(\frac{\Gamma}{\omega_0 - \omega} + \frac{\Gamma}{\omega_0 + \omega}\right)^2 I(\mathbf{r}) \tag{5.7}$$

However, this description is limited to the perturbative case, where the saturation is avoided by either large detuning or small intensities. In the case of optical dipole traps, this conditions is verified since the light is far-detuned from any resonance, yet $|\Delta| = |\omega - \omega_0| \ll \omega_0$ is still fulfilled. Moreover, it allows one to make an important approximation, the so-called rotating-wave approximation. There, the counter-rotating term $\Gamma/(\omega_0 + \omega)$ can be neglected compared to the fast-rotating term $\Gamma/(\omega_0 - \omega)$, and the above expressions can be simplified to:

$$U_{\mathrm{dip}}(\mathbf{r}) = \frac{3\pi c^2}{2\omega_0^3}\left(\frac{\Gamma}{\Delta}\right) I(\mathbf{r}) \tag{5.8}$$

$$\gamma_{\mathrm{sc}}(\mathbf{r}) = \frac{3\pi c^2}{2\hbar\omega_0^3}\left(\frac{\Gamma}{\Delta}\right)^2 I(\mathbf{r}) \tag{5.9}$$

These two equations are key results when it comes to understanding the principle of dipole trapping. Indeed, atoms can be trapped in a potential and maintained a low temperature only if the heating rate, coming mostly from the scattering of light, is low enough. Here, the scaling plays in favor of a low ratio of scattering rate to trapping depth, since the dependence

on the detuning is not the same:

$$U_{\mathrm{dip}}(\mathbf{r}) \propto \frac{I(\mathbf{r})}{\Delta} \text{ and } \gamma_{\mathrm{sc}}(\mathbf{r}) \propto \frac{I(\mathbf{r})}{\Delta^2} \tag{5.10}$$

For far-detuned light, it means that a large potential can be reached, while the scattering (and hence) heating is kept low. Additionally, the sign of the detuning is also changing the trapping potential. For red-detuned light ($\Delta < 0$), the potential forms a well, where the energy is minimized at the highest intensity point. On the other hand, blue-detuned light ($\Delta < 0$) makes the dipole potential repulsive, and the energy is minimized at the lowest intensity point. While both situations can be used for ODTs, a blue-detuned trap requires more complicated beam shapes to collect atoms in a low-intensity region. This is typically made by using hollow beams or light sheets to create trapping potentials [268]. Interestingly, an ODT made with blue-detuned light can impart less heating on the atoms in certain circumstances. In a 3D harmonic trap, the ratio of heating rates is given by [134]:

$$\frac{\dot{T}_{blue}}{\dot{T}_{red}} = \frac{3\kappa}{2}\frac{k_B T}{|U_0|} \tag{5.11}$$

where U_0 is the trap depth at its center and κ a scaling factor depending on the trap geometry. This ratio shows that blue-detuned traps are advantageous in tight confinements ($|U_0| \gg k_B T$), or with uniform potentials where the boundaries are made with "hard walls" ($\kappa \ll 1$). However, the calculations made in [269] show that the heating rate is identical in the case of optical lattices. Finally, one also needs to consider the available technology for such traps, and more often than not, a red-detuned trap is easier to produce with high-power lasers, typically operating at $1064\,\mathrm{nm}$ with $10\,\mathrm{W}$ to $100\,\mathrm{W}$ of output power.

5.1.2 Quantum picture

A more precise picture can be obtained by a semi-classical treatment of the problem. Interestingly, the results from such a treatment yield the exact same results as the Lorentz model in the perturbative, non-saturated case. The only difference is the presence of an additional scaling factor on the force exerted on the electron, the so-called oscillator strength. However, if the system is strongly excited, the classical model cannot take into account saturation effects and its validity breaks down. A powerful model was established several decades ago, where the atom and laser photons are treated a one system: the dressed-states [270]. Starting with a *closed two-level* approximation for the atom, the Hamiltonian of the system is written as:

$$\hat{H} = \hat{H}_A + \hat{H}_F + \hat{V} \tag{5.12}$$

where the three terms are the Hamiltonians of the atom, of the field, and of the atom-field coupling respectively. Here, the coupling term connects the ground and excited states of the atom, and is treated as a perturbation. It takes the usual form $\hat{V} = e\hat{\mathbf{r}} \cdot \mathbf{E} = -\hat{\boldsymbol{\mu}} \cdot \mathbf{E}$ where $e\hat{\boldsymbol{\mu}} = -e\hat{\mathbf{r}}$ is the dipole operator. In the dressed-state picture, the eigenstates of the Hamiltonian are now a combination of the atomic internal state, and the number of photon in a mode of the field. They are usually written as $|g, n\rangle$ and $|e, n-1\rangle$, where the atom is in its ground or excited state, and the number of photons is either n or $n-1$. These states are bunched in manifolds of total energy $\mathcal{E}_n$, and the manifolds are separated by the energy

$\mathcal{E}_{n+1} - \mathcal{E}_n = \hbar\omega$ of a photon. However, the atom-light coupling connects the states of a given manifold, and thus induce an energy shift that can be calculated with second-order perturbation theory. For our two-level approach, the energy shift is given by:

$$\Delta E_{e,g} = \pm\frac{|\langle e|\hat{V}|g\rangle|^2}{E_e - E_g} = \pm\frac{|\langle e|\hat{\mu}|g\rangle|^2}{\hbar\Delta}\,|E|^2 \tag{5.13}$$

where the ground and excited states shift are given by the plus or minus sign respectively. An important precision is that with the coupling, the eigenstates are not the $|g, n\rangle$ and $|e, n-1\rangle$ anymore, but an admixture of them. Said another way, the atom stays in its ground state most of the time (due to low saturation), and the effective energy-shifted ground state becomes the relevant one for the potential felt by the atom. A second precision concerns the damping rate Γ derived in the classical picture. The Larmor formula cannot be applied anymore, and this rate must be determined another way. In this *two-level* framework, it is typically equated to the decay rate from the excited level [134, 266], and has to be calculated by the dipole matrix element of the driven transition:

$$\Gamma = \frac{\omega_0^3}{3\pi\epsilon_0\hbar c^3}|\langle e|\hat{\mu}|g\rangle|^2 \tag{5.14}$$

The energy shift can then be simplified further, and takes the form:

$$\Delta E_{e,g} = \pm\frac{3\pi c^2}{2\omega_0^3}\frac{\Gamma}{\Delta}I(\mathbf{r}) \tag{5.15}$$

This energy shift, also called "Stark shift" or "light shift", corresponds to the dipole potential already derived in Eq. (5.8). As it is dependent on the local intensity $I(\mathbf{r})$, one can understand why a gaussian beam creates a potential well with a gaussian shape. Finally, one can characterize the strength of the coupling between the two states with Rabi frequency Ω, which depends on the dipole operator as:

$$\Omega = \frac{\langle e|\hat{\mu}|g\rangle}{\hbar}|E| \tag{5.16}$$

and write the above expressions in their famous form:

$$U_{\text{dip}} = \frac{\hbar\Omega^2}{4\Delta} \tag{5.17}$$

and

$$\gamma_{\text{sc}} = \frac{\Gamma\Omega^2}{4\Delta^2} \tag{5.18}$$

As a last step, a more realistic description of the problem at hand requires a *multi-level atom* model to capture all the interesting aspects of dynamical polarizability. In that case, one needs to add the contributions to the energy shift from all individual upper states, in the sum-over-states approach. With our formalism, the principle can be expressed (for the ground state) as:

$$\Delta E_g = \sum_i \frac{|\langle e_i|\mu_i|g\rangle|^2}{E_i - E_g} = \frac{3\pi c^2}{2\omega_0^3}\sum_i \frac{\Gamma_i}{\Delta_i}I(\mathbf{r}) \tag{5.19}$$

and the last Eqs. (5.17) and (5.18) can be written as:

$$U_{\mathrm{dip}}^{(\mathrm{tot})} = \sum_i U_{\mathrm{dip}}^{(i)} = \sum_i \frac{\hbar\Omega_i^2}{4\Delta_{\mathrm{i}}} \tag{5.20}$$

and

$$\gamma_{\mathrm{sc}}^{(\mathrm{tot})} = \sum_i \gamma_{\mathrm{sc}}^{(i)} = \sum_i \frac{\Gamma\Omega_i^2}{4\Delta_i^2} \tag{5.21}$$

These equations contain all the ingredients necessary to have an intuitive understanding of the dynamical polarizability. Because we now take into account all excited states with their spontaneous decay rate, the situation becomes more complex than a simple two-level system with a single resonance. Instead, for a given laser wavelength, some levels will be blue- or red-detuned and their contributions will be shifting the atomic state energy to higher or lower energy. Naturally, such a shift happens for the atomic ground state, but to excited states as well. Several special cases can then emerge from this. For example, a *magic wavelength* corresponds to the situation where the ground state and an excited state are shifted by the exact same amount. This remarkable feature is typically exploited in high-precision systems such as atomic clocks [271]. A second special case, of particular interest here, is the *tune-out wavelength*: the polarizability's vanishing point, where all contributions from the different states cancel out and $\Delta E = 0$. The tune-out wavelength is specific to an atom's internal state, and corresponds to the wavelength at which the atom does not feel any light shift, thus any trapping potential. This feature can be used for state-dependent or species-dependent traps, as explained in Section 2.3.1. Here, this chapter focuses on the measurement of Erbium's tune-out wavelength close to its $841\,\mathrm{nm}$ transition.

In the most general case, where the laser light is elliptically polarized with the unit vector polarization **e**, the dipole potential can be written as [162, 272]:

$$\begin{aligned} U(\mathbf{r},\theta_p,\theta_k,\mathcal{A},\omega) &= -\frac{1}{2\epsilon_0 c} I(\mathbf{r}) \mathfrak{Re}(\alpha_{tot}) \\ &= -\frac{1}{2\epsilon_0 c} I(\mathbf{r}) \Bigg[\mathfrak{Re}(\alpha_s(\omega)) + \mathcal{A}\cos(\theta_k)\frac{m_J}{2J}\mathfrak{Re}(\alpha_v(\omega)) \\ &\quad + \frac{3m_J^2 - J(J+1)}{J(2J-1)} \cdot \frac{3\cos^2(\theta_p)-1}{2} \mathfrak{Re}(\alpha_t(\omega)) \Bigg] \end{aligned} \tag{5.22}$$

where $|\mathbf{e}\cdot\mathbf{e}_z|^2 = \cos^2(\theta_p)$, θ_k is the angle between z and the wave vector **k**, $\mathcal{A}$ is the ellipticity parameter, and m_J is the magnetic sublevel of the atom. The scalar, vectorial and tensorial components of the polarizability were noted as α_s, α_v, α_t and are given by:

$$\begin{aligned} \alpha_s(\omega) &= -\sqrt{\frac{1}{3(2J+1)}}\alpha_J^{(0)}(\omega), \\ \alpha_v(\omega) &= +\sqrt{\frac{2J}{(J+1)(2J+1)}}\alpha_J^{(1)}(\omega), \\ \alpha_t(\omega) &= +\sqrt{\frac{2J(2J-1)}{3(J+1)(2J+1)(2J+3)}}\alpha_J^{(2)}(\omega), \end{aligned} \tag{5.23}$$

with

$$\begin{aligned}\alpha_J^{(K)}(\omega) =& \sqrt{2K+1} \times \sum_{J'} (-1)^{J+J'} \\ &\times \begin{Bmatrix} 1 & K & 1 \\ J & J' & J \end{Bmatrix} |\langle J'||\mathbf{d}||J\rangle|^2 \\ &\times \frac{1}{\hbar}\mathrm{Re}\left[\frac{1}{\Delta^-_{J'J} - i\gamma_{J'}/2} + \frac{(-1)^K}{\Delta^+_{J'J} - i\gamma_{J'}/2}\right].\end{aligned} \tag{5.24}$$

Here, the sum includes all dipole allowed transitions from J to J' ($\Delta J = \pm 1, 0$), the curly brackets matrix denotes the Wigner 6-j symbol, $\gamma_{J'}$ is the excited state natural line width and $\Delta^{\pm}_{J'J} = \omega_{J'J} \pm \omega$ is the detuning from the $J \to J'$ transition.

The three components of the polarizability can be intuitively understood as follows. The scalar part depends only on the light's frequency, and has a fully isotropic character; it does not depend on the field polarization or direction and shifts all atomic states m_J identically. The vector part depends on the atomic sublevel m_J and on the light's ellipticity, and two cases must be distinguished. When the light is linearly polarized, the vector shift is the same for all m_J states and no light shift is induced; this part vanishes. When the light is circularly polarized, the vector shift is not identical for the m_J states, and the light lifts their degeneracy, thus behaving as a "fictitious magnetic field" [273]. Finally, the tensor part contains the anisotropy [266]: it depends on the angle θ_p between the atom's quantization axis and the polarization axis, but also on the quantum numbers J and m_J^2.

5.1.3 The case of Erbium-Lithium

With the above considerations, it becomes easy to understand why Er and Li have dramatically different polarizabilities. To begin with, some remarks can be made on the different polarizability contributions. First, the vector part requires $J \geq 1/2$ and the tensor part $J \geq 1$ to be non-zero. This is relevant for many cases. For example, atoms in a $J = 0$ state (such as Sr, Yb or noble gases in their ground state) only have the scalar contribution to their dynamical polarizability [141]. For atoms in a $J = 1/2$ state (such as alkali in their ground state), the tensor part is vanishing due to the Wigner 6-j symbol, and only the scalar and vector components are present. Second, like most experiments, our measurements were done with linearly polarized light (see Section 5.2.2). It means that for Li, the only contribution to the polarizability is scalar. In contrast, Er has a complex electronic configuration, with a submerged shell where the $4f^{12}$ shell is open while the $6s^2$ shell is closed, resulting in a $J = 6$ ground state. The highly non-isotropic electronic distribution gives rise to a very rich atomic spectrum, with transitions ranging from the Hz to the MHz scale. Having such a large angular momentum also explains the strong magnetic properties of Er, and its strong tensor polarizability [272, 274]. Their respective polarizabilities, in this context, can thus be simplified to:

$$U_{\mathrm{Li}}(r, \theta_p, \omega) = -\frac{1}{2\epsilon_0 c} I(r) \mathfrak{Re}(\alpha_s(\omega)) \tag{5.25}$$

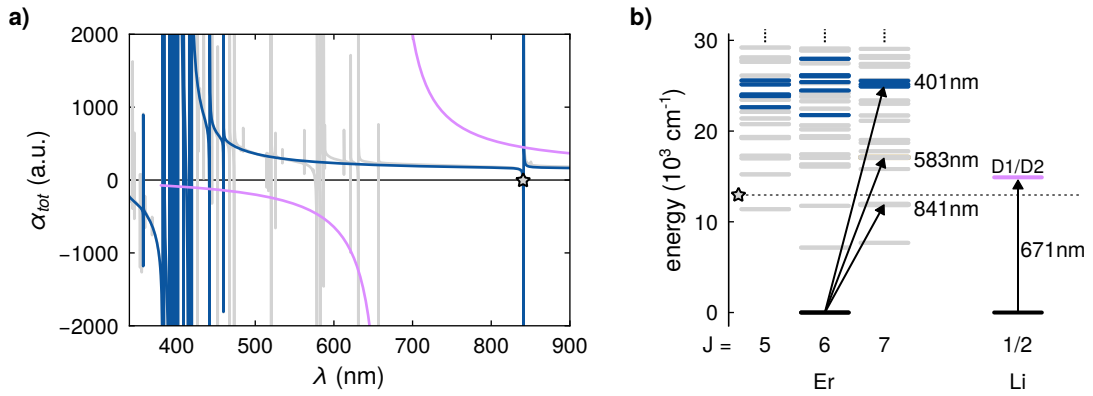

Figure 5.1 | Dynamical polarizability of Er and Li. a) The calculated polarizabilities of Er (grey, blue) and Li (pink) are calculated for the $350\,\mathrm{nm}$-$900\,\mathrm{nm}$ range. The full polarizability of Er (grey) is obtained when accounting for all transitions; the filtered polarizability (blue) is calculated after keeping only the wide UV transitions and the narrow transition at $841\,\mathrm{nm}$. **b)** Atomic levels involved in the calculated polarizability of Er (left) and Li (right), where the colors correspond to the lines on figure a). The main transitions, typically used for laser cooling, are indicated with arrows. The tune-out wavelength of interest is indicated by the star symbol on both figures.

and

$$U_{\mathrm{Er}}(r,\theta_p,\omega) = -\frac{1}{2\epsilon_0 c} I(r)\left[\mathfrak{Re}(\alpha_s(\omega)) + \frac{3\cos^2(\theta_p)-1}{2}\mathfrak{Re}(\alpha_t(\omega))\right] \tag{5.26}$$

where the prefactor $\frac{3m_J^2 - J(J+1)}{J(2J-1)} = 1$ for Er in its ground state $|J=6, m_J=-6\rangle$.

The difference between Er and Li is best illustrated with the calculations of their respective dynamical polarizability, shown in Fig. 5.1. These calculations were done based on Eqs. (5.25) and (5.26), with the theoretical data of Er from [162], where experimental values for the $401\,\mathrm{nm}$ [165], $583\,\mathrm{nm}$ [275] and $841\,\mathrm{nm}$ [48] transitions were included. The polarizability of Li was taken from [161]. There, the difference between these atoms is striking: while Lithium has only one transition at $671\,\mathrm{nm}$ and a corresponding broad divergence in its polarizability, Erbium has a very rich spectrum, where transitions are grouped mostly in the UV or blue range, from $350\,\mathrm{nm}$ to $480\,\mathrm{nm}$, as well as around $580\,\mathrm{nm}$ and $630\,\mathrm{nm}$. It is also clear that Er's spectrum is governed by its wide transitions at $400\,\mathrm{nm}$, as represented in Fig. 5.1. On the left figure, the grey line is the calculated polarizability of Er based on all transitions and states currently known. The blue line is based on a filtered set of transitions, for which the Einstein coefficient is larger than the threshold: $A_{\mathrm{ij}} > 2\cdot 10^6\,\mathrm{s}^{-1}$ and to which the $841\,\mathrm{nm}$ was added manually. Such a selection highlights two important features. First, the global envelope of Er's polarizability, with its divergence around $400\,\mathrm{nm}$ and similar to that of Li, becomes clearly visible. Second, it also shows that the tune-out wavelength, close to Er's $841\,\mathrm{nm}$ transition, is also mostly determined by the UV/blue transitions and the nearby infrared transition.

Finally, it also displays why ErLi is an interesting platform for species-selective trapping, as mentioned already in Section 2.3.1. On the one hand, although Er's tune-out seems close to its $841\,\mathrm{nm}$ transition, the linewidth is quite narrow, at $\Gamma_{841} = 2\pi\cdot 8\,\mathrm{kHz}$. In comparison, the tune-out wavelength is expected to be found at a blue-detuning of $|\Delta| \gtrsim 100\,\mathrm{GHz} \approx 10^7\cdot\Gamma_{841}^{\mathrm{Er}}$.

For such a detuning, the scattering rate is very low, on the order of $\gamma^{\mathrm{Er}} = 10\,\mathrm{mHz}$. On the other hand, the tune-out is also located far away from the Li D_1 and D_2 transitions at $671\,\mathrm{nm}$, at a red -detuning of $|\Delta| \gtrsim 10^7 \cdot \Gamma^{\mathrm{Li}}_{671}$. At this wavelength, Li atoms can thus be trapped in an ODT with a low scattering rate of $\gamma^{\mathrm{Li}} \approx 10\,\mathrm{mHz}$ as well, providing favorable conditions for a species-selective trap.

5.2 Experimental setup

The experimental setup used to measure Erbium's tune-out was designed in a way such that, after reaching degeneracy, the Erbium BEC and the Lithium DFG would have significant overlap. The Erbium cloud would be trapped in a $1064\,\mathrm{nm}$ ODT, and the Lithium cloud in a $841\,\mathrm{nm}$ ODT operating on the tune-out wavelength. This configuration requires careful planning, to determine adequate trap shapes so that the condensed Bose gas does not shrink to a small fraction of the Fermi gas' volume.

5.2.1 Designing the optical traps

Erbium trap The first step is to determine the Erbium trap's shape, based on the available laser power and final BEC size, when the Er atoms form a pure condensate with $T = 0\,\mathrm{K}$. An important criterion for that trap was that it should be tight enough to confine against gravity even at low intensity, to allow evaporation without any helping measure (such as magnetic levitation) while maintaining good overlap with the superimposed Lithium cloud. Although many beam sizes had to be considered, Fig. 5.2 shows the calculated characteristics of the trap for two beams overlapping at $90\,°$, with $1/e$-waists of $w_{\mathrm{v,h}} = 35 \times 590\,\mu\mathrm{m}$. There, the trapping potential is calculated for different laser powers, where one can see the significant tilt due to gravity. When lowering the laser power from $10\,\mathrm{W}$ to $5\,\mathrm{W}$ per beam to evaporate Erbium, the trap becomes very shallow and its local minimum shifts to lower positions, from $z = -5\,\mu\mathrm{m}$ to $z = -13\,\mu\mathrm{m}$. For a pure BEC, a good way to evaluate the trap depth is by comparing it to the cloud's chemical potential. As a rule of thumb, a good relative depth for an ODT is given by $U/\mu \approx 10$ for efficient loading without heating, and $U/\mu \gtrsim 1$ to keep atoms in a shallow trap. If the trap depth is less than the chemical potential, the atoms are not trapped anymore and start to spill out. The relative trap depth was calculated here for clouds of 10^3, 10^4, and 10^5 Erbium atoms. Assuming a pure BEC, the chemical potential can be calculated with [276]:

$$\mu_{\mathrm{Er}} = \frac{\hbar\bar{\omega}}{2}\left(\frac{15Na_{\mathrm{s}}}{a_{\mathrm{ho}}}\right)^{2/5} \tag{5.27}$$

where $\bar{\omega} = (\omega_x\omega_y\omega_z)^{1/3}$ is the mean trap frequency, a_{s} is the Er-Er scattering length (set to $100a_0$ in the calculations) and $a_{\mathrm{ho}} = \sqrt{\hbar/m\bar{\omega}}$ is the harmonic oscillator length. Here, the mean trap frequency was calculated for all laser powers by approximating the real, anharmonic potential with a local harmonic trap. The relative trap depth decreases quickly when the laser power goes below $P = 6\,\mathrm{W}$, and completely opens at $P = 4.8\,\mathrm{W}$.

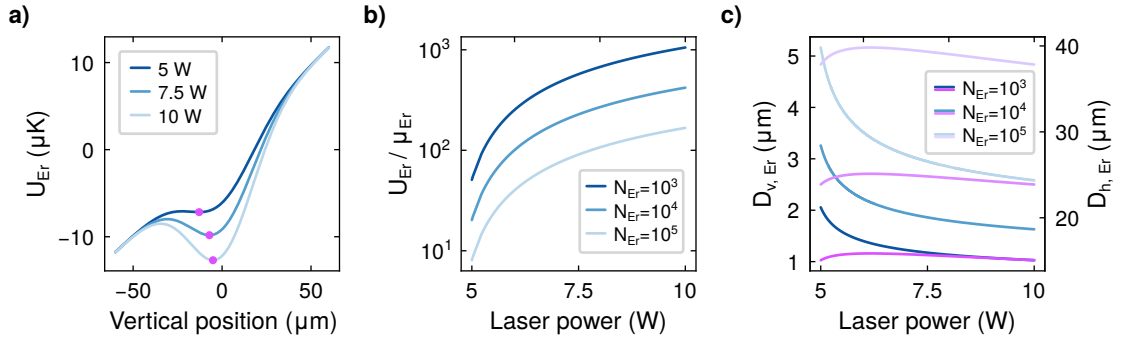

Figure 5.2 | Design of the Erbium trap. a) Total trap potential, for crossed trapping beams of $30 \times 590\,\mu\mathrm{m}$ waists, and $10\,\mathrm{W}$ (light blue) down to $5\,\mathrm{W}$ (dark blue) per beam. The tilt is due to gravity and leads to gravitational sag, visible here as the displacement of the trap minimum (pink dots). **b)** Relative trap depth (scaled to the chemical potential) for various atom numbers in the BEC. **c)** BEC diameters in vertical (blue, left axis) and horizontal (pink, right axis) directions. The cloud size scales weakly with N_{Er}, so the trap can be used for large ranges of atom numbers.

The resulting cloud size can now be calculated, in the Thomas-Fermi approximation, with [276]:

$$R_{\mathrm{i}}^{\mathrm{Er}} = \sqrt{\frac{2\mu}{m_{\mathrm{Er}}}}\frac{1}{\omega_{\mathrm{i}}} \tag{5.28}$$

where i denotes the different radii for a non-isotropic trap. With this trap geometry, an Erbium BEC would have diameters ranging from $\mathrm{D_{v,h}} = (2 \times 15)\,\mu\mathrm{m}$ for 10^3 atoms, to $\mathrm{D_{v,h}} = (5 \times 35)\,\mu\mathrm{m}$ for 10^5 atoms.

Lithium trap The Lithium trap was designed in parallel with the Erbium trap, to ensure that the Fermi gas inside would not keep a much larger diameter than the Erbium BEC because of the Fermi pressure. Just like the previous paragraph, only the calculations with the final values for the trap are shown here. The approach was to make the Lithium trap with a dimple beam, focused to small waists to reach high intensities and strong confinement. The notion of dimple is clear when looking at the calculated trapping potentials shown in Fig. 5.3. There, the potential is the sum of the $1064\,\mathrm{nm}$ and $841\,\mathrm{nm}$ beams, with the dimple beam focused to $1/e$-waists of $w_{\mathrm{v,h}} = 5 \times 20\,\mu\mathrm{m}$. Thanks to the larger polarizability of Li at $841\,\mathrm{nm}$ compared to $1064\,\mathrm{nm}$ ($\alpha_{841}^{\mathrm{Li}} \approx 2 \cdot \alpha_{1064}^{\mathrm{Li}}$), the tight focus of the dimple beam provides a very strong confinement compared to the large $1064\,\mathrm{nm}$ beams. The relative trap depth was also determined, although for the dimple beam alone. Indeed, if the dimple is not deep enough compared to the DFG's chemical potential, the atoms would start to spread in the large ODT and degeneracy would not be achieved. The relative trap depth is defined here as the ratio of the trap depth over the Fermi energy, which is the natural energy scale for a non-interacting, spin-polarized Fermi gas. Thanks to the combination of larger polarizability and tight focus, the power requirements are rather low: for a realistic atom number $N_{\mathrm{Li}} = 10^4$ in the DFG, the dimple is still dominating over the large ODT down to $P \approx 7\,\mathrm{mW}$.

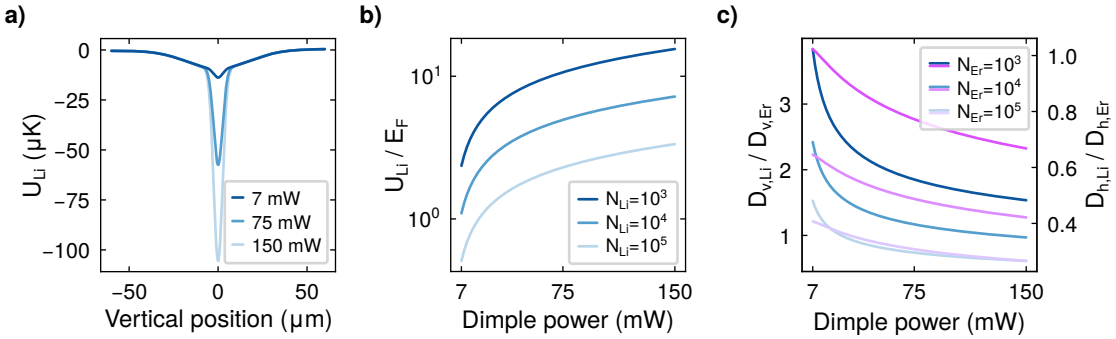

Figure 5.3 | Design of the Lithium trap. a) Total trap potential, for a dimple beam of $5 \times 20\,\mu\mathrm{m}$ waists, and $150\,\mathrm{mW}$ (light blue) down to $7\,\mathrm{mW}$ (light blue). The dimple beam is superimposed with the Erbium trap, here at $5\,\mathrm{W}$ per beam. The gravitational tilt, although present on this image, is clearly weaker than for Erbium. **b)** Relative trap depth (scaled to the Fermi energy) for various atom numbers in the DFG. **c)** DFG diameters in vertical (blue, left axis) and horizontal (pink, right axis) directions, scaled to the previously calculated Erbium BEC size. The horizontal size is given only for the tightly-confining axis of the dimple (see text). With these trap sizes, the DFG is larger than the BEC in the vertical direction, but smaller in the tight horizontal direction.

Similarly as Erbium, the Lithium cloud size is calculated, in the degenerate limit, according to [131]:

$$R_i^{\mathrm{Li}} = \sqrt{\frac{2E_F}{m_{\mathrm{Li}}}}\frac{1}{\omega_i} \tag{5.29}$$

where μ is assimilated to the Fermi energy $E_F = \hbar\bar{\omega}(3N_{\mathrm{Li}})^{1/3}$, i denotes the different spatial axes and ω_i the associated trap frequency. The calculated DFG size is shown on Fig. 5.3, scaled to the BEC size. It is given only for the tightly-confining axis of the dimple beam, and not for the weakly-confining axis along the beam's propagation direction. In the latter case, the Li DFG is expected to be much larger than the Er BEC because the trap confinement is given by the Rayleigh length of $z_R = 1.5\,\mathrm{mm}$. To maintain a full overlap of the clouds, a second beam would be required to close the weakly-confining axis, and constrict the Li cloud in a smaller volume. As expected, the Fermi pressure maintains the DFG in a more spherical shape than the BEC even with the large aspect ratio of the traps. Here, the vertical diameter is larger than the BEC, from a ratio of $D_{\mathrm{v,Li}} = 3.8 \cdot D_{\mathrm{v,Er}}$ for $N_{\mathrm{Er}} = 10^3$, to $D_{\mathrm{v,Li}} = 1.5 \cdot D_{\mathrm{v,Er}}$ for $N_{\mathrm{Er}} = 10^5$. However, on the horizontal plane the ratio is inverted, with $D_{\mathrm{h,Li}} = 0.65 \cdot D_{\mathrm{h,Er}}$ for $N_{\mathrm{Er}} = 10^3$, to $D_{\mathrm{v,Li}} = 0.25 \cdot D_{\mathrm{h,Er}}$ for $N_{\mathrm{Er}} = 10^5$. Here, the realistic number of $N_{\mathrm{Er}} = 10^4$ provides a satisfying overlap of the clouds, where the thermalization can be expected to occur via sympathetic cooling.

5.2.2 Implementing the optical traps

The two traps were built in the glass cell, to hold the atoms after being transported from their respective MOT chambers. The setup is represented in Fig. 5.4. The large $1064\,\mathrm{nm}$ crossed ODT was made by shining two beams of waists $(w_{\mathrm{h}}, w_{\mathrm{v}}) = (590 \times 35)\,\mu\mathrm{m}$, at an angle of $55\,^\circ$ and with up to $10\,\mathrm{W}$ per beam. The interferences were suppressed by using two different diffraction orders from AOMs used for intensity control, for a total frequency shift

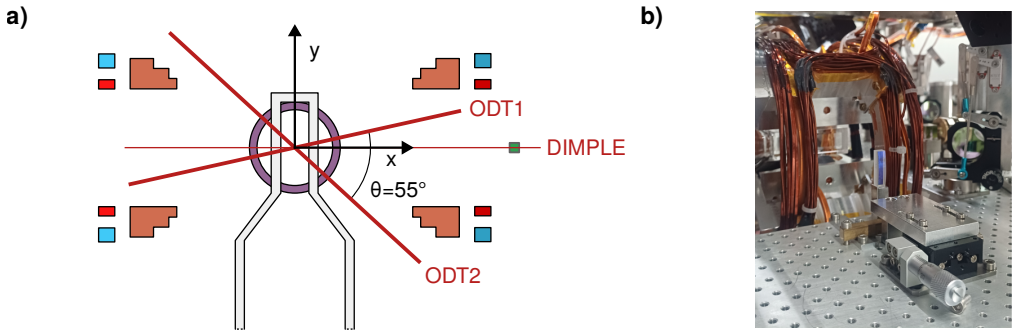

Figure 5.4 | Tune-out measurement setup. **a)** Cut, top view from the glass cell with the trapping beams. "ODT1" and "ODT2" are the elliptical $1064\,\mathrm{nm}$ ODT beams used for the large trap. "DIMPLE" is the $841\,\mathrm{nm}$ tight beam used to find Erbium's tune-out wavelength. The various coils (Feshbach: orange, offsets: red and blue, cut lens: green) around the experiment are also drawn. **a)** Cut lens placed closed to the glass cell, to tightly focus the dimple beam. Finding the focal point required a precise positioning with the translation stage to maximize the trap frequencies.

of $150\,\mathrm{MHz}$. However, one of the ODT beams is is freqeucny-shifted in the same direction as the transport beams and they can interefere together, leading to undesired heating. The heating was detected by lifetime measurements, which indicated a suppression of the interferences for a detuning $\Delta \geq 15\,\mathrm{MHz}$ between the ODT and transport beams. More details on the optical setup can be found in Section 3.3.6.

The dimple trap simply consists of a single beam, derived from the TiSa laser with the setup explained in Section 3.3.5. This beam is focused to waists of $(w_\mathrm{h}, w_\mathrm{v}) = (21 \times 5)\,\mu\mathrm{m}$, by going through the various telescopes placed on the path, and focused to its final values by a "cut lens" placed approximately $10\,\mathrm{cm}$ away from the glass cell. The lens has a focal length of $100\,\mathrm{mm}$, and was cut on the sides to minimize its footprint and the amount of blocked optical access. A picture of the lens and its mounting stage is shown in Fig. 5.4. The micrometer stage used to align the focus of the beam is also visible here, as well as the glass cell in the background. This lens is also used for an imaging path for both Er and Li, with a large magnification for good detection of clouds after the transport or with very short time of flights (TOF). However, this imaging axis is rarely used, since the usual TOF required for temperature measurements imply that the clouds are not imaged on the camera chip anymore.

5.3 Measurements

5.3.1 Experimental sequence

All the measurements performed in the glass cell and reported here were performed on the individual species, without using a mixture. Because the goal was to measure the tune-out wavelength and its (non-) dissipative effects, using a mixture was not necessary and would only add a layer of complexity for no substantial gain. The following subsection goes over the experimental sequences used for both species. For Erbium, more information on each of

the steps can be found in their dedicated sections in Chapter 4. For Lithium, the cooling and transport steps can be found described in the companion thesis [109].

Erbium sequence The procedure used for Erbium follows the standard approach [177, 189] for this species, and differs slightly from the sequence explained in Section 4.2.2 in the transport step. We describe the sequence from the point where the Er atoms are trapped in their ODT, with the additional contribution of high-power transport beam. To transport the atoms in the glass cell, the second transport beam is ramped up to $30\,\mathrm{W}$ to form a 1D-lattice. Then, the ODT is ramped down in $50\,\mathrm{ms}$ and the atoms are moved into the cell, over $50\,\mathrm{cm}$ in $165\,\mathrm{ms}$ by detuning one of the transport beam. The acceleration is done in $9.6\,\mathrm{ms}$ to a maximum detuning and velocities of $6\,\mathrm{MHz}$ and $3.2\,\mathrm{m/s}$. The corresponding acceleration of $333\,\mathrm{m/s^2}$, lower than the natural acceleration $a_{\mathrm{nat}} = 47\,\mathrm{m/s^2}$ introduced earlier (see Section 4.2.2). Finally, the atoms are transferred in the elliptical ODT presented in the previous section. The transfer is made by ramping up the ODT power in $10\,\mathrm{ms}$, followed by a ramp down of the transport beams power in $400\,\mathrm{ms}$. Once the lattice gone, the magnetic fields are also transferred from the racetracks to the cell coils, with simultaneous ramps of $200\,\mathrm{ms}$. This transfer requires careful compensation of the magnetic fields, to prevent the Erbium atoms from being pulled to the side of the trap by a stray magnetic gradient. Because the trap is weakly confining in the horizontal plane, even a small gradient of $1\,\mathrm{G/cm}$ is enough to pull a significant fraction of the atoms out of the trap. The compensation is done by two offset coils (along the x-axis of Fig. 5.4) driven by independent power supplies to provide both offset and gradient. The vertical confinement is strong enough to switch off the levitation field, and the vertical offset is reduced to $4.9\,\mathrm{G}$ in order to prevent the magnetic zero from crossing the atomic cloud. With this sequence, the atoms are loaded in the elliptical ODT at a temperature of $T_{\mathrm{Er}} \approx 1\,\mu\mathrm{K}$, and the tune-out measurements can be done.

Lithium sequence The preparation sequence of Lithium follows closely that of Erbium. First, the MOT is loaded from a decreasing-field Zeeman slower, where the end part of the ZS field matches the MOT gradient. Both are operating on the D_2 line of Li at $671\,\mathrm{nm}$. One particularity of the setup is the presence of an additional Transversal Cooling (TC), at the oven's output and before the ZS. This transversal cooling operates on the D_1 line, and optically pumps (OP) the atom in their $|F, m_F\rangle = |3/2, -3/2\rangle$ state. This state is the only state addressed by the ZS and as such, with the combination of OP and TC, a MOT loading rate of $2 \cdot 10^7$ atoms/s was observed. After loading the MOT for $5\,\mathrm{s}$, the compression happens over $60\,\mathrm{ms}$ and the cMOT is held for $20\,\mathrm{ms}$ of thermalization. At that point, the cMOT hold approximately 10^8 atoms, cooled down to $300\,\mu\mathrm{K}$.

The atoms are transferred in a $1070\,\mathrm{nm}$ multimode ODT, produced by two beams overlapping at a small angle of $10\,^\circ$, focused to waist of $65\,\mu\mathrm{m}$ and with $150\,\mathrm{W}$ each. One of the transport beam is also added to the trap, although its contribution is small compared to the ODT itself. The Lithium cloud is then a spin mixture of $|F, m_F\rangle = |1/2, \pm 1/2\rangle$ (usually denoted $|1\rangle$ and $|2\rangle$), and is cooled down by evaporation at $320\,\mathrm{G}$, with a laser power ramp down in $3\,\mathrm{s}$. Here, a full evaporation already reaches the degenerate regime. However, the second transport beam is ramped up in power $200\,\mathrm{ms}$ before the end of the evaporation to

load the lattice, and the atoms are transported in the glass cell. The transport is done over $1\,\mathrm{m}$, and takes $112\,\mathrm{ms}$.

When the atoms arrive in the cell, their population in the $|1/2,-1/2\rangle$ state is transferred to the $|3/2,-3/2\rangle$ by a rapid adiabatic passage. The transfer is made with a $100\,\mathrm{kHz}$-wide RF-field sweep in $25\,\mathrm{ms}$, at a field of $3.4\,\mathrm{G}$. These states, usually denoted $|1\rangle$ and $|3\rangle$, have more favorable scattering properties, and it makes it possible to load the same elliptical $1064\,\mathrm{nm}$ trap as for Erbium without going to the required high fields ($320\,\mathrm{G}$ or $600\,\mathrm{G}$ and higher) for the $|1\rangle$-$|2\rangle$ mixture. Once in the favorable mixture for scattering, the lattice is ramped down in $10\,\mathrm{ms}$, followed by the dimple ramp up over $3\,\mathrm{s}$. Finally, the ODT is ramped down in $100\,\mathrm{ms}$, and the Lithium atoms are held in the dimple trap only, at a final temperature of $T_{\mathrm{Li}} \approx 10\,\mu\mathrm{K}$.

5.3.2 Parametric heating and tune-out detection

Several methods can be used to locate a tune-out wavelength for an atom. A commonly used technique is Kapitza-Dirac diffraction [143, 144, 150, 152, 154], where the atoms are placed in an optical lattice and the number of atoms diffracted by Bragg scattering is measured. At the tune-out wavelength, no side-peaks can be observed on the long TOF measurements. However, to be applied to Erbium atoms, this technique requires the atoms to be in a BEC state, otherwise their thermal spread is too fast to resolve the side peaks reliably. Other tune-out measurements have been performed with different approaches, such as interferometry [147, 151] or direct measurement of the trap frequency [277]. In our setup, the natural choice was to measure the tune-out via parametric heating, a technique relying on periodic modulation of the trapping potential[141, 155, 277, 278]. In this approach, the trap is modulated at its resonant heating frequency to induce atom losses during the long modulation time. The tune-out is identified as the point where the modulation vanishes for the atoms, and the losses are minimized. The main advantages of this technique are its long integration times and reduced systematic effects compared to the atom interferometers, as well as its low technical complexity.

Owing to our trapping configuration, measuring the trap frequency was rather straightforward. The results presented in Fig. 5.5 are atom loss spectroscopy measurements, where the trap and tune-out frequencies were detected. First, after trapping the Erbium atoms in the $1064\,\mathrm{nm}$ elliptical ODT, the dimple beam was turned on for $1\,\mathrm{s}$ with a full-amplitude modulation (from 0 to $500\,\mathrm{mW}$) at different modulation frequencies. Away from the tune-out, the observed trap frequency, visible in Fig. 5.5 with its first two harmonics, was located at $280\,\mathrm{Hz}$. Second, the tune-out frequency was identified for a given angle θ_p between the atoms' quantization axis (magnetic field) and the linearly-polarized dimple light. It was done by modulating the dimple beam at the trap frequency to resonantly heat the Erbium cloud for $5\,\mathrm{s}$, and measuring the losses. The tune-out is extracted by applying a gaussian fit to the atom survival signal to know precisely where the atom losses are minimized. Once the tune-out located, it was possible to confirm it by performing the measurement of the trap frequency again. As expected, and visible in Fig. 5.5, the measurement changes qualitatively, and no resonance is visible anymore when the dimple is set on the tune-out. The position of the tune-out was also measured for different intensities of the $1064\,\mathrm{nm}$ trap, and it could be confirmed experimentally that the tune-out results were independent of this parameter.

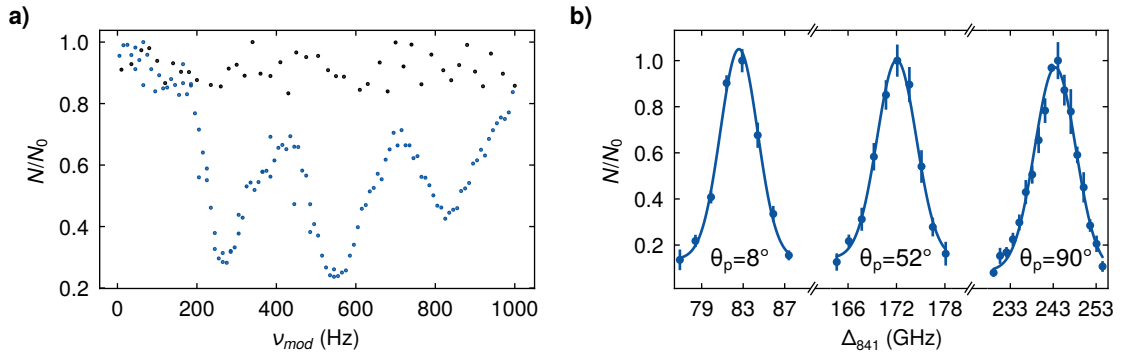

Figure 5.5 | Detection of Erbium's tune-out wavelength. a) Parametric heating of Erbium in the $1064\,\mathrm{nm}$ elliptical ODT by the $841\,\mathrm{nm}$ dimple. Away from the tune-out (blue dots), the measured trapped atom number shows minima at three modulation frequencies, corresponding to the $1064\,\mathrm{nm}$ trap frequency at $280\,\mathrm{Hz}$ and its first two harmonics at $560\,\mathrm{Hz}$ and $840\,\mathrm{Hz}$. On the tune-out (black dots), no additional atom loss is observed and the noise is attributed to experimental instabilities. **b)** Tune-out detection for various angles θ_p. The maximal atom number for each set of measurements (all normalized here) determines the frequency of the tune-out for the given θ_p. This number is determined by a gaussian fit (blue line) of the data to each set separately. The detuning value is given with respect to the $841\,\mathrm{nm}$ transition.

5.3.3 Anisotropy of the tune-out

The tune-out anisotropy was measured by repeating the previous experiments with varying θ_p. Three sets of measurement, done at $\theta_p = 8\,^\circ, 52\,^\circ$ and $90\,^\circ$, are presented in Fig. 5.5. These measurements, obtained for a total of 9 angle values, are summarized in Fig. 5.6. On this figure, the tune-out frequency is drawn as a function of the angle θ_p and shows the expected anisotropic behaviour. It was measured to be in a range of $\Delta_0 = 80\,\mathrm{GHz}$ to $\Delta_{90} = 245\,\mathrm{GHz}$ for $\theta_p = 0\,^\circ$ to $90\,^\circ$, blue-detuned from the $841\,\mathrm{nm}$ transition. However, the measured values show a discrepancy with the theoretical calculations of the tune-out wavelength, especially at large angles. To quantify the mismatch between theory and experiment, the different contributions to the total polarizability are written explicitly as:

$$\alpha_\mathrm{s} = \frac{\alpha_{\mathrm{s},841}}{\Delta} + \alpha_{\mathrm{s},0} \tag{5.30}$$

and

$$\alpha_\mathrm{t} = \frac{\alpha_{\mathrm{t},841}}{\Delta} + \alpha_{\mathrm{t},0} \tag{5.31}$$

where the subscripts 841 and 0 denote the contributions of the nearby $841\,\mathrm{nm}$ line and the "background" contribution from all other (far-detuned) transitions respectively. This approximation is reasonable since the background contribution of all distant lines is essentially constant over the range of interest. The tune-out condition can then be formulated as:

$$\Delta_\theta = -\frac{\alpha_{\mathrm{s},841} + \frac{1}{2}\left(3\cos\theta^2 - 1\right)\alpha_{\mathrm{t},841}}{\alpha_{\mathrm{s},0} + \frac{1}{2}\left(3\cos\theta^2 - 1\right)\alpha_0} \tag{5.32}$$

which corresponds to the condition where the local contribution of the nearby line is exactly cancelled by the "background" contribution from the other lines. Fitting this equation to the

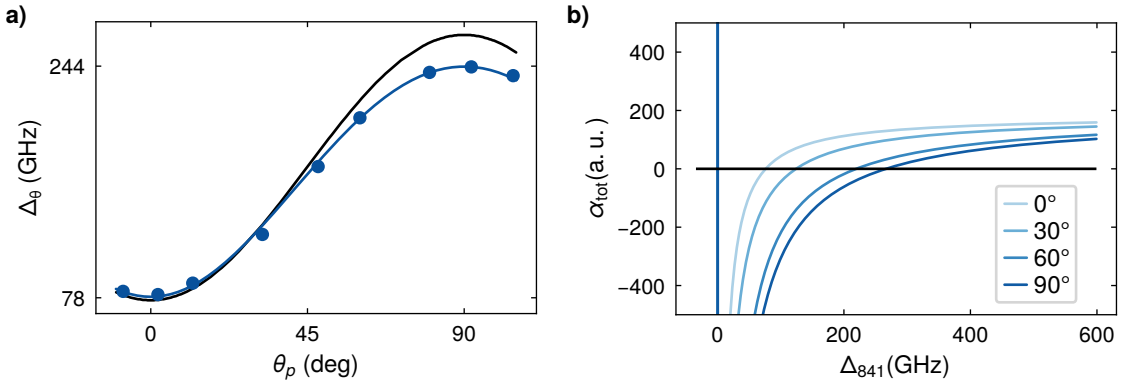

Figure 5.6 | Anisotropy of Erbium's tune-out and polarizability. a) Angular dependence of the tune-out wavelength. The tune-out wavelength measurements (blue dots) are extracted from several sets of measurements (partially shown in Fig. 5.5) and fitted with Eq. (5.32) (blue line). The theoretical plot (black line) shows good agreement with the small angles, but significant deviation for large angles. The discrepancy was attributed to an incorrect knowledge of the tensor part of the polarizability (see text). The detuning value is given with respect to the $841\,\mathrm{nm}$ transition. **b)** Calculated polarizability of Erbium close to the $841\,\mathrm{nm}$ transition for various θ_p angles. The zero-crossing shift corresponds to the change in tune-out wavelength shown in a).

measurements yields $\alpha_{s,0} = (193 \pm 5)\,\mathrm{a.u.}$ and $\alpha_{t,0} = (-17 \pm 0.4)\,\mathrm{a.u.}$, with $1\,\mathrm{a.u.} = 4\pi\epsilon_0 a_b^3$, where a_b is the Bohr radius. In comparison, the theoretical predictions of $\alpha_{s,0}^{\mathrm{th}} = 184\,\mathrm{a.u.}$ and $\alpha_{s,0}^{\mathrm{th}} = -1.6\,\mathrm{a.u.}$ show a good agreement for the scalar part, but a large 10-fold difference in the tensor part. Although error on the measured polarizabilities are limited by the current uncertainty of the linewidth $\Gamma_{841} = (8.0 \pm 0.2)\,\mathrm{kHz}$, the experiment-theory mismatch was attributed to the spectral data and theoretical model for the Erbium atom. The ab-initio and benchmarked calculations for a heavy atom are notoriously difficult [272, 274, 279], and rely on precise knowledge of the electronic structure and subsequent atomic transitions. In our case, the data available and used for the calculations [162] contained some values which did not agree with experimentally measured values, an issue that can already explain the observed difference.

5.3.4 Non-dissipative, species-selective trapping

With the tune-out wavelength found and characterized, it is now possible to use it as a species-selective trap. To reduce the scattering-induced dissipation, the tune-out is set to the largest detuning $\Delta_{90} = 245\,\mathrm{GHz}$ obtained for the orthogonal configuration. To quantify the dissipative effect of the dimple beam due to light scattering, the lifetimes of both Er and Li were measured and reported in Fig. 5.7.

For Erbium, the cloud was held in the $1064\,\mathrm{nm}$ trap and exposed to the $841\,\mathrm{nm}$ light, set on the tune-out. The power of the dimple beam was set to $500\,\mathrm{mW}$, which corresponds to a trap depth of $U_{\mathrm{Li}} = 200\,\mathrm{k_B} \cdot \mu\mathrm{K}$ for Li, and linearly polarized with $\theta_p = 90\,^\circ$. The Er cloud was held in the trap for up to $t_{\mathrm{hold}} = 100\,\mathrm{s}$, and the lifetimes of $\tau_{841}^{\mathrm{Er}} = 66 \pm 16\,\mathrm{s}$ and $\tau^{\mathrm{Er}} = 58 \pm 18\,\mathrm{s}$, with and without dimple respectively, were obtained by an exponential fit to the decay

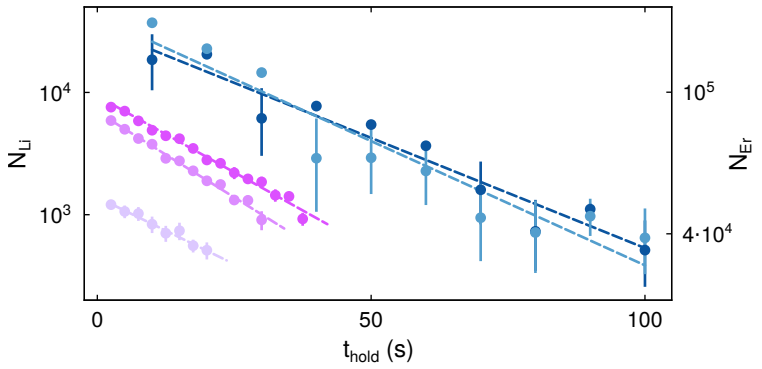

Figure 5.7 | Lifetimes of Erbium and Lithium in the species-selective trap. The lifetime of Erbium was measured in the $1064\,\mathrm{nm}$ trap, with (dark blue) and without (light blue) exposure to the tune-out beam with $P_{841} = 500\,\mathrm{mW}$. The lifetime of Lithium was measured in the tune-out beam at 100, 300 and $500\,\mathrm{mW}$ (light to dark pink), corresponding to trap depths of 40, 120 and $200\,\mu\mathrm{K}$. Each point is an average of 10 measurements, and the error bars represent the standard error of the mean.

curves. The non-dissipative character of the trap is demonstrated by the identical lifetimes, indicating that no heating due to light scattering could be detected this way. Moreover, it is straightforward to estimate the scattering rate of Er on the basis of Eq. (5.21). As a pessimistic estimate, the scattering rate can be overestimated by assuming a constant light intensity over the whole cloud, set to be the dimple peak intensity. In that case, the calculated scattering rate of Er is $\gamma_{\mathrm{Er}} = 1.5\,\mathrm{Hz}$, leading to an energy increase of $\dot{T}_{\mathrm{Er}} = 2E_r\gamma = 250\,\mathrm{nK/s}$ where $E_r = (\hbar k^2)/2m$ is the recoil energy imparted by a single photon. Since the geometric overlap of the Erbium cloud and dimple beam is only about $5\,\%$, the heating rate can be scaled down to $\dot{T}_{\mathrm{Er,eff}} \approx 12.5\,\mathrm{nK/s}$. One can also get a convenient heating rate depending on the Li trap depth when normalizing these numbers to it, and get: $\dot{T}_{\mathrm{Er}}/U_{\mathrm{Li}} = 1.3\,\mathrm{nK}/(\mu\mathrm{K}\cdot\mathrm{s})$.

For Lithium, the atoms were held in the dimple beam alone, however for shorter holding times and for different dimple beam powers. Although the average lifetime of $\tau_{841}^{\mathrm{Li}} = 15.7 \pm 1.9\,\mathrm{s}$ is shorter than for Er, the scattering rate is coincidentally identical, with $\gamma_{\mathrm{Li}} = 1.5\,\mathrm{Hz}$. However, the energy input rate is 28-fold increased to $\dot{T}_{\mathrm{Li}}/U_{\mathrm{Li}} = 40\,\mathrm{nK}/(\mu\mathrm{K}\cdot\mathrm{s})$ due to its lower mass.

Two additional points are worth mentioning. First, the energy input rate is not always the good metric to look at for experiments. In the case of small atom number (for example, 100 atoms in a lattice setup), the timescale provided by the scattering rate γ can be long enough to perform experiments without a single scattering event taking place. Second, it is interesting to note that the lifetime of lithium is power-independent. This suggests that the trap has reached a fundamental limit imposed by photon scattering, for which both the trap depth and energy input rate scale linearly with the laser intensity. This becomes apparent when writing the energy input scaled to the trap depth as:

$$\frac{\dot{T}}{U_{\mathrm{dip}}} = \frac{2E_r\gamma}{U_{\mathrm{dip}}} \propto \frac{\Gamma}{\hbar\Delta} \tag{5.33}$$

When this photon-scattering limit is reached, the power-independent lifetime becomes an intrinsic property of dipole traps, and was observed for both Er and Li in the $1064\,\mathrm{nm}$ trap.

Chapter 6

Quantum mixture of Erbium and Lithium

6.1 Experimental setup and sequence

The measurements presented in this chapter were obtained with a different optical setup and sequence than that of Chapter 5, as we explain now. This new setup is also one iteration step further than the results presented in [109], where the Optical Dipole Trap has been modified. With the implementation of a tighter trap, the comparably higher trap frequencies led to a faster evaporation, and ultimately to the formation of a quantum mixture of Er and Li. The results presented in this chapter were all obtained at the end of this work, and represent the current situation at the time of writing.

The optical setup is sketched in Fig. 6.1a, where the difference with Fig. 5.4 is clear. The trap is now made by the contribution of three beams in total: the Front Beam (FB), the Cross Beam 1 (CB1) and the Cross Beam 2 (CB2), all operating at $1064\,\mathrm{nm}$. The FB, propagating along the direction of the transport beams ($y-$axis), has an elliptical profile with waists $(w_\mathrm{h}, w_\mathrm{v})_\mathrm{FB} = (29 \times 16)\,\mu\mathrm{m}$. It is used to confine atoms along the $x-$ and $z-$axes. Then, CB1 and CB2 are co-propagating beams close to the $x-$axis, used to close the trap along the $y-$axis. They are not used simultaneously but sequentially, to tighten the trap during the evaporation. Their waists are $(w_\mathrm{h}, w_\mathrm{v})_\mathrm{CB1} = (360 \times 43)\,\mu\mathrm{m}$ and $(w_\mathrm{h}, w_\mathrm{v})_\mathrm{CB2} = (32 \times 225)\,\mu\mathrm{m}$ respectively, and they cross FB at an angle of approximately $80\,^\circ$ due to the presence of the cut lens on the side of the glass cell.

Regarding the experimental sequence, several major changes have occurred compared to the previous chapter. First, both species are now transported simultaneously to the glass cell. After loading Li in the transport lattice as before, the cloud is moved to the Er chamber, where the Magneto-Optical Trap (MOT) is still loading. Then, the yellow MOT is compressed and Er atoms are loaded in the transport beams directly from the cMOT, without the "filtering" step of the ODT. This way, both Er and Li are transported to the glass cell together, thus simplifying the sequence considerably. Although it makes the Erbium cloud much larger than before (on the order of $1\,\mathrm{mm}$), transferring this cloud in the cell ODT proved to be fine heating-wise, and even yielded a higher atom number for Er. At that point, about $4 \cdot 10^6$ Er atoms and 10^5 Li atoms have been transported to the glass cell, before their transfer in the cell ODT.

The next steps of the sequence, required to transfer the atoms in the final ODT, are drawn in Fig. 6.1b. First, an optimized offset field of $B_z = 2.2\,\mathrm{G}$ is applied in $40\,\mathrm{ms}$ to the transport fields ($\nabla B = 4.2\,\mathrm{G/cm}$ and $B_\mathrm{tp} = 13.5\,\mathrm{G}$, see Section 4.2.2) to hold the atoms. Then the FB and CB1 trapping beams are ramped up in $200\,\mathrm{ms}$ to $P_\mathrm{FB} = 2\,\mathrm{W}$ and

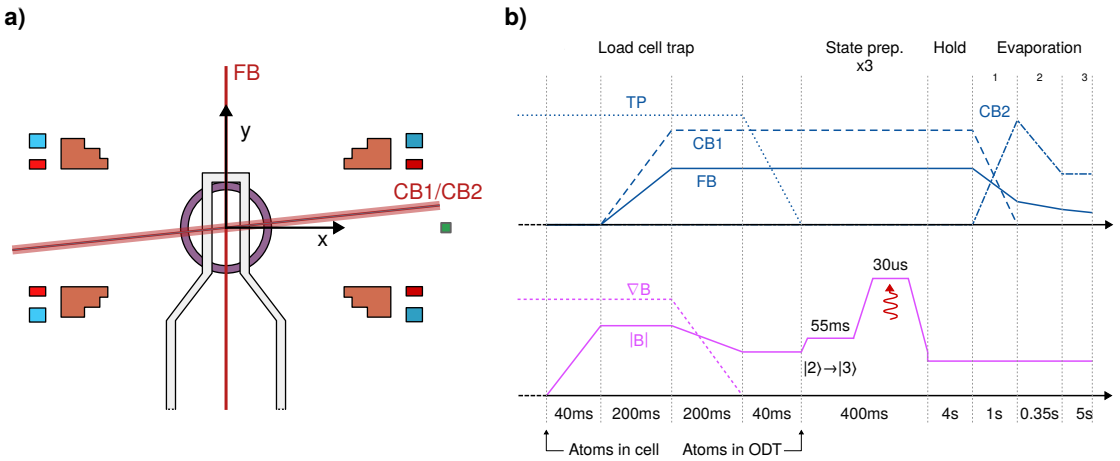

Figure 6.1 | Experimental setup and sequence for the quantum mixture. a) The setup is similar to Fig. 5.4 except for the laser beams. They have been replaced with three new beams: the Front Beam (FB), Cross Beam 1 (CB1) and Cross Beam 2 (CB2) for an increased trap frequency and cross-species thermalization time (see text). **b)** Sketch of the experimental sequence showing the power of relevant laser beams (top) and magnetic components (bottom) for the handling of atoms in the glass cell. The atoms are loaded in the cell ODT, followed by a spin purification of Li in $|1\rangle$, and the final evaporation into the quantum regime. The complete cycle time (including the loading and transport steps - not shown here) is approximately $15\,\mathrm{s}$.

$P_{\mathrm{CB1}} = 20\,\mathrm{W}$. The generated trap has a depth of $U_{\mathrm{Er}} = 141\,\mu\mathrm{K}$ and $U_{\mathrm{Li}} = 216\,\mu\mathrm{K}$ for each species. However, the large mass of Erbium effectively reduces the trap to $U_{\mathrm{Er,g}} = 129\,\mu\mathrm{K}$ because of the gravitational pull. To calculate the corresponding trap frequencies, the trapping potential (tilted by gravity) was numerically approximated by a harmonic potential which describes the bottom of the trap well despite the anharmonicity (see also Section 5.2). The frequencies were found to be $(\nu_x, \nu_y, \nu_z)_{\mathrm{Er}} = (611, 526, 1489)\,\mathrm{Hz}$ for Er and $(\nu_x, \nu_y, \nu_z)_{\mathrm{Li}} = (4164, 3260, 9751)\,\mathrm{Hz}$ for Li. In the setup, the trap frequencies were measured within the $10\,\%$ of these calculated values via parametric heating, attesting of the reasonably good alignment of the beams.

Once the trap ready, the levitation gradient and offset field are ramped down to $0\,\mathrm{G/cm}$ and $1.9\,\mathrm{G}$ in $200\,\mathrm{ms}$, while a side gradient of $\nabla B_{\mathrm{y}} = 0.25\,\mathrm{G/cm}$ is added to prevent Er atoms from spilling through the side of the trap. Then follows the extinction of the transport beams in $40\,\mathrm{ms}$. At that point, both species are held in the ODT only, but the Li cloud is still in a $|1\rangle - |2\rangle$ mixture. The atomic ensemble is purified into a spin-polarized cloud of Li in state $|1\rangle$ to prevent eventual heating effects or atom loss. The state preparation is performed by population transfer of the atoms in state $|2\rangle$ to $|3\rangle$ *via* rapid adiabatic passage [131]. The magnetic field is set to $B_z = 2\,\mathrm{G}$, and an RF-coil oriented along the $y-$axis drives the $|2\rangle \rightarrow |3\rangle$ transition with a frequency sweep at $225.4 \pm 0.175\,\mathrm{MHz}$ over $55\,\mathrm{ms}$. The field is then ramped to the usual imaging conditions, and the atoms pumped in the $|3\rangle$ state are ejected from the trap with a $30\,\mu\mathrm{s}$-pulse of resonant light. This procedure is repeated three times, after which no atoms in either $|2\rangle$ or $|3\rangle$ are detectable anymore.

The final step to reach quantum degeneracy is the evaporation, performed with three distinct ramps. The first ramp (evap1) is a transfer from CB1 to CB2, which are ramped

to $0\,\mathrm{W}$ and $25\,\mathrm{W}$ in $1\,\mathrm{s}$, while FB is ramped down to $1\,\mathrm{W}$. The second ramp (evap2) is a quick reduction of the laser beam powers, to $0.65\,\mathrm{W}$ and $2\,\mathrm{W}$ in $1\,\mathrm{s}$ for FB and CB2 respectively. The third ramp (evap3) is the last evaporation phase, where only FB is ramping down, to approximately $0.38\,\mathrm{W}$ in $5\,\mathrm{s}$. During the entire process, the magnetic field is set at $B_z = 1.4\,\mathrm{G}$, which was determined to be the best value for evaporation, in agreement with [170].

6.2 Reaching double degeneracy

Before the evaporation ramps start and the mixture is brought to the quantum regime, an additional waiting step is necessary to fully load the final cell trap. This waiting step, not mentioned before, occurs between the state preparation of Li, and the beginning of the evaporation (see Fig. 6.1b). The measurements shown in Fig. 6.2 are the atom number and temperature in the ODT for various waiting times, up to $20\,\mathrm{s}$. These measurements were obtained in two different configurations: with an Er-Li mixture, and with a cloud of Er atoms only. The configuration with Li alone could not be achieved, since the thermalization (and subsequent loading of the trap) is not possible at low field, due to the weak Li-Li interactions.

In the Er-Li configuration, the thermalization of Li is ensured by the cold bath of Er atoms around. As a result, the transfer from the large transport beam into the first ODT requires several seconds for the atoms to scatter into the trap. This effect can be seen clearly on the Li atom number, which increases during the first $5\,\mathrm{s}$ of holding time. The increase is explained by atoms coming from the wings of the trap, which slowly scatter into the ODT with the help of Er, as already observed in our experiment before [109]. In contrast, the number of Er atoms decreases at a constant rate for the entire duration, showing that the transfer is already done at the end of the state-preparation stage. Interestingly, things change qualitatively in the absence of Li atoms. In that case, Er behaves like Li and displays a rather long loading time as well, with atom number increasing during the first $10\,\mathrm{s}$ before decaying at the same rate during the second half of the holding stage.

The curves shown in Fig. 6.2a were fitted with a saturated exponential increase for Li and Er (in Er-Li and Er configurations respectively) and with a linear decrease for Er (in Er-Li configuration). From these fits, one can extract the initial atom numbers, time-constant for the loading rate, and the decay rate. In the Er-Li configuration, we obtain:

$$\begin{aligned} N^i_{\mathrm{Er}} &= 1.65 \cdot 10^5 \text{ and } N^i_{\mathrm{Li}} = 3.1 \cdot 10^3 \\ N^f_{\mathrm{Er}} &= 0.8 \cdot 10^5 \text{ and } N^f_{\mathrm{Li}} = 6.8 \cdot 10^3 \end{aligned} \tag{6.1}$$

with a decay rate and time constant of:

$$\dot{N}_{\mathrm{Er}} = -4 \cdot 10^3\,/\mathrm{s} \text{ and } \tau_{\mathrm{Li}} = 1.7\,\mathrm{s} \tag{6.2}$$

In the Er-alone configuration, for the rising part we obtain:

$$N^i_{\mathrm{Er}} = 0.9 \cdot 10^5 \tag{6.3}$$

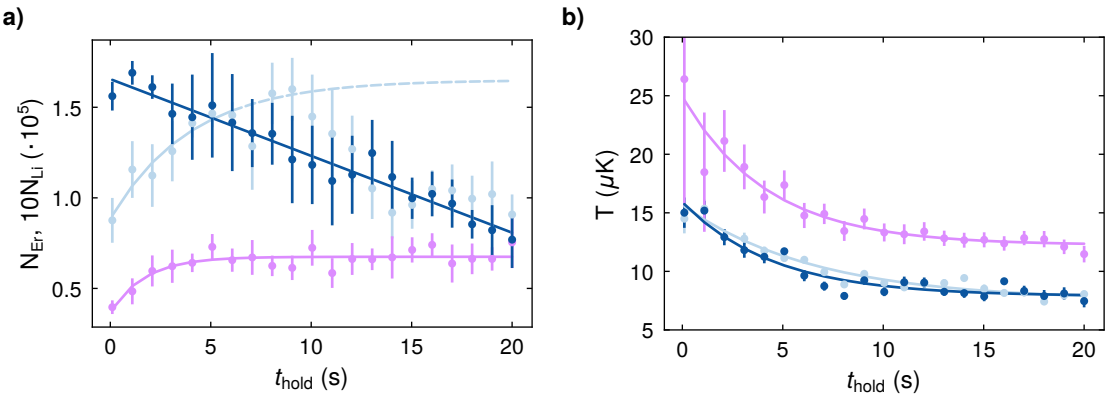

Figure 6.2 | Accumulation and thermalization of atoms in the trap before evaporation. a) Atom number of Er (blue) and Li (pink) during the holding step. The number of Er atoms shows a qualitative difference in the Er-Li (dark blue) and Er-alone (light blue) cases. **b)** Temperature of Er (blue) and Li (pink) during the holdig step. The solid lines are fit to the data; the dashed lines serve as guide for the eye (see text).

with a time constant of:

$$\tau_{\mathrm{Er}} = 4.0\,\mathrm{s} \tag{6.4}$$

Moreover, the transfer from the transport beams to the ODT heats the atoms, which then thermalize during the same holding phase. The temperatures of both clouds, measured *via* time-of-flight thermometry (see Section B.2) and reported in Fig. 6.2b, show a high initial value, followed by a decay towards equilibrium over the entire holding time. The relevant numbers for this long thermalization were obtained again via an exponential decay fit, from which the initial and final temperatures, as well as the time constant were found to be:

$$T^i_{\mathrm{Er\ alone}} = 17.2\,\mu\mathrm{K}, \quad T^i_{\mathrm{Er}} = 15.9\,\mu\mathrm{K}, \quad T^i_{\mathrm{Li}} = 24.9\,\mu\mathrm{K}$$
$$T^i_{\mathrm{Er\ alone}} = 7.9\,\mu\mathrm{K}, \quad T^f_{\mathrm{Er}} = 7.9\,\mu\mathrm{K}, \quad T^f_{\mathrm{Li}} = 12.2\,\mu\mathrm{K}$$

with

$$\tau_{\mathrm{Er\ alone}} = 4.8\,\mathrm{s}, \tau_{\mathrm{Er}} = 4.5\,\mathrm{s}, \tau_{\mathrm{Li}} = 4.2\,\mathrm{s} \tag{6.5}$$

The qualitative differences between the Er-Li and Er-alone configurations are not fully understood, and would require a proper investigation to draw any serious conclusion. However, several comments can be made. To begin with, it would seem that Er-Li has faster dynamics than Er-alone, based on the following observations. While the number of trapped Er atoms increases over several seconds in the Er-alone configuration, the peak value is already reached at the first point of the Er-Li measurement. Coincidentally, the fit of N_{Er} indicates a saturation value of $1.65 \cdot 10^5$ atoms in the Er-alone case, which is exactly the initial number of the Er-Li case. This aspect would suggest that when Er is alone, it takes several seconds for the all the atoms to reach the trap, while the presence of Li makes the Er cloud denser in the beginning, resulting in a faster transfer. On the temperature side, it appears that Er atoms are barely affected by the additional heat load brought by the Li atoms. This appears clearly in Fig. 6.2b, where the two Er curves are almost identical. The only detectable difference was the initial temperature of Er (extracted from the fit),

which increases from $15.9\,\mu$K to $17.2\,\mu$K, followed by a slightly shorter thermalization time, which decreases from $4.8\,$s to $4.5\,$s. The equilibrium temperature of $7.9\,\mu$K is also the same in both situations. An interesting point here is the temperature offset between Er and Li. It starts with Li being hotter than Er by $\sim 10\,\mu$K, but decreases to a difference of $\sim 4\,\mu$K at equilibrium. This difference, although not fully understood, is also visible in other works with quantum mixtures that include Li [214, 280]. As we shall see, the difference decreases further during the evaporation, until it becomes smaller than $1\,\mu$K in the last stage of evaporation. However, it also confirms a central point of our experiment, which was unknown in the beginning of this thesis: Er and Li can thermalize together.

We can now turn to the final result of this work: the formation of a quantum mixture of ^{166}Er and ^{6}Li. The atom number and temperature of both Er and Li, shown in Fig. 6.3a, were measured along the evap2 and evap3 ramps, when the atoms are in the final trap made by FB and CB2. During the entire process, the number of Li atoms stays constant at $N_{\mathrm{Li}} \approx 1500$, while Er atoms are being evaporated until none remain at $t_{\mathrm{evap}} = 5.5\,$s. Thus, Li atoms are being sympathetically cooled by the surrounding Er atoms, which take the thermal energy out of the system when they escape the trap *via* forced evaporation. At the beginning of evap2, $T_{\mathrm{Er}} = 9\,\mu$K and $T_{\mathrm{Li}} = 10\,\mu$K, and they decrease quickly to reach $T_{\mathrm{Er}} = 2.7\,\mu$K and $T_{\mathrm{Li}} = 3.4\,\mu$K by the beginning of evap3. After a total of $5\,$s of evaporation, the measured temperatures were $T_{\mathrm{Er}} = 0.4\,\mu$K and $T_{\mathrm{Li}} = 0.7\,\mu$K, both below their BEC and Fermi temperatures. Interestingly, it seems that the temperature of Li follows that of Er during evap2, but they start splitting apart in evap3. This effect could be originating from a reduced overlap between the clouds, since the gravitational sag of Er progressively increases up to $3\,\mu$m, which is on the order of the clouds' diameters. However, a clear separation was not observed, and the thermalization of Li keeps on going through the whole evaporation. The increasing temperature difference was instead attributed to the thermometry itself, since time-of-flight measurements are increasingly unreliable as the degeneracy increases.

So far, these temperatures were obtained with TOF measurements, which depend on a Gaussian fit of the released cloud, and cannot be reliably used in the quantum regime. For Er, which reaches its condensation onset at $4.4\,$s, only the last few points need to be remeasured to extract the temperature with a bimodal fit. However, Li enters the degenerate regime much earlier, close to the end of evap2. Although a Gaussian fit can reliably capture the shape of a Fermi cloud for temperatures as low as $T/T_F \approx 0.5$ [109, 131], the precise measurement of a Fermi gas' degeneracy requires a fit of the cloud's shape with its exact 2D-density distribution (integrated along the imaging's direction). For Er, a bimodal fit to the 1D (integrated) profile encompasses the thermal and condensed fractions *via* [276]:

$$n(x) = n_{0,\mathrm{th}} e^{-x^2/2\sigma_x^2} + n_{0,\mathrm{c}} \left(1 - \left[\frac{x}{w}\right]^2\right)^2 \tag{6.6}$$

where σ_x is the thermal cloud radius, and w the BEC radius. From such a fit, one can retrieve the condensed fraction by integrating the two contributions, and the critical temperature can be obtained with:

$$k_B T_c \approx 0.94 \hbar\omega N^{1/3} \tag{6.7}$$

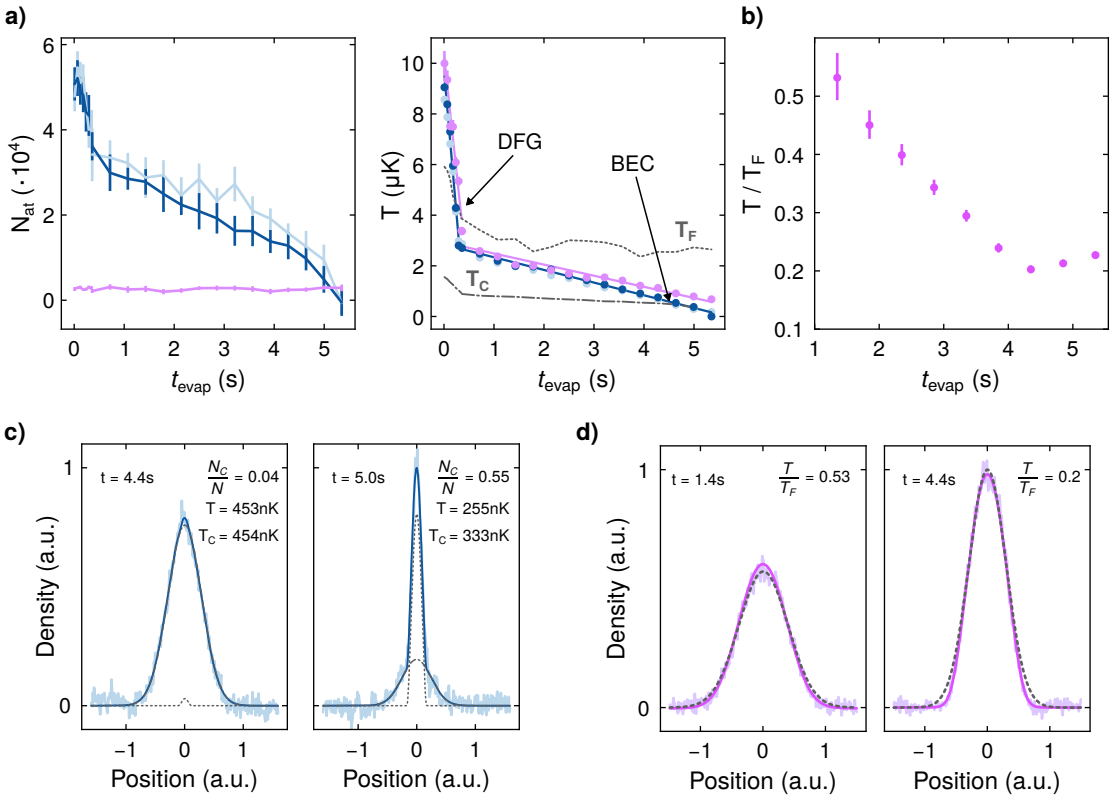

Figure 6.3 | Evaporation to the quantum regime for Er and Li. a) Atom number (left) and temperature (right) of Er (blue) and Li (pink) during the evap2 and evap3 ramps. The number of Li atoms remains constant, while Er is being evaporated from the trap, demonstrating an efficient sympathetic cooling. The atom number and temperature of Er in the absence of Li atoms (light blue) is identical to the Er-Li situation (dark blue). The Fermi (dotted) and critical (dash-dotted) temperatures were obtained with the calculated trap frequencies and measured atom numbers during the entire evaporation. **b)** Degeneracy of the Li cloud during the evaporation. The numerical value was obtained from a 2D fit of the absorption pictures' profile; the increase at the end is attributed to a impure spin polarization (see text). **c)** Integrated profiles of the Er cloud at the BEC onset (left) and end of evaporation (right). The bimodal fit includes a thermal (dotted) and a condensed (dash-dotted) part, from which the condensed fraction and critical temperature are obtained. **d)** Slice profiles of the Li absorption pictures. The Gaussian fit (dotted) is done on the wings of the cloud only. The Fermi fit (dark pink) is done on the 2D column density. The deviation from a Gaussian cloud is clearly observed at high degeneracy.

For Li, the fit is best performed on the 2D column density *via* [131]:

$$n_{\mathrm{F,2D}}(x,y) = n_{\mathrm{2D},0}\frac{\mathrm{Li}_2\left(-\exp\left[q-(\frac{x^2}{R_x^2}+\frac{y^2}{R_y^2})f(e^q)\right]\right)}{\mathrm{Li}_2(-e^q)} \tag{6.8}$$

with

$$R_i^2 = \frac{2k_BT}{m\omega_i^2}f(e^{\mu\beta}) \text{ and } f(x) = \frac{1+x}{x}ln(1+x) \tag{6.9}$$

where Li_2 is the polylogarithm of order 2, $q=\mu\beta$ is the fugacity, and R_i the Fermi radius along the i-direction[1]. From the fit, the degeneracy is obtained with:

$$\frac{T}{T_F} = [-6\mathrm{Li}_3(-e^q)]^{-1/3} \tag{6.10}$$

Using these fits, it was possible to determine precisely the degeneracy of the Li cloud as well as the BEC onset and condensed fraction of Er. The value of T/T_F is given in Fig. 6.3b, for which an independent dataset had to be taken at a later date than the TOF measurements. The fitted Fermi profiles show that Li is already in the DFG state at $t_{\mathrm{evap}} = 1.4\,\mathrm{s}$ with $T/T_F = 0.5$, and decreases linearly to the minimal value of $T/T_F = 0.2$ at $t_{\mathrm{evap}} = 4.4\,\mathrm{s}$. For the last second of evaporation, it seems that the relative temperature goes up again, reaching $T/T_F = 0.23$ at $t_{\mathrm{evap}} = 5.4\,\mathrm{s}$. This undesired heating, which does not appear on the previous data (Fig. 6.3a), was attributed to experimental instabilities that lead to a non-pure state preparation of Li. An investigation of this stage revealed that a large part of the atoms were still present in the state $|2\rangle$ (about $25\,\%$), a situation which resulted in an effectively deformed Fermi surface at high degeneracy, which the fit could not properly account for. After solving the issue, it seems that the Li cloud can now reach $T/T_F = 0.15$, a result which still needs confirmation at the time of writing.

Finally, the precise fits of Er and Li along the evaporation are also presented in Fig. 6.3cd. On the one hand, the fit to the partially condensed Er cloud reveals a final temperature of $T_{\mathrm{Er}} = 255\,\mathrm{nK}$, for a condensed fraction of $N_c/N = 0.55$. At the last evaporation point ($t_{\mathrm{evap}} = 5.4\,\mathrm{s}$), the trap is fully open for Er and no atoms remain. On the other hand, the fit to the DFG of Li shows the clear deviation from a gaussian cloud for the lowest $T_{\mathrm{Li}}/T_F = 0.2$ measurement.

[1] More precisely, this quantity is the size of a Fermi gas, constructed from the limits of a thermal cloud at $T \gg T_F$ and the Fermi radius at $T = 0$ (see [131])

Chapter 7

Conclusion and outlook

This thesis presented the design, construction and first experimental results of a novel apparatus capable of producing quantum mixtures of ^{166}Er and ^{6}Li. In the present work, a strong emphasis was put on the Erbium side; the Lithium side can be found in the companion thesis of Florian Kiesel [109]. We began with an explanation of our machine's central motivation with a brief introduction to the Fermi-Hubbard model and its open questions, followed by a presentation of the currently known limits to cooling. We explained how, with the aid of a species-selective trap, our experiment could achieve the ambitious goal of producing a Fermi gas with unprecedented degeneracy. We then proceeded to a thorough description of the different subsystems implemented over the course of the thesis, consisting of the vacuum apparatus, laser setups and magnetic coil systems.

The performance of our apparatus was also characterized, demonstrating the successful laser-cooling of Er atoms down to the microkelvin range, using state-of-the-art techniques. Starting from a hot gas at $\sim 1300\,\mathrm{K}$, the atoms travel through a spin-flip Zeeman Slower operating on the $401\,\mathrm{nm}$-transition aided with an Angled Slowing step, before their capture by a magneto-optical trap operating on the $583\,\mathrm{nm}$-transition. There, we observe a loading rate of up to $5 \cdot 10^7\,\mathrm{atoms/s}$, with a saturation value of up to $7 \cdot 10^8$ atoms. After compression, the cloud's temperature was measured to be $8\,\mu\mathrm{K}$. The transfer to an Optical Dipole Trap is reported as well, wherein up to $4 \cdot 10^6$ atoms could be loaded and further cooled to $4.5\,\mu\mathrm{K}$. The subsequent transfer into, and successful transport of the atoms over $50\,\mathrm{cm}$ towards the glass cell is also documented, with a final number of up to $4 \cdot 10^6$ atoms reaching the end of transport.

We then proceeded to the measurement of the tune-out wavelength of Erbium near its $841\,\mathrm{nm}$-transition. The tune-out's anisotropy was also characterized, and its position was found to be from $78\,\mathrm{GHz}$ to $245\,\mathrm{GHz}$ red-detuned from the transition. Most importantly, a species-selective trap of ^{6}Li was demonstrated using the tune-out wavelength, for which a power-independent lifetime of $15\,\mathrm{s}$ was observed. Finally, we demonstrated the production of a Bose-Fermi quantum degenerate mixture of ^{166}Er and ^{6}Li, achieved by the simultaneous sympathetic cooling of Li by Er, and the forced evaporation of Er from the trap. The efficient cross-species thermalization led to a Fermi gas with $T/T_F = 0.2$, trapped along a BEC with a condensed fraction of $55\,\%$.

Outlook

Species-selective trapping

The next natural step of our experiment is the implementation of a species-selective trap operating at Erbium's previously measured tune-out wavelength. Such a trap offers several decisive advantages.

First, loading Lithium into a tighter confinement with higher trap frequencies increases its absolute temperature while leaving the degeneracy parameter T/T_F unchanged. In the presence of a surrounding cold Er bath, this temperature increase can be compensated by sympathetic cooling, provided that the cooling power of Er is sufficient. In this regime, a careful optimization of the experimental parameters could lead to a substantial improvement of the Lithium degeneracy. Preliminary measurements are currently underway in the laboratory to explore this approach. So far, the first tests have proven very promising, with an immediate enhancement of the Lithium degeneracy, reaching $T/T_F = 0.1$.

Second, the tune-out trap enables a high degree of species-selective control. In particular, when combined with our tilt stages, it allows for a controlled displacement of the trap during the evaporation sequence. Thanks to their angular precision, these stages can be used to compensate the gravitational sag of Er, thereby maintaining an optimal spatial overlap between the two atomic clouds throughout the evaporation.

Third, this configuration provides independent control over Er via its dedicated trapping potential. Depending on the targeted application, the Er cloud can either be evaporated into the Bose-Einstein condensate regime or maintained in a classical state. In the condensed regime, the Er cloud can serve as a precise thermometer for the fermionic Lithium gas [123]. When kept classical, its larger size and higher specific heat capacity make it an efficient coolant, enhancing evaporative and sympathetic cooling performance.

Polaron physics

Looking further ahead, our experiment is particularly well suited for the investigation of polaron physics [281, 282]. This regime emerges in a two-component mixture, when one species is sufficiently dilute to be treated as a mobile impurity immersed in a many-body bath formed by the other component. Polaron physics describes how this mobile impurity is dressed by excitations of its surrounding medium, forming a quasiparticle called a polaron. As the impurity moves, it distorts the environment, and the combined object behaves as a single entity with renormalized properties such as an effective mass, energy, and lifetime.

The Er-Li mixture enables the exploration of distinct polaron regimes, with either Bose or Fermi polarons according to the choice of the minority species. In particular, an infinite-mass impurity can be realized with the help of the large mass imbalance, or with a tight tune-out trap. Polaron oscillations can also be investigated using the combination of the species-selective trap and the tilt stages. In this scheme, Li atoms are confined in the species-selective trap, which can then be rapidly displaced using the tilt stages to excite center-of-mass oscillations of the Lithium cloud.

Efimov effect

The Efimov effect [283] is a phenomenon arising from two-body interactions, in a three-body system. It manifests itself as an infinite sequence of weakly bound trimer states (called Efimov states), even when no two-body bound state exists. Although originally predicted in the context of nuclear physics, the Efimov effect is also realized in ultracold atomic systems, where it manifests as enhanced three-body loss rates in the vicinity of Feshbach resonances. Compared to homonuclear gases, heteronuclear mixtures offer a richer Efimov spectrum, which becomes increasingly dense with larger mass imbalance (see [159] and references therein). Moreover, the presence of broad interspecies Feshbach resonances facilitates the experimental observation of this effect, a feature that appears to be naturally available in the Er-Li mixture [171].

Lattice physics

In the long term, the implementation of several key subsystems is still required to reach the milestone of lattice physics, and access both Fermi-Hubbard and Bose-Hubbard models. Recently, the implementation of a tune-out lattice has been initiated as part of a Master's project. Our approach differs from the entropy-engineering scheme of [43], as the cooling is instead provided by the Er reservoir, while the doping is controlled directly through the loading of Li.

In-situ and spin-resolved imaging will be provided by a high-resolution objective already positioned near the glass cell, prepared for the implementation of a quantum gas microscope. The objective is intended to be used in combination with near-resonant optical tweezers for Li, operating at 675 nm, implemented using a Spatial Light Modulator (SLM) and mapped onto the lattice sites. This novel scheme is inspired from a similar imging setup with $1064\,\mathrm{nm}$-tweezers [284], where a robust fluorescence imaging technique was demonstrated. In comparison, the near-resonant tweezers require much less power for the same trap depth, and have a smaller diffraction limit (hence a higher resolution). This approach additionally relies on in-trap D_1 gray-molasses cooling of Li, which also provides the fluorescence photons collected by the objective. The construction and testing of this subsystem is already under way as part of another Master's project.

Finally, both the polarons and lattice projects benefit from a subsystem equipped with a Digital Micromirror Device (DMD). The DMD will be used to flatten the potential of either the optical dipole trap or the lattice, since a homogeneous potential landscape is essential for controlled studies of polaron and lattice physics. Once again, this project is already well under way as a Master's thesis.

Appendix A

Supplemental Material for Chapter 4

This appendix presents the kind of scans and measurements which can (and sometimes have to) be done to find the optimal parameters of the different preparation steps. The measurements presented here focus on the different steps presented in Chapter 4. The MOT loading discussed in Section A.1, and the cMOT temperature in Section A.2. Then, the ODT loading is discussed in Section A.3, and finally the transport setup is presented in Section A.4.

A.1 MOT

The MOT can be quickly optimized by a series of 1D scans, on essentially all the parameters. However, such iterative scans can lead one to a local maximum, especially if the scans are not repeated.

The measurements in Fig. A.1 provide a global overview of the MOT parameters for optimal loading. They were all obtained by absorption imaging in the Erbium chamber (along the vertical direction), after $1\,\mathrm{s}$ MOT loading time in Section A.1, $5\,\mathrm{s}$ MOT loading time in Section A.2, and with 3 repetitions per point. The MOT itself is too dilute to be imaged without compression, so the absorption pictures were taken after compressing the MOT to the default cMOT parameters. These "2D+1" maps were obtained as a way to have a visual representation of the MOT position, by checking slices in a 3D parameter space. On the left, the MOT offsets fields B_x and B_y were scanned from $-2.5\,\mathrm{G}$ to $+2.5\,\mathrm{G}$ to determine the best MOT position in the horizontal plane. On the right, the MOT frequency and gradient were scanned to determine the optimal MOT volume, provided that the position is centered correctly before. The frequency was scanned from $45\,\Gamma$ to $78\,\Gamma$, and the gradient from $3.5\,\mathrm{G/cm}$ to $7\,\mathrm{G/cm}$. In both situations, the maps were measured at different vertical offsets B_z, from $0\,\mathrm{G}$ to $3\,\mathrm{G}$. The final values, used in our experiment at the time of writing, are summarized in Table A.1.

Interestingly, at low values of B_z ($0\,\mathrm{G}$ and lower), it is possible to see the effect the (A)ZS beams on the atom number. On the figures (for $B_z = 0 - 1\,\mathrm{G}$), it appears as a local minimum with an additional "blob" on the right part of the signal, close to $B_x = 2\,\mathrm{G}$. When decreasing B_z further, this effect gets stronger, until the MOT cannot be loaded anymore. Even further, it becomes possible to load the MOT above the blue beams, although this was never investigated.

A.2 cMOT

The cMOT temperature, after a long enough thermalization time and assuming that no sub-Doppler mechanism is taking place, depends solely on the scattering rate. Said otherwise, the laser parameters are the important experimental knobs that can be used to reach the Doppler temperature. As it stems from Eq. (4.1), one can reach this temperature with a detuning of $\Delta = -\Gamma/2$, and with peak intensity lower than the saturation intensity. Typically, the lowest temperatures are reached for intensities of $I \sim 0.1 I_{\mathrm{sat}}$ [237, 285].

Here, we make a systematic study of the cMOT to understand and calibrate its behaviour to our control system. The MOT was loaded for $5\,\mathrm{s}$ before compression, to be closer to the actual cycle times during experiments. Because of the large atom number in that situation, the imaging beam was detuned to image only 1/10 of the atom number and avoid saturation. The compression ramps are identical to that used in the main text, see Section 4.1.2. The parameters scanned is this study are the laser detuning and intensity. The laser detuning was scanned from $-5\,\Gamma$ to $-18\,\Gamma$, and the intensity from $0.01\,\mathrm{I_{sat}}$ to $0.35\,\mathrm{I_{sat}}$. The cMOT was imaged after $5\,\mathrm{ms}$ and $20\,\mathrm{ms}$ time-of-flight (TOF), to ensure that the cloud has enough time to expand, while staying within the camera's view.

The cMOT was characterized by measuring its atom number and diameter at short and long TOFs, to extract its temperature and pseudo-density from only two points. The diameter is obtained by fitting a Gaussian profile to the imaged cloud, which can be done even at short TOF with the vertical imaging. The temperature requires more points to be measured properly (see Chapter B), but the ratio of the cloud size between these two TOFs is already a good indicator. The pseudo-density is only an estimate of the cloud's density, given simply by the ratio of atom number to the cloud size: $n_{\mathrm{pseudo}} = N_{\mathrm{at}}/w_x w_y$, and corresponds to an average column density.

The results shown in Fig. A.2 can be understood well by looking at the right column. There, we plot the ratio of the atom number, cloud diameter, and pseudo-density between the two shots at $5\,\mathrm{ms}$ and $20\,\mathrm{ms}$. The coldest cMOT can be expected to be in the area where the cloud expanded the least, i.e. where the ratio of cloud size is the smallest (center right). This area also matches with the highest density ratio (lower right). The highest initial density can be found at a detuning of $\sim -8\,\Gamma$ (lower left), but it is due to atom loss and not colder temperatures. This is confirmed the sharp diameter ratio increase (center right), where the cloud is actually hotter because the laser is closer to resonance.

The temperature measurements were done in the high density ratio area (lower right), and indicated there by the star symbols. The values reported in Table A.2 indicate that the cMOT temperature is heavily influenced by the laser detuning, and to a lesser extent by the laser power. There, the cloud goes from $\sim 13\,\mu\mathrm{K}$ (upper stars line) to $\sim 8.5\,\mu\mathrm{K}$ (lower stars line). Finally, it is important to note that the optimal cMOT parameters are different depending on the figure of merit. The coldest cMOT is reached at $-16.8\,\Gamma$ and $0.02\,\mathrm{I_{sat}}$, but the best transfer to the ODT in terms of atom number is reached at $-14.5\,\Gamma$ and $0.13\,\mathrm{I_{sat}}$, where the cloud temperature is $\sim 14\,\mu\mathrm{K}$.

A.3 ODT

The procedure followed here is essentially the same as for the MOT, explained in Section A.1. Just like the MOT, the ODT loading can be quickly optimized with 1D scans on the cMOT parameters. However, the parameters in question are mutually dependent and one can rather easily fall into a local maximum.

A very good mapping can be obtained by the "2D+1" maps shown in Fig. A.3, and the final parameters are summarized in Table A.3. To get these measurements, the cMOT is roughly aligned to the ODT in the first place, before doing the precise scans. Then, the ODT loading is measured for a MOT loading time of $2\,\mathrm{s}$, a compression ramp of $300\,\mathrm{ms}$ and a thermalization time of $150\,\mathrm{ms}$. The MOT beams are then shuttered, and the atoms held in the ODT for $500\,\mathrm{ms}$ with a levitating field of $4.2\,{}^{\mathrm{G}}/_{\mathrm{cm}}$. For these measurements, the transport beams were not turned on; adding them during the ODT loading typically doubles the atom number.

The precise alignment is done as follows. First, the cMOT horizontal position is scanned via the B_x and B_y offsets, at different B_z values. Then, the final compression parameters (cMOT detuning and power) are scanned for each optimal position at their respective B_z offsets. From the shape of the measurements in the two columns, it appears that the transfer from cMOT to ODT is very consistent. First, the horizontal position barely changes for different vertical positions, and the signal keeps its overall shape. Second, the optimal detuning simply moves towards larger values when the vertical position is changed, while the signal's shape stays consistent as well. From this, it is clear that the vertical displacement is simply compensated by the cMOT resonant "shell" via the detuning. There, it can also be inferred that larger negative B_z values move the cMOT upwards. Finally, it is interesting to note that the horizontal position has a "hole" close to $(B_x, B_y) = (0.4, 0.3)\,\mathrm{G}$. This was attributed to an overlap of the ODT with the magnetic zero, leading to dipolar losses in the Erbium cloud.

A.4 Transport

The Figs. A.4 and A.5 display extended information compared to the summary presented in Section 4.2.2. They focus on the characterization of the transport setup by scanning its magnetic fields and dynamics respectively.

In addition to the explanations given in the main text, it is interesting to also take a look at the cloud's shape. The shape was extracted from the absorption pictures by a 2D fit of the thermal cloud, and the pseudo-density was defined as $PD = N/\omega_x\omega_y$. The latter corresponds to the column density of the cloud, integrated along the imaging direction. In both measurements sets, a filter was applied on the atom number to be able to fit the data, with $N \geq N_{\mathrm{th}} = 6 \cdot 10^4$.

On Fig. A.4, the Feshbach resonance observed at $20\,\mathrm{G}$ enlarges the cloud in both directions, resulting in a lower pseudo-density. Interestingly, the vertical diameter shows a strong dependence on the levitation gradient, with a seemingly bimodal behaviour. When the cloud is under-levitated, the atoms accumulate at the bottom of the transport lattice and the

cloud's vertical diameter is $\approx 180\,\mu\mathrm{m}$ When it is slightly over-levitated, it abruptly increases to $\approx 220\,\mu\mathrm{m}$. Although the difference is not large, the threshold lies clearly along the levitation diagonal of $4.0\,\mathrm{G/cm}$ (see Section 4.2.2), and deviations from this position impact the transfer to the cell's trap (unfortunately not measured here).

On Fig. A.5, the transport resonances mentioned in Section 4.2.2 are clearly visible on the cloud's diameter. These resonances are only dependent on the maximum velocity of the transport lattice, and can be understood as follows. During the transport, experimental imperfections (*e.g.* the back-reflections of the transport beams) induce a "bumpiness" for the atoms, at a given frequency. When that frequency is resonant with some physical quantities involved (such as the local trap frequency), some form of parametric heating can take place and heat the cloud. Here, the pattern was always strongly dependent on the transport beams'alignment, and changed after every realignment procedure. For this reason, and because it also never proved to be problematic in our sequence, the problem at hand was not properly investigated and no real conclusion was drawn. Instead, the transport is always parametrized to be away from these resonances, for both Er and Li. Especially here, the resonances seem to be akin to a breathing mode, where an increase in the vertical diameter is compensated by a decrease in the horizontal diameter, leading to an overall flat pseudo-density. The only trend that was of real interest to us was the monotonous increase of atom number for low accelerations but high velocities. In the end, the transport also needs to take into account the presence of Lithium atoms and their own preferential parameters, which are usually in a region of much higher accelerations and velocities.

		MOT	cMOT
$B_x/B_y/B_z$	(G)	0.7 / 0.7 / 1.25	0.3 / 0.37 / -0.1
∇B	(G/cm)	4.85	3.5
Detuning	(Γ)	-57	-13.7
Laser power	(I_{sat})	16	0.02-0.1

Table A.1 | MOT and cMOT parameters. The default parameters for MOT and cMOT used in the experiment. The cMOT parameters have to be adapted to the desired goal, such as coldest cloud or best ODT loading.

I_0/I_{sat}	Detuning (Γ)		
	13.7	14.7	16.8
0.11	13.3 μK	12.8 μK	12.6 μK
0.07	10.5 μK	10.1 μK	9.60 μK
0.02	8.70 μK	8.55 μK	8.30 μK

Table A.2 | cMOT temperatures. The cMOT temperature was measured for the different points indicated by stars in Fig. A.2. Here, the laser power is the most relevant parameter for a cold cloud, with a stronger influence than laser detuning. The lowest temperature was measured to be $8.3\,\mu$K for a detuning of $16.8\,\Gamma$, although at the price of slightly lower atom number.

		cMOT
$B_x/B_y/B_z$	(G)	0.27 / 0.37 / -0.1
∇B	(G/cm)	3.5
Detuning	(Γ)	-14.7
Laser power	(I_{sat})	0.13

Table A.3 | cMOT parameters for ODT loading. Parameters extracted from the measurements of Fig. A.3, obtained with ODT beams alone (no transport beams).

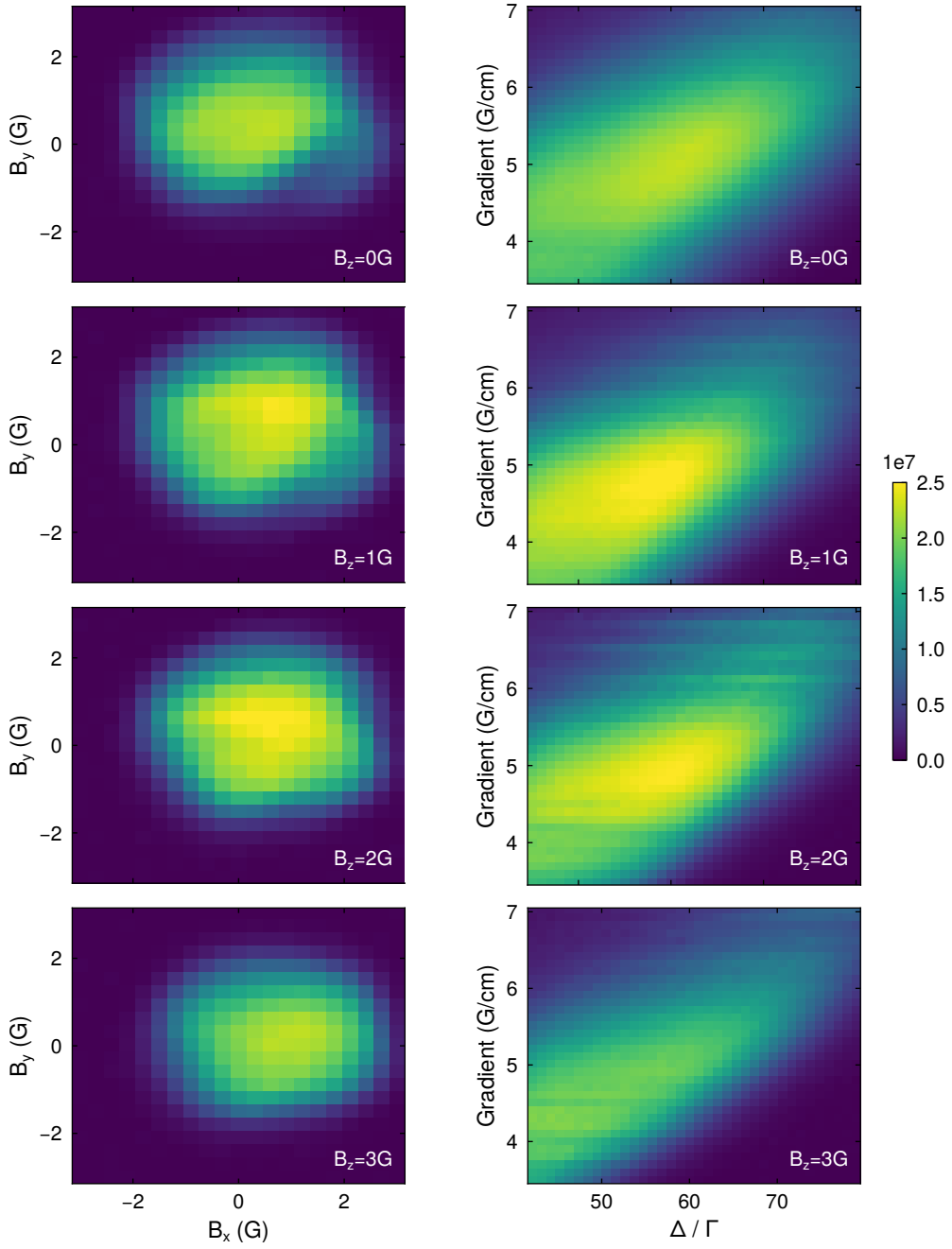

Figure A.1 | MOT optimization. 2D maps of the MOT position in the horizontal plane (left) and its volume (right). The horizontal position is changed with the magnetic offsets and the volume with the laser detuning and magnetic gradient. The measurements were done for several vertical offsets to align the MOT to its best loading position.

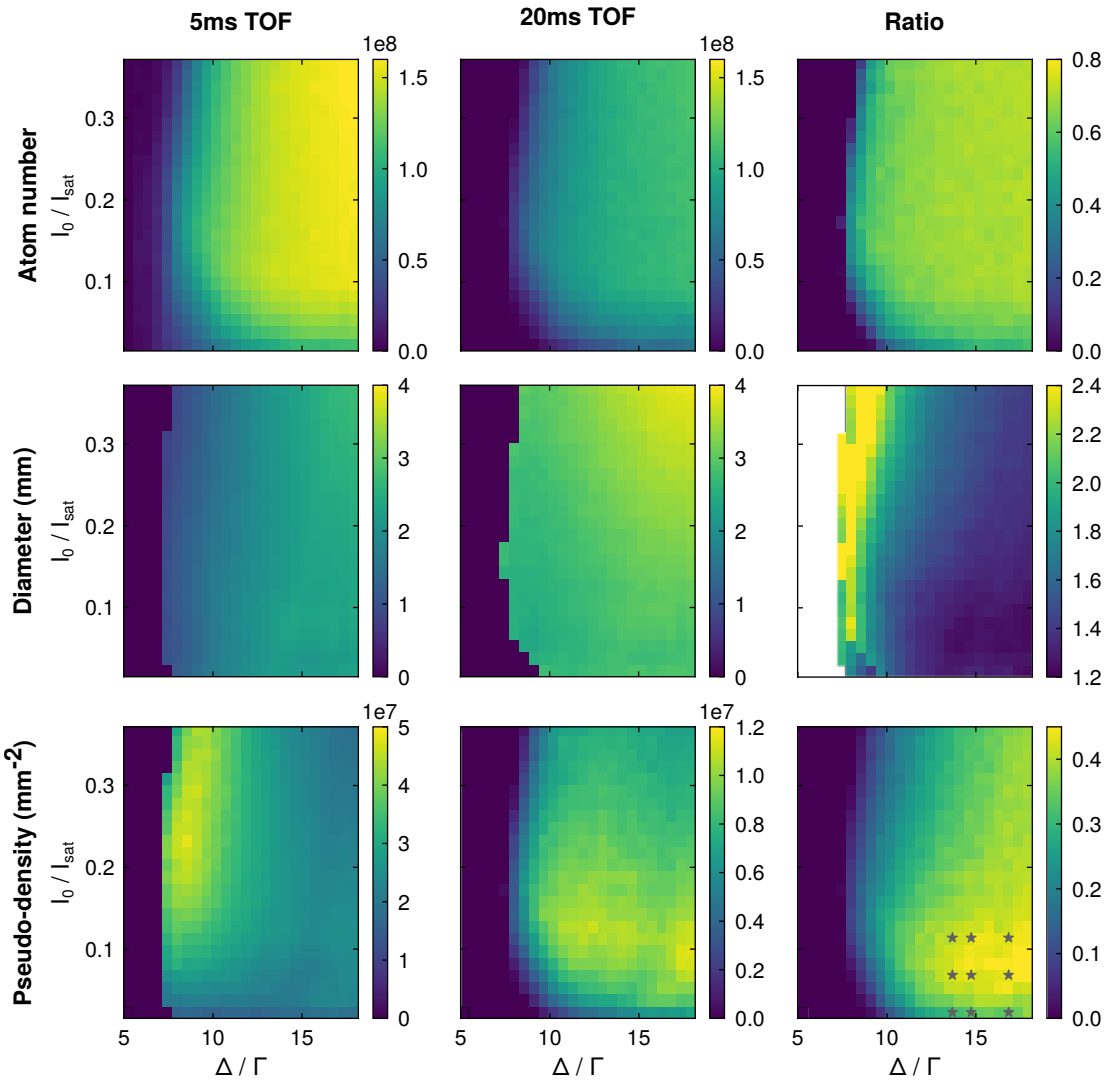

Figure A.2 | cMOT optimization. The cMOT is studied by looking at atom number (upper row), cloud diameter (middle row) and pseudo-density (lower row). The plots are functions of laser detuning and power at the end of the compression ramp. It was measured at $5\,\mathrm{ms}$ TOF (left column) and $20\,\mathrm{ms}$ TOF (middle column); the ratio of the different quantities (right column) is a good tool to know where to compress the MOT for a cold or dense cloud. The stars in the bottom right figure (density ratio) indicate where the temperature was measured. The temperature dependence on laser power is stronger than the dependence on laser frequency (see text). The cMOT can reach temperatures down to $8\,\mu\mathrm{K}$.

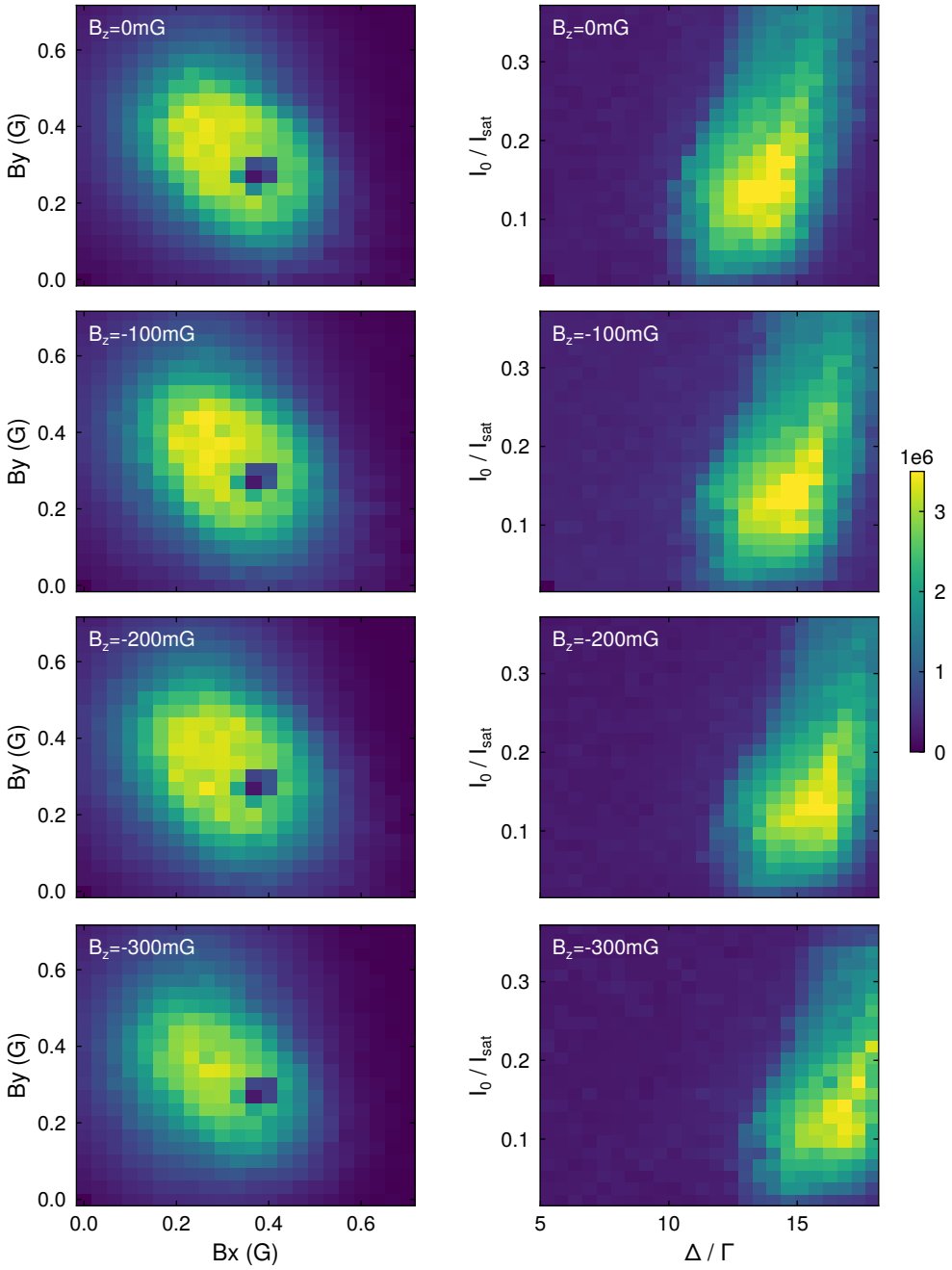

Figure A.3 | cMOT to ODT transfer optimization. The ODT loading from the cMOT is studied by looking at the number of trapped atoms after $500\,\mathrm{ms}$ in the dipole trap (with levitation), for different horizontal offset fields (left) and cMOT detunings and powers (right). The scans were repeated for different vertical offset fields (rows), to obtain the "2D+1" representation of the parameter space. The measurements were done for a MOT loading of $2\,\mathrm{s}$, at an ODT power of $130\,\mathrm{W}$ per beam and with 4 repetitions. The peak atom number is approx. $3.5 \cdot 10^6$, about $10\,\%$ of the atoms from the cMOT. On the left row, the dark dot is a local loss of atoms due to the proximity of the magnetic zero (see text). On the right row, the shift towards higher detuning for higher B_z offsets is consistent with the vertical displacement of the cMOT.

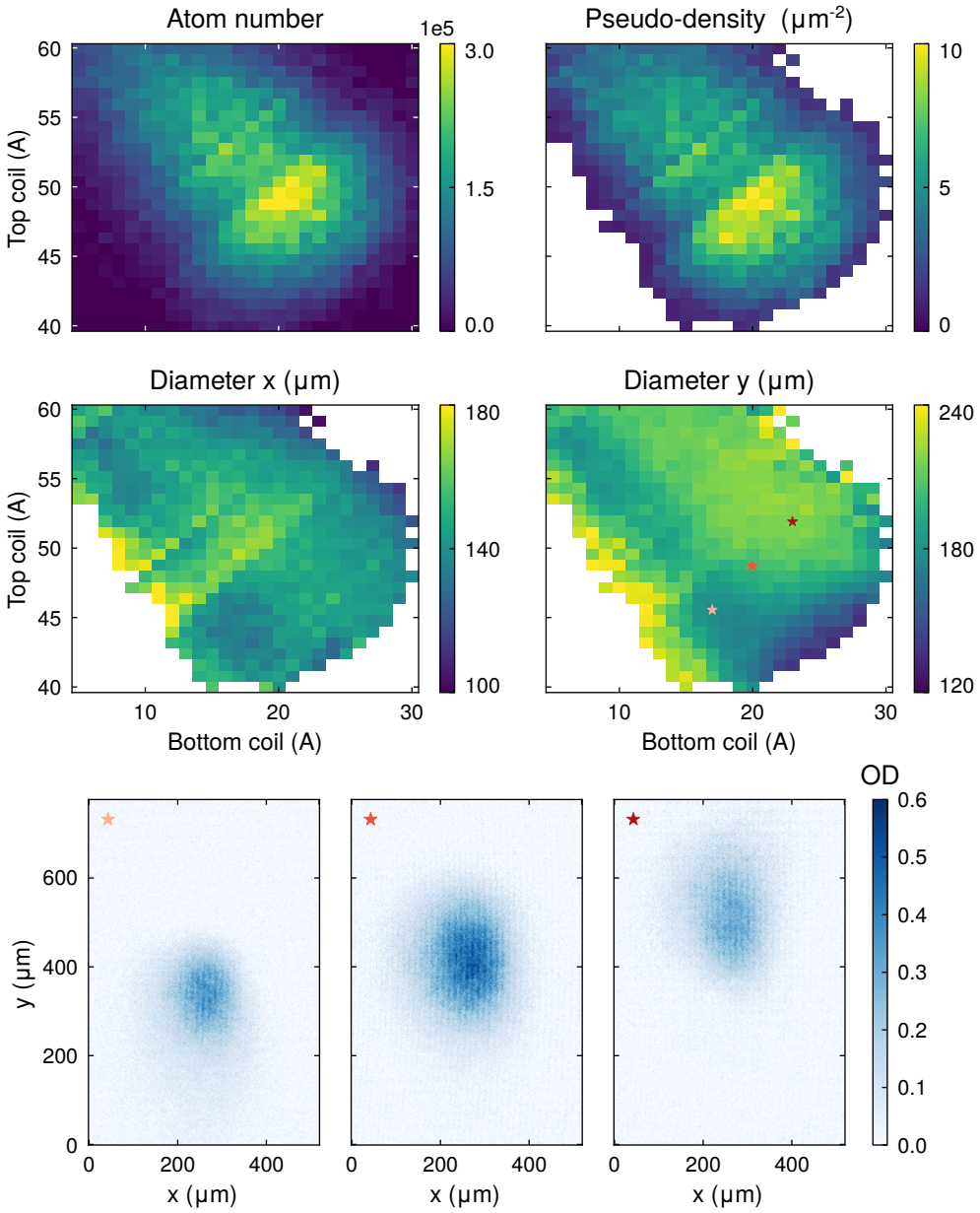

Figure A.4 | Transport fields optimization Atom number (upper left), cloud diameters (middle row) and pseudo-density (upper right) of the transported clouds for varying racetracks fields. The standard transport values at $(I_b, I_t) = (20\,\mathrm{A}, 48\,\mathrm{A})$ (star symbol) are set to the maximum of transported atom number. The Feshbach resonance is clearly visible on both the atom number and cloud size. The over- or under-levitation is also visible on the cloud's size and position. Absorption pictures of the transported cloud (bottom row) are shown for different points of the 2D map.

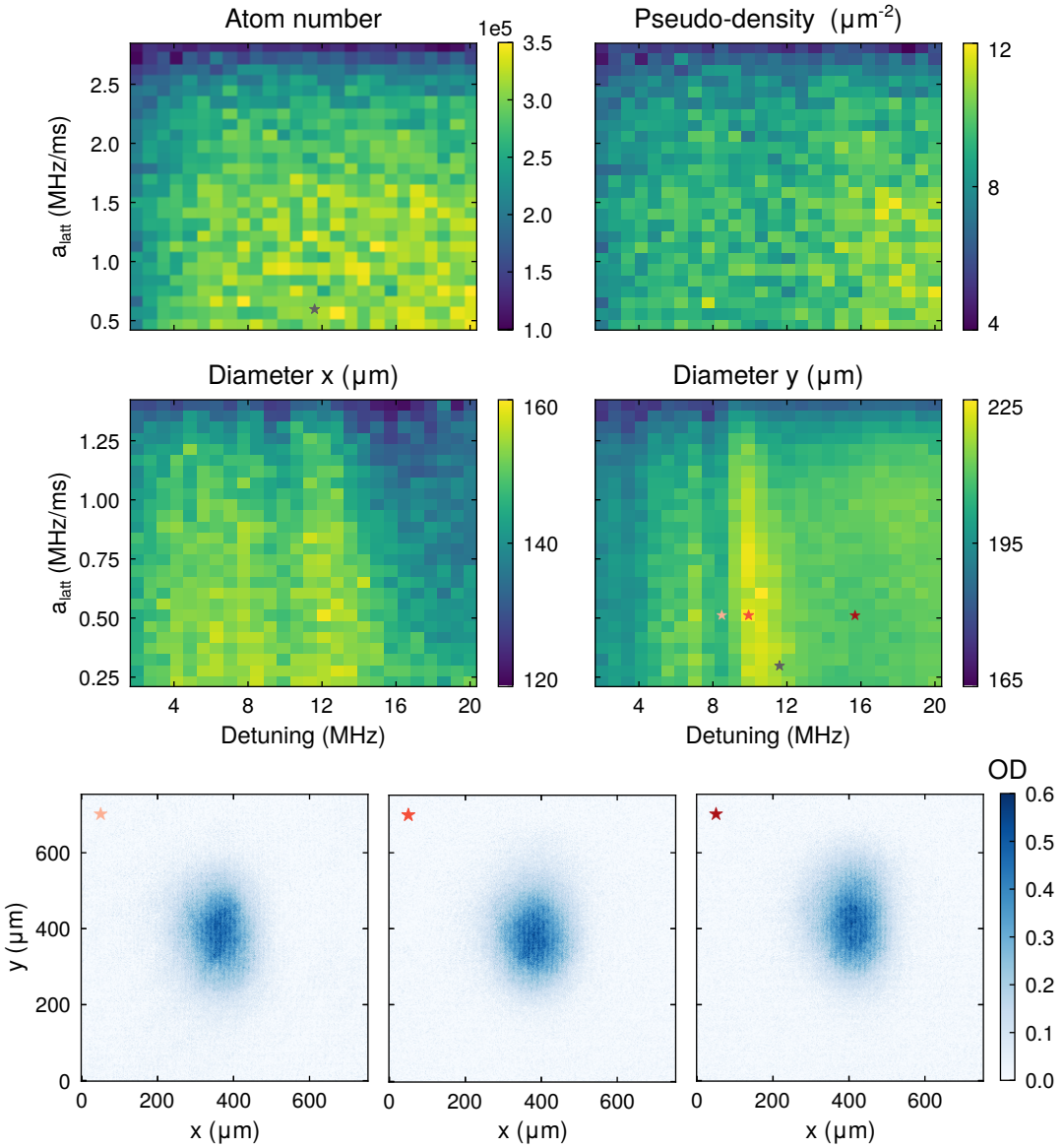

Figure A.5 | Transport speeds optimization Atom number (upper left), cloud diameters (middle row) and pseudo-density (upper right) of the transported clouds for varying accelerations and maximum speeds. The standard transport values at $(\Delta, a_{\mathrm{latt}}) = (11.6\,\mathrm{MHz}, 0.58\,\mathrm{MHz/ms})$ (star symbol) are set to be in the high-density region, and away from the transport resonances. They correspond to velocities and accelerations of $(v, a) = (6.2\,\mathrm{m/s}, 308\,\mathrm{m/s^2})$ The transport resonances the cloud's size, especially the vertical diameter. Absorption pictures of the transported cloud (bottom row) are shown for different points of the 2D map.

Appendix B

Detection methods

B.1 Absorption imaging

Absorption imaging is the standard procedure used to take pictures of the atomic ensemble in most ultracold atoms experiments. The principle is straightforward: a collimated beam of resonant light is sent on the atoms, which then absorb the photons and spontaneously re-emit them (given that the intensity is much lower than the transition's saturation intensity). The plane containing is then imaged and focused on the sensor of a CCD camera[1]. A second image is taken shortly after the image with the absorbed light (typically from $50\,\mu\mathrm{s}$ to $150\,\mathrm{ms}$ depending on the imaging setup and imaged atoms), to be used as a reference. Finally, a third picture can eventually be taken with no imaging light or atoms, to measure the dark noise of the camera itself to subtract it from the previous images. In our case, the camera was found to be stable enough from shot-to-shot to avoid using the third image, but a precise imaging scenario should take this effect into account. On the picture with atoms, the light intensity is reduced by the absorption according to the Beer-Lambert law:

$$I = I_0 e^{-n(x,y)\sigma} \tag{B.1}$$

where $n(x,y)$ is the column density of the cloud and σ the cross-section given by:

$$\sigma = \frac{\sigma_0}{1 + I_0/I_{\mathrm{sat}} + (2\Delta/\Gamma)^2} \tag{B.2}$$

with $\sigma_0 = \hbar\omega\Gamma/2I_{\mathrm{sat}}$ the cross-section on resonance, Δ the detuning, Γ the transition's linewidth and I_{sat} the saturation intensity. From these equations, the Optical Density (OD), defined as $\mathrm{OD}(x,y) = n(x,y)\sigma$, can be retrieved immediately from the ratio of the two images:

$$\mathrm{OD} = \ln \frac{I_{\mathrm{background}}}{I_{\mathrm{atoms}}} \tag{B.3}$$

The conversion from OD to atom number is then obtained by integrating the image:

$$N = \iint_{-\infty}^{\infty} n(x,y)dxdy = \frac{1}{\sigma}\iint_{-\infty}^{\infty} \mathrm{OD}(x,y)dxdy \tag{B.4}$$

[1] Allied Vision Technologies GmbH, Manta G-145B NIR mono PoE W270

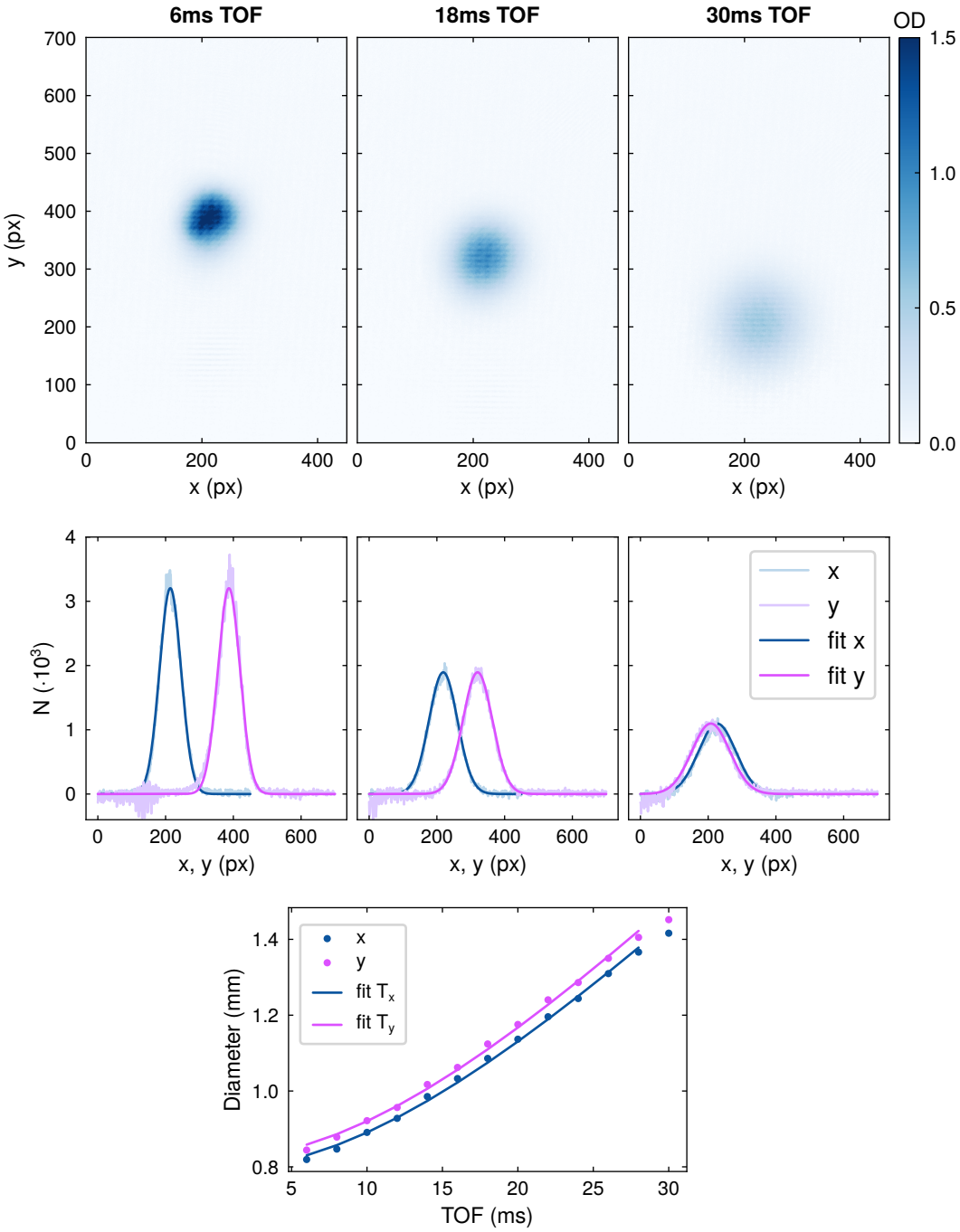

Figure B.1 | TOF thermometry. The absorption pictures (top row) of an Er cloud, released from a cMOT at $8\,\mu\mathrm{K}$, are fitted with a 2D-gaussian function (middle row), from which the temperature is derived (bottom row). The last points of the TOF were not included in the temperature fit because the cloud had fallen far enough to be partially out of the imaging field of view, and in an area with lower imaging light intensity, thus underestimating the cloud size.

Finally, absorption imaging has a bound on its reachable resolution, given by the Abbe diffraction limit:

$$d = \frac{\lambda}{2\mathrm{NA}} \tag{B.5}$$

where λ is the imaging light's wavelength and NA the numerical aperture of the imaging system. Examples of such absorption pictures are given in Fig. B.1. The last usual quantity is the Phase-Space Density (PSD), defined by:

$$\mathcal{D} = n\lambda_{\mathrm{dB}}^3 \tag{B.6}$$

with $\lambda_{\mathrm{dB}} = \sqrt{2\pi\hbar^2/mk_BT}$ the de Broglie wavelength. The PSD is actually the proper metric to quantify how close one is from the quantum regime. Essentially, reaching a PSD of the order of $\mathcal{D} \approx 1$ marks the onset of degeneracy, for BECs or DFGs. In particular, the onset of Bose-Einstein condensation happens at $\mathcal{D} \approx 2.6$ for atoms in a harmonic trap, and diverges for high degeneracy. For fermions, the Pauli blocking prevents the PSD from diverging, and $\mathcal{D}$ grows asymptotically with lower temperatures.

B.2 TOF thermometry

Most of the temperature values given in this thesis were obtained by Time-of-Flight (TOF) thermometry, where the temperature is extracted from the expansion of the cloud after its release from a trap. For a thermal cloud governed by Maxwell-Boltzmann distribution, the cloud's size during expansion is given by:

$$\sigma(t) = \sqrt{\sigma_0^2 + \bar{v}^2 t^2} \tag{B.7}$$

where the average velocity $\bar{v}$ of the atoms is used to define an associated temperature $T = m\bar{v}^2/k_{\mathrm{B}}$.

An example of such TOF thermometry is given in Fig. B.1, for a cloud of Er atoms released from a compressed Magneto-Optical Trap (MOT) with a measured temperature of $8\,\mu\mathrm{K}$. This method is particularly adequate for classical clouds with a high enough optical density, but several effects can lead to inaccurate results [276]. For example, residual magnetic fields and gradients, or a slow quench of the trap itself can influence the ballistic expansion of the cloud and lead to falsified measurements. The atom number can also be biased if the saturation parameter is close to (or above) unity, or too low and the beam is fully absorbed by the cloud.

B.3 Fermi thermometry

As discussed in Section 6.2 and [109, 131], the temperature of a Degenerate Fermi Gas (DFG) cannot be derived properly by TOF thermometry for $T/T_F \lesssim 0.5$. For a thermal cloud, the entirety of the cloud size gives the temperature, which is obtained from a gaussian fit. For a DFG, the Fermi pressure results in a shape close to that of a gaussian, but where the

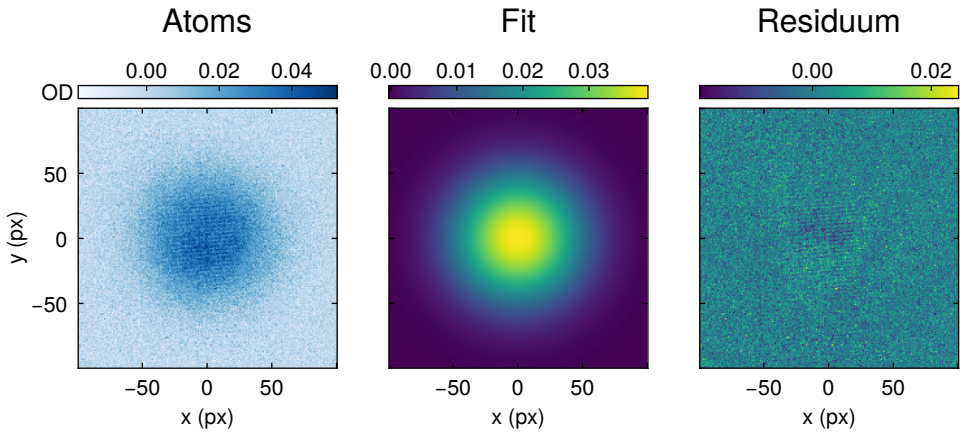

Figure B.2 | Fermi thermometry. Absorption picture of a DFG of Li (left), 2D-fit of the cloud (center), and residuals from the fit to the raw data (right). The OD of the absorption picture is rather low due to the long TOF ($4\,\mathrm{ms}$) and low atom number ($\sim$3000). The residuum shows value on the order of $5 \cdot 10^{-}4$, as well as the high-frequency noise also visible on the fitted data. This data point corresponds to the coldest $T/T_F = 0.2$ mentioned in Section 6.2.

information regarding the temperature lies in the low-density wings of distribution (*i.e.* at the Fermi surface). The thermometry of deeply degenerate Fermi clouds is thus famously difficult, since it is limited by the Signal-to-Noise Ratio (SNR) of the cloud's edges. Here, it is possible to fit the density distribution with a 2D-fit of the column density given by the absorption imaging. In that case, the 2D function for Fermi profiles is then:

$$n_{\mathrm{F,2D}}(x,y) = n_{\mathrm{2D},0} \frac{\mathrm{Li}_2\left(-\exp\left[q - (\frac{x^2}{R_x^2} + \frac{y^2}{R_y^2}) f(e^q)\right]\right)}{\mathrm{Li}_2(-e^q)} \tag{B.8}$$

where the fugacity $q = \mu\beta$, the logarithm of the fugacity, determines the shape of the cloud. For clouds with radial symmetry, it is also possible to make an azimuthal average to obtain a 1D profile[2] with an enhanced SNR, especially close to the edge. Finally, it is important to note that such a radial average is far superior to an integration along an axis, since this operation would result in a mixing of regions with high or low *local* degeneracy, hence destroying the sought signal. In our experiments, the Fermi gas of ^{6}Li is routinely fitted with the function given above; the procedure is illustrated in Fig. B.2.

Finally, below $T/T_F \lesssim 0.1$, the 2D fit reaches its limit as well, since the shape gets increasingly more difficult to distinguish from the $T = 0$ case. At that point, unless an exceptional imaging system is used for the absorption pictures, the standard solution is to use a second species as a thermometer, assuming that the cross-species thermalization occurs. Of course, the second species should either be classical or bosonic (but only partially condensed) to avoid the issue.

[2]One must be careful here: the radially-averaged profile corresponds to a slice through the 2D profile, and not an integrated profile along one of the directions

B.4 Bose thermometry

The thermometry of bosons is more accessible than its fermionic counterpart. It consists in doing bimodal fits to the absorption pictures, where the appearance of a sharp peak on top of the (gaussian) velocity is often presented as the "smoking gun" of condensation. The fit can be done either on the 2D-profiles from imaging, or on a 1D-profile obtained by integration of the absorption picture along one axis. In the 2D case, the fit is made with:

$$n(x,y) = n_{0,\mathrm{th}} e^{-x^2/2\sigma_x^2 - y^2/2\sigma_y^2} + n_{0,\mathrm{c}} \left(1 - \left[\frac{x}{w_x}\right]^2 - \left[\frac{y}{w_y}\right]^2\right)^2 \tag{B.9}$$

while the integrated case is best fitted with:

$$n(x) = n_{0,\mathrm{th}} e^{-x^2/2\sigma_x^2} + n_{0,\mathrm{c}} \left(1 - \left[\frac{x}{w}\right]^2\right)^2 \tag{B.10}$$

where $w_i = \sqrt{2\mu/m\omega_i^2}$ is the half-length of the trapped BEC along the direction i. From such a fit, one can retrieve both the absolute and critical temperatures of the cloud, given by:

$$k_B T \approx 0.94 \hbar\omega N^{1/3} \left(1 - \frac{N_C}{N_{\mathrm{tot}}}\right)^{1/3} \tag{B.11}$$

and

$$k_B T_c \approx 0.94 \hbar\omega N^{1/3} \tag{B.12}$$

which are linked *via*:

$$\frac{N_c}{N_{\mathrm{tot}}} = 1 - \left(\frac{T}{T_C}\right)^3 \tag{B.13}$$

Appendix C

Assembly and baking

The assembly of the vacuum system took over several weeks, between the assembly of the different parts, closing all the leaks, and baking the apparatus. An important preliminary step was the air-baking of the main chamber. Air-baking the vacuum components at $450\,^{\circ}\mathrm{C}$ for 24 hours creates a layer of oxidation, which in turn prevents the outgassing of hydrogen from the walls [286]. During the process, the sharp edges of the CF connections were protected with blind flanges and silver-annealed gaskets, screwed to the chamber by silvered screws. After the baking, the oxidation layer of the stainless steel chamber turned it to a bronze color, while the blind flanges came out goldened. This oxidation layer also makes the baking much faster, since we could reach the floor value of the turbopump in approximately one day (compared to a typical week long of baking).

A hard-learned lesson was also to **keep your molecular turbopump connected and pumping when you activate the getter materials of the NEG pumps**. Otherwise, the surrounding ion pumps will get saturated, and a good vacuum not possible anymore. Fortunately, the ion pumps can also be purged by removing their permanent magnet and baking them at $400\,^{\circ}\mathrm{C}$ for $8\,\mathrm{h}$. In our case, it was possible to purge them very nicely into the turbopump overnight, and the procedure resulted in an even faster pressure decay during the last cooldown.

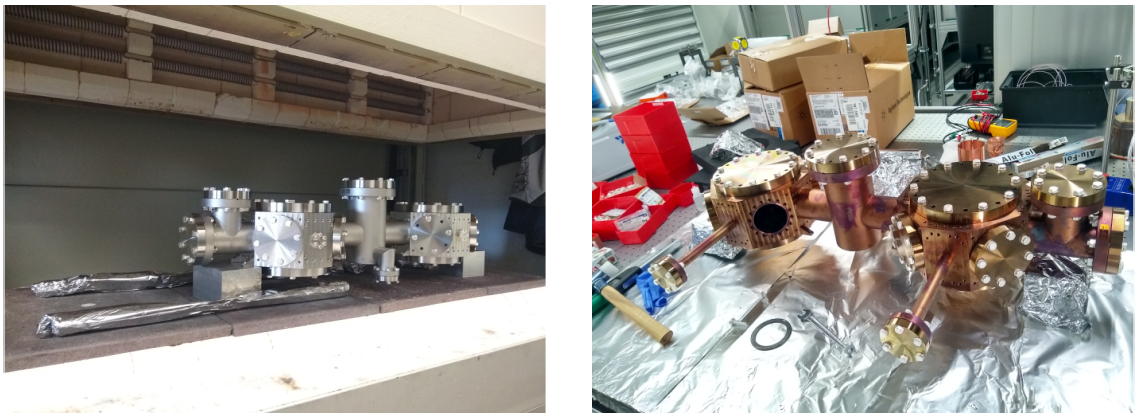

Figure C.1 | Air baking of the main vacuum chamber The main vacuum chamber was placed in a large oven (left), to be air-baked at $450\,^{\circ}\mathrm{C}$ for $24\,\mathrm{h}$. After the air-baking, the surface is oxidized and now has a bronze color (right).

Figure C.2 | Filling and closing the Er oven. Approximately $100\,\mathrm{g}$ of Er chunks (left) were placed in the oven. After placing the small chunks in the crucible, it is maintained in place at the exit of the oven by a Tantalum filament (right, star shaped).

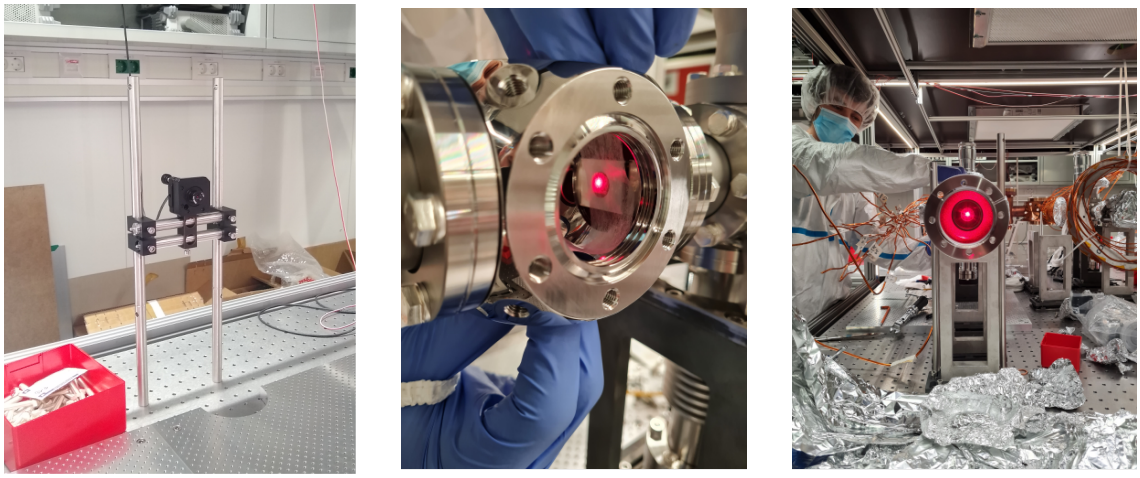

Figure C.3 | Vacuum assembly with laser alignment. One laser pointer per arm (Er/Li) was fixed at one end of the table and aligned to it. The vacuum parts were assembled by continuously checking the line-of-sight through the machine, a task optics-cleaning papers excel at. Special thanks to our student Max, for not hesitating one second before sacrificing his phone camera for the greater cause (no camera was harmed in the making of this machine).

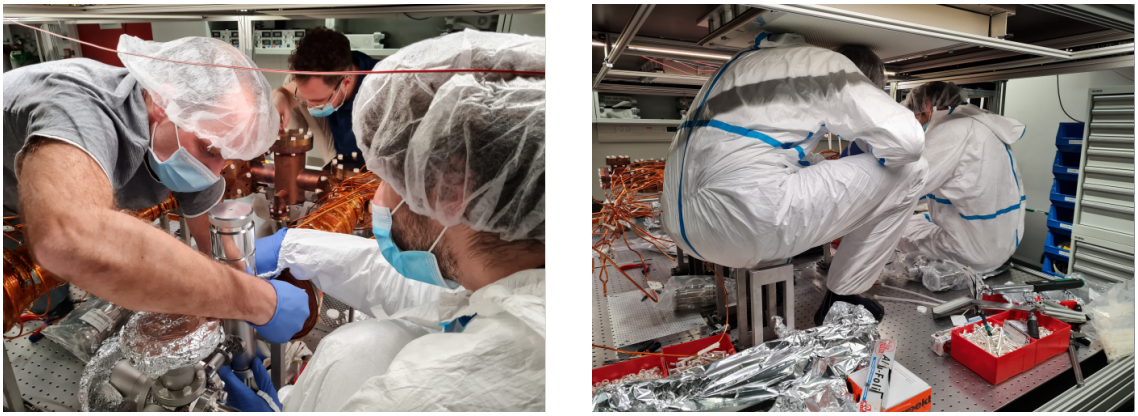

Figure C.4 | Perks of assembling a vacuum system. Left: a clueless PhD student in its natural habitat, learning from the utmost expert. Right: demonstration of the creative usage of optical tables required to assemble such a system.

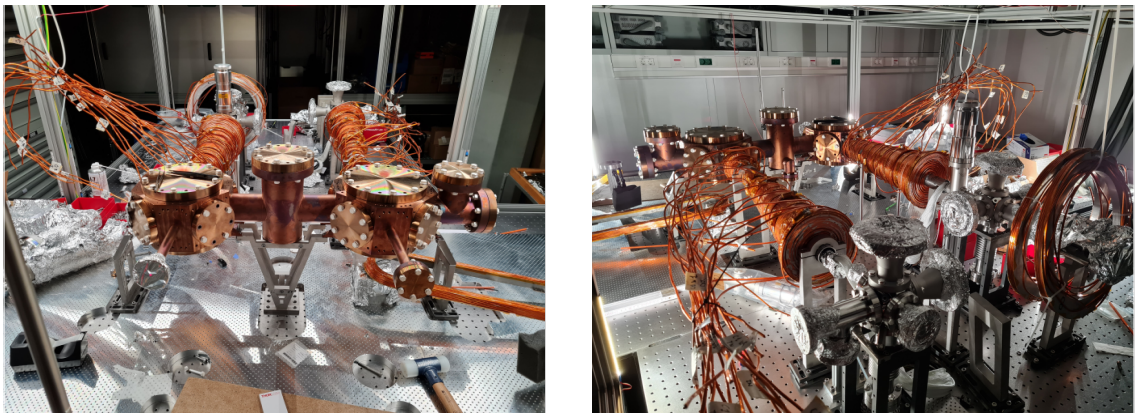

Figure C.5 | Vacuum apparatus under construction.

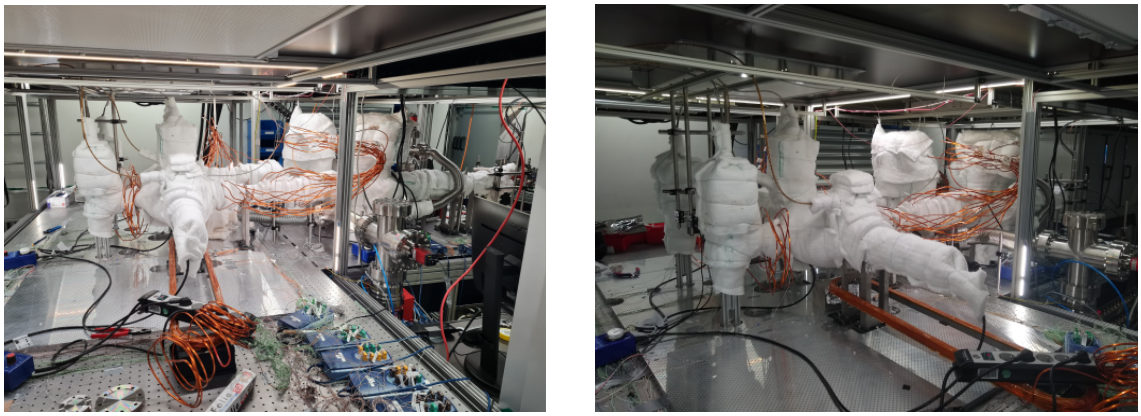

Figure C.6 | Wrapped machine for baking. The entire apparatus was wrapped in heating filaments and covered in insulating material to ensure a homogeneous thermalization during the baking, to prevent any cold spot inside which could result in degraded vacuum. One must be careful with the placement of heating filaments, to keep the viewports at a maximum temperature of $180\,^{\circ}$. Sensors were placed inside to monitor the temperature in many strategic spots.

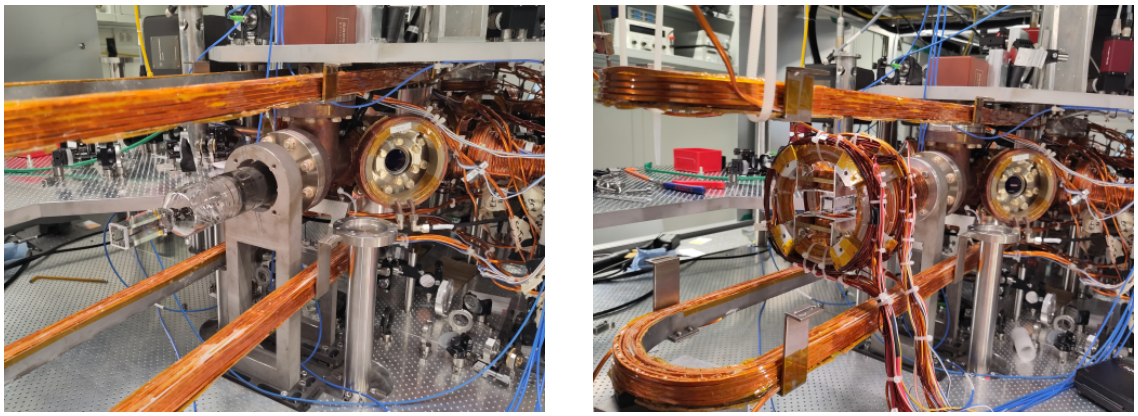

Figure C.7 | Mounting of glass cell coils setup. The bare glass cell (left) was kept protected with a metallic tube until the coils setup was brought around it (right). The racetracks coils are above and below the cell; in the background one can see the Er chamber as well.

Bibliography

[1] Hänsch, T. W. and A. L. Schawlow. *Cooling of Gases by Laser Radiation*, Optics Communications **13**., 68–69 (Jan. 1975). DOI: 10.1016/0030-4018(75)90159-5 (cit. on p. 1).

[2] Phillips, W. D. and H. Metcalf. *Laser Deceleration of an Atomic Beam*, Physical Review Letters **48**., 596–599 (Mar. 1982). DOI: 10.1103/physrevlett.48.596 (cit. on pp. 1, 38).

[3] Ertmer, W., R. Blatt, J. R. Hall, and M. Zhu. *Laser Manipulation of Atomic Beam Velocities: Demonstration of Stopped Atoms and Velocity Reversal*, Physical Review Letters **54**., 996–999 (1985). DOI: 10.1103/PhysRevLett.54.996 (cit. on pp. 1, 38).

[4] Raab, E. L., M. Prentiss, A. Cable, S. Chu, and D. E. Pritchard. *Trapping of Neutral Sodium Atoms with Radiation Pressure*, Physical Review Letters **59**., 2631–2634 (Dec. 1987). DOI: 10.1103/physrevlett.59.2631 (cit. on pp. 1, 70).

[5] Lett, P. D., R. N. Watts, C. I. Westbrook, W. D. Phillips, P. L. Gould, and H. J. Metcalf. *Observation of Atoms Laser Cooled below the Doppler Limit*, Physical Review Letters **61**., 169–172 (July 11, 1988). DOI: 10.1103/PhysRevLett.61.169 (cit. on pp. 1, 38).

[6] Dalibard, J. and C. Cohen-Tannoudji. *Laser Cooling below the Doppler Limit by Polarization Gradients: Simple Theoretical Models*, Journal of the Optical Society of America B **6**., 2023 (Nov. 1989). DOI: 10.1364/josab.6.002023 (cit. on pp. 1, 28).

[7] Aspect, A., E. Arimondo, R. Kaiser, N. Vansteenkiste, and C. Cohen-Tannoudji. *Laser Cooling below the One-Photon Recoil Energy by Velocity-Selective Coherent Population Trapping*, Physical Review Letters **61**., 826–829 (Aug. 15, 1988). DOI: 10.1103/PhysRevLett.61.826 (cit. on p. 1).

[8] Anderson, M. H., J. R. Ensher, M. R. Matthews, C. E. Wieman, and E. A. Cornell. *Observation of Bose-Einstein Condensation in a Dilute Atomic Vapor*, Science **269**., 198–201 (July 1995). DOI: 10.1126/science.269.5221.198 (cit. on p. 1).

[9] Davis, K. B., M. O. Mewes, M. R. Andrews, N. J. van Druten, D. S. Durfee, D. M. Kurn, and W. Ketterle. *Bose-Einstein Condensation in a Gas of Sodium Atoms*, Physical Review Letters **75**., 3969–3973 (Nov. 1995). DOI: 10.1103/physrevlett.75.3969 (cit. on p. 1).

[10] Bradley, C. C., C. A. Sackett, J. J. Tollett, and R. G. Hulet. *Evidence of Bose-Einstein Condensation in an Atomic Gas with Attractive Interactions*, Physical Review Letters **75**., 1687–1690 (Aug. 28, 1995). DOI: 10.1103/PhysRevLett.75.1687 (cit. on p. 1).

[11] DeMarco, B. *Onset of Fermi Degeneracy in a Trapped Atomic Gas*, Science **285**., 1703–1706 (Sept. 1999). DOI: 10.1126/science.285.5434.1703 (cit. on pp. 1, 11).

[12] Ketterle, W. and N. J. V. Druten. *Evaporative Cooling of Trapped Atoms*, Advances In Atomic, Molecular, and Optical Physics, 181–236 (1996). DOI: 10.1016/s1049-250x(08)60101-9 (cit. on pp. 1, 10).

[13] Andrews, M. R., C. G. Townsend, H.-J. Miesner, D. S. Durfee, D. M. Kurn, and W. Ketterle. *Observation of Interference Between Two Bose Condensates*, Science **275**., 637–641 (Jan. 31, 1997). DOI: 10.1126/science.275.5300.637 (cit. on p. 1).

[14] Truscott, A. G., K. E. Strecker, W. I. McAlexander, G. B. Partridge, and R. G. Hulet. *Observation of Fermi Pressure in a Gas of Trapped Atoms*, Science **291**., 2570–2572 (Mar. 30, 2001). DOI: 10.1126/science.1059318 (cit. on pp. 1, 11).

[15] Madison, K. W., F. Chevy, W. Wohlleben, and J. Dalibard. *Vortex Formation in a Stirred Bose-Einstein Condensate*, Physical Review Letters **84**., 806–809 (Jan. 31, 2000). DOI: 10.1103/PhysRevLett.84.806 (cit. on p. 1).

[16] Abo-Shaeer, J. R., C. Raman, J. M. Vogels, and W. Ketterle. *Observation of Vortex Lattices in Bose-Einstein Condensates*, Science **292**., 476–479 (Apr. 20, 2001). DOI: 10.1126/science.1060182 (cit. on p. 1).

[17] Zwierlein, M. W., J. R. Abo-Shaeer, A. Schirotzek, C. H. Schunck, and W. Ketterle. *Vortices and Superfluidity in a Strongly Interacting Fermi Gas*, Nature **435**., 1047–1051 (June 2005). DOI: 10.1038/nature03858 (cit. on p. 1).

[18] Greiner, M., C. A. Regal, and D. S. Jin. *Emergence of a Molecular Bose–Einstein Condensate from a Fermi Gas*, Nature **426**., 537–540 (Dec. 2003). DOI: 10.1038/nature02199 (cit. on pp. 1, 11).

[19] Jochim, S., M. Bartenstein, A. Altmeyer, G. Hendl, S. Riedl, C. Chin, J. Hecker Denschlag, and R. Grimm. *Bose-Einstein Condensation of Molecules*, Science **302**., 2101–2103 (Dec. 2003). DOI: 10.1126/science.1093280 (cit. on p. 1).

[20] Zwierlein, M. W., C. A. Stan, C. H. Schunck, S. M. F. Raupach, S. Gupta, Z. Hadzibabic, and W. Ketterle. *Observation of Bose-Einstein Condensation of Molecules*, Physical Review Letters **91**., 250401 (Dec. 15, 2003). DOI: 10.1103/PhysRevLett.91.250401 (cit. on p. 1).

[21] Dulieu, O. and A. Osterwalder. *Cold Chemistry*. Royal Society of Chemistry, 2017. DOI: 10.1039/9781782626800 (cit. on p. 1).

[22] Greiner, M., O. Mandel, T. Esslinger, T. W. Hänsch, and I. Bloch. *Quantum Phase Transition from a Superfluid to a Mott Insulator in a Gas of Ultracold Atoms*, Nature **415**., 39–44 (Jan. 2002). DOI: 10.1038/415039a (cit. on pp. 1, 9).

[23] Jördens, R., N. Strohmaier, K. Günter, H. Moritz, and T. Esslinger. *A Mott Insulator of Fermionic Atoms in an Optical Lattice*, Nature **455**., 204–207 (Sept. 2008). DOI: 10.1038/nature07244 (cit. on pp. 1, 9).

[24] Schneider, U., L. Hackermüller, S. Will, Th. Best, I. Bloch, T. A. Costi, R. W. Helmes, D. Rasch, and A. Rosch. *Metallic and Insulating Phases of Repulsively Interacting Fermions in a 3D Optical Lattice*, Science **322**., 1520–1525 (Dec. 5, 2008). DOI: 10.1126/science.1165449 (cit. on pp. 1, 9).

[25] Schäfer, F., T. Fukuhara, S. Sugawa, Y. Takasu, and Y. Takahashi. *Tools for Quantum Simulation with Ultracold Atoms in Optical Lattices*, Nature Reviews Physics **2**., 411–425 (July 2020). DOI: 10.1038/s42254-020-0195-3 (cit. on pp. 1, 10).

[26] Chin, C., R. Grimm, P. Julienne, and E. Tiesinga. *Feshbach Resonances in Ultracold Gases*, Reviews of Modern Physics **82**., 1225–1286 (Apr. 2010). DOI: 10.1103/revmodphys.82.1225 (cit. on pp. 1, 6, 82).

[27] Feynman, R. P. *Simulating Physics with Computers*, International Journal of Theoretical Physics **21**., 467–488 (June 1982). DOI: 10.1007/bf02650179 (cit. on p. 2).

[28] Hubbard, J. *Electron Correlations in Narrow Energy Bands*, Proceedings of the Royal Society of London. Series A. Mathematical and Physical Sciences **276**., 238–257 (Nov. 26, 1963). DOI: 10.1098/rspa.1963.0204 (cit. on pp. 2, 5).

[29] Keimer, B., S. A. Kivelson, M. R. Norman, S. Uchida, and J. Zaanen. *From Quantum Matter to High-Temperature Superconductivity in Copper Oxides*, Nature **518**., 179–186 (Feb. 12, 2015). DOI: 10.1038/nature14165 (cit. on pp. 2, 6, 8, 9).

[30] Bednorz, J. G. and K. A. Müller. *Possible highT c Superconductivity in the BaLaCuO System*, Zeitschrift für Physik B Condensed Matter **64**., 189–193 (June 1986). DOI: 10.1007/BF01303701 (cit. on pp. 2, 5).

[31] Zhou, X., W.-S. Lee, M. Imada, N. Trivedi, P. Phillips, H.-Y. Kee, P. Törmä, and M. Eremets. *High-Temperature Superconductivity*, Nature Reviews Physics **3**., 462–465 (May 2021). DOI: 10.1038/s42254-021-00324-3 (cit. on p. 2).

[32] Gross, C. and W. S. Bakr. *Quantum Gas Microscopy for Single Atom and Spin Detection*, Nature Physics **17**., 1316–1323 (Nov. 2021). DOI: 10.1038/s41567-021-01370-5 (cit. on pp. 2, 9, 10, 46).

[33] LeBlanc, J. P. F. *et al. Solutions of the Two-Dimensional Hubbard Model: Benchmarks and Results from a Wide Range of Numerical Algorithms*, Physical Review X **5**., 041041 (Dec. 14, 2015). DOI: 10.1103/PhysRevX.5.041041 (cit. on pp. 2, 9).

[34] Qin, M., T. Schäfer, S. Andergassen, P. Corboz, and E. Gull. *The Hubbard Model: A Computational Perspective*, Annual Review of Condensed Matter Physics **13**., 275–302 (Mar. 10, 2022). DOI: 10.1146/annurev-conmatphys-090921-033948 (cit. on pp. 2, 6, 9).

[35] Tarruell, L. and L. Sanchez-Palencia. *Quantum Simulation of the Hubbard Model with Ultracold Fermions in Optical Lattices*. Jan. 4, 2019. DOI: 10.48550/arXiv.1809.00571. URL: http://arxiv.org/abs/1809.00571 (visited on 11/27/2025). Pre-published (cit. on pp. 2, 5–9).

[36] Bohrdt, A., L. Homeier, C. Reinmoser, E. Demler, and F. Grusdt. *Exploration of Doped Quantum Magnets with Ultracold Atoms*, Annals of Physics. Special Issue on Philip W. Anderson **435**, 168651 (Dec. 1, 2021). DOI: 10.1016/j.aop.2021.168651 (cit. on pp. 2, 8, 9).

[37] Hadzibabic, Z., S. Gupta, C. A. Stan, C. H. Schunck, M. W. Zwierlein, K. Dieckmann, and W. Ketterle. *Fiftyfold Improvement in the Number of Quantum Degenerate Fermionic Atoms*, Physical Review Letters **91**., 160401 (Oct. 16, 2003). DOI: 10.1103/PhysRevLett.91.160401 (cit. on pp. 2, 13).

[38] Delehaye, M., S. Laurent, I. Ferrier-Barbut, S. Jin, F. Chevy, and C. Salomon. *Critical Velocity and Dissipation of an Ultracold Bose-Fermi Counterflow*, Physical Review Letters **115**. (Dec. 2015). DOI: 10.1103/physrevlett.115.265303 (cit. on p. 2).

[39] Bernier, J.-S., C. Kollath, A. Georges, L. De Leo, F. Gerbier, C. Salomon, and M. Köhl. *Cooling Fermionic Atoms in Optical Lattices by Shaping the Confinement*, Physical Review A **79**., 061601 (June 3, 2009). DOI: 10.1103/PhysRevA.79.061601 (cit. on pp. 2, 10).

[40] Mazurenko, A., C. S. Chiu, G. Ji, M. F. Parsons, M. Kanász-Nagy, R. Schmidt, F. Grusdt, E. Demler, D. Greif, and M. Greiner. *A Cold-Atom Fermi–Hubbard Antiferromagnet*, Nature **545**., 462–466 (May 2017). DOI: 10.1038/nature22362 (cit. on pp. 2, 10).

[41] Chalopin, T. *et al. Probing the Magnetic Origin of the Pseudogap Using a Fermi-Hubbard Quantum Simulator*. Version 1. 2024. DOI: 10.48550/ARXIV.2412.17801. URL: https://arxiv.org/abs/2412.17801 (visited on 11/29/2025). Pre-published (cit. on pp. 2, 8, 10).

[42] Kendrick, L. H., A. Kale, Y. Gang, A. D. Deters, M. Lebrat, A. W. Young, and M. Greiner. *Pseudogap in a Fermi-Hubbard Quantum Simulator*. Version 1. 2025. DOI: 10.48550/ARXIV.2509.18075. URL: https://arxiv.org/abs/2509.18075 (visited on 12/03/2025). Pre-published (cit. on pp. 2, 10).

[43] Xu, M., L. H. Kendrick, A. Kale, Y. Gang, C. Feng, S. Zhang, A. W. Young, M. Lebrat, and M. Greiner. *A Neutral-Atom Hubbard Quantum Simulator in the Cryogenic Regime*, Nature **642**., 909–915 (June 2025). DOI: 10.1038/s41586-025-09112-w (cit. on pp. 2, 8, 10, 109).

[44] Brown-Hayes, M., Q. Wei, C. Presilla, and R. Onofrio. *Thermodynamical Approaches to Efficient Sympathetic Cooling in Ultracold Fermi-Bose Atomic Mixtures*, Physical Review A **78**., 013617 (July 2008). DOI: 10.1103/physreva.78.013617 (cit. on pp. 3, 13).

[45] LeBlanc, L. J. and J. H. Thywissen. *Species-Specific Optical Lattices*, Physical Review A **75**., 053612 (May 2007). DOI: 10.1103/physreva.75.053612 (cit. on pp. 3, 17).

[46] Baroni, C., G. Lamporesi, and M. Zaccanti. *Quantum Mixtures of Ultracold Gases of Neutral Atoms*, Nature Reviews Physics **6**., 736–752 (Dec. 2024). DOI: 10.1038/s42254-024-00773-6 (cit. on pp. 3, 13).

[47] Presilla, C. and R. Onofrio. *Cooling Dynamics of Ultracold Two-Species Fermi-Bose Mixtures*, Physical Review Letters **90**., 030404 (Jan. 2003). DOI: 10.1103/physrevlett.90.030404 (cit. on pp. 3, 13).

[48] Ban, H. Y., M. Jacka, J. L. Hanssen, J. Reader, and J. J. McClelland. *Laser Cooling Transitions in Atomic Erbium*, Optics Express **13**., 3185 (2005). DOI: 10.1364/opex.13.003185 (cit. on pp. 3, 26, 28, 90).

[49] Gehm, E. "Preparation of an Optically-Trapped Degenerate Fermi Gas of ^{6}Li> Finding the Route to Degeneracy." PhD thesis. Duke University, 2003 (cit. on pp. 3, 20, 28).

[50] De Martino, A., F. Kiesel, J. Auch, K. Karpov, and C. Gross. *Dissipationless Tune-out Trapping for a Lanthanide–Alkali-Metal Quantum Gas Mixture*, Physical Review A **112**., L051304 (Nov. 14, 2025). DOI: 10.1103/rykg-qn6s (cit. on pp. 3, 17, 18).

[51] Gutzwiller, M. C. *Effect of Correlation on the Ferromagnetism of Transition Metals*, Physical Review Letters **10**., 159–162 (Mar. 1, 1963). DOI: 10.1103/PhysRevLett.10.159 (cit. on p. 5).

[52] Kanamori, J. *Electron Correlation and Ferromagnetism of Transition Metals*, Progress of Theoretical Physics **30**., 275–289 (Sept. 1963). DOI: 10.1143/PTP.30.275 (cit. on p. 5).

[53] Anderson, P. W. *The Resonating Valence Bond State in La_2 CuO_4 and Superconductivity*, Science **235**., 1196–1198 (Mar. 6, 1987). DOI: 10.1126/science.235.4793.1196 (cit. on p. 5).

[54] Bloch, I., J. Dalibard, and W. Zwerger. *Many-Body Physics with Ultracold Gases*, Reviews of Modern Physics **80**., 885–964 (July 2008). DOI: 10.1103/revmodphys.80.885 (cit. on pp. 5, 11).

[55] Loh, E. Y., J. E. Gubernatis, R. T. Scalettar, S. R. White, D. J. Scalapino, and R. L. Sugar. *Sign Problem in the Numerical Simulation of Many-Electron Systems*, Physical Review B **41**., 9301–9307 (May 1, 1990). DOI: 10.1103/PhysRevB.41.9301 (cit. on p. 6).

[56] Ho, A. F., M. A. Cazalilla, and T. Giamarchi. *Quantum Simulation of the Hubbard Model: The Attractive Route*, Physical Review A **79**., 033620 (Mar. 19, 2009). DOI: 10.1103/PhysRevA.79.033620 (cit. on p. 7).

[57] Bakr, W. S., Z. Ba, and M. L. Prichard. *Microscopy of Ultracold Fermions in Optical Lattices*. July 5, 2025. DOI: 10.48550/arXiv.2507.04042. URL: http://arxiv.org/abs/2507.04042 (visited on 11/28/2025). Pre-published (cit. on pp. 8–10).

[58] Šimkovic, F., R. Rossi, A. Georges, and M. Ferrero. *Origin and Fate of the Pseudogap in the Doped Hubbard Model*, Science **385**., eade9194 (Sept. 20, 2024). DOI: 10.1126/science.ade9194 (cit. on pp. 8, 9).

[59] Arovas, D. P., E. Berg, S. A. Kivelson, and S. Raghu. *The Hubbard Model*, Annual Review of Condensed Matter Physics **13**., 239–274 (Mar. 10, 2022). DOI: 10.1146/annurev-conmatphys-031620-102024 (cit. on p. 9).

[60] Wu, W., M. S. Scheurer, S. Chatterjee, S. Sachdev, A. Georges, and M. Ferrero. *Pseudogap and Fermi-Surface Topology in the Two-Dimensional Hubbard Model*, Physical Review X **8**., 021048 (May 22, 2018). DOI: 10.1103/PhysRevX.8.021048 (cit. on p. 9).

[61] Kao, H. C., D. Li, and B. Rosenstein. *Unified Intermediate Coupling Description of Pseudogap and Strange Metal Phases of Cuprates*, Physical Review B **107**., 054508 (Feb. 24, 2023). DOI: 10.1103/PhysRevB.107.054508 (cit. on p. 9).

[62] Proust, C. and L. Taillefer. *The Remarkable Underlying Ground States of Cuprate Superconductors*, Annual Review of Condensed Matter Physics **10**., 409–429 (Mar. 10, 2019). DOI: 10.1146/annurev-conmatphys-031218-013210 (cit. on p. 9).

[63] Zheng, B.-X., C.-M. Chung, P. Corboz, G. Ehlers, M.-P. Qin, R. M. Noack, H. Shi, S. R. White, S. Zhang, and G. K.-L. Chan. *Stripe Order in the Underdoped Region of the Two-Dimensional Hubbard Model*, Science **358**., 1155–1160 (Dec. 2017). DOI: 10.1126/science.aam7127 (cit. on p. 9).

[64] Qin, M., C.-M. Chung, H. Shi, E. Vitali, C. Hubig, U. Schollwöck, S. R. White, S. Zhang, and Simons Collaboration on the Many-Electron Problem. *Absence of Superconductivity in the Pure Two-Dimensional Hubbard Model*, Physical Review X **10**., 031016 (July 21, 2020). DOI: 10.1103/PhysRevX.10.031016 (cit. on p. 9).

[65] Huang, E. W., T. Liu, W. O. Wang, H.-C. Jiang, P. Mai, T. A. Maier, S. Johnston, B. Moritz, and T. P. Devereaux. *Fluctuating Intertwined Stripes in the Strange Metal Regime of the Hubbard Model*, Physical Review B **107**., 085126 (Feb. 15, 2023). DOI: 10.1103/PhysRevB.107.085126 (cit. on p. 9).

[66] Xu, H., C.-M. Chung, M. Qin, U. Schollwöck, S. R. White, and S. Zhang. *Coexistence of Superconductivity with Partially Filled Stripes in the Hubbard Model*, Science **384**., eadh7691 (May 10, 2024). DOI: 10.1126/science.adh7691 (cit. on p. 9).

[67] Köhl, M., H. Moritz, T. Stöferle, K. Günter, and T. Esslinger. *Fermionic Atoms in a Three Dimensional Optical Lattice: Observing Fermi Surfaces, Dynamics, and Interactions*, Physical Review Letters **94**., 080403 (Mar. 4, 2005). DOI: 10.1103/PhysRevLett.94.080403 (cit. on p. 9).

[68] Rom, T., Th. Best, D. Van Oosten, U. Schneider, S. Fölling, B. Paredes, and I. Bloch. *Free Fermion Antibunching in a Degenerate Atomic Fermi Gas Released from an Optical Lattice*, Nature **444**., 733–736 (Dec. 2006). DOI: 10.1038/nature05319 (cit. on p. 9).

[69] Chin, J. K., D. E. Miller, Y. Liu, C. Stan, W. Setiawan, C. Sanner, K. Xu, and W. Ketterle. *Evidence for Superfluidity of Ultracold Fermions in an Optical Lattice*, Nature **443**., 961–964 (Oct. 2006). DOI: 10.1038/nature05224 (cit. on p. 9).

[70] Greif, D., T. Uehlinger, G. Jotzu, L. Tarruell, and T. Esslinger. *Short-Range Quantum Magnetism of Ultracold Fermions in an Optical Lattice*, Science **340**., 1307–1310 (June 14, 2013). DOI: 10.1126/science.1236362 (cit. on p. 9).

[71] Hart, R. A., P. M. Duarte, T.-L. Yang, X. Liu, T. Paiva, E. Khatami, R. T. Scalettar, N. Trivedi, D. A. Huse, and R. G. Hulet. *Observation of Antiferromagnetic Correlations in the Hubbard Model with Ultracold Atoms*, Nature **519**., 211–214 (Mar. 2015). DOI: 10.1038/nature14223 (cit. on p. 9).

[72] Bakr, W. S., J. I. Gillen, A. Peng, S. Fölling, and M. Greiner. *A Quantum Gas Microscope for Detecting Single Atoms in a Hubbard-regime Optical Lattice*, Nature **462**., 74–77 (Nov. 2009). DOI: 10.1038/nature08482 (cit. on p. 9).

[73] Sherson, J. F., C. Weitenberg, M. Endres, M. Cheneau, I. Bloch, and S. Kuhr. *Single-Atom-Resolved Fluorescence Imaging of an Atomic Mott Insulator*, Nature **467**., 68–72 (Sept. 2010). DOI: 10.1038/nature09378 (cit. on p. 9).

[74] Parsons, M. F., F. Huber, A. Mazurenko, C. S. Chiu, W. Setiawan, K. Wooley-Brown, S. Blatt, and M. Greiner. *Site-Resolved Imaging of Fermionic Lithium 6 in an Optical Lattice*, Physical Review Letters **114**., 213002 (May 2015). DOI: 10.1103/physrevlett.114.213002 (cit. on p. 9).

[75] Omran, A., M. Boll, T. A. Hilker, K. Kleinlein, G. Salomon, I. Bloch, and C. Gross. *Microscopic Observation of Pauli Blocking in Degenerate Fermionic Lattice Gases*, Physical Review Letters **115**., 263001 (Dec. 23, 2015). DOI: 10.1103/PhysRevLett.115.263001 (cit. on pp. 9, 28).

[76] Cheuk, L. W., M. A. Nichols, M. Okan, T. Gersdorf, V. V. Ramasesh, W. S. Bakr, T. Lompe, and M. W. Zwierlein. *Quantum-Gas Microscope for Fermionic Atoms*, Physical Review Letters **114**., 193001 (May 13, 2015). DOI: 10.1103/PhysRevLett.114.193001 (cit. on p. 9).

[77] Haller, E., J. Hudson, A. Kelly, D. A. Cotta, B. Peaudecerf, G. D. Bruce, and S. Kuhr. *Single-Atom Imaging of Fermions in a Quantum-Gas Microscope*, Nature Physics **11**., 738–742 (Sept. 2015). DOI: 10.1038/nphys3403 (cit. on p. 9).

[78] Edge, G. J. A., R. Anderson, D. Jervis, D. C. McKay, R. Day, S. Trotzky, and J. H. Thywissen. *Imaging and Addressing of Individual Fermionic Atoms in an Optical Lattice*, Physical Review A **92**., 063406 (Dec. 8, 2015). DOI: 10.1103/PhysRevA.92.063406 (cit. on p. 9).

[79] Greif, D., M. F. Parsons, A. Mazurenko, C. S. Chiu, S. Blatt, F. Huber, G. Ji, and M. Greiner. *Site-Resolved Imaging of a Fermionic Mott Insulator*, Science **351**., 953–957 (Feb. 26, 2016). DOI: 10.1126/science.aad9041 (cit. on p. 10).

[80] Cheuk, L. W., M. A. Nichols, K. R. Lawrence, M. Okan, H. Zhang, and M. W. Zwierlein. *Observation of 2D Fermionic Mott Insulators of $^{40}\mathrm{K}$ with Single-Site Resolution*, Physical Review Letters **116**., 235301 (June 10, 2016). DOI: 10.1103/PhysRevLett.116.235301 (cit. on p. 10).

[81] Parsons, M. F., A. Mazurenko, C. S. Chiu, G. Ji, D. Greif, and M. Greiner. *Site-Resolved Measurement of the Spin-Correlation Function in the Fermi-Hubbard Model*, Science **353**., 1253–1256 (Sept. 16, 2016). DOI: 10.1126/science.aag1430 (cit. on p. 10).

[82] Cheuk, L. W., M. A. Nichols, K. R. Lawrence, M. Okan, H. Zhang, E. Khatami, N. Trivedi, T. Paiva, M. Rigol, and M. W. Zwierlein. *Observation of Spatial Charge and Spin Correlations in the 2D Fermi-Hubbard Model*, Science **353**., 1260–1264 (Sept. 16, 2016). DOI: 10.1126/science.aag3349 (cit. on p. 10).

[83] Cocchi, E., L. A. Miller, J. H. Drewes, M. Koschorreck, D. Pertot, F. Brennecke, and M. Köhl. *Equation of State of the Two-Dimensional Hubbard Model*, Physical Review Letters **116**., 175301 (Apr. 25, 2016). DOI: 10.1103/PhysRevLett.116.175301 (cit. on p. 10).

[84] Chiu, C. S., G. Ji, A. Bohrdt, M. Xu, M. Knap, E. Demler, F. Grusdt, M. Greiner, and D. Greif. *String Patterns in the Doped Hubbard Model*, Science **365**., 251–256 (July 19, 2019). DOI: 10.1126/science.aav3587 (cit. on p. 10).

[85] Ji, G. *et al. Coupling a Mobile Hole to an Antiferromagnetic Spin Background: Transient Dynamics of a Magnetic Polaron*, Physical Review X **11**., 021022 (Apr. 27, 2021). DOI: 10.1103/PhysRevX.11.021022 (cit. on p. 10).

[86] Koepsell, J., J. Vijayan, P. Sompet, F. Grusdt, T. A. Hilker, E. Demler, G. Salomon, I. Bloch, and C. Gross. *Imaging Magnetic Polarons in the Doped Fermi–Hubbard Model*, Nature **572**., 358–362 (Aug. 2019). DOI: 10.1038/s41586-019-1463-1 (cit. on p. 10).

[87] Koepsell, J. *et al. Microscopic Evolution of Doped Mott Insulators from Polaronic Metal to Fermi Liquid*, Science **374**., 82–86 (Oct. 2021). DOI: 10.1126/science.abe7165 (cit. on p. 10).

[88] Nichols, M. A., L. W. Cheuk, M. Okan, T. R. Hartke, E. Mendez, T. Senthil, E. Khatami, H. Zhang, and M. W. Zwierlein. *Spin Transport in a Mott Insulator of Ultracold Fermions*, Science **363**., 383–387 (Dec. 2018). DOI: 10.1126/science.aat4387 (cit. on p. 10).

[89] Hartke, T., B. Oreg, C. Turnbaugh, N. Jia, and M. Zwierlein. *Direct Observation of Nonlocal Fermion Pairing in an Attractive Fermi-Hubbard Gas*, Science **381**., 82–86 (July 7, 2023). DOI: 10.1126/science.ade4245 (cit. on p. 10).

[90] Brown, P. T., D. Mitra, E. Guardado-Sanchez, P. Schauß, S. S. Kondov, E. Khatami, T. Paiva, N. Trivedi, D. A. Huse, and W. S. Bakr. *Spin-Imbalance in a 2D Fermi-Hubbard System*, Science **357**., 1385–1388 (Sept. 29, 2017). DOI: 10.1126/science.aam7838 (cit. on p. 10).

[91] Brown, P. T. *et al. Bad Metallic Transport in a Cold Atom Fermi-Hubbard System*, Science **363**., 379–382 (Jan. 25, 2019). DOI: 10.1126/science.aat4134 (cit. on p. 10).

[92] Gall, M., N. Wurz, J. Samland, C. F. Chan, and M. Köhl. *Competing Magnetic Orders in a Bilayer Hubbard Model with Ultracold Atoms*, Nature **589**., 40–43 (Jan. 7, 2021). DOI: 10.1038/s41586-020-03058-x (cit. on p. 10).

[93] Boll, M., T. A. Hilker, G. Salomon, A. Omran, J. Nespolo, L. Pollet, I. Bloch, and C. Gross. *Spin- and Density-Resolved Microscopy of Antiferromagnetic Correlations in Fermi-Hubbard Chains*, Science **353**., 1257–1260 (Sept. 16, 2016). DOI: 10.1126/science.aag1635 (cit. on pp. 10, 46).

[94] Koepsell, J., S. Hirthe, D. Bourgund, P. Sompet, J. Vijayan, G. Salomon, C. Gross, and I. Bloch. *Robust Bilayer Charge Pumping for Spin- and Density-Resolved Quantum Gas Microscopy*, Physical Review Letters **125**., 010403 (July 2, 2020). DOI: 10.1103/PhysRevLett.125.010403 (cit. on p. 10).

[95] Hartke, T., B. Oreg, N. Jia, and M. Zwierlein. *Doublon-Hole Correlations and Fluctuation Thermometry in a Fermi-Hubbard Gas*, Physical Review Letters **125**., 113601 (Sept. 2020). DOI: 10.1103/physrevlett.125.113601 (cit. on p. 10).

[96] Yan, Z. Z., B. M. Spar, M. L. Prichard, S. Chi, H.-T. Wei, E. Ibarra-García-Padilla, K. R. Hazzard, and W. S. Bakr. *Two-Dimensional Programmable Tweezer Arrays of Fermions*, Physical Review Letters **129**., 123201 (Sept. 2022). DOI: 10.1103/physrevlett.129.123201 (cit. on p. 10).

[97] Mongkolkiattichai, J., L. Liu, D. Garwood, J. Yang, and P. Schauss. *Quantum Gas Microscopy of Fermionic Triangular-Lattice Mott Insulators*, Physical Review A **108**., l061301 (Dec. 2023). DOI: 10.1103/physreva.108.l061301 (cit. on p. 10).

[98] Brown, P. T., E. Guardado-Sanchez, B. M. Spar, E. W. Huang, T. P. Devereaux, and W. S. Bakr. *Angle-Resolved Photoemission Spectroscopy of a Fermi–Hubbard System*, Nature Physics **16**., 26–31 (Jan. 2020). DOI: 10.1038/s41567-019-0696-0 (cit. on p. 10).

[99] Shao, H.-J. *et al. Antiferromagnetic Phase Transition in a 3D Fermionic Hubbard Model*, Nature **632**., 267–272 (Aug. 2024). DOI: 10.1038/s41586-024-07689-2 (cit. on p. 10).

[100] Lebrat, M., M. Xu, L. H. Kendrick, A. Kale, Y. Gang, P. Seetharaman, I. Morera, E. Khatami, E. Demler, and M. Greiner. *Observation of Nagaoka Polarons in a Fermi–Hubbard Quantum Simulator*, Nature **629**., 317–322 (May 9, 2024). DOI: 10.1038/s41586-024-07272-9 (cit. on p. 10).

[101] Prichard, M. L., B. M. Spar, I. Morera, E. Demler, Z. Z. Yan, and W. S. Bakr. *Directly Imaging Spin Polarons in a Kinetically Frustrated Hubbard System*, Nature **629**., 323–328 (May 9, 2024). DOI: 10.1038/s41586-024-07356-6 (cit. on p. 10).

[102] Xu, M., L. H. Kendrick, A. Kale, Y. Gang, G. Ji, R. T. Scalettar, M. Lebrat, and M. Greiner. *Frustration- and Doping-Induced Magnetism in a Fermi–Hubbard Simulator*, Nature **620**., 971–976 (Aug. 31, 2023). DOI: 10.1038/s41586-023-06280-5 (cit. on p. 10).

[103] Young, A. W., W. J. Eckner, N. Schine, A. M. Childs, and A. M. Kaufman. *Tweezer-Programmable 2D Quantum Walks in a Hubbard-regime Lattice*, Science **377**., 885–889 (Aug. 19, 2022). DOI: 10.1126/science.abo0608 (cit. on p. 10).

[104] Meng, Z., L. Wang, W. Han, F. Liu, K. Wen, C. Gao, P. Wang, C. Chin, and J. Zhang. *Atomic Bose–Einstein Condensate in Twisted-Bilayer Optical Lattices*, Nature **615**., 231–236 (Mar. 9, 2023). DOI: 10.1038/s41586-023-05695-4 (cit. on p. 10).

[105] Hofrichter, C., L. Riegger, F. Scazza, M. Höfer, D. R. Fernandes, I. Bloch, and S. Fölling. *Direct Probing of the Mott Crossover in the SU (N) Fermi-Hubbard Model*, Physical Review X **6**., 021030 (June 1, 2016). DOI: 10.1103/PhysRevX.6.021030 (cit. on p. 10).

[106] Ozawa, H., S. Taie, Y. Takasu, and Y. Takahashi. *Antiferromagnetic Spin Correlation of SU (N) Fermi Gas in an Optical Superlattice*, Physical Review Letters **121**., 225303 (Nov. 28, 2018). DOI: 10.1103/PhysRevLett.121.225303 (cit. on p. 10).

[107] Taie, S., E. Ibarra-García-Padilla, N. Nishizawa, Y. Takasu, Y. Kuno, H.-T. Wei, R. T. Scalettar, K. R. A. Hazzard, and Y. Takahashi. *Observation of Antiferromagnetic Correlations in an Ultracold SU(N) Hubbard Model*, Nature Physics **18**., 1356–1361 (Oct. 15, 2020). DOI: 10.1038/s41567-022-01725-6 (cit. on p. 10).

[108] Tusi, D. *et al. Flavour-Selective Localization in Interacting Lattice Fermions*, Nature Physics **18**., 1201–1205 (Oct. 2022). DOI: 10.1038/s41567-022-01726-5 (cit. on p. 10).

[109] Kiesel, F. "Cooling ^{6}Li to Quantum Degeneracy by ^{166}Er in a Novel Ultracold Fermi-Bose Gas Mixture." PhD thesis. University of Tuebingen, 2025 (cit. on pp. 10, 12, 14, 18, 20, 23, 28, 30, 32, 42, 47, 49, 56, 62, 67, 73–75, 83, 95, 100, 102, 104, 107, 122).

[110] Stellmer, S., B. Pasquiou, R. Grimm, and F. Schreck. *Laser Cooling to Quantum Degeneracy*, Physical Review Letters **110**. (June 2013). DOI: 10.1103/physrevlett.110.263003 (cit. on pp. 10, 16).

[111] Urvoy, A., Z. Vendeiro, J. Ramette, A. Adiyatullin, and V. Vuletić. *Direct Laser Cooling to Bose-Einstein Condensation in a Dipole Trap*, Physical Review Letters **122**., 203202 (May 2019). DOI: 10.1103/physrevlett.122.203202 (cit. on p. 10).

[112] Aikawa, K., A. Frisch, M. Mark, S. Baier, R. Grimm, and F. Ferlaino. *Reaching Fermi Degeneracy via Universal Dipolar Scattering*, Physical Review Letters **112**. (Jan. 2014). DOI: 10.1103/physrevlett.112.010404 (cit. on pp. 11, 25).

[113] Lu, M., N. Q. Burdick, and B. L. Lev. *Quantum Degenerate Dipolar Fermi Gas*, Physical Review Letters **108**. (May 2012). DOI: 10.1103/physrevlett.108.215301 (cit. on p. 11).

[114] Hadzibabic, Z., C. A. Stan, K. Dieckmann, S. Gupta, M. W. Zwierlein, A. Görlitz, and W. Ketterle. *Two-Species Mixture of Quantum Degenerate Bose and Fermi Gases*, Physical Review Letters **88**., 160401 (Apr. 4, 2002). DOI: 10.1103/PhysRevLett.88.160401 (cit. on p. 11).

[115] DeMarco, B., S. B. Papp, and D. S. Jin. *Pauli Blocking of Collisions in a Quantum Degenerate Atomic Fermi Gas*, Physical Review Letters **86**., 5409–5412 (June 11, 2001). DOI: 10.1103/PhysRevLett.86.5409 (cit. on p. 11).

[116] Geist, W. and T. A. B. Kennedy. *Evaporative Cooling of Mixed Atomic Fermions*, Physical Review A **65**., 063617 (June 2002). DOI: 10.1103/physreva.65.063617 (cit. on p. 11).

[117] Partridge, G. B., W. Li, R. I. Kamar, Y.-a. Liao, and R. G. Hulet. *Pairing and Phase Separation in a Polarized Fermi Gas*, Science **311**., 503–505 (Jan. 27, 2006). DOI: 10.1126/science.1122876 (cit. on pp. 11, 13).

[118] Ku, M. J. H., A. T. Sommer, L. W. Cheuk, and M. W. Zwierlein. *Revealing the Superfluid Lambda Transition in the Universal Thermodynamics of a Unitary Fermi Gas*, Science **335**., 563–567 (Feb. 2012). DOI: 10.1126/science.1214987 (cit. on p. 11).

[119] Helson, V., T. Zwettler, F. Mivehvar, E. Colella, K. Roux, H. Konishi, H. Ritsch, and J.-P. Brantut. *Density-Wave Ordering in a Unitary Fermi Gas with Photon-Mediated Interactions*, Nature **618**., 716–720 (June 22, 2023). DOI: 10.1038/s41586-023-06018-3 (cit. on p. 11).

[120] Stellmer, S., R. Grimm, and F. Schreck. *Production of Quantum-Degenerate Strontium Gases*, Physical Review A **87**. (Jan. 2013). DOI: 10.1103/physreva.87.013611 (cit. on p. 11).

[121] Hara, H., Y. Takasu, Y. Yamaoka, J. M. Doyle, and Y. Takahashi. *Quantum Degenerate Mixtures of Alkali and Alkaline-Earth-Like Atoms*, Physical Review Letters **106**., 205304 (May 19, 2011). DOI: 10.1103/PhysRevLett.106.205304 (cit. on pp. 11, 13, 30).

[122] Ravensbergen, C., V. Corre, E. Soave, M. Kreyer, E. Kirilov, and R. Grimm. *Production of a Degenerate Fermi-Fermi Mixture of Dysprosium and Potassium Atoms*, Physical Review A **98**., 063624 (Dec. 20, 2018). DOI: 10.1103/PhysRevA.98.063624 (cit. on p. 11).

[123] Lous, R. S., I. Fritsche, M. Jag, B. Huang, and R. Grimm. *Thermometry of a Deeply Degenerate Fermi Gas with a Bose-Einstein Condensate*, Physical Review A **95**., 053627 (May 2017). DOI: 10.1103/physreva.95.053627 (cit. on pp. 12, 108).

[124] Yao, X.-C., H.-Z. Chen, Y.-P. Wu, X.-P. Liu, X.-Q. Wang, X. Jiang, Y. Deng, Y.-A. Chen, and J.-W. Pan. *Observation of Coupled Vortex Lattices in a Mass-Imbalance Bose and Fermi Superfluid Mixture*, Physical Review Letters **117**., 145301 (Sept. 27, 2016). DOI: 10.1103/PhysRevLett.117.145301 (cit. on p. 13).

[125] Lous, R. S., I. Fritsche, M. Jag, F. Lehmann, E. Kirilov, B. Huang, and R. Grimm. *Probing the Interface of a Phase-Separated State in a Repulsive Bose-Fermi Mixture*, Physical Review Letters **120**., 243403 (June 2018). DOI: 10.1103/physrevlett.120.243403 (cit. on p. 13).

[126] Papp, S. B., J. M. Pino, and C. E. Wieman. *Tunable Miscibility in a Dual-Species Bose-Einstein Condensate*, Physical Review Letters **101**., 040402 (July 24, 2008). DOI: 10.1103/PhysRevLett.101.040402 (cit. on p. 13).

[127] DeSalvo, B. J., K. Patel, J. Johansen, and C. Chin. *Observation of a Degenerate Fermi Gas Trapped by a Bose-Einstein Condensate*, Physical Review Letters **119**., 233401 (Dec. 2017). DOI: 10.1103/physrevlett.119.233401 (cit. on p. 13).

[128] Modugno, G., G. Roati, F. Riboli, F. Ferlaino, R. J. Brecha, and M. Inguscio. *Collapse of a Degenerate Fermi Gas*, Science **297**., 2240–2243 (Sept. 27, 2002). DOI: 10.1126/science.1077386 (cit. on p. 13).

[129] Grimm, R. and C. Baroni. *Fermionic Quantum Mixtures with Tunable Interactions*, (Nov. 2023). DOI: 10.48550/ARXIV.2311.01220 (cit. on p. 13).

[130] Shin, Y., M. W. Zwierlein, C. H. Schunck, A. Schirotzek, and W. Ketterle. *Observation of Phase Separation in a Strongly Interacting Imbalanced Fermi Gas*, Physical Review Letters **97**., 030401 (July 18, 2006). DOI: 10.1103/PhysRevLett.97.030401 (cit. on p. 13).

[131] Ketterle, W. and M. W. Zwierlein. *Making, Probing and Understanding Ultracold Fermi Gases*, (Jan. 2008). DOI: 10.1393/ncr/i2008-10033-1 (cit. on pp. 14, 93, 101, 104, 106, 122).

[132] Onofrio, R. *Cooling and Thermometry of Atomic Fermi Gases*, Physics-Uspekhi **59**., 1129–1153 (Nov. 1, 2016) (cit. on p. 14).

[133] Bali, S., K. M. O'Hara, M. E. Gehm, S. R. Granade, and J. E. Thomas. *Quantum-Diffractive Background Gas Collisions in Atom-Trap Heating and Loss*, Physical Review A **60**., R29–R32 (July 1999). DOI: 10.1103/physreva.60.r29 (cit. on pp. 14, 15).

[134] Grimm, R., M. Weidemüller, and Y. B. Ovchinnikov. *Optical Dipole Traps for Neutral Atoms*, Advances In Atomic, Molecular, and Optical Physics, 95–170 (2000). DOI: 10.1016/s1049-250x(08)60186-x (cit. on pp. 15, 84, 86, 87).

[135] Timmermans, E. *Degenerate Fermion Gas Heating by Hole Creation*, Physical Review Letters **87**., 240403 (Nov. 2001). DOI: 10.1103/physrevlett.87.240403 (cit. on p. 15).

[136] Côté, R., R. Onofrio, and E. Timmermans. *Sympathetic Cooling Route to Bose-Einstein Condensate and Fermi-liquid Mixtures*, Physical Review A **72**., 041605 (Oct. 27, 2005). DOI: 10.1103/PhysRevA.72.041605 (cit. on p. 15).

[137] Savard, T. A., K. M. O'Hara, and J. E. Thomas. *Laser-Noise-Induced Heating in Far-off Resonance Optical Traps*, Physical Review A **56**., R1095–R1098 (Aug. 1, 1997). DOI: 10.1103/PhysRevA.56.R1095 (cit. on p. 15).

[138] Gehm, M. E., K. M. O'Hara, T. A. Savard, and J. E. Thomas. *Dynamics of Noise-Induced Heating in Atom Traps*, Physical Review A **58**., 3914–3921 (Nov. 1, 1998). DOI: 10.1103/PhysRevA.58.3914 (cit. on p. 15).

[139] Partes, C. "FPGA-based Laser Intensity Stabilization for the Suppression of Noise-Induced Atom Heating in Optical Lattices." BA thesis. University of Tübingen, 2025 (cit. on p. 15).

[140] Xu, M. "Quantum Phases in Fermi Hubbard Systems with Tunable Frustration." PhD thesis. Harvard University, 2025 (cit. on p. 15).

[141] Höhn, T. O., E. Staub, G. Brochier, N. D. Oppong, and M. Aidelsburger. *State-Dependent Potentials for the 1S0 and 3P0 Clock States of Neutral Ytterbium Atoms*, (May 2023). DOI: 10.48550/ARXIV.2305.20084 (cit. on pp. 15, 17, 18, 89, 96).

[142] Arora, B., M. S. Safronova, and C. W. Clark. *Tune-out Wavelengths of Alkali-Metal Atoms and Their Applications*, Physical Review A **84**., 043401 (Oct. 2011). DOI: 10.1103/physreva.84.043401 (cit. on p. 17).

[143] Kao, W., Y. Tang, N. Q. Burdick, and B. L. Lev. *Anisotropic Dependence of Tune-out Wavelength near Dy 741-Nm Transition*, Optics Express **25**., 3411 (Feb. 2017). DOI: 10.1364/oe.25.003411 (cit. on pp. 17, 96).

[144] Catani, J., G. Barontini, G. Lamporesi, F. Rabatti, G. Thalhammer, F. Minardi, S. Stringari, and M. Inguscio. *Entropy Exchange in a Mixture of Ultracold Atoms*, Physical Review Letters **103**., 140401 (Sept. 2009). DOI: 10.1103/physrevlett.103.140401 (cit. on pp. 17, 18, 96).

[145] Copenhaver, E., K. Cassella, R. Berghaus, and H. Müller. *Measurement of a Li7 Tune-out Wavelength by Phase-Patterned Atom Interferometry*, Physical Review A **100**., 063603 (Dec. 2019). DOI: 10.1103/physreva.100.063603 (cit. on p. 17).

[146] Décamps, B., J. Vigué, A. Gauguet, and M. Büchner. *Measurement of the 671-Nm Tune-out Wavelength of Li7 by Atom Interferometry*, Physical Review A **101**., 033614 (Mar. 2020). DOI: 10.1103/physreva.101.033614 (cit. on p. 17).

[147] Holmgren, W. F., R. Trubko, I. Hromada, and A. D. Cronin. *Measurement of a Wavelength of Light for Which the Energy Shift for an Atom Vanishes*, Physical Review Letters **109**., 243004 (Dec. 2012). DOI: 10.1103/physrevlett.109.243004 (cit. on pp. 17, 96).

[148] Trubko, R., M. D. Gregoire, W. F. Holmgren, and A. D. Cronin. *Potassium Tune-out-Wavelength Measurement Using Atom Interferometry and a Multipass Optical Cavity*, Physical Review A **95**., 052507 (May 2017). DOI: 10.1103/physreva.95.052507 (cit. on p. 17).

[149] McKay, D. C. *Slow Thermalization between a Lattice and Free Bose Gas*, Physical Review Letters **111**. (2013). DOI: 10.1103/PhysRevLett.111.063002 (cit. on p. 17).

[150] Herold, C. D., V. D. Vaidya, X. Li, S. L. Rolston, J. V. Porto, and M. S. Safronova. *Precision Measurement of Transition Matrix Elements via Light Shift Cancellation*, Physical Review Letters **109**., 243003 (Dec. 2012). DOI: 10.1103/physrevlett.109.243003 (cit. on pp. 17, 96).

[151] Leonard, R. H., A. J. Fallon, C. A. Sackett, and M. S. Safronova. *High-Precision Measurements of the Rb87 D-line Tune-out Wavelength*, Physical Review A **92**., 052501 (Nov. 2015). DOI: 10.1103/physreva.92.052501 (cit. on pp. 17, 96).

[152] Schmidt, F., D. Mayer, M. Hohmann, T. Lausch, F. Kindermann, and A. Widera. *Precision Measurement of the Rb87 Tune-out Wavelength in the Hyperfine Ground State F=1 at 790 Nm*, Physical Review A **93**., 022507 (Feb. 2016). DOI: 10.1103/physreva.93.022507 (cit. on pp. 17, 96).

[153] Rubio-Abadal, A., J.-y. Choi, J. Zeiher, S. Hollerith, J. Rui, I. Bloch, and C. Gross. *Many-Body Delocalization in the Presence of a Quantum Bath*, Physical Review X **9**., 041014 (Oct. 2019). DOI: 10.1103/physrevx.9.041014 (cit. on p. 17).

[154] Ratkata, A., P. D. Gregory, A. D. Innes, A. J. Matthies, L. A. McArd, J. M. Mortlock, M. S. Safronova, S. L. Bromley, and S. L. Cornish. *Measurement of the Tune-out Wavelength for Cs133 at 880 Nm*, Physical Review A **104**., 052813 (Nov. 2021). DOI: 10.1103/physreva.104.052813 (cit. on pp. 17, 96).

[155] Heinz, A., A. J. Park, N. Šantić, J. Trautmann, S. G. Porsev, M. S. Safronova, I. Bloch, and S. Blatt. *State-Dependent Optical Lattices for the Strontium Optical Qubit*, Physical Review Letters **124**., 203201 (May 2020). DOI: 10.1103/physrevlett.124.203201 (cit. on pp. 17, 96).

[156] Höhn, T. O., R. A. Villela, E. Zu, L. Bezzo, R. M. Kroeze, and M. Aidelsburger. *Determining the 3P0 Excited-State Tune-out Wavelength of 174Yb in a Triple-Magic Lattice*, (Dec. 2024). DOI: 10.48550/ARXIV.2412.14163 (cit. on p. 17).

[157] Hewitt, T., T. Bertheas, M. Jain, Y. Nishida, and G. Barontini. *Controlling the Interactions in a Cold Atom Quantum Impurity System*, (Oct. 2023). DOI: 10.48550/ARXIV.2310.02771 (cit. on pp. 17, 18).

[158] Vaidya, V. D., J. Tiamsuphat, S. L. Rolston, and J. V. Porto. *Degenerate Bose-Fermi Mixtures of Rubidium and Ytterbium*, Physical Review A **92**., 043604 (Oct. 5, 2015). DOI: 10.1103/PhysRevA.92.043604 (cit. on pp. 17, 18).

[159] Lippi, E. *et al. An Experimental Platform for Studying the Heteronuclear Efimov Effect with an Ultracold Mixture of ^{6}Li and ^{133}Cs Atoms*, Few-Body Systems **66**. (Nov. 2024). DOI: 10.1007/s00601-024-01971-9 (cit. on pp. 17, 18, 30, 109).

[160] Mosk, A., S. Kraft, M. Mudrich, K. Singer, W. Wohlleben, R. Grimm, and M. Weidemüller. *Mixture of Ultracold Lithium and Cesium Atoms in an Optical Dipole Trap*, Applied Physics B **73**., 791–799 (Dec. 2001). DOI: 10.1007/s003400100743 (cit. on p. 18).

[161] Barakhshan, P., A. Bhosale, A. Kiruga, R. Eigenmann, M. S. Safronova, and B. Arora. *A Portal for High-Precision Atomic Data and Computation: Design and Best Practices*. Dec. 20, 2022. DOI: 10.48550/arXiv.2212.10665. URL: http://arxiv.org/abs/2212.10665 (visited on 10/23/2025). Pre-published (cit. on pp. 18, 90).

[162] Becher, J. H., S. Baier, K. Aikawa, M. Lepers, J.-F. Wyart, O. Dulieu, and F. Ferlaino. *Anisotropic Polarizability of Erbium Atoms*, Physical Review A **97**. (Jan. 2018). DOI: 10.1103/physreva.97.012509 (cit. on pp. 18, 19, 88, 90, 98).

[163] Frisch, A. "Dipolar Quantum Gases of Erbium." PhD thesis. University of Innsbruck, 2014 (cit. on pp. 20, 21, 24, 28, 33, 34, 36, 39, 40).

[164] Phelps, G. "A Dipolar Quantum Gas Microscope." PhD thesis. Harvard University, 2019 (cit. on pp. 21, 33, 40).

[165] Frisch, A., K. Aikawa, M. Mark, F. Ferlaino, E. Berseneva, and S. Kotochigova. *Hyperfine Structure of Laser-Cooling Transitions in Fermionic Erbium-167*, Physical Review A **88**. (Sept. 2013). DOI: 10.1103/physreva.88.032508 (cit. on pp. 22, 90).

[166] Arimondo, E., M. Inguscio, and P. Violino. *Experimental Determinations of the Hyperfine Structure in the Alkali Atoms*, Reviews of Modern Physics **49**., 31–75 (Jan. 1, 1977). DOI: 10.1103/RevModPhys.49.31 (cit. on p. 23).

[167] Judd, B. R. and I. Lindgren. *Theory of Zeeman Effect in the Ground Multiplets of Rare-Earth Atoms*, Physical Review **122**., 1802–1812 (June 1961). DOI: 10.1103/physrev.122.1802 (cit. on pp. 23, 24).

[168] Conway, J. G. and B. G. Wybourne. *Low-Lying Energy Levels of Lanthanide Atoms and Intermediate Coupling*, Physical Review **130**., 2325–2332 (June 15, 1963). DOI: 10.1103/PhysRev.130.2325 (cit. on p. 23).

[169] Frisch, A., M. Mark, K. Aikawa, F. Ferlaino, J. L. Bohn, C. Makrides, A. Petrov, and S. Kotochigova. *Quantum Chaos in Ultracold Collisions of Gas-Phase Erbium Atoms*, Nature **507**., 475–479 (Mar. 2014). DOI: 10.1038/nature13137 (cit. on pp. 24, 82).

[170] Krstajić, M., P. Juhász, J. Kučera, L. R. Hofer, G. Lamb, A. L. Marchant, and R. P. Smith. *Characterization of Three-Body Loss in ^{166}Er and Optimized Production of Large Bose-Einstein Condensates*, Physical Review A **108**., 063301 (Dec. 1, 2023). DOI: 10.1103/PhysRevA.108.063301 (cit. on pp. 24, 102).

[171] Schäfer, F., N. Mizukami, and Y. Takahashi. *Feshbach Resonances of Large-Mass-Imbalance Er-Li Mixtures*, Physical Review A **105**., 012816 (Jan. 24, 2022). DOI: 10.1103/PhysRevA.105.012816 (cit. on pp. 24, 109).

[172] Schäfer, F., Y. Haruna, and Y. Takahashi. *Observation of Feshbach Resonances in an ^{167}Er-^{6}Li Fermi-Fermi Mixture*, (Feb. 2023). DOI: 10.48550/ARXIV.2302.14253 (cit. on p. 24).

[173] González-Martínez, M. L. and P. S. Żuchowski. *Magnetically Tunable Feshbach Resonances in Li+Er*, Physical Review A **92**., 022708 (Aug. 24, 2015). DOI: 10.1103/PhysRevA.92.022708 (cit. on p. 25).

[174] Bohn, J. L., M. Cavagnero, and C. Ticknor. *Quasi-Universal Dipolar Scattering in Cold and Ultracold Gases*, New Journal of Physics **11**., 055039 (May 2009). DOI: 10.1088/1367-2630/11/5/055039 (cit. on p. 25).

[175] Lahaye, T., T. Koch, B. Fröhlich, M. Fattori, J. Metz, A. Griesmaier, S. Giovanazzi, and T. Pfau. *Strong Dipolar Effects in a Quantum Ferrofluid*, Nature **448**., 672–675 (Aug. 2007). DOI: 10.1038/nature06036 (cit. on p. 25).

[176] Lu, M., N. Q. Burdick, S. H. Youn, and B. L. Lev. *Strongly Dipolar Bose-Einstein Condensate of Dysprosium*, Physical Review Letters **107**. (Oct. 2011). DOI: 10.1103/physrevlett.107.190401 (cit. on pp. 25, 69).

[177] Aikawa, K., A. Frisch, M. Mark, S. Baier, A. Rietzler, R. Grimm, and F. Ferlaino. *Bose-Einstein Condensation of Erbium*, Physical Review Letters **108**., 210401 (May 21, 2012). DOI: 10.1103/PhysRevLett.108.210401 (cit. on pp. 25, 30, 95).

[178] Kadau, H., M. Schmitt, M. Wenzel, C. Wink, T. Maier, I. Ferrier-Barbut, and T. Pfau. *Observing the Rosensweig Instability of a Quantum Ferrofluid*, Nature **530**., 194–197 (Feb. 2016). DOI: 10.1038/nature16485 (cit. on p. 26).

[179] Ferrier-Barbut, I., H. Kadau, M. Schmitt, M. Wenzel, and T. Pfau. *Observation of Quantum Droplets in a Strongly Dipolar Bose Gas*, Physical Review Letters **116**. (May 2016). DOI: 10.1103/physrevlett.116.215301 (cit. on p. 26).

[180] Böttcher, F., J.-N. Schmidt, M. Wenzel, J. Hertkorn, M. Guo, T. Langen, and T. Pfau. *Transient Supersolid Properties in an Array of Dipolar Quantum Droplets*, Physical Review X **9**. (Mar. 2019). DOI: 10.1103/physrevx.9.011051 (cit. on p. 26).

[181] Chomaz, L. *et al. Long-Lived and Transient Supersolid Behaviors in Dipolar Quantum Gases*, Physical Review X **9**. (Apr. 2019). DOI: 10.1103/physrevx.9.021012 (cit. on p. 26).

[182] Tanzi, L., E. Lucioni, F. Famà, J. Catani, A. Fioretti, C. Gabbanini, R. h. 1. Bisset, L. Santos, and G. Modugno. *Observation of a Dipolar Quantum Gas with Metastable Supersolid Properties*, Physical Review Letters **122**. (Apr. 2019). DOI: 10.1103/physrevlett.122.130405 (cit. on p. 26).

[183] Dalibard, J. *Laser Cooling of Atomic Gases*. Cours du Collège de France. Vol. 143. Collège de France, 2015 (cit. on pp. 26, 28, 30, 70).

[184] Barry, J. F., D. J. McCarron, E. B. Norrgard, M. H. Steinecker, and D. DeMille. *Magneto-Optical Trapping of a Diatomic Molecule*, Nature **512**., 286–289 (Aug. 21, 2014). DOI: 10.1038/nature13634 (cit. on p. 26).

[185] Patscheider, A., B. Yang, G. Natale, D. Petter, L. Chomaz, M. J. Mark, G. Hovhannesyan, M. Lepers, and F. Ferlaino. *Observation of a Narrow Inner-Shell Orbital Transition in Atomic Erbium at 1299 Nm*, Physical Review Research **3**., 033256 (Sept. 2021). DOI: 10.1103/physrevresearch.3.033256 (cit. on pp. 26, 28).

[186] McClelland, J. and J. Hanssen. *Laser Cooling without Repumping: A Magneto-Optical Trap for Erbium Atoms*, Physical Review Letters **96**. (Apr. 2006). DOI: 10.1103/physrevlett.96.143005 (cit. on pp. 26, 69, 70).

[187] Su, L., A. Douglas, M. Szurek, A. H. Hébert, A. Krahn, R. Groth, G. A. Phelps, O. Marković, and M. Greiner. *Fast Single Atom Imaging for Optical Lattice Arrays*, Nature Communications **16**., 1017 (Jan. 25, 2025). DOI: 10.1038/s41467-025-56305-y (cit. on p. 26).

[188] Frisch, A., K. Aikawa, M. Mark, A. Rietzler, J. Schindler, E. Zupanič, R. Grimm, and F. Ferlaino. *Narrow-Line Magneto-Optical Trap for Erbium*, Physical Review A **85**. (May 2012). DOI: 10.1103/physreva.85.051401 (cit. on pp. 26, 70, 72).

[189] Phelps, G. A., A. Hébert, A. Krahn, S. Dickerson, F. Öztürk, S. Ebadi, L. Su, and M. Greiner. *Sub-Second Production of a Quantum Degenerate Gas*, (July 2020) (cit. on pp. 27, 30, 60, 72, 95).

[190] Heidt, E. "Optimization of the Erbium Laser System and Implementation of a Narrow-Line Magneto-Optical Trap for the ErLi Experiment." MA thesis. University of Tübingen, 2025 (cit. on pp. 27, 49, 53, 55, 60).

[191] Kramida, A., Y. Ralchenko, J. Reader, N. A. Team, and T. Report. *NIST Atomic Spectra Database*. National Institute of Standards and Technology, Gaithersburg, MD., 2018. DOI: 10.18434/T4W30F (cit. on p. 27).

[192] Duarte, P. M., R. A. Hart, J. M. Hitchcock, T. A. Corcovilos, T.-L. Yang, A. Reed, and R. G. Hulet. *All-Optical Production of a Lithium Quantum Gas Using Narrow-Line Laser Cooling*, Physical Review A **84**., 061406 (Dec. 2011). DOI: 10.1103/physreva.84.061406 (cit. on p. 28).

[193] Chu, S., L. Hollberg, J. E. Bjorkholm, A. Cable, and A. Ashkin. *Three-Dimensional Viscous Confinement and Cooling of Atoms by Resonance Radiation Pressure*, Physical Review Letters **55**., 48–51 (July 1985). DOI: 10.1103/physrevlett.55.48 (cit. on pp. 28, 38).

[194] Cohen-Tannoudji, C., J. Dupont-Roc, and G. Grynberg. *Processus d'interaction Entre Photons et Atomes*. EDP Sciences / CNRS Éditions, 2001 (cit. on p. 30).

[195] Metcalf, H. J. and P. Van Der Straten. *Laser Cooling and Trapping*. Graduate Texts in Contemporary Physics. New York, NY: Springer New York, 1999. DOI: 10.1007/978-1-4612-1470-0 (cit. on pp. 30, 38, 70).

[196] Foot, C. J. *et al. Atomic Physics*. Vol. 7. Oxford University Press, 2005 (cit. on pp. 30, 38, 70).

[197] Hoffman, D. M., J. H. Thomas, and B. Singh. *Handbook of Vacuum Science and Technology*. San Diego, CA: Academic Press, 1998 (cit. on p. 30).

[198] O'Hanlon, J. F. *Vacuum Technology, 3rd Edition*. John Wiley & Sons, June 2003. 536 pp. (cit. on pp. 30, 35).

[199] Trautmann, A., P. Ilzhöfer, G. Durastante, C. Politi, M. Sohmen, M. J. Mark, and F. Ferlaino. *Dipolar Quantum Mixtures of Erbium and Dysprosium Atoms*, Physical Review Letters **121**., 213601 (Nov. 21, 2018). DOI: 10.1103/PhysRevLett.121.213601 (cit. on p. 30).

[200] Ravensbergen, C., E. Soave, V. Corre, M. Kreyer, B. Huang, E. Kirilov, and R. Grimm. *Resonantly Interacting Fermi-Fermi Mixture of 161Dy and 40K*, Physical Review Letters **124**., 203402 (May 2020). DOI: 10.1103/physrevlett.124.203402 (cit. on p. 30).

[201] Ivanov, V. V., A. Khramov, A. H. Hansen, W. H. Dowd, F. Münchow, A. O. Jamison, and S. Gupta. *Sympathetic Cooling in an Optically Trapped Mixture of Alkali and Spin-Singlet Atoms*, Physical Review Letters **106**., 153201 (Apr. 11, 2011). DOI: 10.1103/PhysRevLett.106.153201 (cit. on p. 30).

[202] Marti, G. E. *Two-Element Zeeman Slower for Rubidium and Lithium*, Physical Review A **81**. (2010). DOI: 10.1103/PhysRevA.81.043424 (cit. on p. 30).

[203] Hopkins, S. A., K. Butler, A. Guttridge, S. Kemp, R. Freytag, E. A. Hinds, M. R. Tarbutt, and S. L. Cornish. *A Versatile Dual-Species Zeeman Slower for Caesium and Ytterbium*, Review of Scientific Instruments **87**., 043109 (Apr. 2016). DOI: 10.1063/1.4945795 (cit. on p. 30).

[204] Krstajić, M. "Experimental Platform for a Box-Trapped Dipolar Quantum Gas." PhD thesis. University of Oxford, 2021 (cit. on pp. 33, 40).

[205] Ramsey, N. *Molecular Beams*. Oxford New York: Clarendon Press Oxford University Press, 1985 (cit. on pp. 33, 40).

[206] Kennard, E. H. *Kinetic Theory of Gases*. Ed. by McGRAW-HILL BOOK COMPANY, I. 1938 (cit. on pp. 33, 40).

[207] Schindler, J. "Characterization of an Erbium Atomic Beam." MA thesis. University of Innsbruck, 2011 (cit. on pp. 33, 34).

[208] Gray, D. E. *American Institute of Physics Handbook*. 3rd ed. New York: Mc Graw-Hill, 1982 (cit. on p. 33).

[209] Lorenz, N. "A Rydberg Tweezer Platform with Potassium Atoms." PhD thesis. Ludwig-Maximilians-Universität München, 2021 (cit. on pp. 35, 48).

[210] Maier, T. "Interactions in a Quantum Gas of Dysprosium Atoms." PhD thesis. University of Stuttgart, 2015 (cit. on p. 36).

[211] Ilzhöfer, P. "Creation of Dipolar Quantum Mixtures of Erbium and Dysprosium." PhD thesis. University of Innsbruck, 2020 (cit. on pp. 36, 37).

[212] Prodan, J., A. Migdall, W. D. Phillips, I. So, H. Metcalf, and J. Dalibard. *Stopping Atoms with Laser Light*, Physical Review Letters **54**., 992–995 (Mar. 1985). DOI: 10.1103/physrevlett.54.992 (cit. on p. 38).

[213] Joffe, M. A., W. Ketterle, A. Martin, and D. E. Pritchard. *Transverse Cooling and Deflection of an Atomic Beam inside a Zeeman Slower*, Journal of the Optical Society of America B **10**., 2257 (Dec. 1, 1993). DOI: 10.1364/JOSAB.10.002257 (cit. on p. 39).

[214] Kalia, J., J. Rivera, R. R. Emran, W. J. S. Hernandez, K. Kwon, and R. J. Fletcher. *Creation of a Degenerate Bose-Bose Mixture of Erbium and Lithium Atoms*. May 30, 2025. DOI: 10.48550/arXiv.2506.00177. URL: http://arxiv.org/abs/2506.00177 (visited on 07/21/2025). Pre-published (cit. on pp. 40, 104).

[215] Jin, S., J. Gao, K. Chandrashekara, C. Gölzhäuser, J. Schöner, and L. Chomaz. *Two-Dimensional Magneto-Optical Trap of Dysprosium Atoms as a Compact Source for Efficient Loading of a Narrow-Line Three-Dimensional Magneto-Optical Trap*, Physical Review A **108**., 023719 (Aug. 18, 2023). DOI: 10.1103/PhysRevA.108.023719 (cit. on p. 40).

[216] Greiner, M., I. Bloch, T. W. Hänsch, and T. Esslinger. *Magnetic Transport of Trapped Cold Atoms over a Large Distance*, Physical Review A **63**., 031401 (Feb. 2001). DOI: 10.1103/physreva.63.031401 (cit. on pp. 43, 77).

[217] Alnis, J., A. Matveev, N. Kolachevsky, Th. Udem, and T. W. Hänsch. *Subhertz Linewidth Diode Lasers by Stabilization to Vibrationally and Thermally Compensated Ultralow-Expansion Glass Fabry-Perot Cavities*, Physical Review A **77**., 053809 (May 12, 2008). DOI: 10.1103/PhysRevA.77.053809 (cit. on p. 48).

[218] Müller, L. "Stabilization of a Diode Laser to a High Finesse Four-Bore Ultra Low Expansion Cavity." BA thesis. University of Tuebingen, 2021 (cit. on p. 49).

[219] Auch, J. "Creation and Characterization of an Erbium MOT." MA thesis. University of Tübingen, 2023 (cit. on pp. 49, 58, 60).

[220] Drever, R. W. P., J. L. Hall, F. V. Kowalski, J. Hough, G. M. Ford, A. J. Munley, and H. Ward. *Laser Phase and Frequency Stabilization Using an Optical Resonator*, Applied Physics B **31**., 97–105 (June 1, 1983). DOI: 10.1007/BF00702605 (cit. on p. 49).

[221] Black, E. D. *An Introduction to Pound–Drever–Hall Laser Frequency Stabilization*, American Journal of Physics **69**., 79–87 (Jan. 2001). DOI: 10.1119/1.1286663 (cit. on p. 49).

[222] Walter, A.-S. "Design and Characterization of an UV-Laser System for Rydberg Experiments with Potassium." MA thesis. Technische Universität München, 2018 (cit. on p. 53).

[223] Hirthe, S. "Laser Setup for Two-PhotonRydberg Excitation of Potassium." MA thesis. Ludwig-Maximilians-Universität München, 2018 (cit. on p. 53).

[224] Adema, J. "A Low Noise Laser System for High Fidelity Rydberg Atom Manipulation." MA thesis. Technische Universität München, 2020 (cit. on p. 53).

[225] Winkler, G. "Second-Harmonic Generation from 802nm to 401nm Using a Beta-Barium Borate Crystal in an Enhancement Cavity." BA thesis. University of Tübingen, 2022 (cit. on pp. 53, 55).

[226] Boyd, R. *Nonlinear Optics*. 4th Edition. Elsevier LTD, Oxford, Apr. 1, 2020 (cit. on p. 53).

[227] Briles, T. C., D. C. Yost, A. Cingöz, J. Ye, and T. R. Schibli. *Simple Piezoelectric-Actuated Mirror with 180 kHz Servo Bandwidth*, Optics Express **18**., 9739–9746 (May 10, 2010). DOI: 10.1364/OE.18.009739 (cit. on p. 55).

[228] Liu, Z. and R. Slavík. *Optical Injection Locking: From Principle to Applications*, Journal of Lightwave Technology **38**., 43–59 (Jan. 2020). DOI: 10.1109/JLT.2019.2945718 (cit. on p. 56).

[229] Kiesel, F., K. Karpov, A. De Martino, J. Auch, and C. Gross. *Long-Term Stable Laser Injection Locking for Quasi-CW Applications*, EPJ Techniques and Instrumentation **12**., 1 (Jan. 10, 2025). DOI: 10.1140/epjti/s40485-024-00113-z (cit. on p. 56).

[230] Okoshi, T., K. Kikuchi, and A. Nakayama. *Novel Method for High Resolution Measurement of Laser Output Spectrum*, Electronics Letters **16**., 630–631 (July 31, 1980). DOI: 10.1049/el:19800437 (cit. on p. 59).

[231] Seo, B., P. Chen, Z. Chen, W. Yuan, M. Huang, S. Du, and G.-B. Jo. *Efficient Production of a Narrow-Line Erbium Magneto-Optical Trap with Two-Stage Slowing*, Physical Review A **102**. (July 2020). DOI: 10.1103/physreva.102.013319 (cit. on p. 69).

[232] Lunden, W., L. Du, M. Cantara, P. Barral, A. O. Jamison, and W. Ketterle. *Enhancing the Capture Velocity of a Dy Magneto-Optical Trap with Two-Stage Slowing*, Physical Review A **101**., 063403 (June 2020). DOI: 10.1103/physreva.101.063403 (cit. on p. 69).

[233] Plotkin-Swing, B., A. Wirth, D. Gochnauer, T. Rahman, K. E. McAlpine, and S. Gupta. *Crossed-Beam Slowing to Enhance Narrow-Line Ytterbium Magneto-Optic Traps*, Review of Scientific Instruments **91**. (Sept. 2020). DOI: 10.1063/5.0011361 (cit. on p. 69).

[234] Lu, M., S. H. Youn, and B. L. Lev. *Trapping Ultracold Dysprosium: A Highly Magnetic Gas for Dipolar Physics*, Physical Review Letters **104**. (Feb. 2010). DOI: 10.1103/physrevlett.104.063001 (cit. on pp. 69, 70).

[235] Lee, J., J. H. Lee, J. Noh, and J. Mun. *Core-Shell Magneto-Optical Trap for Alkaline-Earth-Metal-like Atoms*, Physical Review A **91**. (May 2015). DOI: 10.1103/physreva.91.053405 (cit. on p. 69).

[236] Kuwamoto, T., K. Honda, Y. Takahashi, and T. Yabuzaki. *Magneto-Optical Trapping of Yb Atoms Using an Intercombination Transition*, Physical Review A **60**., R745–R748 (Aug. 1999). DOI: 10.1103/physreva.60.r745 (cit. on p. 70).

[237] Loftus, T. H., T. Ido, M. M. Boyd, A. D. Ludlow, and J. Ye. *Narrow Line Cooling and Momentum-Space Crystals*, Physical Review A **70**. (Dec. 2004). DOI: 10.1103/physreva.70.063413 (cit. on pp. 70, 111).

[238] Berglund, A. J., S. A. Lee, and J. J. McClelland. *Sub-Doppler Laser Cooling and Magnetic Trapping of Erbium*, Physical Review A **76**., 053418 (Nov. 2007). DOI: 10.1103/physreva.76.053418 (cit. on p. 70).

[239] Maier, T., H. Kadau, M. Schmitt, A. Griesmaier, and T. Pfau. *Narrow-Line Magneto-Optical Trap for Dysprosium Atoms*, Optics Letters **39**., 3138 (May 2014). DOI: 10.1364/ol.39.003138 (cit. on p. 70).

[240] Ilzhöfer, P. *Two-Species Five-Beam Magneto-Optical Trap for Erbium and Dysprosium*, Physical Review A **97**. (2018). DOI: 10.1103/PhysRevA.97.023633 (cit. on p. 72).

[241] Abdel Karim, O., A. Muzi Falconi, R. Panza, W. Liu, and F. Scazza. *Single-Atom Imaging of ^173Yb in Optical Tweezers Loaded by a Five-Beam Magneto-Optical Trap*, Quantum Science and Technology **10**., 045019 (Aug. 2025). DOI: 10.1088/2058-9565/adf7cf (cit. on p. 72).

[242] Ravensbergen, C. "Creation of a Fermi-Fermi Mixture of Dysprosium and Potassium with Resonant Interactions." PhD thesis. University of Innsbruck, 2020 (cit. on p. 75).

[243] Wu, Y.-P., X.-C. Yao, H.-Z. Chen, X.-P. Liu, X.-Q. Wang, Y.-A. Chen, and J.-W. Pan. *A Quantum Degenerate Bose–Fermi Mixture Of^{41} K And^{6} Li*, Journal of Physics B: Atomic, Molecular and Optical Physics **50**., 094001 (May 15, 2017). DOI: 10.1088/1361-6455/aa658b (cit. on p. 77).

[244] Pertot, D., D. Greif, S. Albert, B. Gadway, and D. Schneble. *Versatile Transporter Apparatus for Experiments with Optically Trapped Bose–Einstein Condensates*, Journal of Physics B: Atomic, Molecular and Optical Physics **42**., 215305 (Nov. 14, 2009). DOI: 10.1088/0953-4075/42/21/215305 (cit. on p. 77).

[245] Jin, S., K. Dai, J. Verstraten, M. Dixmerias, C. Salomon, B. Peaudecerf, T. de Jongh, and T. Yefsah. *A Multi-Purpose Platform for Analog Quantum Simulation*, (Apr. 2023). DOI: 10.48550/ARXIV.2304.08433 (cit. on p. 77).

[246] Léonard, J., M. Lee, A. Morales, T. M. Karg, T. Esslinger, and T. Donner. *Optical Transport and Manipulation of an Ultracold Atomic Cloud Using Focus-Tunable Lenses*, New Journal of Physics **16**., 093028 (Sept. 2014). DOI: 10.1088/1367-2630/16/9/093028 (cit. on p. 77).

[247] Gross, Ch., H. C. J. Gan, and K. Dieckmann. *All-Optical Production and Transport of a Large Li 6 Quantum Gas in a Crossed Optical Dipole Trap*, Physical Review A **93**., 053424 (May 26, 2016). DOI: 10.1103/PhysRevA.93.053424 (cit. on p. 77).

[248] Gustavson, T. L. *Transport of Bose-Einstein Condensates with Optical Tweezers*, Physical Review Letters **88**. (2001). DOI: 10.1103/PhysRevLett.88.020401 (cit. on p. 77).

[249] Schmid, S., G. Thalhammer, K. Winkler, F. Lang, and J. H. Denschlag. *Long Distance Transport of Ultracold Atoms Using a 1D Optical Lattice*, New Journal of Physics **8**., 159–159 (Aug. 30, 2006). DOI: 10.1088/1367-2630/8/8/159 (cit. on p. 77).

[250] Unnikrishnan, G., C. Beulenkamp, D. Zhang, K. P. Zamarski, M. Landini, and H.-C. Nägerl. *Long Distance Optical Transport of Ultracold Atoms: A Compact Setup Using a Moiré Lens*, Review of Scientific Instruments **92**., 063205 (June 11, 2021). DOI: 10.1063/5.0049320 (cit. on p. 77).

[251] Juhász, P. *Optical Trapping and Transport of Ultracold Erbium Atoms*. University of Oxford, 2019 (cit. on p. 77).

[252] Schrader, D., S. Kuhr, W. Alt, M. Müller, V. Gomer, and D. Meschede. *An Optical Conveyor Belt for Single Neutral Atoms*, Applied Physics B **73**., 819–824 (Dec. 2001). DOI: 10.1007/s003400100722 (cit. on p. 77).

[253] Klostermann, T., C. R. Cabrera, H. Von Raven, J. F. Wienand, C. Schweizer, I. Bloch, and M. Aidelsburger. *Fast Long-Distance Transport of Cold Cesium Atoms*, Physical Review A **105**., 043319 (Apr. 26, 2022). DOI: 10.1103/PhysRevA.105.043319 (cit. on pp. 77, 78).

[254] Matthies, A. J., J. M. Mortlock, L. A. McArd, A. P. Raghuram, A. D. Innes, P. D. Gregory, S. L. Bromley, and S. L. Cornish. *Long-Distance Optical-Conveyor-Belt Transport of Ultracold Cs 133 and Rb 87 Atoms*, Physical Review A **109**., 023321 (Feb. 15, 2024). DOI: 10.1103/PhysRevA.109.023321 (cit. on pp. 77, 78).

[255] Marchant, A. L., S. Händel, T. P. Wiles, S. A. Hopkins, and S. L. Cornish. *Guided Transport of Ultracold Gases of Rubidium up to a Room-Temperature Dielectric Surface*, New Journal of Physics **13**., 125003 (Dec. 7, 2011). DOI: 10.1088/1367-2630/13/12/125003 (cit. on p. 77).

[256] Middelmann, T., S. Falke, C. Lisdat, and U. Sterr. *Long-Range Transport of Ultracold Atoms in a Far-Detuned One-Dimensional Optical Lattice*, New Journal of Physics **14**., 073020 (July 11, 2012). DOI: 10.1088/1367-2630/14/7/073020 (cit. on p. 77).

[257] Renn, M. J., D. Montgomery, O. Vdovin, D. Z. Anderson, C. E. Wieman, and E. A. Cornell. *Laser-Guided Atoms in Hollow-Core Optical Fibers*, Physical Review Letters **75**., 3253–3256 (Oct. 30, 1995). DOI: 10.1103/PhysRevLett.75.3253 (cit. on p. 77).

[258] Langbecker, M., R. Wirtz, F. Knoch, M. Noaman, T. Speck, and P. Windpassinger. *Highly Controlled Optical Transport of Cold Atoms into a Hollow-Core Fiber*, New Journal of Physics **20**., 083038 (Aug. 28, 2018). DOI: 10.1088/1367-2630/aad9bb (cit. on p. 77).

[259] Xu, X., K. Kim, W. Jhe, and N. Kwon. *Efficient Optical Guiding of Trapped Cold Atoms by a Hollow Laser Beam*, Physical Review A **63**., 063401 (May 4, 2001). DOI: 10.1103/PhysRevA.63.063401 (cit. on p. 77).

[260] Crane, L. "Characterization of Quasi-Bessel Beams for Long Distance Atom Transport." BA thesis. University of Tübingen, 2022 (cit. on p. 78).

[261] Durnin, J. *Exact Solutions for Nondiffracting Beams I The Scalar Theory*, Journal of the Optical Society of America A **4**., 651 (Apr. 1, 1987). DOI: 10.1364/JOSAA.4.000651 (cit. on p. 78).

[262] Brzobohatý, O., T. Cižmár, and P. Zemánek. *High Quality Quasi-Bessel Beam Generated by Round-Tip Axicon*, Optics Express **16**., 12688 (Aug. 18, 2008). DOI: 10.1364/OE.16.012688 (cit. on p. 78).

[263] Petrov, D. S. and G. V. Shlyapnikov. *Interatomic Collisions in a Tightly Confined Bose Gas*, Physical Review A **64**., 012706 (June 5, 2001). DOI: 10.1103/PhysRevA.64.012706 (cit. on p. 82).

[264] Wouters, M., J. Tempere, and J. T. Devreese. *Feshbach Resonances in a Quasi-Two-Dimensional Atomic Gas*, Physical Review A **68**., 053603 (Nov. 3, 2003). DOI: 10.1103/PhysRevA.68.053603 (cit. on p. 82).

[265] Klostermann, T. M. "Construction of a Caesium Quantum Gas Microscope." PhD thesis. Ludwig-Maximilians-Universität München, 2021 (cit. on p. 83).

[266] King, B. E. *Angular Momentum Coupling and Rabi Frequencies for Simple Atomic Transitions*, arXiv (2008) (cit. on pp. 84, 87, 89).

[267] Grynberg, G., A. Aspect, C. Fabre, and C. Cohen-Tannoudji. *Introduction to Quantum Optics*. Cambridge University Press, 2009. DOI: 10.1017/cbo9780511778261 (cit. on p. 84).

[268] Gaunt, A. L., T. F. Schmidutz, I. Gotlibovych, R. P. Smith, and Z. Hadzibabic. *Bose-Einstein Condensation of Atoms in a Uniform Potential*, Physical Review Letters **110**. (May 2013). DOI: 10.1103/physrevlett.110.200406 (cit. on p. 86).

[269] Gerbier, F. and Y. Castin. *Heating Rates for an Atom in a Far-Detuned Optical Lattice*, Physical Review A **82**., 013615 (July 13, 2010). DOI: 10.1103/PhysRevA.82.013615 (cit. on p. 86).

[270] Dalibard, J. and C. Cohen-Tannoudji. *Dressed-Atom Approach to Atomic Motion in Laser Light: The Dipole Force Revisited*, Journal of the Optical Society of America B **2**., 1707 (Nov. 1985). DOI: 10.1364/josab.2.001707 (cit. on p. 86).

[271] Ludlow, A. D., M. M. Boyd, J. Ye, E. Peik, and P. O. Schmidt. *Optical Atomic Clocks*, Reviews of Modern Physics **87**., 637–701 (June 2015). DOI: 10.1103/revmodphys.87.637 (cit. on p. 88).

[272] Lepers, M., J.-F. Wyart, and O. Dulieu. *Anisotropic Optical Trapping of Ultracold Erbium Atoms*, Physical Review A **89**. (Feb. 2014). DOI: 10.1103/physreva.89.022505 (cit. on pp. 88, 89, 98).

[273] Kien, F. L., P. Schneeweiss, and A. Rauschenbeutel. *Dynamical Polarizability of Atoms in Arbitrary Light Fields: General Theory and Application to Cesium*, The European Physical Journal D **67**. (May 2013). DOI: 10.1140/epjd/e2013-30729-x (cit. on p. 89).

[274] Li, H., J.-F. Wyart, O. Dulieu, S. Nascimbène, and M. Lepers. *Optical Trapping of Ultracold Dysprosium Atoms: Transition Probabilities, Dynamic Dipole Polarizabilities and van Der Waals C6 Coefficients*, Journal of Physics B: Atomic, Molecular and Optical Physics **50**., 014005 (Dec. 2016). DOI: 10.1088/1361-6455/50/1/014005 (cit. on pp. 89, 98).

[275] Hartog, E. A. D., J. P. Chisholm, and J. E. Lawler. *Radiative Lifetimes of Neutral Erbium*, Journal of Physics B: Atomic, Molecular and Optical Physics **43**., 155004 (July 2010). DOI: 10.1088/0953-4075/43/15/155004 (cit. on p. 90).

[276] Ketterle, W., D. S. Durfee, and D. M. Stamper-Kurn. *Making, Probing and Understanding Bose-Einstein Condensates*, (Apr. 1999) (cit. on pp. 91, 92, 104, 122).

[277] Henson, B. M., R. I. Khakimov, R. G. Dall, K. G. H. Baldwin, L.-Y. Tang, and A. G. Truscott. *Precision Measurement for Metastable Helium Atoms of the 413 Nm Tune-Out Wavelength at Which the Atomic Polarizability Vanishes*, Physical Review Letters **115**., 043004 (July 2015). DOI: 10.1103/physrevlett.115.043004 (cit. on p. 96).

[278] Bause, R., M. Li, A. Schindewolf, X.-Y. Chen, M. Duda, S. Kotochigova, I. Bloch, and X.-Y. Luo. *Tune-Out and Magic Wavelengths for Ground-State Na23K40 Molecules*, Physical Review Letters **125**., 023201 (July 2020). DOI: 10.1103/physrevlett.125.023201 (cit. on p. 96).

[279] Li, H., J.-F. Wyart, O. Dulieu, and M. Lepers. *Anisotropic Optical Trapping as a Manifestation of the Complex Electronic Structure of Ultracold Lanthanide Atoms: The Example of Holmium*, Physical Review A **95**., 062508 (June 2017). DOI: 10.1103/physreva.95.062508 (cit. on p. 98).

[280] Xie, K., X. Li, Y.-Y. Zhou, J.-H. Luo, S. Wang, Y.-Z. Nie, H.-C. Shen, Y.-A. Chen, X.-C. Yao, and J.-W. Pan. *Feshbach Spectroscopy of Ultracold Mixtures of ^{6}Li and ^{174}Dy Atoms*, (Feb. 2025). DOI: 10.48550/ARXIV.2502.08099 (cit. on p. 104).

[281] Grusdt, F., N. Mostaan, E. Demler, and L. A. P. Ardila. *Impurities and Polarons in Bosonic Quantum Gases: A Review on Recent Progress*, (Oct. 2024). DOI: 10.48550/ARXIV.2410.09413 (cit. on p. 108).

[282] Schirotzek, A., C.-H. Wu, A. Sommer, and M. W. Zwierlein. *Observation of Fermi Polarons in a Tunable Fermi Liquid of Ultracold Atoms*, Physical Review Letters **102**. (June 2009). DOI: 10.1103/physrevlett.102.230402 (cit. on p. 108).

[283] Efimov, V. *Energy Levels Arising from Resonant Two-Body Forces in a Three-Body System*, Physics Letters B **33**., 563–564 (Dec. 1970). DOI: 10.1016/0370-2693(70)90349-7 (cit. on p. 109).

[284] Blodgett, K. N., D. Peana, S. Phatak, L. M. Terry, M. P. Montes, and J. Hood. *Imaging a ^{6}Li Atom In An Optical Tweezer 2000 Times with Lambda-Enhanced Gray Molasses*, (May 2023). DOI: 10.48550/ARXIV.2305.02405 (cit. on p. 109).

[285] Chang, R., A. L. Hoendervanger, Q. Bouton, Y. Fang, T. Klafka, K. Audo, A. Aspect, C. I. Westbrook, and D. Clément. *Three-Dimensional Laser Cooling at the Doppler Limit*, Physical Review A **90**. (Dec. 2014). DOI: 10.1103/physreva.90.063407 (cit. on p. 111).

[286] Bills, D. G. *Ultimate Pressure Limitations*, Journal of Vacuum Science and Technology **6**., 166–173 (Jan. 1, 1969). DOI: 10.1116/1.1492650 (cit. on p. 125).

Acknowledgments

The past six years have been quite the adventure. From an empty room (empty as in “full of PCB”) to a fully functional lab where quantum gases are made routinely, the path was definitely challenging. This entire work was only possible thank to Christian, who had the vision for this crazy machine, and who trusted both Florian and I to set the foundations of this next-gen experiment. I want to thank him for his supervision, encouragements, crucial help for his clueless PhD students when they needed it, and his love of zip ties. It was a real pleasure to work on this project.

I want to thank Florian Kiesel, my partner in crime, for his contribution to the Lithium side of the machine, his perseverance and his reliability, but mostly for putting up with me all these years. So long, and thanks for the all brezels, Mr. Lithium!

Of course, none of the work done in this thesis could have been achieved without the hard work of our (not so) junior PhD students.
I want to thank Jonas Auch, for sticking with us since our early days. He started as a HiWi, grew as a Bachelor student, elevated himself to the position of Master student, before joining the ranks of the ErLi PhD students. You are now officially the new Mr. Erbium.
I want to thank my dear colleague and comrade Kirill Karpov for his brilliant ideas, tremendous support and remarkable productivity since his arrival. Our internal level of toxicity could never have been the same without your central contribution, a feat demonstrated once again by your explicit demand to appear in this section according to your own terms. You truly are a member of the ErLi team.
I want to thank Eduard Heidt, our freshest PhD student, for his decision of starting a doctorate in our team. He followed the same path as Jonas, starting from the youngest age, had many months to observe the situation of the lab, and yet, decided to join us for his own thesis. You knew exactly what you were signing for, and still decided to go for it. One can only respect such a reckless decision.
I can now leave the lab with peace of mind, knowing that the machine is now in such good hands!

Over the years, many other students have contributed as well. I want to thank all of them: Jan-Ole Ernst, Liam Crane, Gregor Winkler, Max Hassunah, Isabel Horrer and Roxana Wedowski for their help with many parts of our laser systems, when building everything up. And for their current help in the lab: Magnus Rusch, Christian Partes, Thomas Herrmann, whose projects are the next building blocks of the experiment.

The help of our mechanics, Norbert Stockmaier, Matthias Hoffelich and Lars Brandenberger, was essential and the machine would not be there without them. Thank you for making our never-ending list of *urgent* things to do as fast as humanly possible.

Finally, I want to thank all members of the K and Sr teams for their help, discussions, letting us steal equipment and always being friendly. Until next time, at the kickers table!

A la mémoire de mon père.